Mathematical Modeling and Direct Numerical Simulation of the Self-Assembly in Biological Chiral Lyotropic Liquid Crystals

Sayyed Ahmad Khadem

Department of Chemical Engineering

McGill University, Montreal

April 2021

A thesis submitted to McGill University in partial

fulfillment of the requirements of the degree of

Doctor of Philosophy

Dedication

To my beloved wife, Faranak, who has unwaveringly supported me in all aspects of my life since we got married,

to my loving mother, Nazi, who has thoughtfully encouraged me to pursue higher education,

to my lovely younger sister, Fatemeh, who has filled me with positive feelings at the right time when needed,

and to all ones who have wholeheartedly supported and been supporting me.

Contributions of the Authors

The author chooses the manuscript-based thesis option following the guidelines stipulated by the Faculty of Graduate and Postdoctoral Studies:

https://www.mcgill.ca/gps/thesis/guidelines/preparation

The contents of Chapters 3-6 of the present thesis are adopted from articles published in peer-reviewed journals. Chapter 6 is a collaborative project in which all experimental data have been measured and provided by the ETH collaborators. Specific mathematical derivations presented in Supplementary Note 15 has been performed by Prof. Alejandro D. Rey. All rest of the theoretical and computational works along with article writings have been performed by the author of this thesis, under the supervision of Prof. Alejandro D. Rey, who is also a co-author.

Acknowledgments

I would like to express my sincere gratitude toward numerous people, without their supports I could not have completed this thesis. First of foremost, I would like to thank my supervisor who kept my passion alive for doing original research and gave me constant guidance and support throughout my Ph.D. research. I would like to thank all members of the Materials Modeling Research Group (MMRG): Samuel Mathews, Ziheng Wang, Oscar Manuel Matus Rivas, Andre Guerra, Xiaodan Zhu, Shaden Daghash, Jonathan Monahan, Oscar Aguilar Gutiérrez, Mahdi Roohnikan, Prof. Emilio Herrera Valencia, and Isaak Daniels, for making a friendly research group together. I am also thankful to Samuel Mathews for reviewing the French translation of my thesis Abstract. I had the chance of getting to know and later making a close friend with Sina Mirzaeifard. I am not able to count his countless kindnesses; special thanks to him as he is one of my nicest friends in a very real sense.

Last but not least, I would like to thank all my family members for their continuous support, encouragement, motivation, and understanding. I would like to especially thank my wife, Faranak, who has stood shoulder to shoulder with me throughout all ups and downs we have encountered since we got married. I am grateful forever for the endless love she gives me, and I love her from the depths of my heart.

Abstract

Biological Chiral Lyotropic Liquid Crystals (BCLLCs) possess promising applications in crucial fields including advance photonic area, biomimicry, stimuli-responsive material design, and more. The wide range of structure-related applications and the highly sought after features of BCLLCs such as biodegradability and biocompatibility drive the need to thoroughly understand BCLLCs self-assembly, and as a result, this field has been placed at the forefront of research and development of advanced materials. Despite remarkable progress achieved over the past decades, the self-assembly in these materials has not been fully understood so far.

In the present Ph.D. thesis, we use multi-scale multi-transport multi-dimensional modeling and Direct Numerical Simulation to study inextricably linked phenomena of phase separation and long-range orientational ordering in the BCLLCs self-assembly, which are of paramount importance in material design and engineering. In particular, we focus on three well-known BCLLCs: collagen, β-lactoglobulin amyloid fibrils (BLG), and cellulose nanocrystals (CNC). We develop phase diagrams for collagen dispersions and explore physics governing the phase transition boundaries. Thereafter, the growth of a single cholesteric droplet is investigated to reveal mechanisms involved through structure formation within a growing chiral droplet. Furthermore, the nucleation-and-growth zone exiting in the phase diagram is explored and exhaustively characterized in the terms of fundamental quantities such as induction time, nucleation duration and droplets' size, morphology, population, growth laws, and more. Machine learning techniques are then utilized to develop wide-range correlations for the characterizations. Using free energy analyses, the physics behind the nucleation-and-growth mechanism is also elucidated in detail. Finally, we bring our focus on an in-depth understanding of the mechanisms involved in the paranematic-to-cholesteric (PN-N*) relaxation of BCLLCs. Not only do we reveal the physics behind the PN-N* relaxation, but also a novel systematic framework is proposed to estimate viscoelastic properties such as Landau elastic constant (L_1) and rotational viscosity, which are hardly measurable for BCLLCs with the existing experimental protocols.

Taken altogether, the results presented in this Ph.D. thesis deepen understanding of BCLLCs self-assembly and contribute to advance both the science and engineering aspects of this field, potentially narrowing down the gap between currently in-use experimental protocols and the sought-after material performance.

Résumé

Les Cristaux Liquides Biologiques Chiraux Lyotropes (CLBCL) possèdent des applications prometteuses dans des domaines cruciaux tels que les études photonique avancées, le biomimétisme, la conception de matériaux sensibles aux stimuli, etc. Le large éventail d'applications liées à la structure et les caractéristiques très recherchées des CLBCL, telles que la biodégradabilité et la biocompatibilité, rendent nécessaire une compréhension approfondie de l'auto-assemblage des CLBCL, et c'est pourquoi ce domaine a été placé à l'avant-garde de la recherche et du développement de matériaux avancés. Malgré les progrès remarquables réalisés au cours des dernières décennies, l'auto-assemblage de ces matériaux n'a pas encore été entièrement compris.

Dans la présente thèse de doctorat, nous utilisons la modélisation multidimensionnelle, multi-échelle et multi-transport, et la simulation numérique directe pour étudier les phénomènes inextricablement liés de séparation de phases et d'ordre d'orientation à longue distance dans l'auto-assemblage des CLBCL, qui sont d'une importance capitale dans la conception et l'ingénierie des matériaux. Nous nous concentrons en particulier sur trois CLBCL bien connus : le collagène, β-lactoglobuline fibrilles amyloïdes, et les nanocristaux de cellulose. Nous développons des diagrammes de phase pour les dispersions de collagène et explorons la physique régissant les limites de transition de phase. Par la suite, la croissance d'une gouttelette cholestérique unique est étudiée pour révéler les mécanismes impliqués par la formation de structure au sein d'une gouttelette chirale en croissance. En outre, la zone de nucléation et de croissance qui sort du diagramme de phase est explorée et caractérisée de manière exhaustive en termes de quantités fondamentales telles que le temps d'induction, la durée de nucléation et la taille des gouttelettes, la morphologie, la population, les lois de croissance, etc. Des techniques d'apprentissage automatique sont ensuite utilisées pour développer des corrélations à grande échelle pour les caractérisations. En utilisant des analyses d'énergie libre, la physique derrière le mécanisme de nucléation et de croissance est également élucidée en détail. Enfin, nous mettons l'accent sur une compréhension approfondie des mécanismes impliqués dans la relaxation paranématique-cholestérique (PN-N*) des CLBCL. Non seulement nous révélons la physique derrière la relaxation PN-N*, mais un nouveau cadre systématique est proposé pour estimer les propriétés viscoélastiques telles que la constante élastique de Landau (L1) et la viscosité rotationnelle, qui sont difficilement mesurables pour les CLBCL avec les protocoles expérimentaux existants.

Dans l'ensemble, les résultats présentés dans cette thèse de doctorat approfondissent la compréhension de l'auto-assemblage des CLBCL et contribuent à faire progresser les aspects scientifiques et techniques de ce domaine, en réduisant potentiellement l'écart entre les protocoles expérimentaux actuellement utilisés et les performances recherchées du matériau.

Contents

List of Figures

List of Tables

Chapter 1. Introduction

1.1 Thesis Motivation

"Look deep into nature, and then you will understand everything better".

Albert Einstein

Earth is about 4.54 billion years old! [1] In the course of such a long span, Nature has evolutionarily devised optimal solutions for the problems it encountered, resulting in the magnificent Nature! To name a very few examples of Nature's fascinating solutions, the color change observed in the plant and animal kingdoms (e.g. the fish Chrysiptera cyanea, the beetle Tmesisternus isabellae, the tropical plant Selaginella willdenowii) due to environmental stimuli [2-7], the transparency of cornea, the mechanical properties of bone, and more. Nature's fascinating solutions have inspired engineers and scientists to employ Nature's solutions in design and fabrication and precursor materials. This approach is known as biomimicry, and the man-made materials fabricated in this way are called bioinspired materials or biomaterials.

There is evidence that hierarchically structured biological materials (e.g. cornea, bone, tendon, beetle exocuticle, plant cell wall, etc.) have had a liquid crystalline stage in their morphogenesis through which their primary structures are formed [8]. Besides, their fibril structures have a profound impact on their properties. Therefore, the bioinspired material design can be successfully expanded through an in-depth understanding of the liquid crystalline ordering. The present Ph.D. thesis focuses on three Biological Chiral Lyotropic Liquid Crystals (BCLLCs): collagen, β-lactoglobulin amyloid fibrils (BLG), and cellulose nanocrystals (CNC) which are ubiquitously found in biological materials—Note that biological materials are those found in nature whereas, as pointed out earlier, biomaterials are man-made.

BCLLCs have shown myriad applications in the advanced material design inspired by Nature, ranging from stimuli-responsive materials in sensor design [9] to fabrication of artificial human organs mimicking their natural counterparts [10, 11]. The promising versatility of these structured materials comes from the fact that BCLLCs' constituents, known as mesogens, are self-assembled in various spatial configurations depending on conditions (e.g. concentration, pH, ionic strength, and confinement), imparting unique macroscopic properties. In other words, BCLLCs possess structure-related properties, leading to countless promising applications. For this reason, BCLLCs have received significant attention in a variety of crucial fields, as discussed in section 2.2 in detail.

Despite the crucial past and recent research, there have still been substantial questions required to be answered so that the self-assembly mechanisms of these highly structured materials, i.e. BCLLCs, can be fully understood and leveraged. Four essential challenges in this area are as follows.

First, in general, the equilibrium thermodynamic phase diagram is a vital requirement for material design. Although the phase diagram of thermotropic LCs, which are low-molecular-weight mesogens, has been thoroughly studied [12], the phase diagram of BCLLCs, which are colloidal fibrous mesogens compared to molecular thermotropic LCs, has not completely explored.

Second, understating the mechanisms involved through the growth of a single cholesteric droplet or tactoid can greatly be beneficial for tailoring material fabrication. Notwithstanding this importance, the growth of a cholesteric seed isolated from other factors (e.g. tactoid collision) has not been fully explained yet.

Third, the nucleation-and-growth stage is another key step in engineering the fabrication of these ordered materials. Although the nucleation and growth (NG) and the governing physics have well been elaborated for classical materials, this importance has not been completely understood for LCs notably BCLLCs.

Fourth, film formation flow is an essential element needed in material engineering. Cholesteric mesogens subjected to flow are aligned along the flow direction, this structure is called para-nematic. There have been impactful studies discussing the flow processing of LCs [13, 14]. However, the dynamics of relaxation from para-nematic to cholesteric in absence of flow have remained unexplored.

The importance of BCLLCs and some challenges in this field have been mentioned thus far. It can be concluded that BCLLCs have crucial applications, however, there are significant challenges that should be addressed first. In this regard, it is well worth quoting from The Physics Nobel Prize winner, P.G. de Gennes, that "liquid crystals are beautiful and mysterious; I am fond of them for both reasons." [15]

This Ph.D. thesis aims to address the above-mentioned unexplored aspects of BCLLCs. We first focus on thermodynamic equilibria to construct the phase diagram of collagen dispersions and to explore factors affecting the phase transition boundaries. We then build on that and use Direct Numerical Simulation (DNS) to understand the complex dynamics of a single growing

cholesteric tactoid embedded in the isotropic phase. Afterward, the NG mechanisms governing cholesteric microstructure formation are elucidated in detail. Finally, we investigate the relaxation of cholesteric mesogens from para-nematic to cholesteric under cylindrical confinement. It should furthermore be noted that DNS used in the present thesis is based on the numerical solution of mesoscopic governing equations, which consist of six nonlinear, stiff, fourth order Partial Differential Equations (see eqs. 2-12 and 2-13). Provided that the spatio-temporal step sizes associated with the numerical technique are sufficiently small, DNS is capable of providing a full description of the multi-scale self-assembly of BCLLCs. DNS captures the self-assembly phenomena taking place in a spatial range of nano- to micro meters, while the time-marching window can be adjusted to retain numerical stability.

The outcomes of the present thesis have deepened the understanding of BCLLCs self-assemblies, paving the way to fabricate high-performance functional materials that are sought-after in various areas such as biomimetic material fabrication [10], biosensing devices [16], stimuli-responsive materials [9], plasmonic mesostructured materials [17], and more.

1.2 Thesis Objectives

The general objective of the present Ph.D. thesis is to develop and apply Liquid Crystals Theory to further reveal underlying principles of BCLLCs self-assemblies by which a part of fundamental long-lasting challenges is addressed. In this thesis, we focus on five main objectives: (1) Development, implementation, and validation of thermodynamic and dynamic models allowing multi-scale, multi-transport, multi-dimensional simulation of BCLLCs self-assembly; (2) Calculation of thermodynamic equilibrium phase diagrams;(3) Dynamics of defect nucleation and annihilation during the growth of cholesteric tactoids in the absence of tactoidal collisions;(4) Dynamics of nucleation and growth regime;(5) Dynamics of relaxation.

The specific objectives are:

1. To formulate the system's net Helmholtz free energy by incorporation of the fundamental physics and adaption of previous theories if needed. The resulting free energy formulation is capable of accurately describing the dispersion's energy from both thermodynamics and kinetics standpoint, ultimately leading to an accurate description of BCLLCs self-assemblies.
2. To develop a foundation to construct the BCLLCs' phase diagrams; in particular, C_a-C_c and T-C_c phase diagrams of collagen fibers dispersed in acetic acid aqueous

solutions; here C_a, C_c, and T stand for acetic acid concentration, collagen fibers concentration, and temperature, respectively. The C_a-C_c phase diagram has been experimentally reported [18], hence that study is used for validation of results obtained in Objective 1. Additionally, the T-C_c phase diagram is also known as the chimney phase diagram, which is well-known in polymer science and considered as the finger-print of rod-like polymeric dispersions. This is another validation assessment of the free energy formulation developed in Objective 1.

3. To understand the factors affecting the phase transition boundaries existing in the collagen phase diagram developed in Objective 2; in particular chirality, acetic acid concentration, collagen concentration, and more.
4. To generalize the validated free energy developed Objective 1 by including the biaxiality (higher order symmetry breaking) impact and to develop dynamical governing equations to simulate the kinetics of cholesteric self-assembly as a function of time and space.
5. To apply the governing equations developed in Objective 4 and to use the C_a-C_c phase diagram constructed in Objective 2 in order to capture the dynamics of cholesteric growth through phase evolution of an isolated cholesteric seed growing in an isotropic matrix—note that isolation means the tactoidal collisions are avoided.
6. To explore the location of the NG zone existing in the biphasic zone of the collagen phase diagram obtained in Objective 2.
7. To characterize the explored NG zone found in Objective 6 in fundamental terms of drop-size distribution, drops' shape, morphology within growing drops and morphological diversities, growth laws, drops' population, and more.
8. To employ machine learning techniques to reduce the computational cost of NG simulations carried out through DNS and to develop a wide-range of correlations for the characterization obtained in Objective 7.
9. To reveal the underlying physics behind the characterizations across the NG zone, achieved in Objective 7.
10. To investigate the dynamical relaxations of BCLLCs mesogens from the para-nematic phase to the cholesteric ground state. For this purpose, the governing equations describing the orientational relaxation are used; these governing equations are obtained in Objective 4.
11. To understand the physical origins behind the relaxations' mechanisms explored in Objective 10.

12. To propose a systematic approach based on the combination of experimental observations and DNS results to estimate important viscoelastic properties such as rotational viscosity and coherence length. This objective is based on Objective 10.

1.3 Thesis Organization

The present thesis focusses on modeling, implementation, and validation of both thermodynamics and dynamics of BCLLCs self-assembly. We present fundamental physics involved in the BCLLCs self-assembly, phase diagrams and the factors controlling the miscibility boundaries, defect formation and defect escape in the evolution of cholesteric tactoids, nucleation and growth, and para-nematic to cholesteric relaxation. A detailed description follows.

Chapter 2 provides the comprehensive background required for the four following research chapters: Chapters 3, 4, 5, and 6. Specifically, Chapter 2 presents the fundamentals of liquid crystalline materials with emphasis on BCLLCs, the state-of-the-art applications of BCLLCs, the need and opportunity for Direct Numerical Simulation (DNS) for BCLLCs self-assemblies, and the theoretical and computational simulation background. The organization of the research chapters is given in Figure 1-1.

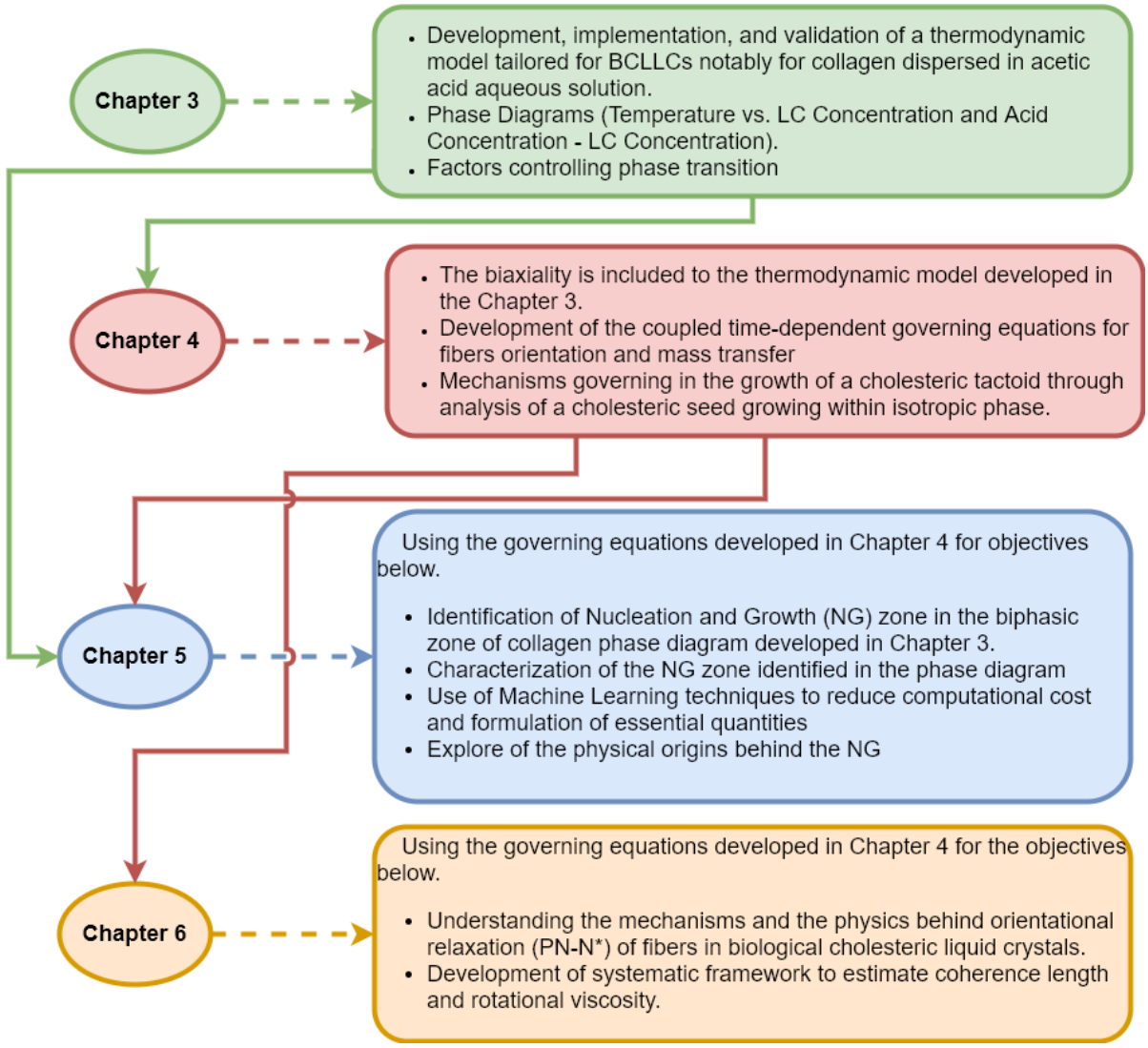

Figure 1-1. Thesis organization flowchart. In each rectangle, the objectives of the chapter are summarized. Also, the solid arrows show the connectivity between chapters.

In Chapter 3, the physics playing role in the chiral nematic phase formation of BCLLCs are identified, and free energy contributions are correspondingly considered in the total free energy of the mesophasic system. Particularly, for electrostatic repulsion, we develop simple mean-field potential instead of using the previous sophisticated theories such as Poisson–Boltzmann theory. The reason is to avoid ending up with a computationally demanding model because the developed model should be used in the governing equations, known as Model C, which itself is inevitably computationally demanding—Model C is explained in Chapters 2, 4, and 5. Thereafter, the performance of the developed thermodynamic model is assessed by the experimental data available for collagen dispersed in an acetic aqueous solution. The validation is carried out via different thermodynamic and liquid crystalline criteria such as C_a-C_c and T-

C_c phase diagrams, order parameter at isotropic-cholesteric interface known as the critical order parameter, and the asymptotic behaviors of the developed total free energy leading to the previous well-established theories. We then rely on the validated thermodynamic model to explore the factors controlling the phase transition boundaries, i.e. the lower and upper binodal curves.

In Chapter 4, the biaxiality contribution is developed and then incorporated into the total free energy to further generalize the free energy developed in Chapter 3. Furthermore, the governing equations to capture dynamics of self-assembly are developed; the governing equations describe the non-conserved field, which is the orientational configuration of mesogens, and the conserved field, which is the fibers' concentration. Finally, the governing equations are then applied to simulate the growth of a small cholesteric seed embedded within the isotropic matrix in collagen dispersions. Such simulation reveals the cholesteric growth mechanisms; in particular, defect formation and escape (frustration effect) are explained.

In Chapter 5, DNS is performed to study the kinetics of isotropic-to-cholesteric (I/N*) phase separation in the collagen dispersions for various quench depths—quench depth is a measure to quantify the percentage that the dispersion concentration exceeds the lower thermodynamic binodal curve. Through extensive simulations of I/N* demixing at various quench depth, the zone in which NG takes place is identified. Thereafter, all three NG stages, which are induction, nucleation, and coarsening, are investigated across the NG zone. Each stage is characterized in terms of the evolution of tactoids' population density, size, morphology, growth laws, and more. Although the simulations of NG by use of DNS are accurate, such simulations are computationally demanding, requiring powerful processors and long running time. For this reason, a Machine Learning technique known as Long Short-term Memory Recurrent Neural Network (LSTM-RNN) is employed to predict the coarsening dynamics; thereby reducing the running time. Afterward, all the data obtained are converted to wide-range algebraic correlations by use of classical regression and symbolic regression, which is another type of machine learning technique. These correlations are advantageous for future studies because they avoid redoing computationally demanding DNS. Finally, the physical origins behind the characterization are revealed by using rigorous free energy analysis.

In Chapter 6, the experimental observations for relaxation from para-nematic phase to chiral nematic phase in β-lactoglobulin amyloid fibrils (BLG) and cellulose nanocrystals (CNC) are first presented—all the experimental data are obtained by our ETH Zurich (Swiss Federal

Institute of Technology, Zurich) collaborators. Although these BCLLCs are similar in various aspects, BLG and CNC have shown different relaxation dynamics, called slow-fast and smooth relaxation, respectively. Afterward, DNS not only accurately predicts these unexpected relaxation behaviors but also sheds light on the underlying physics. An extensive parametric study is also carried out, leading to the generalization of the results that the dynamics relaxation behavior for BCLLCs strongly depends on material properties such as chirality, coherence length, and rotational viscosity. Additionally, a systematic platform based on the combination of experiment and simulation is proposed for estimation of rotational viscosity and coherence length, which are elusively measurable for BCLLCs with the previous conventional standard.

Finally, in Chapter 7, the main outcomes of this thesis along with the recommendation for future works are presented.

References (Chapter 1)

1. National Geographic. https://www.nationalgeographic.org/topics/resource-library-age-earth/?q=&page=1&per_page=25.

2. Liu, F.; Dong, B.; Liu, X.; Zheng, Y.; Zi, J., Structural color change in longhorn beetles Tmesisternus isabellae. Optics Express **2009,** 17 (18), 16183-16191.

3. Strout, G.; Russell, S. D.; Pulsifer, D. P.; Erten, S.; Lakhtakia, A.; Lee, D. W., Silica nanoparticles aid in structural leaf coloration in the Malaysian tropical rainforest understorey herb Mapania caudata. Annals of botany **2013,** 112 (6), 1141-1148.

4. Sun, J.; Bhushan, B.; Tong, J., Structural coloration in nature. Rsc Advances **2013,** 3 (35), 14862-14889.

5. Zhang, Y. P.; Chodavarapu, V. P.; Kirk, A. G.; Andrews, M. P., Structured color humidity indicator from reversible pitch tuning in self-assembled nanocrystalline cellulose films. Sensors and Actuators B: Chemical **2013,** 176, 692-697.

6. Hadley, N. F., Wax secretion and color phases of the desert tenebrionid beetle Cryptoglossa verrucosa (LeConte). Science **1979,** 203 (4378), 367-369.

7. Hinton, H. E.; Jarman, G. M., Physiological colour change in the elytra of the hercules beetle, Dynastes hercules. Journal of Insect Physiology **1973,** 19 (3), 533-549.

8. Neville, A. C., Biology of Fibrous Composites: Development Beyond the Cell Membrane. Cambridge University Press: 1993.

9. Kose, O.; Tran, A.; Lewis, L.; Hamad, W. Y.; MacLachlan, M. J., Unwinding a spiral of cellulose nanocrystals for stimuli-responsive stretchable optics. Nature Communications **2019,** 10 (1), 510.

10. Tidu, A.; Ghoubay-Benallaoua, D.; Teulon, C.; Asnacios, S.; Grieve, K.; Portier, F.; Schanne-Klein, M.-C.; Borderie, V.; Mosser, G., Highly concentrated collagen solutions leading to transparent scaffolds of controlled three-dimensional organizations for corneal epithelial cell colonization. Biomaterials science **2018,** 6 (6), 1492-1502.

11. Kikuchi, M.; Ikoma, T.; Itoh, S.; Matsumoto, H. N.; Koyama, Y.; Takakuda, K.; Shinomiya, K.; Tanaka, J., Biomimetic synthesis of bone-like nanocomposites using the self-organization mechanism of hydroxyapatite and collagen. Composites Science and Technology **2004,** 64 (6), 819-825.

12. Dierking, I., Polymer-modified Liquid Crystals. Royal Society of Chemistry: 2019.

13. Aguilar Gutierrez, O. F.; Rey, A. D., Biological plywood film formation from para-nematic liquid crystalline organization. Soft Matter **2017**.

14. Gutierrez, O. F. A.; Rey, A. D., Theory and Simulation of Cholesteric Film Formation Flows of Dilute Collagen Solutions. Langmuir **2016,** 32 (45), 11799-11812.

15. Gennes, P. G. d.; Prost, J., The physics of liquid crystals. 2nd ed. ed.; Clarendon Press ; Oxford University Press: Oxford, New York, 1995.

16. Popov, P.; Honaker, L. W.; Kooijman, E. E.; Mann, E. K.; Jákli, A. I., A liquid crystal biosensor for specific detection of antigens. Sensing and bio-sensing research **2016,** 8, 31-35.

17. Liu, Q.; Campbell, M. G.; Evans, J. S.; Smalyukh, I. I., Orientationally ordered colloidal co-dispersions of gold nanorods and cellulose nanocrystals. Advanced Materials **2014,** 26 (42), 7178-7184.

18. Gobeaux, F.; Belamie, E.; Mosser, G.; Davidson, P.; Panine, P.; Giraud-Guille, M. M., Cooperative Ordering of Collagen Triple Helices in the Dense State. Langmuir **2007,** 23 (11), 6411-6417.

Chapter 2. Background

2.1 Liquid Crystals (LCs)

The liquid crystalline phase possesses two features: long-range orientational order and varying positional order. The former confers the properties of crystalline solids to LCs, making LCs crystal-like. The latter bestows the properties of isotropic liquids to LCs, making LCs liquid-like. In other words, LCs possess both the crystallinity of crystals and the fluidity of isotropic liquids simultaneously. For this reason, the liquid crystalline phase is considered as an intermediate state between crystalline solids and isotropic liquids [1, 2].

In general, LCs are categorized according to the phase transition driving force, which can be temperature and/or concentration. Materials whose liquid crystalline phase emerges due to temperature change are called thermotropic LCs. On the other hand, materials whose liquid crystalline phase is concentration-driven are known as lyotropic [1, 2]. The mechanism of liquid crystalline phase formation in thermotropic and lyotropic LCs are primarily van der Waals interactions and excluded volume interactions, respectively [1, 3, 4].

The "mesogen" and "mesophase" are referred to as LC constituent (e.g. LC molecule, compound, fiber, colloid, etc.) and liquid crystalline phase, respectively. Mesogens are required to have a large aspect ratio; for example, they can be rod-like or disk-like—the present Ph.D. thesis focus on rod-like LCs. The average orientation of the long axis of mesogens is called director, represented by the unit vector, **n**, see Figure 2-1. In addition to the above-mentioned classification, based on the macroscopic orientational architecture created by **n**, LCs can be classified into three prime categories: nematic, smectic, and cholesteric, see Figure 2-1.

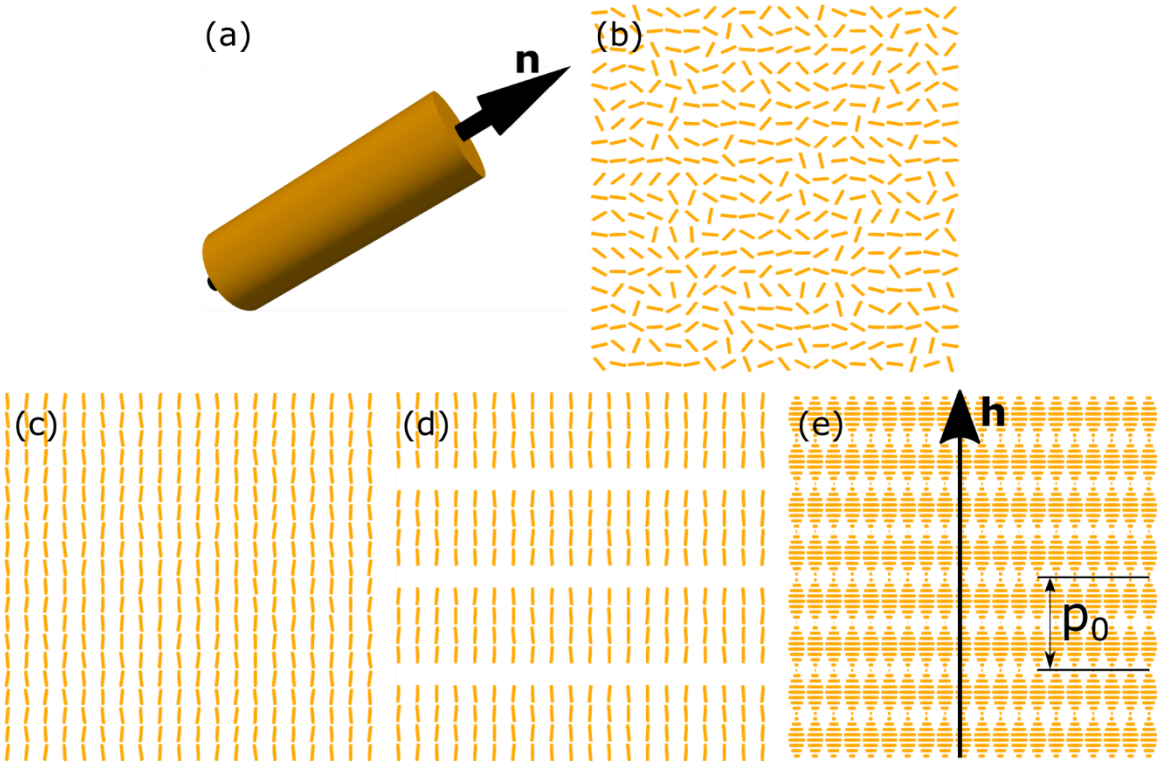

Figure 2-1. Schematic representation of (a) rod-like mesogen and director, (b) isotropic phase, (c) nematic phase, (c) smectic phase, and (d) cholesteric phase, the helix axis, and pitch length p_0.

In the isotropic phase, mesogens have neither oriental order nor positional order, see Figure 2-1. This phase is denoted by I. In the nematic phase, indicated by N, there exist orientational order in the absence of positional order. Mesogens orient so that their long axes are almost aligned along a particular direction. Unlike the nematic phase, the smectic phase retains partial positional order. The smectic phase has a layered structure; in each layer, mesogens are self-assembled similar to the nematic phase. The cholesteric phase emerges if the mesogens are intrinsically chiral or a chiral dopant is added to the nematic phase. In the cholesteric phase, denoted by N*, LC constituents have a helicoidal twist around the helical axis, **h**, which is perpendicular to the director field, **n**; hence the cholesteric phase can be considered as a multi-layer nematic phase so that the average director field slightly twist when moving from layer to layer. For this reason, the cholesteric phase is also known as twisted nematic or chiral nematic. To characterize the helicoidal twist, the distance between 2π rotation is called the pitch shown by p_0, see Figure 2-1. Furthermore, the chiral wavevector is defined as $q = 2\pi/p_0$. When the cholesteric phase is subjected to a flow, the helices unwind, and in consequence, mesogens are aligned along the flow direction. The resulting phase resembles a nematic. Under such condition, the phase is technically called para-nematic, denoted by PN. In the present Ph.D.

thesis, we bring our focus on the following liquid crystalline phase: Isotropic (I), Nematic (N), Cholesteric or Chiral Nematic or Twisted Nematic (N*), and Para-nematic (PN).

2.2 Biological Chiral Lyotropic Liquid Crystals and Applications

The present Ph.D. thesis's focus is on Biological Chiral Lyotropic Liquid Crystals (BCLLCs). In general, biological mesogens typically have elongated rod-like shape and exhibit a lyotropic phase transition [5]. The solidified state of BCLLCs can be abundantly found in nature; a few are listed in Table 2-1.

Table 2-1. Representative examples of well-known BCLLCs and their analogues in nature [1, 6, 7].

BCLLC	Biological analogues in nature
Collagen	bones, cornea, and tendon
Chitin	Exoskeleton of insects, crustaceans, and arthropods
Cellulose	Plants

BCLLCs have opened the opportunity for the fabrication of high-performance materials in crucial areas [5, 8]. In particular, three BCLLCs have been investigated in this Ph.D. thesis; Collagen, Cellulose Nanocrystals (CNC), and β-lactoglobulin Amyloid (BLG).

Three long polypeptide chains are twisted together to form a triple helical structure known as Type I Collagen. The triple helical structure has a long aspect ratio and is considered as a needle-like mesogen, making the building block of the liquid crystalline phase. The triple helical collagen commonly possesses a 1.5 nm bare diameter and 300 nm length. In addition, due to presence of special chemical groups on the collage backbone, the fibers take positive charges, leading to an effective diameter more than two or three times the bare one [9].

The chiral nematic is the widely reported mesophase for collagen. The phase transition is concentration-driven; thus, collagen dispersion falls into the class of lyotropic liquid crystals [9, 10]. The macroscopic architecture observed for collagen fibers dispersed in acidic aqueous solutions highly resembles the structured collagen-based tissues which are ubiquitously found in human soft and hard organs such as cornea, bone, tendon, etc [11]. For example, osteon is the essential building block of compact bone. In this crucial tissue, the arrangement of collagen

fibers is a cylindrically chiral structure. This structure has also been observed in collagen mesophase [12, 13], and even in other BCLLCs [14]. Furthermore, collagen mesogens can form a cornea-like structure [15]. Due to this resemblance and the fact that there are rich mammalian and non-mammalian resources for collagen as a primary precursor, the biomimetic fabrication of collagen-based tissues (e.g. artificial cornea [15, 16] and bone [17, 18]) has attracted growing interest.

The suspension of CNC leads to lyotropic cholesteric mesophase. Cellulose is the main precursor is fascinating from various aspects; cellulose is biocompatible, biodegradable, low-cost, and mass-producible [19]. Moreover, CNC has shown promising applications due to its mesophasic structures; for example, the advanced photonic applications [8, 20, 21], stimuli-responsive materials, and sensor design [22, 23].

β-lactoglobulin Amyloid, known as BLG, is a protein-based LC that possesses homogenous nematic, bipolar nematic, and cholesteric mesophases depending on the confinement volume [24]. This lyotropic fibrous mesogen has come to great interest due to its application in vital areas. For example, biology and medicine, particularly the BLG role in neurodegenerative diseases; namely Parkinson's and Alzheimer's [24, 25]. Moreover, BLG can be utilized in the manufacturing of functional materials [26].

2.3 Need for Mathematical Modelling and Direct Numerical Simulation of BCLLCs Self-assembly

Mathematical modeling and numerical simulation can greatly contribute to advance the engineering and science aspects of BCLLCs self-assembly because such theoretical studies can play a complementary role in experimental studies, avoiding trial-and-error fabrication. In particular, Direct Numerical Simulation (DNS) plays central role in revealing the mesoscopic nature of self-assembly in BCLLCs because of the fact that the spatio-temporal resolutions can be adjusted at the expense of computational costs.

Repetition of experimental runs can be both expensive and time-consuming. In this regard, theoretical studies can be advantageous. For example, in reference [9], with a considerable number of experimental runs, the phase diagram of collagen has been partly reported. Chapter 3 has shown that thermodynamics principles along with numerical techniques allow to precisely determine phase transition boundaries and to obtain a wealth of insights on how these boundaries are affected by experimental conditions. Another excellent example is Chapter 5 in which Direct Numerical Simulation (DNS) provides a thorough analysis of the nucleation and

growth of collagen tactoids (droplets). In Chapter 5, the nucleation-and-growth zone existing in the biphasic zone of the phase diagram is identified, moreover, the fundamental quantities regarding tactoids population, morphology, size, and more are characterized in detail and corresponding correlations have been reported. However, gaining such information experimentally would be significantly demanding from both time and cost perspective.

The BCLLCs self-assembly is a multi-scale phenomenon, meaning that the self-assembly contains inextricably linked sub-phenomena taking place in the range of nano-meter to micron-meter—These sub-phenomena may take place simultaneously and/or in sequence. This makes some information barely accessible in experimental research, however theoretical studies can accurately describe such multi-scale space at the expense of computational cost. In addition, theoretical studies can thoroughly capture the dynamics of BCLLCs self-assembly even at a small timescale. Chapter 4 is exemplary because it demonstrates that DNS can capture defect formation and escape, which take place in a few nano-meter and in a short time span.

More importantly, the theoretical studies are capable of rationalizing the experimental observations by which an in-depth understanding of the BCLLCs self-assembly is achieved. This can be vividly seen in Chapter 6 where theoretical analysis not only reveals the physical origins behind the observations but also generalize the results obtained from the experiment.

2.4 Equilibrium Phase Diagram

Liquid crystalline materials can exhibit various ordered phases (e.g. isotropic, nematic, cholesteric, etc.) under different conditions [9, 24]. For this reason, knowing the phase diagram and the factors controlling the phase transitions are imperative in order to take control of self-assembly. The objectives of this section are as follows. The fundamental physics involved in phase transition is discussed in section 2.4.1. Section 2.4.2 explains Onsager's landmark research which is the cornerstone in theoretical studies associated with the phase transition of lyotropic liquid crystals. Finally, section 2.4.3 elaborates the thermodynamic fundamentals for determining the boundaries of order-disorder phase transition by which the phase diagram is constructed.

2.4.1 Preliminaries

2.4.1.1 Persistence Length

In polymer science, the rigidity of a polymer chain is quantified by the persistence length, which is defined as a length "over which the orientations of the bonds become uncorrelated. [27]". Therefore, increasing persistence length indicates that the chain is more rigid. In a similar vein, the lower persistence length shows that the chain is less rigid; thus, the chain is more flexible. Furthermore, fibers are required to have high persistence length (i.e. to be rigid) in order to attain the liquid crystalline phase.

Long fibers normally take a worm-like shape in the neutral solution, driving the solution away from the liquid crystalline phase. Fibers prefer the worm-like shape, i.e. low persistence length, because the intrachain attractive force along the fiber backbone is dominant. Hence, reducing the intrachain attractive force is a practical way to reach a higher persistence length. For this purpose, the dispersion's ionic strength should be increased by for example dissolution of salt or adding an acid, making more mobile ions available. When there are more mobile ions in the dispersion, more like-charges (ions) can be deposited on the backbone of worm-like fibers. Gaining like-charges is the prime cause that worm-like fibers turn to rigid ones because like-charges deposited on the fibers backbone increases intrachain repulsive forces, leading to weakening the effect of attractive forces in the net intrachain forces along the backbone [28], see Figure 2-2.

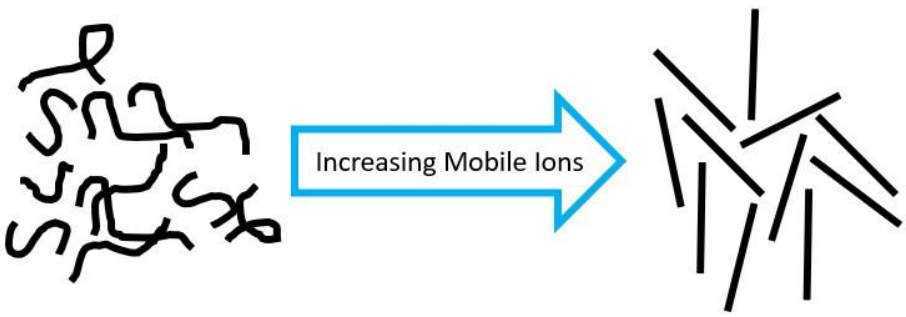

Figure 2-2. The flexibility of fibers in a dispersion can change from worm-like (low persistence length) to rigid (high persistence length) through increasing ionic strength.

In partial summary, to show birefringent properties, the concentration of mobile ions in the dispersion must be increased until the fibers become sufficiently rigid.

2.4.1.2 Effective Diameter, Length, and Volume

In the LC theories associated with order-disorder phase transition, the diameter, length, and volume of fibers along with fibers volume fraction are described by two adjectives: either

effective or bare (i.e. uncharged). This section aims to explain these important terminologies which are frequently used in this context.

Owing to particular chemical structures of BCLLCs, the BCLLCs mesogens can be charge-carrier because some like-charges can be deposited on the mesogens' outer surface; thereby repelling each other. In LC theory, such mesogens are treated as charged hard particles dispersed in the solution. Collagen rod-like fibers dispersed in acidic aqueous solution is an exemplar of charge-carriers because, depending on the dispersion's pH, a certain number of positive charges, H^+, are absorbed on the collagen backbone, making collagen fibers similar to positively charged hard rods dispersed in an acidic solution, see Figure 2-3.

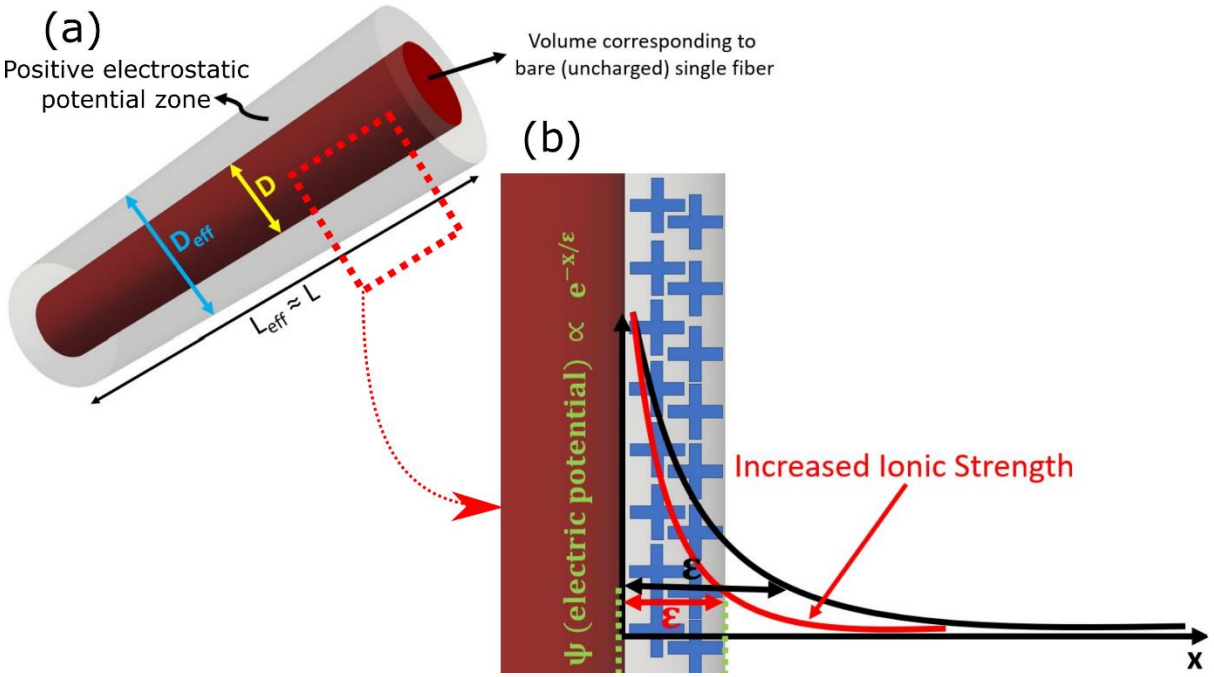

Figure 2-3. (a) The schematic representation of a needle-like mesogen charged positively along with the resulting repulsion region around it. All three fibrous LCs investigated in this thesis have such rod-shaped rigid geometry. (b) The decaying electrostatic potential close to the positively charged surface of the mesogen, and the qualitative behavior of the electrostatic potential with respect to the increase of ionic strength. As the solution concentration of mobile ions increases, the ionic strength increases, and correspondingly more ions attach to the mesogen surface, causing that the electrostatic potential drops in a shorter distance.

To consider the repulsion effect, the geometry of fibers is modified by including the repulsion zone as part of the fiber. Hence, $D_{eff} = D + \varepsilon$ and $L_{eff} = L + \varepsilon$ where ε is the distance over which the electrostatic effect due to charged attached on the mesogen surface persists:

$$\varepsilon = \alpha\kappa^{-1} \qquad 2\text{-}1$$

The formulation of the Debye screening length, κ^{-1}, and double-layer thickness parameter, α, are discussed in Chapters 3 and 4. Interestingly, the repulsion zone is reduced by increasing

mobile ion concentration due to a physical principle called “screening” or “shielding”. This principle explains that when the ionic strength increases due to the addition of salt or acid into the dispersion, more mobile ions whose charges are opposite to the mesogen surface are attracted to the mesogen surface as a result of electrostatic forces. This attraction leads to the fact that the electrostatic potential induced by the charged mesogens decreases, in consequence, ε becomes shorter. Thus, the net effect is summarized as the more ionic strength leads to a thinner ε.

It should be further noted that mesogens considered in this thesis have rod-shaped with a very large aspect ratio, making mesogens look like a needle. Given the geometry of mesogens, it can be appreciated that the length of mesogen, L, is considerably larger than ε; thereby making L_{eff} and L almost identical. However, ε is comparable with bare diameter; hence, the effective diameter, D_{eff}, is used instead of the bare diameter, D, in LC analysis.

2.4.1.3 Excluded Volume

In general, in a dispersion of particles whose aspect ratio is sufficiently large, the “excluded volume” comes into play. The excluded volume is defined as the volume which is inaccessible for particles because of the configuration of other particles. This concept is presented in Figure 2-4.

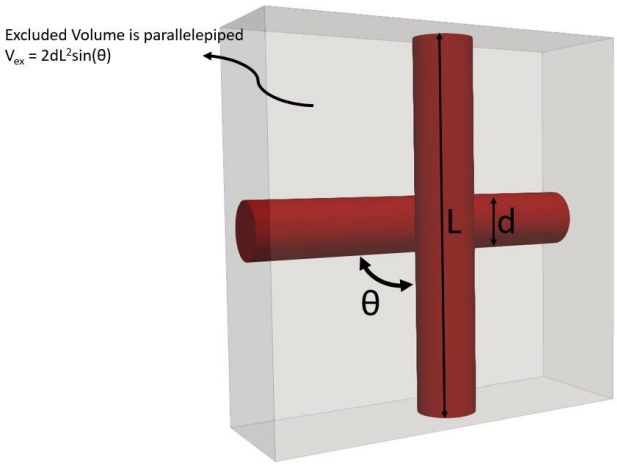

Figure 2-4. The schematical illustration of the excluded volume formed by two fibers. The spatial configuration of two adjacent rods forms a parallelepiped space that can’t be occupied by other fibers. The parallelepiped volume is called “excluded volume”.

2.4.2 Onsager

In the renowned Onsager's work [4], the coexisting regime between isotropic and nematic phase has been theoretically proven:

$$\phi_{lb} = 3.3\frac{D_{eff}}{L} \qquad 2\text{-}2$$

ϕ_{lb} is called effective volume fraction, showing the lower binodal threshold where the isotropic become unstable. D_{eff} and L are effective diameter and fiber length. The upper binodal threshold, ϕ_{ub}, distinguishing the biphasic zone from the nematic regime in the phase diagram, is also expressed by

$$\phi_{ub} = 4.5\frac{D_{eff}}{L} \qquad 2\text{-}3$$

In Onsager's theory, phase ordering is considered as an exclusively entropy-driven phenomenon. As fibers in the dispersion adopt a long-range orientational order, two simultaneous mechanisms take place. First, the orientational entropy is reduced because fibers become aligned along a common direction. Second, the translational entropy increases since ordering makes more space accessible for fibers to translate longer distances in comparison with the isotropic phase in which fibers are randomly aligned and the translation is greatly blocked. In other words, through phase ordering, the excluded volume is reduced; hence more space becomes available for the fibers' translation, which leads to an increase in translational entropy. Onsager was the first who theoretically explained the above-mentioned physical understanding of the isotropic-to-nematic (I/N) phase transition. He revealed that the dispersion's free energy is reduced if the excluded volume is reduced, meaning that the long-range orientational ordering takes place, and in consequence, the systems go through the phase transition from isotropic to nematic order.

2.4.3 Generic Approach for Phase Diagram Construction

The standard thermodynamic approach to determine binodal curves in a phase diagram is to use the chemical potential. The chemical potential of component A in phase P, μ_A^P, is defined as

$$\mu_A^p = \frac{\partial f}{\partial n_A} \qquad 2\text{-}4$$

where f and n_A denote free energy of system and moles of component A (e.g. LC and solvent), respectively. The superscript P stands for the phase (e.g. p=Isotropic, Nematic, or Cholesteric). This crucial thermodynamic property is related to mass transfer; the difference between the chemical potentials of a component in two phases describes the tendency of that component for being transferred between two phases. Accordingly, the equality of chemical potentials indicates that the net mass transfer is zero, and phases reach equilibrium. Given the chemical potential, the equilibrium phase diagram is constructed based on the thermodynamic criterion that the chemical potentials of each component in all the phases coexisting together must be equal to each other, $\mu_i^P = \mu_i^Q$ [29].

As can be inferred from equation 2-4, the definition of system free energy is needed to construct the phase diagram. Depending on the system under study, the governing physics are identified, and correspondingly the system free energy, f, is defined; for example, Chapter 3 elaborates on the free energy contributions involved in a binary solution comprising a needle-like mesogen and small-sized solvent.

In partial conclusion, the steps required for determining the phase transition boundaries are as follows.

1) Definition of the system Helmholtz free energy density, f. In this stage, all the physics which can have an impact on the self-assembly should be found and included in the system free energy, f.
2) Use equation 2-4 to develop an analytical relation for the chemical potential of each component in different phases.
3) Apply the criterion of phase equilibria, $\mu_i^P = \mu_i^Q$. In this stage, a system of nonlinear equations is obtained.
4) In addition to the equations formulated in the previous step, there is a need of applying mass conservation law to make sure that the initial mass of each component inserted in the system should be equal to the sum of masses of that component in all phases present in the system. The corresponding mathematical description is $m_i = \sum_j m_i^j$ where m_i is the mass of component i and j indicates phases present in the dispersion. Therefore, the component mass balance should be augmented with the equations developed in step 3.

5) The resulting nonlinear system of equations is then solved numerically; thereby computing the phase transition boundaries.

2.5 Dynamical Modeling of BCLLCs

The equilibrium thermodynamic analysis discussed in the previous section, 2.4, result in knowing the upper and lower miscibility boundaries, which are essential for analyses associated with transport phenomena. This section elaborates the spatiotemporal modeling by which mass transfer coupled with fiber orientation can be captured as a function of time and space.

Before proceeding to develop the spatiotemporal model describing the multi-scale evolution of mesogenic particles, the contributing factors and their impacts on the total free energy for the mesophasic systems need to be established. The organization of this section is as follows. The free energy formulation is explained in section 2.5.1 in detail. Having formulated the total free energy in section 2.5.1, the governing equations, known as Model C, are then formulated and discussed in section 2.5.2.

2.5.1 Total Free Energy

In general, the total free energy of a mesophasic solution, F, consists of five free energy contributions.

$$F = \int_V (f_h + f_e + f_m + f_i + f_c)\, dV \qquad 2\text{-}5$$

V stands for volume or area in three- or two-dimensional simulations, respectively. These contributions are listed in Table 2-2, and elaborated in the sections below.

Table 2-2. Summary of five free energy contributions used in the present Ph.D. thesis, and their physical interpretation [1].

Free Energy Contribution	Symbol	Physical Interpretation
Homogenous	f_h	The order-disorder phase transition.
Bulk elasticity	f_e	The three common deformation modes; splay, twist, and bend.
Mixing	f_m	Entropy and enthalpy due to mixing.
Concentration gradient	f_i	Cost of interface formation.
Coupling	f_c	Mesogens configuration in the interfacial layer.

2.5.1.1 Q-tensor

The long-range orientational order in a mesophase is described by

$$\mathbf{Q} = S\left(\mathbf{nn} - \frac{\boldsymbol{\delta}}{3}\right) + \frac{1}{3}P(\mathbf{mm} - \mathbf{ll}) \qquad 2\text{-}6$$

S and P represent the degree of mesogens' alignment around the uniaxial director, **n**, and biaxial directors, **m** and **l**. For example, S=1 shows that all fibers are perfectly aligned along the uniaxial director, **n**, showing perfect crystal structure. On the other hand, S=0 represents fibers that are uncorrelated with **n**, indicating the isotropic phase. Consequently, the uniaxial order parameter, S, lies between 0 and 1 for the typical liquid crystalline phase. S can also be negative, describing the orientational ordering for disc-like mesogens, which is out of the present thesis's scope—readers are referred to the following references for more information [2, 30, 31]. All directors, **n**, **m**, and **l**, are perpendicular with respect to each other. In light of the **Q**-tensor definition given in equation 2-6, the **Q**-tensor has useful features; **Q**-tensor is symmetric, $\mathbf{Q}=\mathbf{Q}^T$, traceless, $Tr(\mathbf{Q})=0$, and is a second-order tensor, $\mathbf{Q}=Q_{i,j}$. Accordingly, **Q**-tensor has only five independent components.

As will be discussed in section 2.5.2, the **Q**-tensor's five independent components are numerically computed as a function of time and space through solving the governing coupled nonlinear parabolic Partial Differential Equations (PDEs). Hence, in the post-processing stage, the computed values are required to be converted to the uniaxial, S, and biaxial, P, order parameters, and uniaxial, **n**, and biaxial, **m**, director fields. This transformation can be obtained through the relation between the **Q**-tensor's eigenvalues and eigenvectors; the uniaxial director, **n**, and biaxial director, **m**, are eigenvectors corresponding to the largest eigenvalue, 2S/3, the

second largest eigenvalue, -(SP)/3, respectively. It should be further mentioned that the biaxiality, P and **m**, is normally negligible for chiral nematic liquid crystals [32, 33].

2.5.1.2 Free energy variation due to phase ordering

Two free energy contributions are involved through the long-range ordering in the mesophasic system: phase transition and bulk elasticity. The corresponding free energy contributions are given by

$$f_h = \frac{A}{2}\mathrm{Tr}(\mathbf{Q}^2) - \frac{B}{3}\mathrm{Tr}(\mathbf{Q}^3) + \frac{C}{4}\left(\mathrm{Tr}(\mathbf{Q}^2)\right)^2 \quad 2\text{-}7$$

$$f_e = L_1[\nabla \times \mathbf{Q} + 2q\mathbf{Q}]^2 + L_2[\nabla \cdot \mathbf{Q}]^2 \quad 2\text{-}8$$

f_h is well-known as Landau-de Gennes (LdG) theory in which A, B, and C are phenomenological concentration-dependent constants. Note that A directly controls if the phase transition takes place or not, moreover, B<0 and C>0 guarantee two minima of the free energy pertinent to disordered phase and ordered phase [2, 34]. f_e comes from the well-established Frank-Oseen-Mermin theory. L_1 and L_2 are Landau elastic constants related to the three main forms of liquid crystalline distortions; splay, twist, and bend whose Frank elastic constants are shown by K_1, K_2, and K_3, respectively [2, 35]. Eq. 2-8 describes nematic phase in case that the pitch length goes to infinity, leading to negligible wavevector (q). Furthermore, eqs. 2-7 and 2-8 correspond to short-range and long-range order.

2.5.1.3 Free energy variation due to mixing

The lyotropic liquid crystalline solutions are comprised of mesogen dispersed in a solvent. Accordingly, mixing free energy is needed to be taken to account. For a given binary mixture, the mixing free energy is described by the well-known Flory-Huggins theory expressed by

$$f_m = \frac{\phi \ln(\phi)}{n} + (1-\phi)\ln(1-\phi) + \chi\phi(1-\phi) \quad 2\text{-}9$$

where ϕ, n, and χ represent effective volume fraction of the mesogen, the number of segments that exist on the backbone of mesogen, and Flory's parameter, respectively.

2.5.1.4 Free energy variation due to interface

If there is an interface in the mesophasic system, two free energy contributions play role in the total free energy of the system: interface formation, f_i, and a preferred orientation of mesogen in the interface, f_c. The corresponding free energy contributions are expressed by

$$f_i = L_\phi(\nabla\phi)^2 \qquad 2\text{-}10$$

$$f_c = L_{\phi-\mathbf{Q}}(\nabla\phi)\cdot(\nabla\cdot\mathbf{Q}) \qquad 2\text{-}11$$

where L_ϕ and $L_{\phi-\mathbf{Q}}$ stand for interface formation and coupling constants.

In the modeling presented in this Ph.D. thesis, there exist two fields in general: conserved and non-conserved fields corresponding to ϕ and $\mathbf{Q}$, respectively. In fact, the coupling between these two terms, equation 2-11, is required to be taken to account in the total free energy. This coupling term can describe the energy cost due to the orientation of mesogen in the interface, which can be tangential or homotropic [36-38].

2.5.2 Governing Equations

The spatio-temporal evolution of conserved, ϕ, and non-conserved filed, $\mathbf{Q}$, is numerically captured through solving the time-dependent Ginzburg–Landau (TDGL) formalism, known as model C in the Hohenberg and Halperin classification [39]:

$$\gamma(\mathbf{Q})\frac{\partial\mathbf{Q}}{\partial t} = -\left(\frac{\delta F}{\delta\mathbf{Q}}\right)^{[s]} \qquad 2\text{-}12$$

$$\frac{\partial\phi}{\partial t} = M_\phi\nabla\cdot\left([\mathbf{I}+\mathbf{Q}]\cdot\nabla\frac{\delta F}{\delta\phi}\right) \qquad 2\text{-}13$$

δ is the functional derivative. $\gamma(\mathbf{Q}) = \eta\left(1-\frac{3}{2}\mathbf{Q}:\mathbf{Q}\right)^2$ is rotational viscosity and η is rotational viscosity constant. $M_\phi$is mass transfer mobility. In equation 2-13, if $\mathbf{Q}=\mathbf{0}$, the equation is simplified to the renowned Cahn-Hilliard theory which has widely been used for simulation of liquid-liquid demixing. The reason that $\mathbf{Q}$ appears in equation 2-13is that mass transfer mobility comprises from isotropic and anisotropic contributions, which are reasonably assumed equal in the present thesis [33, 40].

The governing equations described by eqs. 2-5 through 2-13 are generic in regard to the description of isotropic, nematic, and cholesteric dispersions; meaning that only the coefficients can take different values depending on the biochemical conditions whereas the essential nature of the expressions remain unchanged.

References

1. Rey, A. D., Liquid crystal models of biological materials and processes. Soft Matter **2010,** 6 (15), 3402-3429.

2. Muševič, I., Liquid Crystal Colloids. Springer International Publishing: 2017.

3. Cladis, P.; Palffy-Muhoray, P., Dynamics and Defects in Liquid Crystals: A Festschrift in Honor of Alfred Saupe. Taylor & Francis: 1998.

4. Onsager, L. J. A. o. t. N. Y. A. o. S., The effects of shape on the interaction of colloidal particles. **1949,** 51 (4), 627-659.

5. Zhao, J.; Gulan, U.; Horie, T.; Ohmura, N.; Han, J.; Yang, C.; Kong, J.; Wang, S.; Xu, B. B., Advances in biological liquid crystals. Small **2019,** 15 (18), 1900019.

6. Mitov, M., Cholesteric liquid crystals in living matter. Soft Matter **2017,** 13 (23), 4176-4209.

7. Neville, A. C., Biology of Fibrous Composites: Development Beyond the Cell Membrane. Cambridge University Press: 1993.

8. Schütz, C.; Bruckner, J. R.; Honorato-Rios, C.; Tosheva, Z.; Anyfantakis, M.; Lagerwall, J. P., From Equilibrium Liquid Crystal Formation and Kinetic Arrest to Photonic Bandgap Films Using Suspensions of Cellulose Nanocrystals. Crystals **2020,** 10 (3), 199.

9. Gobeaux, F.; Belamie, E.; Mosser, G.; Davidson, P.; Panine, P.; Giraud-Guille, M. M., Cooperative Ordering of Collagen Triple Helices in the Dense State. Langmuir **2007,** 23 (11), 6411-6417.

10. Giraud-Guille, M. M.; Mosser, G.; Belamie, E., Liquid crystallinity in collagen systems in vitro and in vivo. Current Opinion in Colloid & Interface Science **2008,** 13 (4), 303-313.

11. Voet, D.; Voet, J. G., Biochemistry. John Wiley & Sons: Hoboken, NJ, 2011.

12. Giraud-Guille, M.-M.; Besseau, L.; Martin, R., Liquid crystalline assemblies of collagen in bone and in vitro systems. Journal of biomechanics **2003,** 36 (10), 1571-1579.

13. Giraud Guille, M. M.; Mosser, G.; Helary, C.; Eglin, D., Bone matrix like assemblies of collagen: From liquid crystals to gels and biomimetic materials. Micron **2005,** 36 (7), 602-608.

14. Khadem, S. A.; Bagnani, M.; Mezzenga, R.; Rey, A. D., Relaxation dynamics in bio-colloidal cholesteric liquid crystals confined to cylindrical geometry. Nature communications **2020,** 11 (1), 1-10.

15. De Sa Peixoto, P.; Deniset-Besseau, A.; Schmutz, M.; Anglo, A.; Illoul, C.; Schanne-Klein, M.-C.; Mosser, G., Achievement of cornea-like organizations in dense collagen I solutions: clues to the physico-chemistry of cornea morphogenesis. Soft Matter **2013,** 9 (47), 11241-11248.

16. Torbet, J.; Malbouyres, M.; Builles, N.; Justin, V.; Roulet, M.; Damour, O.; Oldberg, Å.; Ruggiero, F.; Hulmes, D. J. S., Orthogonal scaffold of magnetically aligned collagen lamellae for corneal stroma reconstruction. Biomaterials **2007,** 28 (29), 4268-4276.

17. Brasinika, D.; Tsigkou, O.; Tsetsekou, A.; Missirlis, Y. F., Bioinspired synthesis of hydroxyapatite nanocrystals in the presence of collagen and l-arginine: Candidates for bone regeneration. Journal of Biomedical Materials Research Part B: Applied Biomaterials **2016,** 104 (3), 458-469.

18. Kikuchi, M.; Ikoma, T.; Itoh, S.; Matsumoto, H. N.; Koyama, Y.; Takakuda, K.; Shinomiya, K.; Tanaka, J., Biomimetic synthesis of bone-like nanocomposites using the self-organization mechanism of hydroxyapatite and collagen. Composites Science and Technology **2004,** 64 (6), 819-825.

19. Giese, M.; Blusch, L. K.; Khan, M. K.; MacLachlan, M. J., Functional materials from cellulose-derived liquid-crystal templates. Angewandte Chemie International Edition **2015,** 54 (10), 2888-2910.

20. Lagerwall, J. P.; Schütz, C.; Salajkova, M.; Noh, J.; Park, J. H.; Scalia, G.; Bergström, L., Cellulose nanocrystal-based materials: from liquid crystal self-assembly and glass formation to multifunctional thin films. NPG Asia Materials **2014,** 6 (1), e80.

21. Finkelmann, H.; Kim, S. T.; Munoz, A.; Palffy-Muhoray, P.; Taheri, B., Tunable mirrorless lasing in cholesteric liquid crystalline elastomers. Advanced Materials **2001,** 13 (14), 1069-1072.

22. Kose, O.; Tran, A.; Lewis, L.; Hamad, W. Y.; MacLachlan, M. J., Unwinding a spiral of cellulose nanocrystals for stimuli-responsive stretchable optics. Nature Communications **2019,** 10 (1), 510.

23. Li, Y.; Jun-Yan Suen, J.; Prince, E.; Larin, E. M.; Klinkova, A.; Thérien-Aubin, H.; Zhu, S.; Yang, B.; Helmy, A. S.; Lavrentovich, O. D.; Kumacheva, E., Colloidal cholesteric liquid crystal in spherical confinement. Nature Communications **2016,** 7 (1), 12520.

24. Nyström, G.; Arcari, M.; Mezzenga, R., Confinement-induced liquid crystalline transitions in amyloid fibril cholesteric tactoids. Nature Nanotechnology **2018,** 13 (4), 330-336.

25. Dobson, C. M., Protein folding and misfolding. Nature **2003,** 426 (6968), 884-890.

26. Knowles, T. P.; Mezzenga, R., Amyloid fibrils as building blocks for natural and artificial functional materials. Advanced Materials **2016,** 28 (31), 6546-6561.

27. Plischke, M.; Bergersen, B., Equilibrium Statistical Physics. World Scientific: 2006.

28. Lovelady, H. H.; Shashidhara, S.; Matthews, W. G., Solvent specific persistence length of molecular type I collagen. Biopolymers **2014,** 101 (4), 329-335.

29. Van Ness, H. C.; Abbott, M.; Swihart, M.; Smith, J. M., Introduction to Chemical Engineering Thermodynamics. McGraw-Hill Education: 2017.

30. De Luca, G.; Rey, A. D., Chiral front propagation in liquid-crystalline materials: Formation of the planar monodomain twisted plywood architecture of biological fibrous composites. Physical review. E, Statistical, nonlinear, and soft matter physics **2004,** 69 (1 Pt 1), 011706.

31. De Luca, G.; Rey, A. D., Dynamic interactions between nematic point defects in the spinning extrusion duct of spiders. The Journal of chemical physics **2006,** 124 (14), 144904.

32. Wulf, A., Biaxial order in cholesteric liquid crystals: Phenomenological argument. **1973,** 59 (12), 6596-6598.

33. Khadem, S. A.; Rey, A. D., Theoretical Platform for Liquid-Crystalline Self-Assembly of Collagen-Based Biomaterials. **2019,** 7 (88).

34. Khadem, S. A.; Rey, A. D., Thermodynamic Modelling of Acidic Collagenous Solutions: From Free Energy Contributions to Phase Diagrams. Soft Matter **2019**.

35. Wright, D. C.; Mermin, N. D., Crystalline liquids: the blue phases. Reviews of Modern Physics **1989,** 61 (2), 385-432.

36. Das, S. K.; Rey, A. D., Computational thermodynamics of multiphase polymer–liquid crystal materials. Computational Materials Science **2006,** 38 (2), 325-339.

37. Das, S. K.; Rey, A. D., Magnetic Field-Induced Shape Transitions in Multiphase Polymer-Liquid Crystal Blends. Macromolecular Theory and Simulations **2006,** 15 (6), 469-486.

38. Das, S. K.; Rey, A. D., Colloidal crystal formation via polymer-liquid-crystal demixing. Europhys. Lett. **2005,** 70 (5), 621-627.

39. Hohenberg, P. C.; Halperin, B. I., Theory of dynamic critical phenomena. Reviews of Modern Physics **1977,** 49 (3), 435-479.

40. Aguilar Gutierrez, O. F.; Rey, A. D., Biological plywood film formation from para-nematic liquid crystalline organization. Soft Matter **2017**.

Chapter 3. Thermodynamic modelling of acidic collagenous solutions: from free energy contributions to phase diagrams

3.1 Preface

As discussed in Chapters 1 and 2, knowing the location of the equilibrium disorder-order phase transition in the phase diagram and the variation of these boundaries with respect to physical properties are of prime importance for engineering the fabrication of the sough-after ordered materials. Notwithstanding the importance, the lower binodal boundary, and upper binodal boundary along with the governing physics controlling these boundaries have not yet been understood for colloidal lyotropic liquid crystals. For this reason, this chapter addresses these crucial subjects: isotropic-to-cholesteric phase transition boundaries and the factors controlling them for collagen fibers dispersed in acidic aqueous solutions.

3.2 Abstract

Tropocollagen is considered one of the main precursors in the fabrication of collagen-based biomaterials. Triple helix acidic solutions of collagen I have been shown experimentally to lead to chiral plywood architectures found in bone and "cornea" like tissues. As these plywoods are solid analogues of liquid crystal architectures, bio-inspired processing and fabrication platforms based on liquid crystal physics and thermodynamics will continue to play an essential role. For tissue engineering applications, it has been shown that dilute isotropic collagen solutions need to be flow processed first and then dehydrated. Thus, a complete fundamental understanding of thermodynamics and free energy contributions in acidic collagen aqueous solutions is necessary to avoid expensive trial-and-error fabrication. To achieve this goal, we analyze the microscopic mechanisms of ordering and interactions in solutions of triple helix collagen, namely mixing, attraction, excluded-volume and chirality. To capture the mentioned physics, we then incorporate and integrate the Flory-Huggins, Maier-Saupe, Onsager and Frank theories. Nonetheless, they together are incapable of providing an acceptable mesophasic description in acidic collagenous solutions because tropocollagen biomacromolecules are positively charged. We then explore a simple and accurate electrostatic mean-field potential. Our results on collagen are in good agreement with experiments and include phase diagrams, phase transition thresholds, and critical isotropic/cholesteric order parameters. The present extended theory is shown to properly converge to classical liquid crystal models and is used to express the phenomenological Landau-de Gennes parameters with more fundamental quantities. This study provides a platform to derive accurate process models for the fabrication of collagen-based materials, considering and benefitting from the full range of underlying interactions.

3.3 Introduction

Type I collagen is ubiquitous within mammalian or even some non-mammalian tissues[1]; thus it is widely considered as the main precursor in the synthesis of collagenous biomaterials. Owing to myriad applications of collagen in bioinspired and biomimetic materials, fabrication of collagenous biomaterials is at the forefront of research and development[2-6]. For example, there are considerable current efforts to fabricate artificial bone or bone regeneration[7, 8] and corneal stroma reconstruction[9, 10].

The functions of these versatile self-assembled biomaterials are affected by the spatial order, packing and organization of tropocollagen macromolecules. In acidic solutions, the primary architectural motif of these highly organized materials is formed at the molecular level. However, a considerable amount of experimental and theoretical studies has been carried out on the properties of collagenous biomaterials at the tissue level[11-15], and molecular studies are few[10, 16-18]. In spite of substantial efforts concerning the fabrication of collagenous biomaterials, in some cases like the fabricated cornea or even bone, the quality of synthesized tissues is not satisfactory when they are compared to the natural counterparts. Furthermore, the required molecular level understanding of phase ordering in collagenous solutions also remains relatively incomplete. It is expected that the development of comprehensive molecular and process models and multi-scale, multi-transport, multi-dimensional simulations of collagen self-assembly can generate impactful fabrication design principles. New bioinspired functional materials and improved biomaterials will emerge through a better fundamental understanding of thermodynamics and the packing process of orientational self-assembly and phase ordering. In the present study, we develop a fundamental theory and apply it to multiscale thermodynamic equilibria that has an essential role in the understanding of collagen orientational self-assembly and self-ordering. We like to emphasize that, in this paper, we only consider the molecular triple helix acidic collagen solutions and higher order fibrillar assemblies are excluded as they are not present in the regimes and conditions under discussion in this paper. Without ambiguity and for brevity in this paper we refer to triple helix collagen as molecular collagen or when convenient as collagen.

The macroscopic chiral molecular collagen solution has an orientational order similar to those found in many biological fibrous composites known as biological plywoods[19]. Biological plywoods possess a liquid crystalline state at the beginning of their morphogenesis[19]. Thus, their formation can be described by liquid crystal physics and thermodynamics[2, 5, 20-23]. Triple helix collagen is a rodlike macromolecule with a high aspect ratio which imparts the long-range

orientational order to collagen in acidic solutions[17, 24]. This biomacromolecule is denatured if the temperature is higher than 45ºC [25], and is lyotropic mesogen[5, 16]. Collagen rods are inherently oleophilic and are capable of carrying positive charges in acidic solutions (pH<4) by which the solubility of collagen in the aqueous solutions becomes possible. The reason for being miscible is the emergence of interchain repulsive interactions among rods that reduce the hydrophobic attractions[26, 27]. That is why the fabrication of collagenous biomaterials must start from dilute acidic isotropic solutions followed by a synchronized water removal process to eventually reach the cholesteric state[28]; synchronized means that the water transport and dehydration kinetics is precisely coupled to the orientational phase ordering process. In addition, when the collagen molecules are dispersed in pure water, they behave as wormlike semiflexible rods. However, being a positive charge carrier gives rigidity to the collagen rods because the intrachain repulsive forces along the backbone overcome the intrinsic softness of backbones[17]. To account for the characteristics of orientational ordering and attractive interactions of collagen macromolecules, we employ the Maier-Saupe theory. This well-established model is able to satisfactorily provide a robust mathematical description in both the long-range orientational order and orientation-dependent attraction that belongs to van der Waals interactions[29-32]. In addition, from a physical viewpoint, through the phase ordering process, the excluded volume of system needs to be minimized. Consequently, the Onsager theory should be included into our model to explain this effect. This theory, which is considered as a cornerstone in liquid crystal theory, provides an accurate result as long as the D/L is much less than 1[32-34]. This requirement, which comes from the second virial approximation, is met in our study because we deal with the dispersions of long, rigid and elongated molecules.

As mentioned above, one of the distinctive characteristic of triple helix collagen rods is the ability to be a carrier of positive charges in acidic solutions. From a theoretical standpoint, the stable configuration of two rods, which are charged is orthogonal[35, 36]. The conclusion can be drawn that the like-charges are a destabilizing effect of ordered phase[37]. To take this fact into account, previous theories need to be modified by the use of effective rod diameter in lieu of the bare one, and a proper term corresponding to the interchain electrostatic interactions is required in the free energy contributions in order to describe the twisting effect. The effective diameter has been brought into focus in the pioneering work of Onsager[34] and other studies[35, 38]. Nevertheless, the macroscopic modeling and validations of mixtures in which rod-like charged macromolecules are dispersed in the small-sized solvent requires further investigation, especially the impact of interchain electrostatic interactions on the stability of mesophases such

as those of acidic collagen solutions. One of the objectives of this article is to address this need by using molecular mean-field treatment. The macroscopic chirality is the last mechanism that we need to include in the free energy contributions. Collagen triple helix rods form the helicoidal structure with the micrometer-sized pitch whose values depends on the concentrations of acid and collagen[18]. In this regard, the Frank and Mermin free energy[39, 40] is a widely used theory that we have employed in this article. In this paper (Appendix B of ESI), the micron-range pitch is a given function of collagen concentration, extracted from experimental data[18].

The specific objectives of this paper are:

1. Formulate the free energy of triple-helix collagen dispersed in the aqueous solutions of acetic acid.

2. Compute and validate with real experimental data[16] when available, isotropic-cholesteric phase transition and phase diagrams as a function of acetic acid.

3. Characterize the effect and impact of molecular level and fundamental parameters on the cholesteric ordering and isotropic-cholesteric phase transitions of collagen solutions.

4. Coarse-grain the model to fit the Flory-Huggins-Landau de Gennes model for future use in process modeling of acidic triple helix collagen films.

5. To establish whether the thermodynamics of acidic collagen solution closely follows the known behavior of rigid and semi-rigid lyotropic liquid crystalline polymers, such as displaying an athermal chimney phase diagram[20].

This paper is organized as follows. Section 3.4.1 gives the derivation of the free energy for a pure chiral charged rigid calamitic mesogen, and in section 3.4.2 we develop the free energy for the binary solution of mesogen in a non-mesogenic solvent. The cholesterogen and solvent are viewed as charge-carrier rigid rod-like particles and dissociable component, respectively. In section 3.5, we discuss how to formulate binodal curves (subsection 3.5.1) and the isotropic-cholesteric phase transition curve (subsection 3.5.2) from the free energy obtained in section 3.4.2. Section 3.6 shows that our suggested model has the identical form with LdG expansion in the vicinity of isotropic-cholesteric (I-N*) phase transition. Hence, the phenomenological coefficients of LdG can be systematically derived from our suggested model. Finally, in section 3.7, we provide a discussion about the main results of this study. The Electronic Supplementary Information (ESI) has four Appendices. Appendix A presents details of the mathematical

derivations for all quantities used in this paper. Appendix B gives details of the model parameters and physical properties. Appendix C presents a systematic validation of the model by demonstrating that it reduces to well-established theories if some mechanisms like chirality, electrostatic, and attractive interactions are ignored[38, 41]. Lastly, in Appendix D, we have provided the nomenclature to make the derivation of model easy-to-follow. The organization and flow of information are summarized in Figure 3-1.

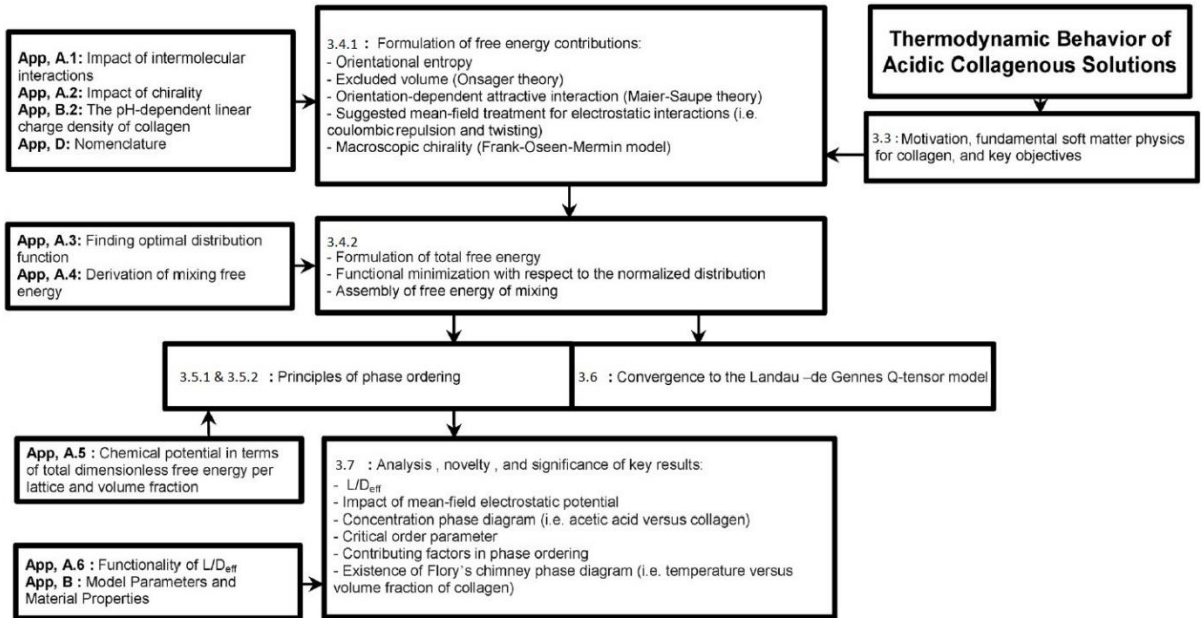

Figure 3-1. Organization of the present study. Numbers on the left top side of boxes are the numbers of (sub)sections.

3.4 Thermodynamic model

3.4.1 Free energy contributions for charged chiral calamitic mesogen

This subsection formulates the required free energy contributions for the accurate description of the thermodynamics of acidic collagenous solutions. For clarity and continuity, we first introduce needed definitions and concepts. The nomenclature used throughout is in Appendix D of ESI. The Onsager theory[34] accounts for the electrostatic repulsion by considering the double layer as a part of rod's diameter. Thus, the effective rod diameter D_{eff} is: [35, 37, 38]

$$D_{eff} = D+\alpha\kappa^{-1} \qquad (3-1)$$

D is the diameter of uncharged rods. Here κ^{-1} is the Debye screening length defined as: $\kappa^{-1} = (8\pi\lambda_B N_{avo} I)^{-\frac{1}{2}}$, where λ_B, $N_{avo}$and I are the Bjerrum length, Avogadro's number and

ionic strength, respectively—the definition of ionic strength is $I=\frac{1}{2}\sum_i m_i Z_i^2$ where m corresponds to molar concentration, Z is charge number, and the sum is taken over all mobile ions[42]. The double-layer thickness parameter α is[37]:

$$\alpha = \ln A' + \gamma_E + \ln 2 - \frac{1}{2} - \frac{4}{\pi}\left[|\sin(\gamma)|\mathrm{Ei}\left(-\frac{A'}{|\sin(\gamma)|}\right)\right]_i \qquad (3-2a)$$

$$A'=A\frac{e^{\kappa D}}{\kappa D},\ A=2\pi\Lambda^2\lambda_B D \qquad (3-2b)$$

$$[f(\mathbf{u},\mathbf{u}')]_i = \frac{1}{16\pi^2}\iint f(\mathbf{u},\mathbf{u}')d\Omega d\Omega' \qquad (3-2c)$$

where γ_E and Λ are Euler constant and linear charge density. Ei is the exponential integral defined as $\mathrm{Ei}(x)=-\int_{-x}^{\infty}\frac{\exp(-t)}{t}dt$. The operator of $[\bullet]_I$ given by eqn. (3-2c), represents the integration over all possible orientations of two rod-shaped mesogens whose orientations are expressed by the molecular rod's unit vectors $\mathbf{u}$ and $\mathbf{u}'$. The solid angle, $d\Omega=\sin(\theta)d\theta d\varphi$, is the surface element of the sphere with a unit radius where θ and φ are polar and azimuthal angle, respectively. The angle between the rods is $\gamma=\cos^{-1}(\mathbf{u}\cdot\mathbf{u}')$. Additionally, for a given molecular orientation, $\psi(\mathbf{u})$ gives the single-rod orientational distribution function on the unit sphere[43].

As mentioned above, several microscopic mechanisms simultaneously govern the thermodynamics of acidic collagen solutions: (1) The orientation-dependent attractive interactions because of Van der Waals dispersion forces, (2) The Columbic repulsion and twisting due to the protonated amine functional groups on the backbone of collagen rods when the solution's pH is lower than a certain value, (3) the excluded volume effect (4) the distortion in their long-range orientational pattern owing to helicoidal structure, (5) the orientational and translational entropy and (6) the enthalpy contribution . Each of these effects is captured by fundamental theory except for the interchain electrostatic interactions (i.e. Columbic repulsion and twisting). More precisely, one widely used approach to simulating the electrostatic mean-field is to take the molecular average of the estimations given by the solution of Poisson–Boltzmann equation over all particles. Yet, we avoid employing it since the objective of this study is to develop a tractable model. In this section, we first integrate the existing theories; namely, Onsager theory to accounts for the minimization of excluded volume, Maier-Saupe theory to describe the orientation-dependent attractive interactions of Van der Waals forces, and Frank distortion free energy to take into account the various possible macroscopic

orientational elasticity of the ordered cholesteric phase. Second, we formulate and incorporate a simple mean-field potential to account for the interchain repulsion and twisting.

The total dimensional Helmholtz free energy for N_A chiral charged mesogens in a volume V is[38, 40]:

$$\frac{\beta F}{N_A}=\beta\mu^{o}\,(T)\text{-}1+\ln c_A'+\sigma\big(\psi(\mathbf{u})\big)+B_2\big(\psi(\mathbf{u})\big)+M\big(\psi(\mathbf{u})\big)+C\big(\psi(\mathbf{u})\big) \qquad (3-3)$$

$\beta=(k_BT)^{-1}$ where k_B and T are Boltzmann constant and absolute temperature; μ^{o} is the standard chemical potential of particle; c_A' is dimensionless number density defined as $c_A'=\upsilon c_A$ where υ is the volume scale and $c_A=N_A/V$ is the number density; $\ln c_A'$, stands for translational entropy that favors the anisotropic phase, and the rest of terms reflect the impact of molecular orientation. $\sigma\big(\psi(\mathbf{u})\big)$, $B_2\big(\psi(\mathbf{u})\big)$, $M\big(\psi(\mathbf{u})\big)$ and $C\big(\psi(\mathbf{u})\big)$ denote the effect of orientational entropy, the excluded volume based on the second virial approximation, the orientation-dependent intermolecular interactions and the geometric chirality of mesogen.

The alignment of rods decreases the orientational entropy, given by[38]:

$$\Delta S_O=-\sigma\big(\psi(\mathbf{u})\big)=-\int \psi(\mathbf{u})\ln\big(4\pi\psi(\mathbf{u})\big)\,d\Omega \qquad (3-4)$$

Notwithstanding the fact that the ordering causes reduction in orientational entropy, the ordering provides excess free volume availability, which means more translational entropy[44]. To consider the excluded-volume, we have used the Onsager theory which is based on the viral expansion truncated to second-virial term, $B_2\big(\psi(\mathbf{u})\big)$. Considering the proper pair-potential between the outer double layers of two macromolecules, the second-virial approximation is [38]:

$$B_2\big(\psi(\mathbf{u})\big)=c_A\bar{\upsilon}_{AA}\rho\big(\psi(\mathbf{u})\big) \qquad (3-5a)$$

$$\rho\big(\psi(\mathbf{u})\big)=\frac{4}{\pi}\iint \Gamma(\gamma)\psi(\mathbf{u})\psi(\mathbf{u}')\,d\Omega d\Omega' \qquad (3-5b)$$

$$\Gamma(\gamma)=|\sin(\gamma)|\times\left\{1+h\left[-\ln|\sin(\gamma)|-\ln 2+\frac{1}{2}\right]\right\} \qquad (3-5c)$$

In eqn. (3-5a), the average excluded-volume between two rods is denoted by $\bar{\upsilon}_{AA}=\pi/4D_{eff}L^2$. Moreover, the term $h=(\kappa D_{eff})^{-1}$ corresponds to magnitude of the twisting effect.

So far, the theory of Onsager has been presented, including the effective diameter due to the role of Columbic electrostatic repulsion in orientational ordering. Although the Onsager theory attributes the phase ordering mechanism to the minimization of excluded volume, the Maier-

Saupe theory considers the van der Waals attraction as driving mechanism for macroscopic orientation of the rods. In reality, these two microscopic mechanisms are not mutually exclusive[32, 45]. In our model, these mechanisms (i.e. excluded volume and orientation-dependent attraction) simultaneously affect the phase ordering because collagen is rod-like macromolecule that has sort of orientation-dependent attractive interactions. We note that the need in the simultaneous use of Onsager and Maier-Saupe theories to capture the physics of a mesophase has been acknowledged and implemented in other real systems. To name a few: polymer dispersed liquid crystals[41, 46], colloid or nano-laden liquid crystals[47, 48], cholesteric cellulose polymers[49] all exhibit both lyotropic and thermotropic behavior, as do other mesogens[50]. Moving on to the Maier-Saupe theory, the orientation-dependent attractive interactions among rod-like macromolecules favors alignment of molecules, and as a result promotes the orientational ordering and lowers the free energy as well[30, 31, 41]. Similar to the approach of Maier-Saupe[30, 31], we have taken the averaged potential interaction directly proportional to the local order parameter, $P_2(\mathbf{u}\cdot\mathbf{n})$, and the macroscopic uniaxial order parameter, S, which is the ensemble average of $P_2(\mathbf{u}\cdot\mathbf{n})$. Hence, the one-body mean field potential of i^{th} rod for attractive interactions on the other existing rods in the system is given by[43]:

$$\beta U_i^{MS} = -\beta U'^{MS} \upsilon_A S P_2\big(\cos(\theta)\big) \qquad (3-6)$$

where U'^{MS} and $\upsilon_A$indicate the positive constant independent of temperature and the molecular mesogen volume, respectively. θ stands for the angle between the molecular unit vector of $\mathbf{u}$, and the uniaxial director, $\mathbf{n}$. If $\mathbf{n}$ is chosen along the z-axis of a spherical coordinate system, θbecomes polar angle. The corresponding averaged energy due to the attractive interactions is given by[43]:

$$E^{MS} = \frac{ZN_A}{2}\iint U_i^{MS}\psi(\mathbf{u})\psi(\mathbf{u}')\,d\Omega d\Omega' \qquad (3-7)$$

where Zis the coordination number. Accordingly, substituting the eqn. (3-6) into eqn. (3-7) leads to the well-known result[51-56]:

$$\frac{\beta E^{MS}}{N_A} = -\beta U^{MS} S^2 c_A \upsilon_A^2 \qquad (3-8)$$

$U^{MS}$is a positive constant independent of temperature defined as $\frac{ZU'^{MS}}{2}$. The positive sign of orientation-dependent attractive parameter shows that E^{MS} decreases when the rods concentration, as well as the order parameter S, increase.

In the present work, we need to take into account the energy contribution of rod-shaped polyelectrolytes that carry like-charges because the amine functional groups of collagen are protonated in acidic pH and collagen rods have positive charges. We use a simple mean-filed potential for interchain electrostatic interactions instead of solving Poisson–Boltzmann equation and averaging over all rods. The reason is to avoid costly and time-consuming approaches[57] while maintaining accuracy and more importantly for future incorporation of the present free energy into macroscopic multi-transport models to describe de-hydration and film formation. The governing physics of mesogen self-assembly are complicated[58, 59], in turn, the simulation of self-assembly inevitably requires the solution of highly nonlinear PDEs which is time expensive[6, 60-62] therefore it is reasonable not to incorporate the Poisson–Boltzmann equation. To take into account the electrostatic forces, we shall formulate the average electrostatic potential.

According to Poisson–Boltzmann equations, two cylindrical charged particles have the tendency to be perpendicularly ordered —this phenomenon is called twisting— because such configuration minimizes the repulsion[44]. Hence, the ordered phase is destabilized because of not only rod repulsion , but also the twisting effect which resists mesogen alignment[35]. Since the orientational ordering of positively charged rods is not energetically favorable, the sign of the electrostatic mean-field potential needs to be positive in order for the energy to increase as the order parameter (or concentration of mesogen) increases. We have then taken the form of the electrostatic mean-field potential similar to Maier-Saupe one with opposite sign, as shown in eqn. (3-9). Thereafter, using eqns. (3-7, 3-9) result in eqn. (3-10) which is the contribution of interchain electrostatic interactions (i.e. repulsion and twisting) to the energy (the further elaboration on the mean-field of repulsion and twisting are in ESI, Appendix A.1):

$$\beta U_i^{elc} = +\beta U'^{elc} \upsilon_A S P_2\big(\cos(\theta)\big) \qquad (3-9)$$

$$\frac{\beta E^{elc}}{N_A} = +\beta U^{elc} S^2 c_A \upsilon_A^2 \qquad (3-10)$$

The concentration of hydronium ions [H_3O^+] —which is simply shown as [H^+]— is directly proportional to the number of charges adsorbed on the backbone of collagen (see Figure 3-12, in ESI, Appendix B.2). As a result, the increase in the concentration of hydronium ions amplifies the repulsive forces as well as the twisting effect and is the underlying cause for the destabilization of the ordered phase. In eqn. (3-10), the term which is capable of describing such physical mechanism is U^{elc}. We consequently expect unlike the U^{MS}, thatU^{elc}should vary as the amount of dissociated salt changes, moreover the $U^{elc}$and [H^+] are positively correlated.

To sum up, the orientation-dependent intermolecular interaction term in eqn. (3-3) can be written as (see ESI, Appendix A.1):

$$M=\beta U S^2 c_A \upsilon_A^2 \qquad (3-11a)$$

$$U=U^{elc}-U^{MS} \qquad (3-11b)$$

In this paper Uis denoted as the potential of orientation-dependent intermolecular interaction. Eqns. (3-11a, b) reveals that the electrostatic repulsion and twisting (our suggested mean-field treatment) competes against the phase ordering while the orientation-dependent attraction (Maier-Saupe model) promotes the long-range orientational ordering. As a consequence, a trade-off between orientation-dependent attraction and repulsion is seen, thereby showing that the increase in acid concentration gives rise to mesophasic destability (increase of free energy) because of repulsion, and on the other hand, the decrease in acid content of solution brings about stability of ordered phase.

It is noted that twisting differs from chirality as discussed in follows. Along the same lines, more recently, Drwenski et al. have used the second virial approximation to prove that the twisting phenomenon does not lead to cholesteric phase[37]. In order to complete the free energy given by eqn. (3-3), we have used the formalism of reference[39, 40] for the chirality term, $C\big(\psi(\mathbf{u})\big)$. The macroscopic gradient elastic free energy of a cholesteric phase is:

$$E^{Cholesteric}=\frac{L_1}{2}(\nabla\times\mathbf{Q}+2q\mathbf{Q})^2\upsilon_A N_A \qquad (3-12a)$$

$$q=\frac{2\pi}{p_0} \qquad (3-12b)$$

$L_1$and $p_0$represent the elastic constant and pitch, respectively. The macroscopic quantity of long-range orientational order and the averaged directions of molecules are described using a quadrupole moment tensor,$\mathbf{Q}$. In spite of the fact that cholesteric liquid crystals possess a small degree of biaxiality[63], we assume that uniaxiality is valid as it is a widely used simplification for large pitch materials[64]. Consequently, $\mathbf{Q}$-tensor is simplified to eqn. (3-13).

$$\mathbf{Q}=S\left(\mathbf{nn}-\frac{\boldsymbol{\delta}}{3}\right) \qquad (3-13)$$

$\boldsymbol{\delta}$ shows the Kronecker delta. The order parameter in eqn. (3-13) is not space-varying as long as the solution reaches the thermodynamic equilibrium. In such a case, the uniaxial director field is expected to obey eqn. (3-14).

$$\mathbf{n}=[\cos(qz)\quad \sin(qz)\quad 0] \qquad (3-14)$$

Substituting eqn. (3-13) and eqn. (3-14) into eqn. (3-12a), one can obtain the contribution of macroscopic phase chirality to the free energy (see ESI, † Appendix A.2):

$$C = \frac{\beta E^{\text{Cholesteric}}}{N_A} = \frac{32\pi^2}{3}\left(\frac{\xi}{p_0}\right)^2\left(\frac{L}{D_{\text{eff}}}\right)S^2 \qquad (3-15)$$

where L and ξ corresponds to the contour length and coherence length defined by $\xi=\sqrt{\frac{a^3 L_1 \beta}{2}}$ in which a^3 indicates the volume of each lattice unit, respectively. It is also noted that the uniaxial cholesteric phase (N*) is defined by a helix unit vector **h**, a signed pitch (the sign refers to left and right helices), a scalar order parameter S, and a director **n**.

3.4.2 Energy contributions for chiral charged mesogen solutions in isotropic solvents

In this subsection, the total free energy of mixing per lattice (difference between the states of solution and pure), which is the driving force for phase ordering and separation, is obtained. Like the approach of Das et al.[54], we classify the constituents of a binary mixture as anisotropic and isotropic; the former capable and the latter incapable of adopting long-range orientational order. In our case, the anisotropic (A) component is collagen rods and the isotropic (I) component consists of acetic acid and water. Extending the free energy based on the reference[41] by considering the interchain electrostatic interactions (i.e. repulsion and twisting) and macroscopic chirality, the free energy of a triple helix acidic aqueous collagen solution reads:

$$\begin{aligned}\beta F^s = {} & N_A\beta\mu_A^o + N_I\beta\mu_I^o - N_A - N_I + N_A \ln c_A' + N_I \ln c_I' + N_A\sigma\big(\psi(\mathbf{u})\big) \\ & + \bar{\upsilon}_{AA}N_A c_A \rho\big(\psi(\mathbf{u})\big) + 2\bar{\upsilon}_{AI}N_I c_A + \bar{\upsilon}_{II}N_I c_I + \beta U c_A \upsilon_A^2 N_A S^2 \\ & + \frac{32\pi^2}{3}\left(\frac{\xi}{p_0}\right)^2 \frac{L}{D_{\text{eff}}} N_A S^2\end{aligned} \qquad (3-16)$$

The degree of molecular alignment along the uniaxial director can be commonly measured by the ensemble average of the second Legendre polynomial:

$$S = \int P_2\big(\cos(\theta)\big)\psi(\mathbf{u})\,d\Omega \qquad (3-17)$$

where the single-rod orientational distribution function is normalized by:

$$\int \psi(\mathbf{u})\,d\Omega = 1 \qquad (3-18)$$

In the isotropic phase the normalized distribution function is a constant equal to $1/4\pi$[43], also $\sigma(\psi(\mathbf{u}))=0$ and $\rho(\psi(\mathbf{u}))=1$[38]. Employing the Euler-Lagrange method to minimize the eqn. (3-16) with respect to the distribution function along with considering the constraint of eqn. (3-18) lead to (see ESI, † Appendix A.3 for details):

$$\ln(4\pi\psi(\theta))=\eta'-2\left(\beta U c_A \upsilon_A^2+\frac{32\pi^2}{3}\left(\frac{\xi}{p_0}\right)^2\frac{L}{D_{eff}}\right)SP_2(\cos(\theta)) \\ -\frac{8}{\pi}\overline{\upsilon}_{AA}c_A\int\Gamma(\gamma)\psi(\theta')d\Omega' \qquad (3-19)$$

As we will discuss later on, the constant of η' is determined using the normalization restriction. The irreducible integral equation of eqn. (3-19) can be further simplified by expanding the eqn. (3-5c) in terms of the second Legendre polynomial[65].

$$\Gamma(\gamma)\approx\frac{\pi}{4}-\frac{5\pi}{32}\left(1-\frac{11}{8}h\right)P_2(\cos(\gamma)) \qquad (3-20a)$$

$$P_2(\cos(\gamma))\approx P_2(\cos(\theta))P_2\left(\cos(\theta')\right) \qquad (3-20b)$$

Substituting eqns. (3-20a-b) into eqn. (3-19) yields:

$$\psi(\theta)=\eta\exp\left(WSP_2(\cos(\theta))\right) \qquad (3-21a)$$

$$W=\lambda_{ExE}+\lambda_{II}+\lambda_{ChE} \qquad (3-21b)$$

$$\lambda_{ExE}=\frac{5}{4}\left(1-\frac{11}{8}h\right)\phi_A^{eff}\frac{L}{D_{eff}}=\frac{5}{4}\left(1-\frac{11}{8}h\right)c_A\overline{\upsilon}_{AA} \qquad (3-21c)$$

$$\lambda_{II}=-\frac{\pi}{2}D_{eff}^2\beta U\phi_A^{eff}L \qquad (3-21d)$$

$$\lambda_{ChE}=-\frac{64\pi^2}{3}\left(\frac{\xi}{p_0}\right)^2\frac{L}{D_{eff}} \qquad (3-21e)$$

whereby the normalized distribution function can be explicitly determined. Here we denote W as the net cholesteric potential because the scalar order parameter, which is the yardstick of ordering, is the exclusively function of W (see eqn. (3-23a)). λ_{ExE}, λ_{II} and λ_{ChE} are coupling parameters of excluded volume-electrostatic, intermolecular interaction and chirality-electrostatic contributions, respectively. Substituting the obtained distribution function, eqn. (3-21a), into the normalization restriction, eqn. (3-18), gives the constant η:

$$\eta=\frac{1}{4\pi I_0} \qquad (3-22a)$$

$$I_0(W,S) = \int_0^1 \exp\left(WSP_2(x)\right) dx \qquad (3-22b)$$

As a result of obtaining the normalized distribution function, we can formulate the order parameter as the self-consistent equation:

$$S=\frac{I_1(W,S)}{I_0(W,S)} \qquad (3-23a)$$

$$I_1(W,S) = \int_0^1 P_2(x)\exp\left(WSP_2(x)\right) dx \qquad (3-23b)$$

Furthermore, the orientation-dependent terms $\sigma\left(\psi(\theta)\right)$, $\rho\left(\psi(\theta)\right)$ are determined by substituting the normalized distribution function into eqn. (3-4).and eqn. (3-5b):

$$\sigma\left(\psi(\theta)\right)=WS^2\text{-}\ln(I_0) \qquad (3-24a)$$

$$\rho\left(\psi(\theta)\right)=1\text{-}\frac{5}{8}\left(1\text{-}\frac{11}{8}h\right)S^2 \qquad (3-24b)$$

In the rest of this subsection, we derive the free energy difference between a mixture and pure components, or mixing free energy. The mixing free energy ΔF_{mixing} is[41, 66]:

$$F=\Delta F_{mixing}(N_A,N_I)=F^s(N_A,N_I)\text{-}F^s(N_A,0)\text{-}F^s(0,N_I) \qquad (3-25)$$

where $F^s(N_A,N_I)$, $F^s(N_A,0)$ and $F^s(0,N_I)$ are free energy of solution, pure anisotropic component in the isotropic state and isotropic components, respectively. We have used the approach mentioned in the reference[41] about the number of segments along the backbone of components. Thus, we have taken $\upsilon_i=a^3n_i$where n_i and a^3indicate the number of segments for i^{th} component and volume of a lattice, respectively. Also,$n_A^{eff}=L/D_{eff}$and $V=a^3N_T$where the total number of lattice site is $N_T=n_A^{eff}N_A+n_IN_I$. Finally, substituting the eqn. (3-16) into eqn. (3-25) leads the total dimensionless free energy per lattice site, $\mathscr{F}$(see ESI,† Appendix A.4 for details):

$$\mathscr{F}=\frac{\beta F}{N_T}=\frac{\phi_A^{eff}\ln\phi_A^{eff}}{n_A^{eff}}+\phi_I^{eff}\ln\phi_I^{eff}+\chi\phi_A^{eff}\phi_I^{eff}+\frac{\phi_A^{eff}}{n_A^{eff}}\left[\frac{1}{2}WS^2\text{-}\ln\left(I_0(W,S)\right)\right] \qquad (3-26)$$

In eqn. (3-26), χ stands for isotropic Flory-Huggins parameter given by eqn. (3-27). This parameter is mainly function of temperature and can be generally estimated as $\chi=\frac{A}{T}$ where A is physical constant related to solubility parameters (see ESI,† Appendix B.1), additionally it determines the miscibility of components in isotropic phase.

$$\chi = a^3 \left(\frac{2\overline{\upsilon}_{AI}}{\upsilon_A \upsilon_I} - \frac{\overline{\upsilon}_{AA}}{\upsilon_A^2} - \frac{\overline{\upsilon}_{II}}{\upsilon_I^2} \right) \qquad (3-27)$$

υ_i and $\overline{\upsilon}_{ij}$ represent the molecular volume of i^{th} component and the averaged excluded volume between components of i and j. The first three terms in eqn. (3-26) are referred to Flory-Huggins theory. Moreover, the last two terms explain the free energy change due to the alignment of the mesogens.

In partial summary, for completeness and to facilitate reading, (a) the key thermodynamic results and (b) the main assumptions and simplifications used in this study are as follows:

(a) Thermodynamic results:

1. The total dimensionless free energy of mixing per lattice site, eqn. (3-26), provides the metastability condition for the phase separation in acidic collagenous solutions — this subject is explained in the subsequent subsection. The chemical potentials of isotropic and cholesteric phases are the criteria by which the binodal boundaries in phase diagrams of concentrations (acetic acid versus the collagen, Figure 3-3) and the ubiquitous athermal chimney (temperature against the collagen volume fraction, Figure 3-7) are determined.

2. Eqn. (3-23a) is a nonlinear algebraic equation whose trivial root corresponds to the isotropic phase and non-trivial root corresponds to the macroscopic order parameter in cholesteric phase. The condition, under which the nontrivial root is obtained, establishes the phase ordering boundary. This subject is further discussed in subsection 3.5.2.

3. Having LdG coefficients in terms of solution's parameters is an important practical result. The linearization of eqn. (3-26) near the order-disorder phase shift ends up like the LdG expansion. Hence, the linearized form of eqn. (3-26) resolves the long-standing problem of quantifying the LdG coefficients. This subject is more elaborated in section 3.6.

(b)Assumptions and simplifications:

1. Although cholesteric phases manifest some small degree of biaxiality, we assume the uniaxiality is the underlying factor in variation of free energy. 2. Rigidity of collagen rods is reasonable on account of the presence of mobile ions. 3. To determine the linear charge density, we use the common assumption that pKa of residues in collagen are kept constant equal to their isolated values while the pH varies and other residues are protonated or deprotonated. 4. The pitch functionality on concentration is taken from experimental data and

is not an output of the model (i.e. there is no minimization of the energy with respect to the macroscopic pitch).

3.5 Phase diagrams

3.5.1 Binodals

The criterion of metastability boundaries, binodal curves, is given by :

$$\mu_i^{Cho}=\mu_i^{Iso} i \in \{A,I\} \qquad (3-28)$$

the superscripts Cho and Iso stand for Cholesteric and Isotropic phase, respectively. Eqns. (3-29a-b) show the chemical potentials in an arbitrary phase j. To rewrite chemical potential in term of total dimensionless free energy per lattice and volume fraction, one can use the fact that for the equal lattice sites $\phi_i = \frac{n_i N_i}{N_T}$, and the chain rule (see ESI,† Appendix A.5) gives:

$$\mu_A^j = \left(\frac{\partial F^j}{\partial N_A}\right)_{N_I,T} = n_A^j \left(\mathscr{F}^j + \phi_I^j \left(\frac{\partial \mathscr{F}^j}{\partial \phi_A^j}\right)_{\phi_I^j,T} \right) \qquad (3-29a)$$

$$\mu_I^j = \left(\frac{\partial F^j}{\partial N_I}\right)_{N_{A,T}} = n_I^j \left(\mathscr{F}^j + \phi_A^j \left(\frac{\partial \mathscr{F}^j}{\partial \phi_I^j}\right)_{\phi_A^j,T} \right) \qquad (3-29b)$$

3.5.2 Isotropic-cholesteric phase transition

The self-consistent equation, eqn. (3-23a), has the nontrivial solution if $W \geq 4.5$; otherwise isotropic phase exists which means the numerical solution of eqn. (3-23a) converges to $S=0$. Moreover, the isotropic-cholesteric transition concentration, eqn. (3-30), is then determined by the equality of the mentioned criterion.

$$\phi_A^{eff,*} = \frac{4.5\frac{D_{eff}}{L} + \frac{64\pi^2}{3}\left(\frac{\xi}{p_0}\right)^2}{\frac{5}{4}\left(1-\frac{11}{8}h\right) - \frac{\pi}{2}D_{eff}^3 \beta U} \qquad (3-30)$$

3.6 Asymptotic analysis

The well-known macroscopic Landau-de Gennes (LdG) **Q**-tensor theory is based on the sum of homogeneous entropic/enthalpic free energy (quartic polynomial in **Q**) plus the gradient Frank elasticity contributions, and is needed for macroscopic process simulations such as the

formation of collagen films. Accurate prediction of spatially homogeneous phase ordering strongly depends on the accurate determination of its phenomenological coefficients appearing in the homogeneous free energy contribution. Next, we derive expressions of the phenomenological coefficients of LdG in terms of the microscopic theories of Flory-Huggins, Onsager, Maier-Saupe, and electrostatic mean-field potential.

The anisotropic part of the free energy, eqn. (3-26), asymptotically becomes equivalent to the LdG formulation if one expands $\ln\left(I_0(W,S)\right)$in the vicinity of the uniaxial I-N* phase transition. Linearization of eqn. (3-26) around the uniaxial I-N* yields:

$$\mathscr{F} = \frac{\phi_A^{eff} \ln \phi_A^{eff}}{n_A^{eff}} + \phi_I^{eff} \ln \phi_I^{eff} + \chi \phi_A^{eff} \phi_I^{eff} + A\mathbf{Q}:\mathbf{Q} + B\mathbf{Q}:(\mathbf{Q}\cdot\mathbf{Q}) + C(\mathbf{Q}:\mathbf{Q})^2 \qquad (3-31a)$$

$$A = \frac{3}{4}\frac{W\phi_A^{eff}}{n_A^{eff}}\left(1-\frac{W}{5}\right) \qquad (3-31b)$$

$$B = -\frac{9}{210}\frac{\phi_A^{eff} W^3}{n_A^{eff}} \qquad (3-31c)$$

$$C = \frac{9}{2800}\frac{\phi_A^{eff} W^4}{n_A^{eff}} \qquad (3-31d)$$

Nonzero value of B implies that the phase transition is first order. Furthermore, the negative value of Band positive value of Cguarantee two minima of the free energy—$\mathbf{Q} = \mathbf{0}$and $\mathbf{Q} > \mathbf{0}$ correspond to isotropic and cholesteric phases, respectively. Therefore, we can see that the obtained coefficients meet all the restrictions of the LdG theory[67]. Biaxiality effects for A, B, C are beyond of the scope of this paper and will be treated in future work.

3.7 Results and discussion

We have assembled and discussed all model parameters and material properties used in this section, in the Appendix B of the ESI. A crucial parameter in the rheology of collagenous films flows (used to fabricate actual collagen films) is the ratio of persistent length to effective diameter of the flowing and rotating unit[3, 6, 20]. Herein, we take the length of collagen as constant equal to its contour length since collagen macromolecules form rigid rods in the presence of mobile ions[17]. Yet, the effective diameter is inversely proportional to the concentrations of both collagen rods and acetic acid (for more information on the functionality of the effective diameter see Appendix A.6). Typically in the present study, L/D_{eff} ranges from

65 to 120 in biphasic to fully cholesteric regimes which is consistent with the values suggested by[6, 68].

Now turn to show the need of including intermolecular electrostatic interactions, and thereafter we examine the correctness of suggested mean-field electrostatic potential.

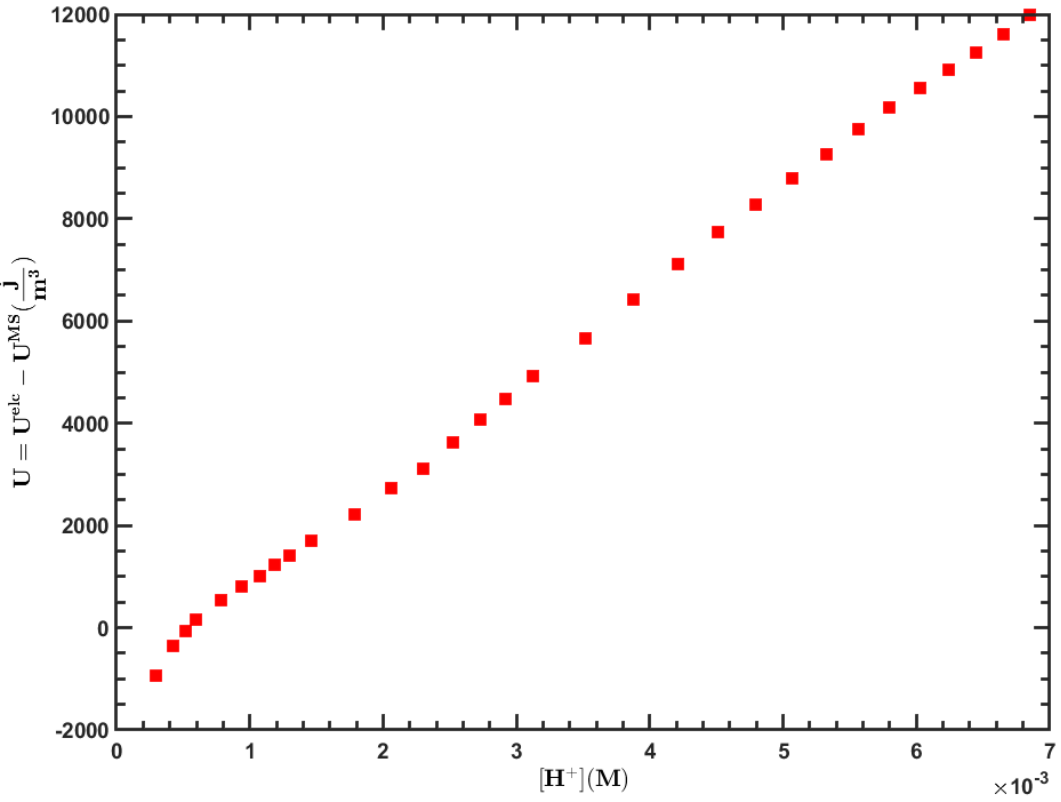

Figure 3-2. The potential of orientation-dependent intermolecular interaction,U, along the phase transition curve. The red squares are calculated based on the phase transition data reported in reference[16].

Figure 3-2 shows the potential of orientation-dependent intermolecular interactions U as a function of the concentration of hydronium ions. To construct this figure, based on the eqns. (3-11b, 3-30), we use the known concentrations of collagen and acetic acid at the order-disorder (isotropic-cholesteric) phase transition, extracted from[16]. In eqns. (3-3, 3-10) we included electrostatic interactions, due to the positive charges on the collagen backbone, which consist of repulsion as well as twisting. Figure 3-2 confirms the existence and essential role of U^{elc} because U^{MS} is a constant and incapable of capturing the experimental data. In the absence of acetic acid in the system, the only orientation-dependent interaction is attraction captured by U^{MS}. When acetic acid is dissolved, the rods take on fixed positive charges, and as a result,

repulsion and twisting emerge. U^{elc} is responsible to describe the interchain electrostatic interactions due to the variation of acetic acid concentration. Furthermore, as elaborated in the Appendix B.2, the linear charge density of collagen rods is inversely proportional to pH, in turn, directly proportional to the concentration of hydronium ions. In other words, the more hydronium ions exist in the solution, the more positive charges collagen macromolecules take. The increase in the number of charges on the collagen backbone makes the repulsion and twisting stronger, which competes with phase ordering. Accordingly, the acetic acid forces the phase ordering process to increase its energetic cost, and hence U^{elc}must be directly proportional to the concentration of hydronium ions as predicted in subsection 3.4.1 and shown in Figure 3-2. Lastly, Figure 3-2 shows that the y-intercept of the extrapolated experimental data would be negative which gives rise to a positive constant for the Maier-Saupe interaction parameter, U^{MS}. This result indicates that our suggested model is consistent with Maier- Saupe theory. Figure 3-2 also reflects the change in the trend of intermolecular interaction as a function of the concentration of mobile hydronium ions. The slope of Uon the concentration of hydronium ions in the very dilute solution of acetic acid is larger than in the concentrated solution. This can be explained through the screening effect. When the concentration of mobile ions is higher, the electrostatic potential is screened and acts over shorter distances as a consequence of the shorter Debye length, whereas at low concentration of mobile ions, the Debye length becomes longer and the electric potential decays over longer distances.

In partial summary, these results of Figure 3-2 show that the model is in agreement with Maier-Saupe's model, and that the chosen the electrostatic mean-field potential (eqn. (3-10)) captures the experimental collagen data.

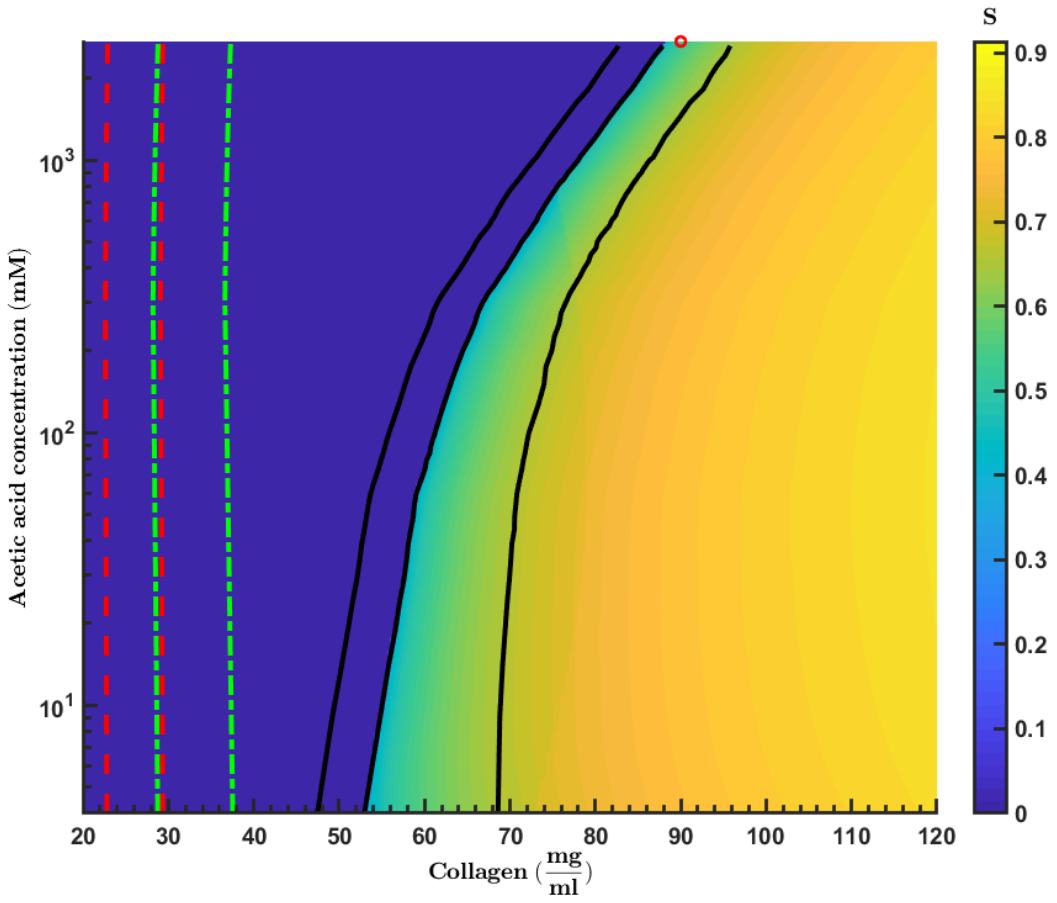

Figure 3-3. Phase diagram of the acidic collagenous solution at 25 °C. The black solid lines from left to right indicate lower binodal curve, I-N* phase transition and upper binodal curve. The color shows the variation of the macroscopic order parameter S in the phase diagram. The red dash lines and green dash-dotted lines are binodal curves for Onsager and SLO theories[44].

Figure 3-3 shows the phase diagram in terms of acetic acid concentration as a function of collagen concentration. The middle curved black solid line, originating at the bottom of the plot at a collagen concentration of around 52mg/ml , is the experimental phase transition boundary extracted from[16] by which and eqn. (3-30) the potential of orientation-dependent intermolecular interaction, U, is obtained (Figure 3-2). The two other curved back solid lines correspond to the predicted binodal curves obtained by solving the nonlinear eqns.(3-28, 3-29a-b). The obtained binodal curves are in acceptable agreement with the experimental results[16]. The color (blue to yellow) is used to show the magnitude of predicted macroscopic scalar order parameter. As the solution becomes more concentrated with collagen rods, the orientational ordering increases. This phase behavior stems from the lyotropic nature of collagen. The red dash-line and green dash-dotted line, which respectively stand for the Onsager and SLO theories[43], show that the acidic collagenous solutions are not only governed by excluded volume and twisting effects.

Experiments indicate that for acetic acid at 2.9M and 90 mg/ml collagen the scalar order parameter is 0.45±0.1 (upper red dot in Figure 3-3). Using eqn.(3-23a) we find that for 90mg/ml collagen and 2.9 M acetic acid our model predicts S=0.47 , again in good agreement with experimental data[16].

It is useful to compare the accuracy of the obtained transition concentration, eqn. (3-30), with classical approaches. Onsager has theoretically shown that the solution comprises of rod-like molecules are able to undergo an order- disorder transition if the concentration of rods exceeds a threshold given by[44]:

$$\phi_A^{eff,*}=K^i\frac{D_{eff}}{L}, K^l=3.3399, K^u=4.4858 \qquad (3-32)$$

The superscripts of l andu stand for lower and upper binodal curves, respectively. The SLO (Stroobants, Lekkerkerker and Odjik) theory includes the effect of twisting to Onsager theory[44]:

$$\phi_A^{eff,*}=\frac{K^{1,i}\frac{D_{eff}}{L}}{1-K^{2,i}h}, K^{1,l}=3.290, K^{2,l}=0.675, K^{1,u}=4.191, K^{2,u}=0.730 \qquad (3-33)$$

Next, we discuss the thermodynamic and phase transition predictions of the Onsager, SLO and present model for acidic aqueous collagen I solutions (see Figure 3-3). We find that although the Onsager theory, eqn. (3-32), has included the effect of electrostatic repulsion as swelling of the bare diameter, D_{eff}, it is not still able to provide an acceptable prediction for the binodal curves. Similarly, SLO theory underestimates the actual phase transition boundary, whereas it gives a better estimation than Onsager theory due to inclusion of the twisting effect. The deviation of the prediction of these fundamental theories from experimental data[16] shows that the acidic solutions of collagen are governed by multiple mechanisms, which in the present model are integrated to accurately describe the energy landscape. Our formulation for the threshold of phase transition, eqn. (3-30), reveals that in addition to repulsion and twisting, mechanisms of orientation-dependent intermolecular interaction and chirality play a role in phase ordering. That is why our approach gives higher collagen concentration values than the Onsager (eqn.(3-32)) and SLO (eqn.(3-33)) predictions.

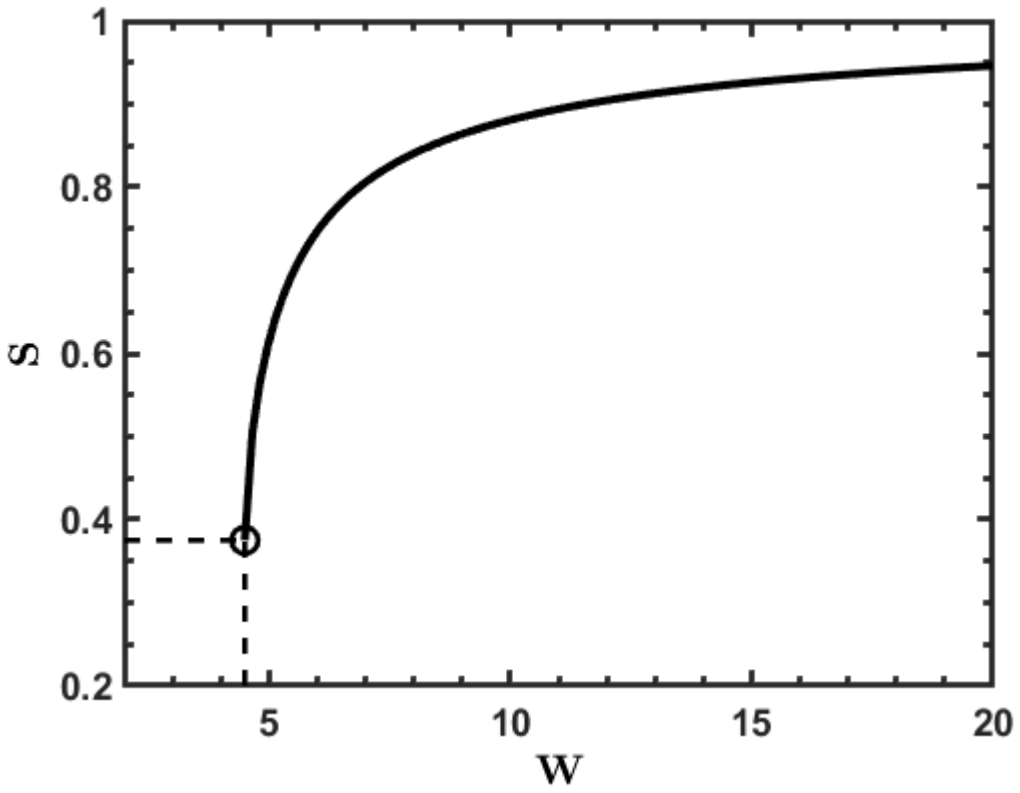

Figure 3-4. The uniaxial order parameter S as a function of the net cholesteric potential W. The predicted value of S at the transition is relatively low and less than 0.4.

Figure 3-4 shows the uniaxial order parameter S as a function of the net cholesteric potential W (eqn. (3-22b, 3-23a-b)). The figure shows that S increases with W and jumps from $S = 0$ isotropic phase to $S_c \approx 0.38$, if the net cholesteric potential crosses the threshold of $W \approx 4.5$. However, the Onsager and LdG theories, which are more tailored for lyotropic liquid crystal, predict the critical scalar order parameter 0.792 and 0. 5 at the phase transition, respectively[33, 67]. Although the critical order parameter for the acidic solutions of collagen has not been documented, one can readily estimate the maximum value of critical order parameter by using the aforementioned experimental order parameter and linear interpolation. The critical concentration of collagen for the solution of 2.9 M acetic acid is nearly 82.5mg/ml (mean value of 80-85 mg/ml)[16]. In addition, the experimental value of the scalar order parameter for the solution of 90 mg/ml collage and 2.9 M acetic acid is 0.45, as shown in Figure 3-3 (the given experimental point is very close to the phase transition boundary). The linear interpolation then estimates the critical order parameter as 0.41. We expect that the actual order parameter at order-disorder phase transition would be lower than 0.41 because the scaling of phase ordering in the vicinity of the phase transition is sharper than linear. In partial conclusion, comparing

with the values of critical order parameter predicted by Onsager and LdG theories, our model performs more accurately.

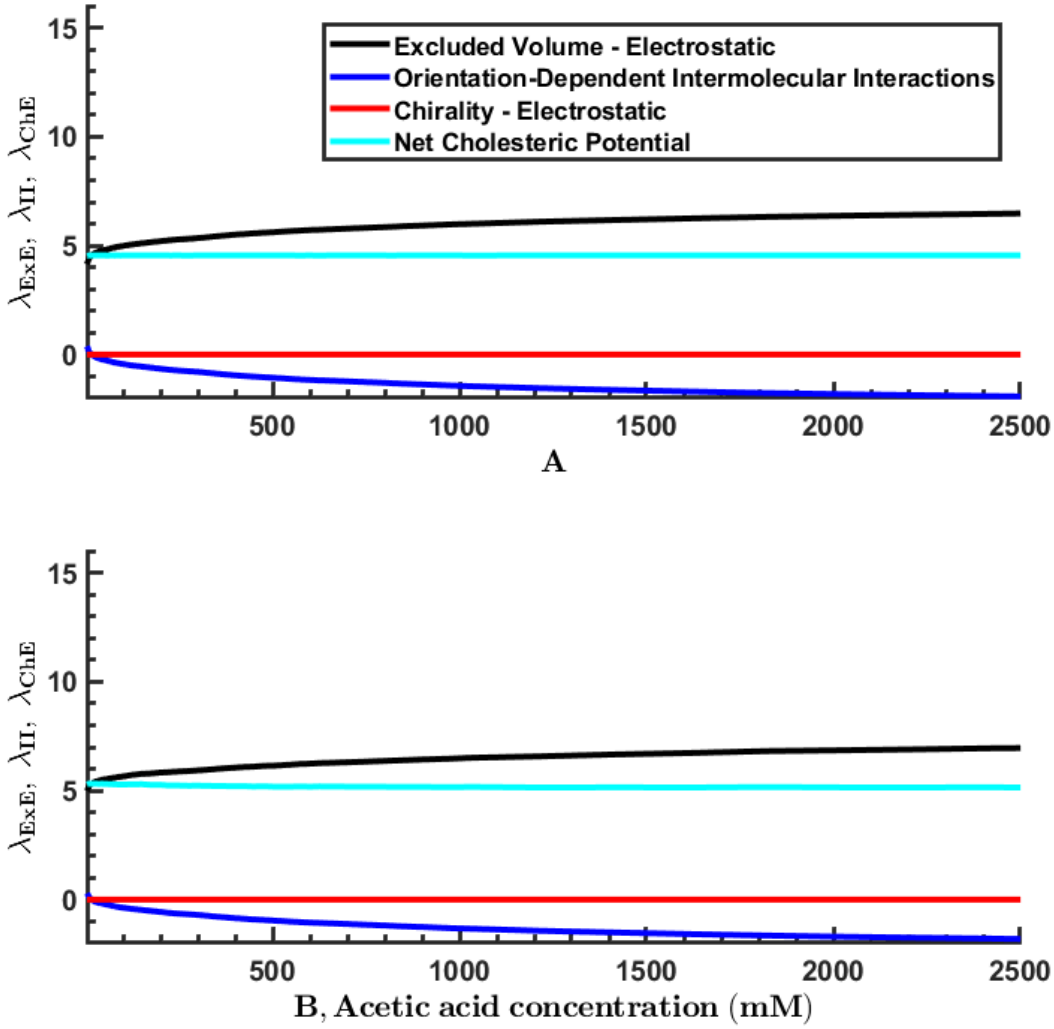

Figure 3-5. Coupling parameters along the A) phase transition curve B) cholesteric metastability curve (cholesteric binodal). See equations 3-21b-e. The sum of these three coupling parameters is the net cholesteric potential W.

It is important to quantify how the three contributions of the net cholesteric potential W (eqn. (3-21b)) vary with acetic acid concentration. Figure 3-5 show the coupling parameters formulated in eqns. (3-21b-e) along the phase transition curve and the cholesteric binodal curve, respectively. When the concentration of acetic acid tends to zero, the number of charges on the collagen rods becomes negligible and the prevailing interaction is attraction. For this reason, in the extremely dilute concentration of acetic acid, the potential of orientation-dependent intermolecular interaction, U, becomes negative which results in making the

coupling parameter of orientation-dependent intermolecular interaction, λ_{II}, positive. Apart from infinitely dilute solution, λ_{II} is negative, and it is monotonically decreasing with acidic acid concentration increases. The negative sign is due to the fact that in acidic solutions of collagen, the dominant interchain interaction is repulsion therefore Uand λ_{II}have to be positive and negative, respectively (see eqn. (3-11b) and eqn. (3-21d)). The monotonically decreasing trend in λ_{II}reflects the intrinsic behavior of collagen rods for taking more positive charges as the concentration of acetic acid increase. While the number of charges on the collagen backbone becomes denser, the repulsion and twisting among the rods become higher and hence$U^{elc} \propto [AA] \propto [H^+] \propto -\lambda_{II}$ where [AA] is the concentration of acetic acid. Accordingly, the graphs of λ_{II} indicate: (i) save for the very dilute concentration of acetic acid, the repulsion and twisting are primary mechanisms and van der Waals attractive interactions is less influential; (ii) these graphs support the need for and accuracy of the electrostatic mean-field potential we have added in section 3.4.1.

Figure 3-5 reveal that the coupling parameter of chirality-electrostatic acquires negative infinitesimal values in the acidic collagenous solutions and plays an insignificant role in the net cholesteric potential as well as in the scalar order parameter. The negative value for λ_{ChE} demonstrates that our work is consistent to previous studies[20, 21, 39]. In our study, due to the negative sign of λ_{ChE} (see eqns. 3-21(e)), the ratio of coherence length over pitch, $\frac{\xi}{p_0}$, is inversely proportional to the net cholesteric potential, W, and the scalar order parameter, S. The uniaxial order parameter S as a function of the length scale $\frac{\xi}{p_0}$ is[39]:

$$S=\frac{1}{4}+\frac{1}{4}\sqrt{9-\frac{24}{P}-\frac{96}{P}\pi^2\left(\frac{\xi}{p_0}\right)^2} \qquad (3-34)$$

where $P=\frac{3c}{c^*}$ represents the cholesteric potential of phase ordering;c^* is number density at the I/N* phase transition. As can easily be seen, $\frac{\xi}{p_0}$ and S are inversely correlated[39]. The negligible impact of chirality on the phase ordering stems from the large pitch of collagen (micron scale). The magnitude of $\left(\frac{\xi}{p_0}\right)^2$ is in the range of 10^{-7} – 10^{-8} and the chirality effect on S is essentially negligible . In general, for small molecular weight rod-like mesogens, the free energy difference for the transition from cholesteric to nematic is considerably smaller than the transition from isotropic to nematic[44]. In the case of acidic solutions of collagen, the micrometer-sized pitch of collagen makes this small difference negligible.

Figure 3-5 A corresponds to the I-N* phase transition curve therefore the value of the net cholesteric potential is kept as a constant equal to 4.5. Although along the metastability curve (Figure 3-5 B) the net cholesteric potential slightly increases, the dependency of Won concentration has not become relatively significant. This shows that the primary growth in the scalar order parameter happens in the cholesteric phase not in the biphasic region. Regarding the coupling parameter of excluded volume-electrostatic, λ_{ExE}, Figure 3-5 demonstrate that it is the dominant term in phase ordering compared to the other terms. There are two main reasons why the coupling parameter of excluded volume-electrostatic, λ_{ExE}, is more significant than orientation-dependent intermolecular interaction, λ_{II}. The increase in concentration of acetic acid increases the effective diameter and shortens the Debye length, in which case, the twisting parameter, $h=(\kappa^{-1}/D_{eff})$, decreases, and also the excluded volume is more affected because it is directly proportional to the effective diameter, $\upsilon_{AA} \propto D_{eff}L^2$ (see eqn. (3-21c)). It should be also considered that $\lambda_{ExE} \propto c_A$and along the phase transition curve the concentration of collagen as well as acetic acid are increased. Finally, all of these factors cause that the effect of excluded volume to become dominant and the monotonically increasing trend in $\lambda_{ExE}$is expected.

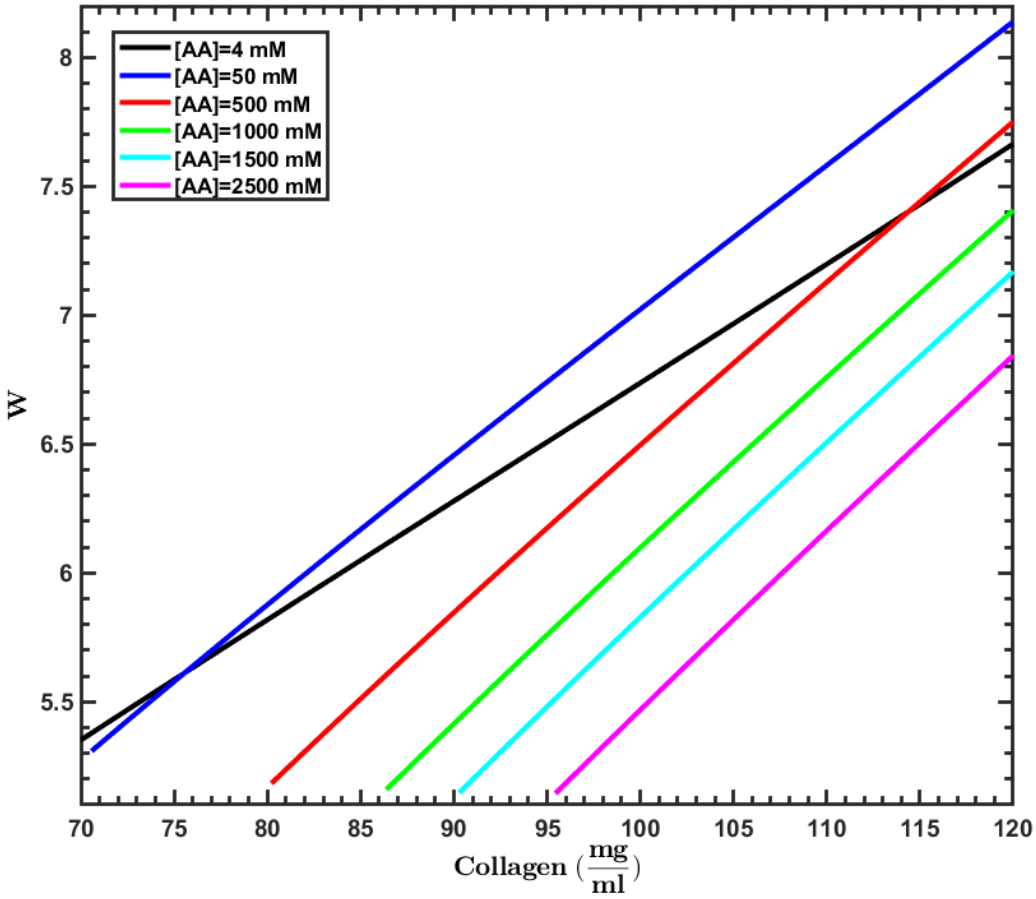

Figure 3-6. Typical variation of the net cholesteric potential with respect to the concentrations of collagen and acetic acid concentration [AA] in the cholesteric region of phase diagram shown in Figure 3-3.

Figure 3-6 characterizes the dependency of the net cholesteric potential as a function of collagen concentration at the various acetic acid concentrations. All lines have positive slopes; therefore, the net cholesteric potential has a linear dependency on the concentration of collagen that reflects the lyotropic nature of the collagenous solution. Under dilute [AA] conditions, due to lack of mobile ions, the Debye length increases and the electrostatic potential can act over longer distances therefore the phase ordering intensity decreases. Thus, the slope of W decrease as [AA] decrease from nearly 50 mM to 4 mM.

To reach a specific W ([AA]>50mM), the required collagen concentration goes up as the solution becomes more acidic. The increase in acetic acid concentration results in reducing the orientational ordering. Hence, $\lambda_{II} < 0$ and λ_{II} decreases by increasing the acetic acid concentration (see eqn. (3-21d)). Because $\lambda_{ExE} > 0$ and $\lambda_{ExE} \propto c_A$, the increase in collagen concentration can compensate the competing disordering effect generated by increasing [AA].

From Figure 3-6, we can similarly conclude that for a constant concentration of collagen, the decrease in [AA] ($50\text{mM} < [\text{AA}] < 2900\text{mM}$) leads to higher orientational S. This important result can be also obtained using the color-plot in the Figure 3-3.

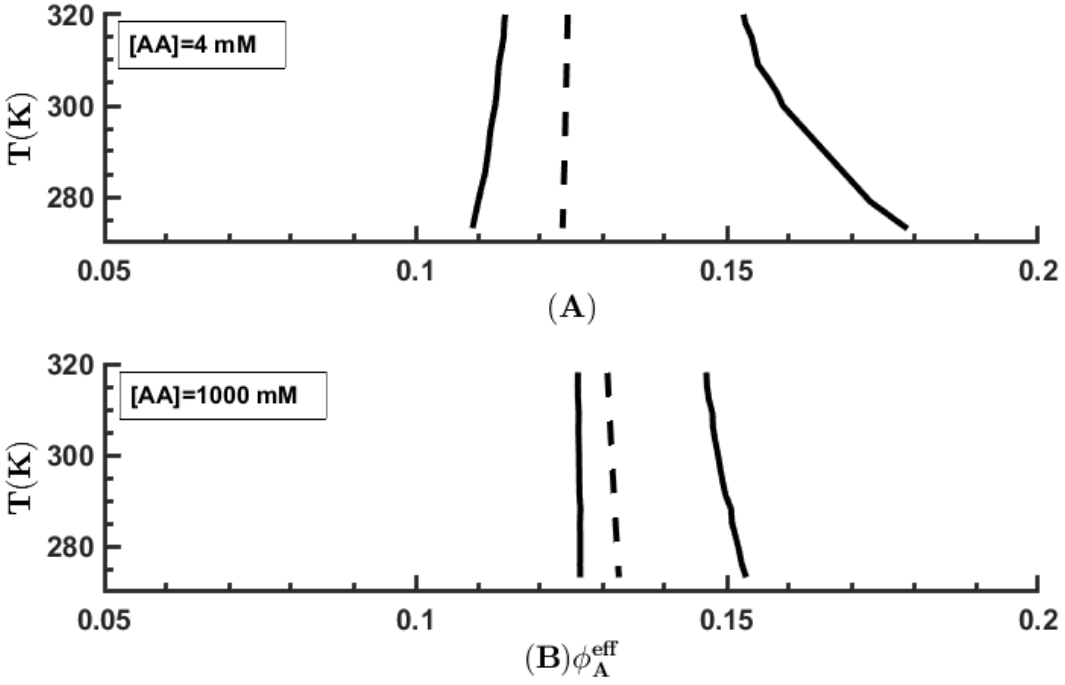

Figure 3-7. The chimney-like equilibrium phase diagrams for the acidic collagenous solutions, A) 4 mM acetic acid and B) 1000 mM acetic acid.

A characteristic feature of lyotropic liquid crystalline temperature-concentration phase diagram is the presence of an athermal bi-phasic chimney, sometimes refereed as the Flory chimney. Since the collagen solution belong to this class of polymers, our model should also predict it. Equally important the biphasic chimney conditions yield micron-range tactoids that serve as liquid crystal fingerprinting and whose shape and size reflect important properties. Consistent with previous experimental and theoretical studies[54], the shape of T-ϕ_A^{eff} diagram displays a chimney, as shown in Figure 3-7. The chosen range of temperature in these figures correspond to a safe range in which collagen is not denatured. The figure shows that on increasing [AA], the chimney becomes narrower and the phase transition boundary slightly shifts right. Therefore, the electrostatic interactions delay the appearance of the biphasic region, and induce the imminent emergence of a birefringent phase (i.e. chiral nematic phase). This behavior can be also interpreted from Figure 3-3 plotted under a constant temperature; the width of biphasic region in this figure becomes broader in bottom where [AA] is lower.

3.8 Conclusions

In this work, we have thoroughly analyzed the driving mechanisms that govern the thermodynamics of acidic collagenous aqueous solutions. For these solutions, we have established a multiscale energy landscape emerging from microscopic entropic and enthalpic mechanisms of mixings, excluded volume, orientation-dependent attractive interactions, interchain electrostatic interactions (i.e. repulsion and twisting), and macroscopic chirality. Regarding the modeling of interchain electrostatic interactions, we have introduced a simple mean-field potential, thereafter we have validated the effectiveness of the proposed potential by experimental data. Moreover, our suggested theory is compatible with the experimental phase diagrams (Figure 3-3[16]), the experimental order parameter[16], and previous theoretical studies[38, 41]. In the vicinity of I-N*, the linearized form of our proposed continuum theory converges to the LdG theory whereby this study has provided a systematic framework to obtain the phenomenological coefficients of LdG (eqns. (3-31b-d)). We have demonstrated that just three coupling parameters (eqn.(3-21 c-e)) can have an impact on the phase ordering. For the acidic collagenous solutions, phase ordering is primarily excluded-volume-driven, moderately affected by the intermolecular interactions (repulsion, twisting and attraction), and almost unaffected by chirality (Figure 3-5). Furthermore, our results have shown that while the excluded volume and the orientation-dependent attractive interactions promote the orientational ordering, the interchain electrostatic interactions (i.e. repulsion and twisting) compete against the emergence of mesophase. Adding acid to the collagenous solutions results in repulsion and twisting which compete with chiral nematic phase ordering. In particular, the role of interchain electrostatic interactions, that we have incorporated in the proposed energy landscape, is to narrow the I-N* biphasic region (Figure 3-7). The present model predicts a chimney-like phase diagram as expected from lyotropic liquid crystal polymers. Our approach possesses the distinguishing features of accuracy and simplicity; therefore, this work has a potential significance to narrow the gap between existing experimental platforms and sought-after material performance.

3.9 Acknowledgement

SAK would like to thank Prof. Belamie and Prof. Matsuyama for explanations of facts cited in this article. SAK acknowledges financial support from the McGill Engineering Doctoral Awards (MEDA) program. This work as supported by a grant from Natural Sciences and

Engineering Research Council of Canada (NSERC). ADR is thankful to McGill University for financial support through the James McGill Professorship appointment.

References (Chapter 3)

1. Rastian Z, Putz S, Wang YJ, Kumar S, Fleissner F, Weidner T, et al. Type I Collagen from Jellyfish Catostylus mosaicus for Biomaterial Applications. ACS Biomater Sci Eng. 2018;4(6):2115-25.

2. Aguilar Gutierrez OF, Rey AD. Biological plywood film formation from para-nematic liquid crystalline organization. Soft Matter. 2017,13, 8076-8088.

3. Brown AI, Kreplak L, Rutenberg AD. An equilibrium double-twist model for the radial structure of collagen fibrils. Soft Matter. 2014;10(42):8500-11.

4. Cameron S, Kreplak L, Rutenberg AD. Polymorphism of stable collagen fibrils. Soft Matter. 2018;14(23):4772-83.

5. Mitov M. Cholesteric liquid crystals in living matter. Soft Matter. 2017;13(23):4176-209.

6. Gutierrez OFA, Rey AD. Theory and Simulation of Cholesteric Film Formation Flows of Dilute Collagen Solutions. Langmuir. 2016;32(45):11799-812.

7. Brasinika D, Tsigkou O, Tsetsekou A, Missirlis YF. Bioinspired synthesis of hydroxyapatite nanocrystals in the presence of collagen and l-arginine: Candidates for bone regeneration. Journal of Biomedical Materials Research Part B: Applied Biomaterials. 2016;104(3):458-69.

8. Kikuchi M, Ikoma T, Itoh S, Matsumoto HN, Koyama Y, Takakuda K, et al. Biomimetic synthesis of bone-like nanocomposites using the self-organization mechanism of hydroxyapatite and collagen. Composites Science and Technology. 2004;64(6):819-25.

9. Torbet J, Malbouyres M, Builles N, Justin V, Roulet M, Damour O, et al. Orthogonal scaffold of magnetically aligned collagen lamellae for corneal stroma reconstruction. Biomaterials. 2007;28(29):4268-76.

10. De Sa Peixoto P, Deniset-Besseau A, Schmutz M, Anglo A, Illoul C, Schanne-Klein M-C, et al. Achievement of cornea-like organizations in dense collagen I solutions: clues to the physico-chemistry of cornea morphogenesis. Soft Matter. 2013;9(47):11241-8.

11. Echalier C, Jebors S, Laconde G, Brunel L, Verdie P, Causse L, et al. Sol-gel synthesis of collagen-inspired peptide hydrogel. Mater Today. 2017;20(2):59-66.

12. Holder AJ, Badiei N, Hawkins K, Wright C, Williams PR, Curtis DJ. Control of collagen gel mechanical properties through manipulation of gelation conditions near the sol-gel transition. Soft Matter. 2018;14(4):574-80.

13. Attalla R, Ling CSN, Selvaganapathy PR. Silicon Carbide Nanoparticles as an Effective Bioadhesive to Bond Collagen Containing Composite Gel Layers for Tissue Engineering Applications. Adv Healthc Mater. 2018;7(5):9.

14. Borzenok SA, Afanas'eva DS, Gushchina MB, Ostrovskii DS, Domogatsky SP, Osidak EO. In Vitro Modeling of Co-Transplantation of Multipotent Stromal Mesenchymal Cells from Orbital Fat Pad and Lipoaspirate of Human Subcutaneous Adipose Tissue in Organ Culture in Collagen Gel. Bull Exp Biol Med. 2018;164(4):543-9.

15. Seifu DG, Meghezi S, Unsworth L, Mequanint K, Mantovani D. Viscoelastic properties of multi-layered cellularized vascular tissues fabricated from collagen gel. Journal of the Mechanical Behavior of Biomedical Materials. 2018;80:155-63.

16. Gobeaux F, Belamie E, Mosser G, Davidson P, Panine P, Giraud-Guille MM. Cooperative Ordering of Collagen Triple Helices in the Dense State. Langmuir. 2007;23(11):6411-7.

17. Lovelady HH, Shashidhara S, Matthews WG. Solvent specific persistence length of molecular type I collagen. Biopolymers. 2014;101(4):329-35.

18. Peixoto PD, Deniset-Besseau A, Schanne-Klein MC, Mosser G. Quantitative assessment of collagen I liquid crystal organizations: role of ionic force and acidic solvent, and evidence of new phases. Soft Matter. 2011;7(23):11203-10.

19. Neville AC. Biology of fibrous composites : development beyond the cell membrane. New York, NY, USA: Cambridge University Press; 1993.

20. Rey AD. Liquid crystal models of biological materials and processes. Soft Matter. 2010;6(15):3402-29.

21. Rey AD, Herrera-Valencia EE. Liquid crystal models of biological materials and silk spinning. 2012;97(6):374-96.

22. Aguilar Gutierrez OF, Rey AD. Structure characterisation method for ideal and non-ideal twisted plywoods. Soft Matter. 2014;10(47):9446-53.

23. Aguilar Gutierrez OF, Rey AD. Geometric reconstruction of biological orthogonal plywoods. Soft Matter. 2016;12(4):1184-91.

24. Voet D, Voet JG. Biochemistry. Hoboken, NJ: John Wiley & Sons; 2011.

25. Lodish H, Berk A, Kaiser CA, Krieger M, Bretscher A, Ploegh H, et al. Molecular Cell Biology: W. H. Freeman; 2016.

26. Ku CS, Sathishkumar M, Mun SP. Binding affinity of proanthocyanidin from waste Pinus radiata bark onto proline-rich bovine achilles tendon collagen type I. Chemosphere. 2007;67(8):1618-27.

27. Nishiyama N, Suzuki K, Nagatsuka A, Yokota I, Nemoto K. Dissociation States of Collagen Functional Groups and their Effects on the Priming Efficacy of HEMA Bonded to Collagen. Journal of Dental Research. 2003;82(4):257-61.

28. Giraud Guille MM, Mosser G, Helary C, Eglin D. Bone matrix like assemblies of collagen: From liquid crystals to gels and biomimetic materials. Micron. 2005;36(7):602-8.

29. Barbero G, Evangelista LR. An Elementary Course on the Continuum Theory for Nematic Liquid Crystals: World Scientific; 2001.

30. Maier W, Saupe Zeitschrift für Naturforschung I. Eine einfache molekular-statistische Theorie der nematischen kristallinflüssigen Phase. Teil l1. 1959;14(10):882-9.

31. Maier W, Saupe Zeitschrift für Naturforschung II. Eine einfache molekular-statistische Theorie der nematischen kristallinflüssigen Phase. Teil II. 1960;15(4):287-92.

32. Simoes M, Pazeti M, Domiciano SJPRE. Maier-Saupe and Onsager approaches as limits of the nematic-isotropic phase transition. 2001;65(1):011707.

33. Wang XJ, Zhou QF. Liquid Crystalline Polymers: World Scientific Publishing Company; 2004.

34. Onsager LJAotNYAoS. The effects of shape on the interaction of colloidal particles. 1949;51(4):627-59.

35. Stroobants A, Lekkerkerker HNW, Odijk T. Effect of electrostatic interaction on the liquid crystal phase transition in solutions of rodlike polyelectrolytes. Macromolecules. 1986;19(8):2232-8.

36. Carri GA, Muthukumar M. Attractive interactions and phase transitions in solutions of similarly charged rod-like polyelectrolytes. 1999;111(4):1765-77.

37. Drwenski T, Dussi S, Hermes M, Dijkstra M, Roij Rv. Phase diagrams of charged colloidal rods: Can a uniaxial charge distribution break chiral symmetry? 2016;144(9):094901.

38. Odijk T. Theory of lyotropic polymer liquid crystals. Macromolecules. 1986;19(9):2313-29.

39. De Luca G, Rey AD. Chiral front propagation in liquid-crystalline materials: Formation of the planar monodomain twisted plywood architecture of biological fibrous composites. Physical review E, Statistical, nonlinear, and soft matter physics. 2004;69(1 Pt 1):011706.

40. Wright DC, Mermin ND. Crystalline liquids: the blue phases. Reviews of Modern Physics. 1989;61(2):385-432.

41. Matsuyama A, Kato T. Theory of binary mixtures of a flexible polymer and a liquid crystal. J Chem Phys. 1996;105(4):1654-60.

42. Grelet E. Hard-Rod Behavior in Dense Mesophases of Semiflexible and Rigid Charged Viruses. Physical Review X. 2014;4(2):021053.

43. Doi M. Soft Matter Physics: OUP Oxford; 2013.

44. Dufresne A. Nanocellulose: From Nature to High Performance Tailored Materials: De Gruyter; 2012.

45. Gupta B, Ilg P. Energetic and Entropic Contributions to the Landau–de Gennes Potential for Gay–Berne Models of Liquid Crystals. 2013;5(2):328.

46. Das SK, Rey AD. Colloidal crystal formation via polymer-liquid-crystal demixing. Europhys Lett. 2005;70(5):621-7.

47. Matsuyamaa A, Hirashima R. Phase separations in liquid crystal-colloid mixtures. J Chem Phys. 2008;128(4):11.

48. Soule ER, Rey AD. Modelling complex liquid crystal mixtures: from polymer dispersed mesophase to nematic nanocolloids. Molecular Simulation. 2012;38(8-9):735-50.

49. Canejo JP, Monge N, Echeverria C, Fernandes SN, Godinho MH. Cellulosic liquid crystals for films and fibers. Liq Cryst Rev. 2017;5(2):86-110.

50. Kodaka M, Shah SN, Tomohiro T, Chudgar NK. Theoretical analysis of mesogenic properties of benzalazine and benzopyran derivatives. J Phys Chem B. 1998;102(7):1219-23.

51. Matsuyama A, Kato T. Theory of binary mixtures of a flexible polymer and a liquid crystal. The Journal of chemical physics. 1996;105(4):1654-60.

52. Soule ER, Rey AD. Oscillating fronts produced by spinodal decomposition of metastable ordered phases. Soft Matter. 2013;9(43):10335-42.

53. Soule ER, Milette J, Reven L, Rey AD. Phase equilibrium and structure formation in gold nanoparticles-nematic liquid crystal composites: experiments and theory. Soft Matter. 2012;8(10):2860-6.

54. Das SK, Rey AD. Computational modelling of multi-phase equilibria of mesogenic mixtures. Computational Materials Science. 2004;29(2):152-64.

55. Das SK, Rey AD. Texture formation under phase ordering and phase separation in polymer-liquid crystal mixtures. J Chem Phys. 2004;121(19):9733-43.

56. Das SK, Rey AD. Computational thermodynamics of multiphase polymer–liquid crystal materials. Computational Materials Science. 2006;38(2):325-39.

57. Kumar R, Kundagrami A, Muthukumar M. Counterion Adsorption on Flexible Polyelectrolytes: Comparison of Theories. Macromolecules. 2009;42(4):1370-9.

58. Almeida APC, Canejo JP, Fernandes SN, Echeverria C, Almeida PL, Godinho MH. Cellulose-Based Biomimetics and Their Applications. 2018;30(19):1703655.

59. Nyström G, Arcari M, Mezzenga R. Confinement-induced liquid crystalline transitions in amyloid fibril cholesteric tactoids. Nature Nanotechnology. 2018;13(4):330-6.

60. Mirzaeifard S, Abel SM. Confined semiflexible polymers suppress fluctuations of soft membrane tubes. Soft Matter. 2016;12(6):1783-90.

61. Zhou Y, Bukusoglu E, Martínez-González JA, Rahimi M, Roberts TF, Zhang R, et al. Structural Transitions in Cholesteric Liquid Crystal Droplets. ACS Nano. 2016;10(7):6484-90.

62. Seč D, Porenta T, Ravnik M, Žumer S. Geometrical frustration of chiral ordering in cholesteric droplets. Soft Matter. 2012;8(48):11982-8.

63. Wulf A. Biaxial order in cholesteric liquid crystals: Phenomenological argument. 1973;59(12):6596-8.

64. Tomar V, Roberts TF, Abbott NL, Hernández-Ortiz JP, de Pablo JJ. Liquid Crystal Mediated Interactions Between Nanoparticles in a Nematic Phase. Langmuir. 2012;28(14):6124-31.

65. Matsuyama A. Theory of binary mixtures of a rodlike polymer and a liquid crystal. 2010;132(21):214902.

66. Flory PJ. Principles of Polymer Chemistry: Cornell University Press; 1979.

67. Gennes PGd, Prost J. The physics of liquid crystals. 2nd ed. ed. Oxford, New York: Clarendon Press ; Oxford University Press; 1995.

68. Echeverria C, Almeida PL, Gutierrez OFA, Rey AD, Godinho MH. Two Negative Minima of the First Normal Stress Difference in a Cellulose-Based Cholesteric Liquid Crystal: Helix Uncoiling. J Polym Sci Pt B-Polym Phys. 2017;55(10):821-30.

3.10 Supporting Information, ESI (Chapter 3)

3.10.1 Appendix A: Details of energy landscape derivation

The purpose of this appendix is to provide the mathematical details and intermediate steps used in deriving the energy landscape given in eqns. (3-8, 3-10, 3-11a, 3-15, 3-21a, 3-22a, 3-26 and 3-29a).

A.1. Impact of interchain interactions

The aim of this subsection is to elaborate the derivation of eqns. (3-8, 3-10, 3-11a). The common assumption about the orientation distribution function is its independency from the azimuthal angle[1-3] in spherical coordinates. Therefore, the $\mathbf{u}$ is variable with respect to only polar angle and $\psi(\mathbf{u}) = \psi(\theta)$.

According to Maier-Saupe theory[2, 4, 5], the averaged potential of orientation-dependent attractive interactions for i^{th} rod among the other macromolecules is given by eqn. (A.1.1) [2, 4-6].

$$\beta U_i^{MS} = -\beta U'^{MS} \upsilon_A S P_2(\cos\theta) \qquad (A.1.1)$$

To obtain the corresponding energy, eqn. (A.1.1) needs to be substituted into eqn. (A.1.2a). Doing so, we get eqn. (A.1.2b) [6].

$$\beta E^{MS} = \frac{ZN_A}{2} \iint \beta U_i^{MS} \psi(\theta)\psi(\theta') \, d\Omega d\Omega' \tag{A.1.2a}$$

$$\beta E^{MS} = -\beta U'^{MS} \upsilon_A S \frac{ZN_A}{2} \int P_2(\cos\theta)\psi(\mathbf{u})d\Omega \int \psi(\mathbf{u}')d\Omega' \tag{A.1.2b}$$

In eqn. (A.1.2b), the first integral indicates the definition of scaler order parameter, and the second integral is the normalization of distribution function that is equal to one (see eqns. (3-17, 3-18)). Therefore, eqn. (A.1.2b) can be rewritten as eqn. (A.1.3).

$$\beta E^{MS} = -\beta U^{MS} \upsilon_A S^2 N_A \tag{A.1.3}$$

Furthermore, $N_A = c_A V$and for pure liquid crystals $V = \upsilon_A N_A$, we then write the contribution of orientation-dependent attractive interactions on the energy landscape as eqn. (A.1.4).

$$\frac{\beta E^{MS}}{N_A} = -\beta U^{MS} S^2 c_A \upsilon_A^2 \tag{A.1.4}$$

It should be noticed that the eqn. (A.1.4) has been also used in the other studies[2, 7, 8]. Now we turn to the modeling of mean-field potential for repulsion and twisting. When two rods are positively charge, the most stable configuration for them becomes orthogonal; see Figure 3-8.

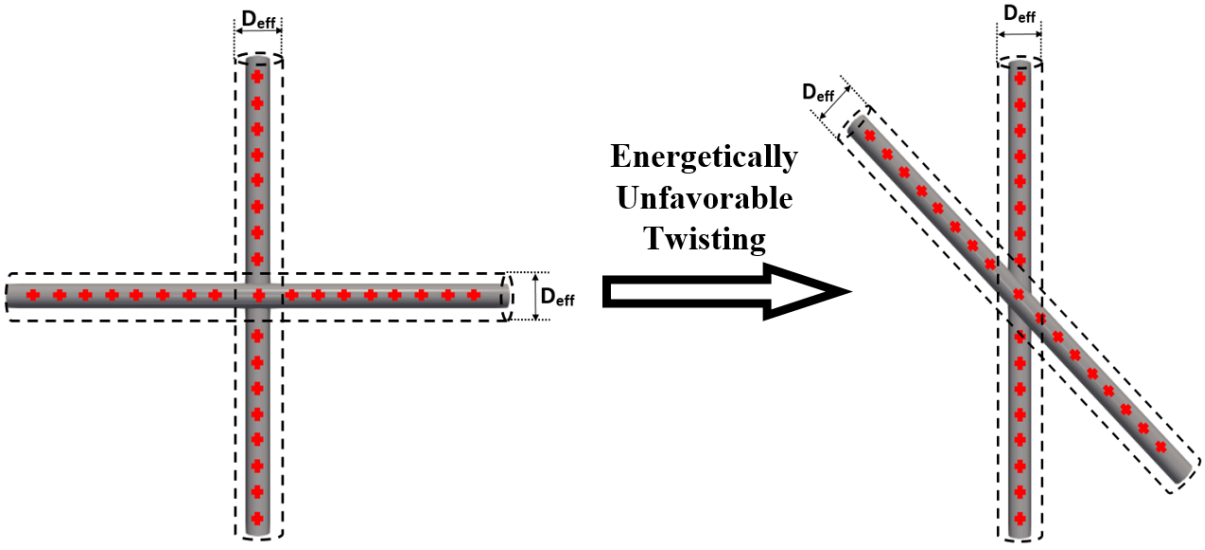

Figure 3-8. Phase ordering of two positively charged rods.

Phase ordering is thus energetically unfavorable process. To model this phenomenon, we use the Maier-Saupe potential with a positive sign (eq. (3-9)). Doing so dictates that the orientational ordering for charged rods gives rise to an increase in the free energy. Similarly,

after taking the molecular average of the obtained mean-field potential (eqn. (A.1.2a)); the eqn. (3-10) of the article is obtained. Finally, the net of orientation-dependent intermolecular interactions reads:

$$M=\frac{\beta E^{MS}}{N_A}+\frac{\beta E^{elc}}{N_A}=\beta\left(U^{elc}\text{-}U^{MS}\right)S^2c_A\upsilon_A^2 \tag{A.1.5}$$

A.2. Impact of chirality

This subsection gives the detailed steps concerning the derivation of eqn. (3-15). The Mermin Frank energy for the macroscopic chirality, $E^{Cholesteric}$, the ideal equilibrium director, **n**, and **Q**-tensor are given by eqn. (A.2.1a-c) [9, 10].

$$E^{Cholesteric}=\frac{L_1}{2}(\nabla\times\mathbf{Q}+2q\mathbf{Q})^2\upsilon_AN_A \tag{A.2.1a}$$

$$\mathbf{Q}=S\left(\mathbf{nn}-\frac{\boldsymbol{\delta}}{3}\right) \tag{A.2.1b}$$

$$\mathbf{n}=[\cos(qz)\quad\sin(qz)\quad 0] \tag{A.2.1c}$$

Using the eqn. (A.2.1b), the $\nabla\times\mathbf{Q}$ reduces to $S\nabla\times\mathbf{nn}$. Second rank tensor of **nn** is constructed by eqn. (A.2.1c).

$$\mathbf{nn}=\begin{bmatrix}\cos^2(qz) & \frac{\sin(2qz)}{2} & 0\\ \frac{\sin(2qz)}{2} & \sin^2(qz) & 0\\ 0 & 0 & 0\end{bmatrix} \tag{A.2.2}$$

Based on the Einstein notation, $\nabla\times\mathbf{nn}=\varepsilon_{ipq}\frac{\partial(\mathbf{nn})_{jq}}{\partial x_p}$ where $\varepsilon_{ipq}$is Levi-Civita function and x_p indicates spatial directions. Thus, using eqn. (A.2.2) leads to $\nabla\times\mathbf{nn}=0$ and eqn. (A.2.1a) reduces to eqn. (A.2.3).

$$E^{Cholesteric}=2L_1q^2\mathbf{Q}:\mathbf{Q} \tag{A.2.3}$$

Now we need to use eqn. (A.2.1b) for further simplification of eqn. (A.2.3).

$$\mathbf{Q}:\mathbf{Q}=S^2\left(\mathbf{nn}:\mathbf{nn}-\frac{1}{3}\mathbf{nn}:\boldsymbol{\delta}-\frac{1}{3}\boldsymbol{\delta}:\mathbf{nn}+\frac{1}{9}\boldsymbol{\delta}:\boldsymbol{\delta}\right) \tag{A.2.4}$$

The $\boldsymbol{\delta}=\mathbf{ii}+\mathbf{jj}+\mathbf{kk}$where **i**, **j**and **k**are unit vector in x, y and z directions, respectively. Hence, $\mathbf{nn}:\boldsymbol{\delta}=\mathbf{nn}:(\mathbf{ii}+\mathbf{jj}+\mathbf{kk})=\mathbf{nn}:\mathbf{ii}+\mathbf{nn}:\mathbf{jj}+\mathbf{nn}:\mathbf{kk}=(\mathbf{n}\cdot\mathbf{i})^2+(\mathbf{n}\cdot\mathbf{j})^2+(\mathbf{n}\cdot$

$\mathbf{k})^2 = \mathbf{n}\cdot\mathbf{n} = 1$. In the similar way, $\boldsymbol{\delta}:\mathbf{nn} = \mathbf{nn}:\boldsymbol{\delta} = 1$. Also, $\mathbf{nn}:\mathbf{nn} = (\mathbf{n}\cdot\mathbf{n})^2 = 1$ and $\boldsymbol{\delta}:\boldsymbol{\delta} = 3$. We then get eqn. (A.2.5).

$$\mathbf{Q}:\mathbf{Q} = \frac{2}{3}S^2 \tag{A.2.5}$$

Now that $\mathbf{Q}:\mathbf{Q}$ is determined, also considering the assumptions $n_A^{eff}=L/D_{eff}$ and $\upsilon_i=a^3n_i{}^2$, the energy due to macroscopic chirality can be rearrange into eqn. (A.2.6).

$$\frac{\beta E^{Cholesteric}}{N_A} = \frac{32\pi^2}{3}\left(\frac{\xi}{p_0}\right)^2 S^2\frac{L}{D_{eff}} \tag{A.2.6}$$

where the nm-scale coherence (correlation) length is defined as $\xi=\sqrt{\frac{a^3L_1\beta}{2}}$.

A.3. Finding optimal distribution function

This subsection aims to explain the intermediate steps in the derivation of the optimal normalized distribution function given by eqns. (3-21a, 3-22a). In this regard, we have to do the following optimization given in eqn. (A.3.1)[2].

$$\begin{cases} \text{minimize}: \dfrac{\delta F^s}{\delta\psi(\theta)} \\ \text{subjectto}: \displaystyle\int \psi(\theta)d\Omega = 1 \end{cases} \tag{A.3.1}$$

$\frac{\delta F^s}{\delta\psi(\theta)}$ is the functional derivative of total free energy of system. This optimization can be transformed into nonlinear algebraic equations by the use of Euler-Lagrange multiplier, eqn. (A.3.2)[11]:

$$\frac{\delta H}{\delta\psi(\theta)} = \frac{\delta F^s}{\delta\psi(\theta)} - \eta'' \int \psi(\theta)d\Omega = 0 \tag{A.3.2}$$

$\frac{\delta H}{\delta\psi(\theta)}$and η'' are called the Hamiltonian function and Lagrange multiplier. Using eqn. (3-16) of the article, we reach eqn. (A.3.3a).

$$\frac{\delta H}{\delta\psi(\theta)} = \frac{N_A}{\beta}\left(\frac{\delta\sigma(\psi(\theta))}{\delta\psi(\theta)} + \overline{\upsilon}_{AA}c_A\frac{\delta\rho(\psi(\theta))}{\delta\psi(\theta)} + \left(Uc_A\upsilon_A^2 + \frac{32\pi^2}{3}\left(\frac{\xi}{p_0}\right)^2\frac{L}{D_{eff}}\right)\frac{\delta S^2}{\delta\psi(\theta)}\right) - \eta''\frac{\delta\int\psi(\theta)d\Omega}{\delta\psi(\theta)} = 0 \quad \text{(A.3.3a)}$$

$$\frac{\delta\sigma(\psi(\theta))}{\delta\psi(\theta)} = 2\pi\sin(\theta)\left(1+\ln(4\pi\psi(\theta))\right) \quad \text{(A.3.3b)}$$

$$\frac{\delta\rho(\psi(\theta))}{\delta\psi(\theta)} = 2\pi\sin(\theta)\frac{8}{\pi}\int\Gamma(\gamma)\psi(\theta')d\Omega' \quad \text{(A.3.3c)}$$

$$\frac{\delta S^2}{\delta\psi(\theta)} = 2S\frac{\delta S}{\delta\psi(\theta)} = 4\pi S\sin(\theta)P_2(\cos\theta) \quad \text{(A.3.3d)}$$

$$\frac{\delta\int\psi(\theta)d\Omega}{\delta\psi(\theta)} = 2\pi\sin(\theta) \quad \text{(A.3.3e)}$$

Substituting eqns. (A.3.3b-e) into eqn. (A.3.3a) gives the irreducible integral equation expressed in eqn. (3-19) of the article whereby the optimal distribution function, eqn. (3-21a) and eqn. (3-22a), can be obtained.

A.4. Derivation of mixing free energy

The objective of this subsection is to clarify the derivation of eqn. (3-26) in full detail. Because in the isotropic state $\sigma(\psi(\theta))=0$and $\rho(\psi(\theta))=1$, and in the pure solution $c_A = (\upsilon_A)^{-1}$, the free energy of the pure components are expressed as eqns. (A.4.1a,b)[2, 12].

$$\beta F^s(N_A,0)=N_A\beta\mu_A^o-N_A+N_A\ln\upsilon-N_A\ln\upsilon_A+\frac{\overline{\upsilon}_{AA}N_A}{\upsilon_A} \quad \text{(A.4.1a)}$$

$$\beta F^s(0,N_I)=N_I\beta\mu_I^o-N_I+N_I\ln\upsilon-N_I\ln\upsilon_I+\frac{\overline{\upsilon}_{II}N_I}{\upsilon_I} \quad \text{(A.4.1b)}$$

The free energy difference between the solution and the pure components in the isotropic state is called mixing free energy[2].

(A.4.2)

$$\beta\Delta F_{mixing}(N_A,N_I)=N_A\ln c_A+N_I\ln c_I+N_A\left(WS^2-\ln(I_0)\right)$$
$$+\bar{\upsilon}_{AA}N_Ac_A\left(1-\frac{5}{8}\left(1-\frac{11}{8}h\right)S^2\right)+2\bar{\upsilon}_{AI}N_Ic_A+\bar{\upsilon}_{II}N_Ic_I+Uc_A\upsilon_A^2N_AS^2$$
$$+\frac{32\pi^2}{3}\left(\frac{\xi}{p_0}\right)^2\frac{L}{D_{eff}}N_AS^2+N_A\ln\upsilon_A-\frac{\bar{\upsilon}_{AA}N_A}{\upsilon_A}+N_I\ln\upsilon_I-\frac{\bar{\upsilon}_{II}N_I}{\upsilon_I}$$

As alluded in subsection 3.4.1 of the article, υwhich is an arbitrary volume, merely plays dimensional consistency not any other role. Herein, one can see that it is included in eqn. (A.4.2). Given $\phi_i=c_i\upsilon_i$, $N_i=\frac{\phi_iV}{\upsilon_i}$, incompressibility $\phi_A+\phi_I=1$, small-sized solve $n_I=1$, and the isotropic Flory-Huggins parameter $\chi=a^3\left(\frac{2\bar{\upsilon}_{AI}}{\upsilon_A\upsilon_I}-\frac{\bar{\upsilon}_{AA}}{\upsilon_A^2}-\frac{\bar{\upsilon}_{II}}{\upsilon_I^2}\right)$, the Flory-Huggins theory gives eqn. (A.4.3b).

$$\beta\Delta F_{mixing}(N_A,N_I)=N_A\ln\phi_A+N_I\ln\phi_I+2\bar{\upsilon}_{AI}N_Ic_A+\bar{\upsilon}_{II}N_I\left(c_I-\frac{1}{\upsilon_I}\right)$$
$$+\bar{\upsilon}_{AA}N_A\left(c_A-\frac{1}{\upsilon_A}\right)$$
$$+N_A\left(WS^2-\ln(I_0)\right)\qquad\text{(A.4.3a)}$$
$$+\left(\bar{\upsilon}_{AA}c_A\left(-\frac{5}{8}\left(1-\frac{11}{8}h\right)\right)+Uc_A\upsilon_A^2\right.$$
$$\left.+\frac{32\pi^2}{3}\left(\frac{\xi}{p_0}\right)^2\frac{L}{D_{eff}}\right)N_AS^2$$

$$\beta\Delta F_{mixing}(N_A,N_I)=N_T\left(\frac{\phi_A\ln\phi_A}{n_A}+\phi_I\ln\phi_I+\phi_A\phi_I\chi+\frac{\phi_A}{n_A}\left(\frac{1}{2}WS^2-\ln(I_0)\right)\right)\qquad\text{(A.4.3b)}$$

A.5. Chemical potential in terms of total dimensionless free energy per lattice and volume fraction

In this subsection, we develop the chemical potential for mesogen in the phase j (i.e. Cho or Iso), eqn. (3-29a). In addition, doing similar mathematical manipulations leads to the chemical potential for the solvent.

Knowing that $\mathscr{F}=\frac{\beta F}{N_T}$, we reach to eqn. (A.5.1).

$$\mu_A^j = \left(\frac{\partial F^j}{\partial N_A}\right)_{N_I,T} = \frac{1}{\beta}\left(N_T\left(\frac{\partial \mathscr{F}}{\partial N_A}\right)_{N_I,T} + \mathscr{F}\left(\frac{\partial N_T}{\partial N_A}\right)_{N_I,T}\right) \quad (A.5.1)$$

To determine the $\frac{\partial N_T}{\partial N_A}$, we should use the definition of $N_T = n_A^{eff} N_A + n_I N_I$.

$$\left(\frac{\partial N_T}{\partial N_A}\right)_{N_I,T} = n_A^{eff} \quad (A.5.2)$$

Now, we should write the $\left(\frac{\partial \mathscr{F}}{\partial N_A}\right)_{N_I,T}$ in term of volume fraction.

$$\left(\frac{\partial \mathscr{F}}{\partial N_A}\right)_{N_I,T} = \left(\frac{\partial \mathscr{F}}{\partial \phi_A}\right)_{N_I,T}\left(\frac{\partial \phi_A}{\partial N_A}\right)_{N_I,T} \quad (A.5.3)$$

The definition of volume fraction with the assumption of equal lattice size is $\phi_A = \frac{n_A^{eff} N_A}{N_T}$, therefore we are now able to determine $\left(\frac{\partial \phi_A}{\partial N_A}\right)_{N_I,T}$.

$$\left(\frac{\partial \phi_A}{\partial N_A}\right)_{N_I,T} = \frac{1}{N_T}\left(n_A^{eff} - \phi_A\left(\frac{\partial N_T}{\partial N_A}\right)_{N_I,T}\right) \quad (A.5.4)$$

Substituting eqn. (A.5.2) to eqn. (A.5.4) gives the desired form of $\left(\frac{\partial \phi_A}{\partial N_A}\right)_{N_I,T}$.

$$\left(\frac{\partial \phi_A}{\partial N_A}\right)_{N_I,T} = \frac{1}{N_T} n_A^{eff} \phi_I \quad (A.5.5)$$

Finally, we should substitute eqns. (A.5.2, A.5.5) to eqn. (A.5.1) to reach the final form that we wanted.

$$\mu_A^j = \left(\frac{\partial F^j}{\partial N_A}\right)_{N_I,T} = n_A^j\left(\mathscr{F}^j + \phi_I^j\left(\frac{\partial \mathscr{F}^j}{\partial \phi_A^j}\right)_{\phi_I^j,T}\right) \quad (A.5.6)$$

A.6. Functionality of L/Deff

The ionic strength of the dispersion of collagen in an aqueous acetic acid solution is represented by:

$$I = \frac{1}{2}\sum_i m_i Z_i^2 = \frac{1}{2}\sum_i m_i \quad (A.6.1)$$

because the charge number of acetic acid is one, $AA \leftrightarrow A^- + H^+$. Now we formulate the summation of molarities for all mobile ions. Let $N_{H^+}^m$ and $N_{A^-}^m$ are the number of hydronium

ions and acetate ions that are mobile in the dispersion. Hence, the total number of mobile ions, N_T^m, is given by

$$N_T^m = N_{H^+}^m + N_{A^-}^m \tag{A.6.2}$$

To determine $N_{A^-}^m$, we shall take into consideration that the number of mobile acetate is the summation of number of existing hydronium ions, N_{H+}^m, and the number of protonated hydrogen that are adsorbed on the collagen backbone, N_{H+}^b. This consideration is due to the principle of charge neutrality, see Figure 3-9.

$$N_{A^-}^m = N_{H+}^m + N_{H+}^b \tag{A.6.3}$$

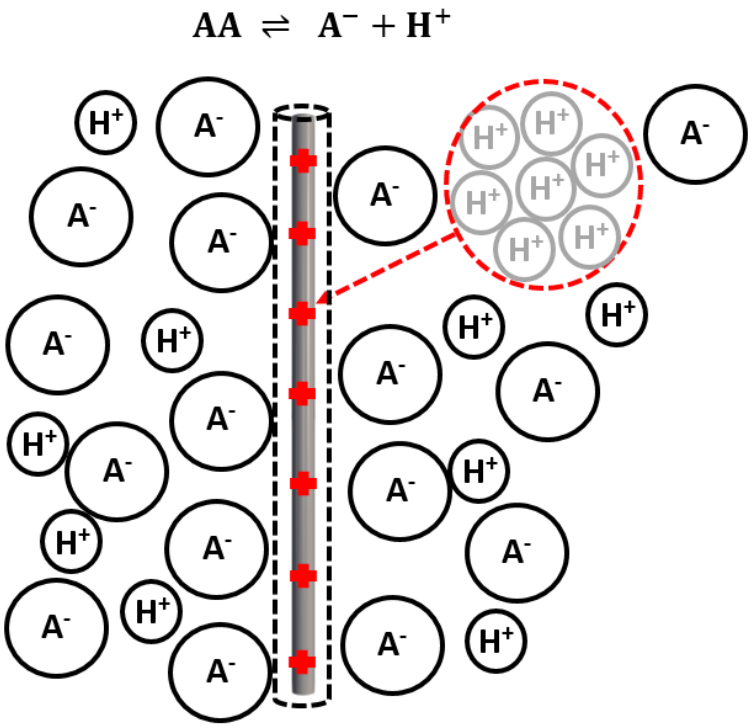

Figure 3-9. Schematic of the principle of charge neutrality. There are 16 H^+ (7 cations on the collagen backbone and 9 cations are mobile in dispersion) and 16 A^-.

The number of protonated hydrogen on the collagen backbone is simply given by $N_{H+}^b = N_A \Lambda(pH) L$. Substituting the eqn. (A.6.3) into eqn. (A.6.2) leads to

$$N_T^m = 2N_{H^+}^m + N_A \Lambda(pH) L = 2m_{H^+}^m V N_{avo} + m_A \Lambda(pH) L V N_{avo} \tag{A.6.4}$$

Hence, the ionic strength of dispersion can be written in known terms.

$$I = m_{H^+}^m + \frac{1}{2} m_A \Lambda(pH) L \tag{A.6.5}$$

Since $m^{m}_{H^+}$ shows the molarity of mobile hydronium ions that do not have tendency to absorbed on the collagen backbone anymore, from equilibrium of acetic acid in water, we can conclude that $m^{m}_{H^+} = \sqrt{k_d[AA]}$[13].

$$I=\sqrt{k_d[AA]} + \frac{1}{2} m_A \Lambda(pH) L \qquad (A.6.6)$$

As discussed later on in Appendix B.2, $\Lambda(pH)$ can be determined by knowing the $m^{m}_{H^+}$because $pH=-\log_{10}^{m^{m}_{H^+}}$[13].

Now that the functionality of ionic strength, eqn. (A.6.6), is obtained, one can readily conclude that

$$[AA] = \text{constant} : m_A \uparrow \Rightarrow I \uparrow \Rightarrow \kappa^{-1} \downarrow \Rightarrow \ D_{eff} \downarrow \Rightarrow L/D_{eff} \uparrow$$

$$m_A = \text{constant} : [AA] \uparrow \Rightarrow I \uparrow \Rightarrow \kappa^{-1} \downarrow \Rightarrow \ D_{eff} \downarrow \Rightarrow L/D_{eff} \uparrow$$

The trend of variation in the ratio of L/D_{eff} with respect to the concentrations of acid and collagen is shown in Figure 3-10.

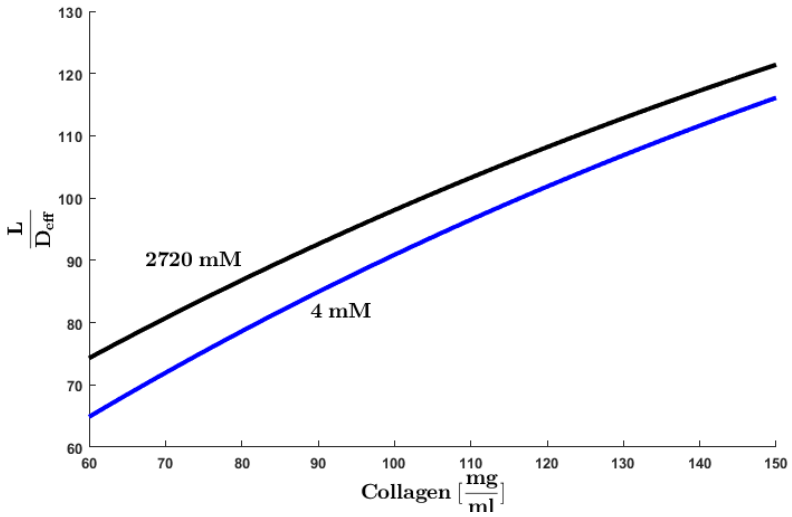

Figure 3-10. Dependence of L/D_{eff} on collagen concentration.

The obtained range of L/D_{eff} is consistent with previous work and data[14].

3.10.2 Appendix B: Model Parameters and Material Properties Used in Computation of Phase Diagrams

In this section, we have first tabulated some physical properties for the components that exist in our study, Table 3-1 Thereafter, other parameters have been brought to the subsequent subsections for further discussion.

Table 3-1. The physical properties of components in acidic collagenous solution.

Physical property	Value	Reference
$\rho_{collagen}\left(\frac{g}{l}\right)$	1120	(15)
$Mw_{Collagen}(Da)$	285,000	(16)
$D_{Bare}(nm)$	1.5	(16)
$L(nm)$	300	(16)
$p_0(\mu m)$	2~22 (depending on the concentrations)	(17)
$\delta(nm)$	5~24 (depending on the concentration of collagen)	(18)

It is worth mentioning that, based on the reference[17]; the experimental pitch (in unit of μm) for the collagenous solutions can be fitted with respect to collagen concentration (in unit of mg/ml). For solutions prepared in 5mM and 500mM acetic acid, the empirical correlations are respectively given by

$$\frac{p_0}{2} = 11C^{-0.02} \quad (B.1)$$

$$\frac{p_0}{2} = 140C^{-0.92} \quad (B.2)$$

For other acetic concentration, we have used the interpolated values. Figure 3-11 shows the trend of experimental pitch with respect to variations of collagen concentrations.

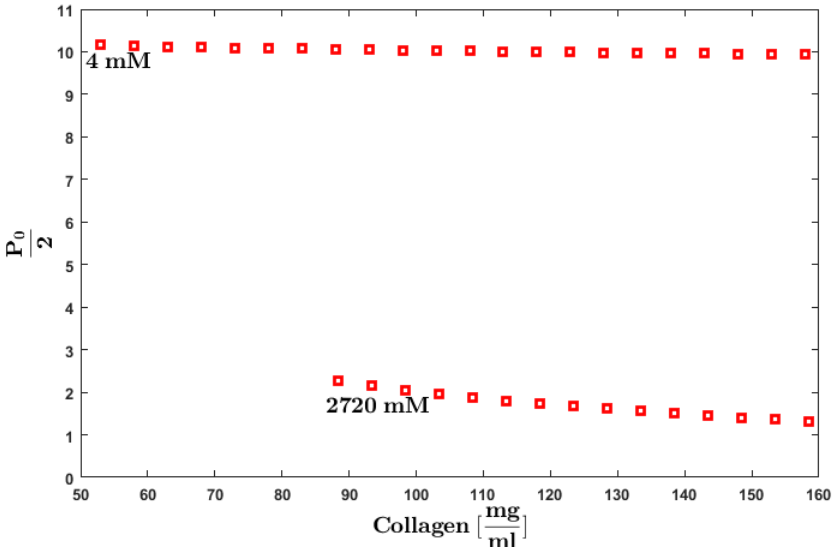

Figure 3-11. Experimental equilibrium pitch extracted from the reference[17].

B.1. Isotropic Flory-Huggins parameter, χ

In this subsection, we aim to provide an acceptable estimation of isotropic Flory-Huggins parameter. Actually, values of parameters in eqn. (3-27) are not always available; instead, we unavoidably turn to an estimation method. As per regular solution theory, the dimensionless isotropic Flory–Huggins interaction parameter, χ, is estimated using Hansen solubility parameters, eqn. (B.1.1)[19].

$$\chi=\alpha\frac{\upsilon_I}{k_B T}\left(\left(\delta_{A,d}-\delta_{I,d}\right)^2+0.25\left(\delta_{A,p}-\delta_{I,p}\right)^2+0.25\left(\delta_{A,h}-\delta_{I,h}\right)^2\right) \quad \text{(B.1.1)}$$

υ_I stands for volume of solvent, which is isotropic component in present work. $\delta_{I,j}$is Hansen solubility parameter; the first subscript shows the component which can be either isotropic (I) or anisotropic (A), the second subscript d, p and h are contributions because of dispersive, polar and hydrogen bonding. In addition, α is the experimental fitting parameter bounded between 0 to 1. The solubility parameters for this system are summarized in Table 3-2[20].

Table 3-2. Solubility parameters

Solubility parameters	Values $\left(\frac{J}{cm^3}\right)^{1/2}$
$\delta_{collagen,d}$	16
$\delta_{collagen,h}$	23.6

Solubility parameters	Values $\left(\frac{J}{cm^3}\right)^{1/2}$
$\delta_{collagen,p}$	20.3
$\delta_{water,d}$	12.2
$\delta_{water,h}$	37.3
$\delta_{water,p}$	27.3
$\delta_{acetic\ acid,d}$	15.4
$\delta_{acetic\ acid,h}$	15.2
$\delta_{acetic\ acid,p}$	9.4
$\delta_{collagen,d}$	16

α has not been documented for collagen. We have unavoidably used experimental value of mesogen with molecules similar to collagen molecules. We have then chosen cellulose acetate because its Flory-Huggins parameter in the dilute solution has reported 0.4[21]. The solvent mainly consists of water molecules, thus we took the radius of solvent as 1.4 Å. Finally, substitution of these physical values into eqn. (B.1.1) leads to following estimation for the dimensionless isotropic Flory-Huggins interaction.

$$\chi > \frac{120}{T(K)} \qquad (B.1.2)$$

(K) shows that the temperature must be absolute in unit of Kelvin.

B.2. The pH-dependent linear charge density of collagen

The aim of this subsection is to present an acceptable method to determine the linear charge density of tropocollagen in various pH because the linear charge density is required in eqn. (3-2b).

Type I collagen is composed of three helical polypeptide chains; two α1(I) chains and one α2(I). Each chain contains roughly 1052 amino acid residues twisted around each other in the form of a right-handed triple helix. Collagen has the repeating triplets of sequence Gly-X-Y where X and Y are often proline (~28%) and hydroxyproline (~38%) residues, respectively[16].

In our study, we have focused on the acidic collagenous solutions because the rods are far away from fibrogenesis and the primary architecture of collagenous plywood are formed. In

the acidic pHs, the amine functional groups are protonated, and as a result the rods become positively charged (Figure 3-12 indicates the linear charge density of collagen Type I against the pH). The eqn. (3-2b) of the article requires the linear charge density of collagen. One approximate but good method to determination of a peptide charge is as follows. We should compare the pK_a of each residues with the pH of solution. If pK_a is greater and pH, that residue gets protonated, otherwise deprotonated. This procedure can readily be done using a protein calculator[22]. Additionally, we have used UniProt Knowledgebase[23] to obtain the sequence of rat tail; rat CO1A1: P02454; rat CO1A2: P02466.

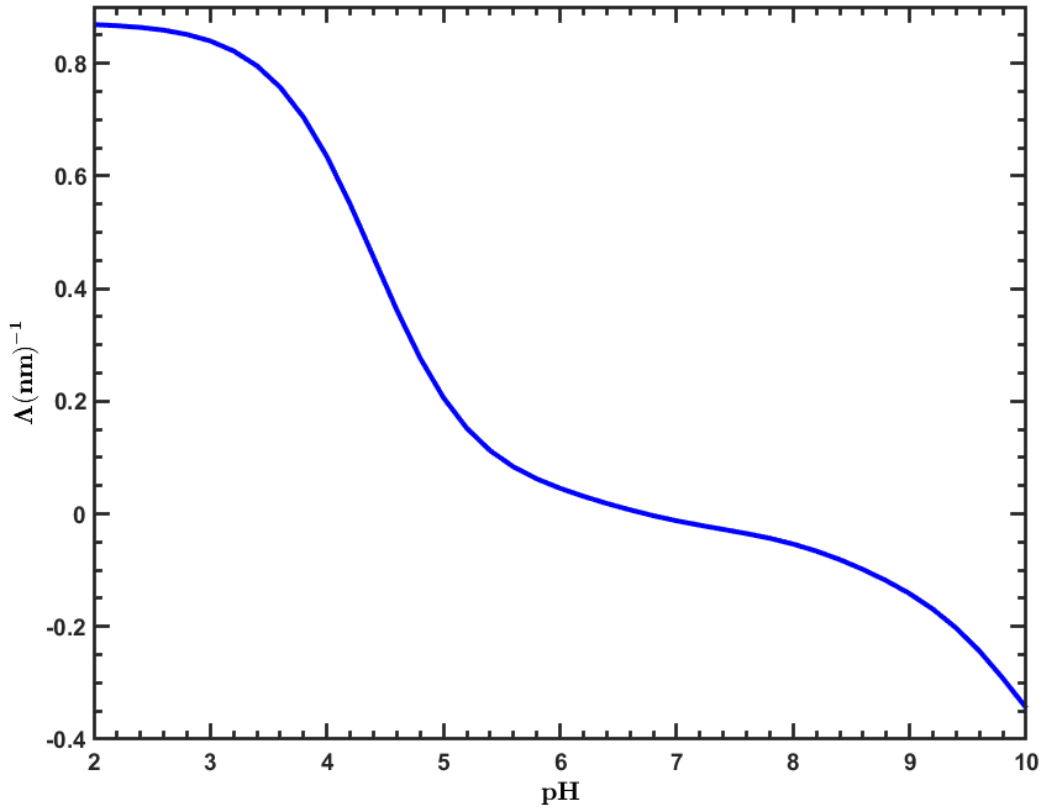

Figure 3-12. The pH-dependent linear charge density of collagen.

The minimum distance between fixed charges on the backbone of a polyelectrolyte cannot be less than the Bjerrum length, which is about λ_B =0.79 nm in our study[6]. Based on the assumption of uniform charge distribution, Figure 3-12 satisfies the mentioned physical constraint because the averaged distance between charges is $L/(|\Lambda|L-1)>1nm>\lambda_B$.

3.10.3 Appendix C: Consistency with previous studies

In this section, we show that our suggested model (eqns.(3-3, 3-26)) can be reduced to the other well-established models if some of the mechanisms are ignored.

C.1. Onsager Model

Under condition that the solution is only comprised of rigid rodlike uncharged mesogens; the main mechanisms become the translational and orientational entropies along with the excluded volume. In eqn. (3-3), if we consider $M(\psi(\mathbf{u}))=C(\psi(\mathbf{u}))=0$, we reach to the energy landscape proposed by Onsager[24].

C.2. Matsuyama et al. Model (ref(2))

The general structure of the energy landscape developed in this study is based on Matsuyama et al. model[2] (comparing eqn. (3.6) of the mentioned reference with eqn. (3-26) in our work). The main difference between our suggested theory and Matsuyama et al. is that, due to the nature of the acidic collagenous solutions, we have also included the mechanisms of chirality and interchain electrostatic (i.e. repulsion and twisting). Here, we aim to show that our proposed theory can be simplified to the Matsuyama et al. theory that has been used in other studies[7, 8, 25, 26]. Giving that the included mechanisms are negligible therefore we should consider the $U^{elc}=h=\kappa^{-1}=0$ and $p_0=\infty$. Doing so, the net cholesteric potential ends up like eqn. (C.2.1a,b).

$$W=\phi_A\frac{L}{D}\left(\frac{5}{4}+\chi_a\right) \qquad (C.2.1a)$$

$$\chi_a=\frac{\pi}{2}D^3\beta U^{MS} \qquad (C.2.1b)$$

Considering our suggested model with the net potential given by eqn. (C.2.1a,b) leads to eqn. (3.6) of reference[2].

3.10.4 Appendix D: Nomenclature

Table 3-3. Nomenclature

Symbol	Units	Definition
a^3	m^3	volume of each lattice unit
$B_2(\psi(\mathbf{u}))$	[-]	excluded volume based on the second virial approximation
$C(\psi(\mathbf{u}))$	[-]	geometric chirality of mesogen
$c_A^{'}$	[-]	dimensionless number density
c_A	m^{-3}	number density
D_{eff}	m	effective diameter
D	m	bare diameter
$d\Omega$	radian	solid angle
E^{MS}	j	Energy due to Maier-Saupe contribution (i.e. attractive interaction)
E^{elc}	j	Energy due to interchain electrostatic interactions (i.e. repulsion and twisting)
$E^{Cholesteric}$	j	Energy due to Frank distorsion (i.e. cholesteric)
Ei	[-]	exponential integral
F^s	j	free energy of solution
h	[-]	magnitude of the twisting effect
h	[-]	helix unit vector
I	molar	ionic strength,
k_B	$m^2.kg.s^{-2}.K^{-1}$	Boltzmann constant, $1.38064852 \times 10^{-23}$
L	m	contour length
L_1	j/m	elastic constant
$M(\psi(\mathbf{u}))$	[-]	the orientation-dependent intermolecular interactions
m_i	molar	molar concentration of i^{th} mobile ion
N_{avo}	mol^{-1}	Avogadro's number, $6.022140857 \times 10^{23}$
N_A and N_I	[-]	number of chiral mesogens and isotropic component

Symbol	Units	Definition
N_T	[-]	total number of lattice site
N_{H+}^{m}	[-]	number of hydronium ions
N_{A-}^{m}	[-]	number of acetate ions
N_T^m	[-]	total number of mobile ions
N_{H+}^{b}	[-]	number of protonated hydrogen that are adsorbed on the collagen backbone
n_A^{eff}	[-]	number of segments on the backbone of mesogen
$\mathbf{n}$	[-]	uniaxial direction
p_0	m	pitch
$P_2(\mathbf{u}\cdot\mathbf{n})$	[-]	second Legendre polynomial of angle between the macromolecule and uniaxial direction (i.e. local order parameter)
q	m^{-1}	pitch wave
$\mathbf{Q}$	[-]	quadrupole moment tensor, well-known as **Q**-tensor
S	[-]	macroscopic uniaxial order parameter
U	$j.m^{-3}$	potential of orientation-dependent intermolecular interaction
U_i^{MS}	j	one-body mean field potential of i^{th} rod for attractive interactions on the other existing rods in the system
U'^{MS}	$j.m^{-3}$	positive constant independent of temperature related to Maier-Saupe parameter
U^{MS}	$j.m^{-3}$	positive constant independent of temperature, Maier-Saupe parameter
U_i^{elc}	j	one-body mean field potential of i^{th} rod for electrostatic interactions (i.e. repulsion and twisting) on the other existing rods in the system
U'^{elc}	$j.m^{-3}$	strength of electrostatic potential (i.e. repulsion and twisting)

Symbol	Units	Definition
U^{elc}	$j.m^{-3}$	strength of electrostatic interaction among the rods (i.e. repulsion and twisting)
u and **u**′	[-]	The orientations of two rod-like macromolecules
V	m^3	volume of system
W	[-]	net cholesteric potential
z	m	z-component of space
Z	[-]	coordination number
Z_i	[-]	charge number of i^{th} mobile ion
α	[-]	double-layer thickness parameter
β	j^{-1}	thermal energy
γ	radian	angle between the rods
γ_E	[-]	Euler constant, 0.5772
δ	[-]	Kronecker delta
$\delta_{i,j}$	$(j.m^{-3})^{1/2}$	solubility parameters, i indicates the substance and j stands for the kind of bonding. j can be d, p and h which are for dispersive, polar and hydrogen bonding, respectively.
ΔS_O	[-]	orientational entropy
η′and η	[-]	constants determined by normalization of distribution function
θ	radian	polar angle
κ^{-1}	m	Debye screening length
λ_B	m	Bjerrum length
λ_{ChE}	[-]	coupling parameters of chirality-electrostatic
λ_{ExE}	[-]	coupling parameters of excluded volume-electrostatic
λ_{II}	[-]	coupling parameters of intermolecular interaction
Λ	charge number per meter	linear charge density

Symbol	Units	Definition
μ^o	j	standard particle chemical potential
ξ	m	coherence length or correlation length
$\sigma(\psi(\mathbf{u}))$	[-]	effect of orientational entropy
$\overline{\upsilon}_{AA}$, $\overline{\upsilon}_{IA}$and $\overline{\upsilon}_{II}$	m^3	average excluded-volume between mesogen-mesogen, mesogen-isotropic component and isotropic component- isotropic component.
$\upsilon_A$and υ_I	m^3	molecular volumes of mesogen and isotropic component
υ	m^3	volume scale, an arbitrary volume
φ	radian	azimuthal angle
$\phi_A^{eff}$and ϕ_I^{eff}	[-]	effective volume fraction of mesogen and isotropic component
χ	[-]	isotropic Flory-Huggins parameter
$\psi(\mathbf{u})$	[-]	single-rod orientational distribution function
$\mathscr{F}$	[-]	total dimensionless free energy per lattice site

References of Supporting Information (Chapter 3)

1. Drwenski T, Dussi S, Hermes M, Dijkstra M, Roij Rv. Phase diagrams of charged colloidal rods: Can a uniaxial charge distribution break chiral symmetry? 2016;144(9):094901.

2. Matsuyama A, Kato T. Theory of binary mixtures of a flexible polymer and a liquid crystal. J Chem Phys. 1996;105(4):1654-60.

3. Lin-Liu YR, Shih YM, Woo C-W. Molecular theory of cholesteric liquid crystals and cholesteric mixtures. Physical Review A. 1977;15(6):2550-7.

4. Maier W, Saupe AJZfNA. Eine einfache molekular-statistische Theorie der nematischen kristallinflüssigen Phase. Teil l1. 1959;14(10):882-9.

5. Maier W, Saupe AJZfNA. Eine einfache molekular-statistische Theorie der nematischen kristallinflüssigen Phase. Teil II. 1960;15(4):287-92.

6. Doi M. Soft Matter Physics: OUP Oxford; 2013.

7. Das SK, Rey AD. Texture formation under phase ordering and phase separation in polymer-liquid crystal mixtures. J Chem Phys. 2004;121(19):9733-43.

8. Gurevich S, Soule E, Rey A, Reven L, Provatas N. Self-assembly via branching morphologies in nematic liquid-crystal nanocomposites. Physical Review E. 2014;90(2).

9. De Luca G, Rey AD. Chiral front propagation in liquid-crystalline materials: Formation of the planar monodomain twisted plywood architecture of biological fibrous composites. Physical review E, Statistical, nonlinear, and soft matter physics. 2004;69(1 Pt 1):011706.

10. Muševič I. Liquid Crystal Colloids: Springer International Publishing; 2017.

11. Sagan H. Introduction to the Calculus of Variations: McGraw-Hill; 1969.

12. Matsuyama A. Phase separations in mixtures of a liquid crystal and a nanocolloidal particle. The Journal of Chemical Physics. 2009;131(20):204904.

13. Silberberg M. Chemistry: The Molecular Nature of Matter and Change: McGraw-Hill; 2006.

14. Gutierrez OFA, Rey AD. Theory and Simulation of Cholesteric Film Formation Flows of Dilute Collagen Solutions. Langmuir. 2016;32(45):11799-812.

15. Cusack S, Miller A. Determination of the elastic constants of collagen by Brillouin light scattering. Journal of Molecular Biology. 1979;135(1):39-51.

16. Voet D, Voet JG. Biochemistry. Hoboken, NJ: John Wiley & Sons; 2011.

17. Peixoto PD, Deniset-Besseau A, Schanne-Klein MC, Mosser G. Quantitative assessment of collagen I liquid crystal organizations: role of ionic force and acidic solvent, and evidence of new phases. Soft Matter. 2011;7(23):11203-10.

18. Gobeaux F, Belamie E, Mosser G, Davidson P, Panine P, Giraud-Guille MM. Cooperative Ordering of Collagen Triple Helices in the Dense State. Langmuir. 2007;23(11):6411-7.

19. Lindvig T, Michelsen ML, Kontogeorgis GM. A Flory–Huggins model based on the Hansen solubility parameters. Fluid Phase Equilibria. 2002;203(1):247-60.

20. Miller RG, Bowles CQ, Chappelow CC, Eick JD. Application of solubility parameter theory to dentin-bonding systems and adhesive strength correlations. 1998;41(2):237-43.

21. Mark JE. Physical Properties of Polymers Handbook: Springer New York; 2007.

22. v3.4 PC. pH-dependent Linear Charge Density 2013 [Available from: http://protcalc.sourceforge.net/.

23. Knowledgebase U. Amino Acids Sequence 2018 [Available from: https://www.uniprot.org/.

24. Odijk T. Theory of lyotropic polymer liquid crystals. Macromolecules. 1986;19(9):2313-29.

25. Susanta KD, Alejandro DR. Computational modelling of multiscale morphologies in polymer–liquid crystal blends. Nanotechnology. 2005;16(7):S330.

26. Das SK, Rey AD. Computational modelling of multi-phase equilibria of mesogenic mixtures. Computational Materials Science. 2004;29(2):152-64.

Chapter 4. Theoretical Platform for Liquid-Crystalline Self-Assembly of Collagen-Based Biomaterials

4.1 Preface

Biaxiality is taken to account in this chapter, generalizing the free energy developed in Chapter 3. Thereafter, the governing equations of phase separation and phase ordering, which are inherently coupled, are developed in order to investigate the cholesteric growth within a single growing tactoid free from tactoidal collisions. This chapter contributes to understanding the phenomena exclusively involved in tactoidal cholesteric growth. In particular, the defect formation and escape mechanism are explored, which is of paramount importance in nano-particle laden systems.

4.2 Abstract

The collagen triple helix is a ubiquitous biomacromolecule used in acidic aqueous solutions as precursor in the fabrication of artificial compact bone and cornea and in tissue engineering. The primary architecture of these highly structured solid tissues is formed during the cholesteric liquid-crystalline stage of their morphogenesis. The theoretical platform that describes the coupled dynamics of phase-ordering and mass transfer developed, implemented and validated here can be used for optimal material design and plays a significant complementary role to future experimental studies. Based on uniaxiality assumption, we have recently developed and validated a theory for the free energy tailored for acidic collagenous dispersions. Here we significantly expand and generalize our previous study, by including biaxiality since cholesteric phases must have a degree of biaxiality. In this work, we first modify the proposed interchain interaction and excluded-volume contribution by use of the addition theorem for spherical harmonics. Then, the Euler-Lagrange minimization followed by expansion around I/N* transition allows us to construct the free energy of ordering in terms of the phenomenological Landau–de Gennes formulation. Finally, we use the time-dependent Ginzburg-Landau equations to study the non-Fickian evolution of a single two dimensional cholesteric tactoid through a shallow quench from the isotropic to biphasic region of the phase diagram. Although equilibrium biaxiality is considerably low for these long-pitch cholesterics, we found that during self-assembly the biaxial order parameter achieves significant larger values than the equilibrium value. Additionally, the relaxed director field becomes both onion-like and defect-less, which is consistent with the twisted bipolar structure observed experimentally. The self-assembly simulations demonstrate that the formulated theoretical platform is not only consistent with previous theoretical and experimental studies but also able to be used to explore new routes for non-equilibrium collagen self-assembly. Taken together,

this study deepens our understanding of cholesteric (chiral nematic N*) mesophase in acidic solutions of tropocollagen, and suggests a systematic spatio-temporal model that is capable of being used to extract the engineering principles for processing of these sought-after biomaterials.

4.3 Keywords

Biaxiality, Liquid-Crystalline Self-assembly, Collagen-Based Bioinspired Materials, Cholesteric Tactoids, Landau–de Gennes Model, Time-dependent Ginzburg-Landau Model, Chiral Nematic Nucleation and Growth, Uphill Diffusion.

4.4 Introduction

Type I Collagen is composed of three left-handed polypeptide helices (denoted by $[\alpha 1(\mathrm{I})]_2[\alpha 2(\mathrm{I})]$) twisted together to yield a right-handed triple helix. This rod-shaped biomacromolecule, also known as tropocollagen, commonly has a 1.5 nm bare diameter and 300 nm height. The tropocollagen falls into the class of fibrous proteins and is abundantly found in both soft and hard human's tissues, namely cornea, tendon, cortical bone, and more[1]. Over the past two decades, biomimetic fabrication of collagen-based biomaterials has received considerable attention in view of the abundant critical applications such as artificial bone[2-5] and cornea[6, 7] reconstruction. Moreover, for in-vitro replication of these collagenous biological tissues, there is fortunately no concern about supply because tropocollagen can be readily accessible through mammalian and non-mammalian resources[8]. Consequently, numerous promising applications of biomimetic fabrication of collagenous biomaterials[9-11] in conjunction with the availability of precursor play a central role in the drive to create the bioinspired collagen-based materials.

The structural pattern of tropocollagen rods bestows great structural-relation properties on collagenous biological materials and biomaterials. Furthermore, their structures are analogous with architecture of tropocollagen in liquid-crystalline states[12], hence these materials are called "solid analogues". This correspondence establishes the role and impact of liquid-crystalline morphogenesis[13-15] and singles out liquid-crystal-based biomimetic material process engineering as a promising route to enhance the quality of collagen-based biomaterials or even to explore new ones[3, 16-19].

Normally, tropocollagen is immiscible in aqueous solutions due to its hydrophobicity. To attain a stable aqueous isotropic phase, which is the starting point of biomimetic fabrication, hydrophobicity of tropocollagen must be reduced by being dispersed in acidic solutions. Basically, numerous amine function groups that are good proton receptors are found along the tropocollagen backbone. Once these functional groups are protonated, the intrachain repulsion causes that the semi-flexible (worm-like) backbones become uncoiled and essentially rigid rods. The existing interchain repulsion also impedes aggregation, in other words the rods have an effective diameter between two or three times the bare one[20-22]. Finally, due to being charge-carrier rigid rod-like molecules, tropocollagen is capable of exhibiting lyotropic cholesteric phase organization. For example, for an acetic acid concentration of $[\mathrm{AC}] \approx 2900\ \mathrm{mM}$, a phase transition from isotropic to chiral nematic (N*) takes places at tropocollagen concentrations of $[\mathrm{C}] \approx 88 \frac{\mathrm{mg}}{\mathrm{ml}}$[21].

Although the primary architecture of these versatile biomaterials is formed at the molecular level (i.e. mesophasic stage), the focus has been at the tissue level[23] and studies on molecular level are few[21, 22]. Furthermore, to the best of authors' knowledge, theoretic studies of cholesteric self-assembly of aqueous acidic tropocollagen solutions have not been carried out, which also reflects the case of chiral nematic phase ordering in general[24-26]. To address this gap, we have recently developed, implemented , and validated a theoretical model tailored for self-assembly of tropocollagen dispersed in acidic aqueous solutions[20]. This thermodynamic theory[20], which is based on the uniaxiality assumption, has integrated microscopic mechanisms of mixing entropy and enthalpy, attraction, repulsion, twisting, excluded-volume and chirality. In the present study, we lift the uniaxiality assumption by generalizing the free energy that includes biaxial effects. This is crucial for cholesteric materials because chiral nematic phase is described by two vectors: the director (**n**) and the chiral axis (**h**), additionally cholesterogens are intrinsically biaxial as discussed by[27, 28]. Incorporation of the biaxial order parameter into the cholesteric self-assembly deserves consideration because biaxiality influences pattern-formation even in nematic mesophase, such as interfacial biaxiality under tangential director orientation[29-32], the biaxial core of singular disclinations[33, 34], and sometimes more pronounced biaxiality under time-dependent conditions than under static equilibrium[35]. For the above reasons we first include biaxiality in the model formulation stage and then focus on its emergence in bulk, defect core, and interfacial regions; which are of significant importance in all structured materials[30, 33, 36-38].

In our previous validated work[20], we showed that our thermodynamic model of acidic collagen solutions captures two key features: (i) the expected chimney diagram predicted by Flory and found experimentally for many lyotropic rod-like liquid-crystalline polymers[39], and (ii) the parabolic bi-phasic funnel in aqueous acidic collagenous solutions under increasing pH, where cholesteric tactoids (drops) emerge from isotropic phases. Study of cholesteric tactoids is important because of three main reasons: (i) tactoid formation process must occur in to chimney and funnel phase diagrams, which are the fingerprint of rod-like macromolecules. Thus, these cholesteric drops are a crucial element in the validation of thermodynamics of rod-shaped rigid macromolecules;(ii) these stable but deformable drops serve a sources of material properties information such as bulk Frank-Oseen-Mermin elasticity[27], novel coupled gradient contributions between nematic order parameter and collagen concentration, and the cholesteric pitch;(iii) characterizing and understanding the emergence, growth, annihilation, and coalescence of tactoids are essential to future developments of collagen-based material processing. To focus on collagen tactoids, as shown in Figure 4-1, we then target the dynamic of self-assembly through a shallow quench from isotropic phase into the bi-phasic funnel of the previously obtained phase diagram[20]. In contrast to the better-known single component monomeric thermotropic tactoids, in the present case concentration is a conserved transport variable that need to be included. For this purpose, we formulate the coupled phase ordering/mass transfer Model C[40, 41] in order to derive the governing equations of collagen self-assembly. Afterward, we impose proper auxiliary conditions (e.g. initial and boundary conditions for the computational domain) on the obtained governing equations to capture a thorough spatio-temporal evolution of a single cholesteric tactoid—see Figure 4-2. This evolution has two steps: (i)emergence of a cholesteric nucleus in a continuous isotropic phase, (ii) followed by the formation of a stable chiral nematic tactoid coexisting with the isotropic phase.

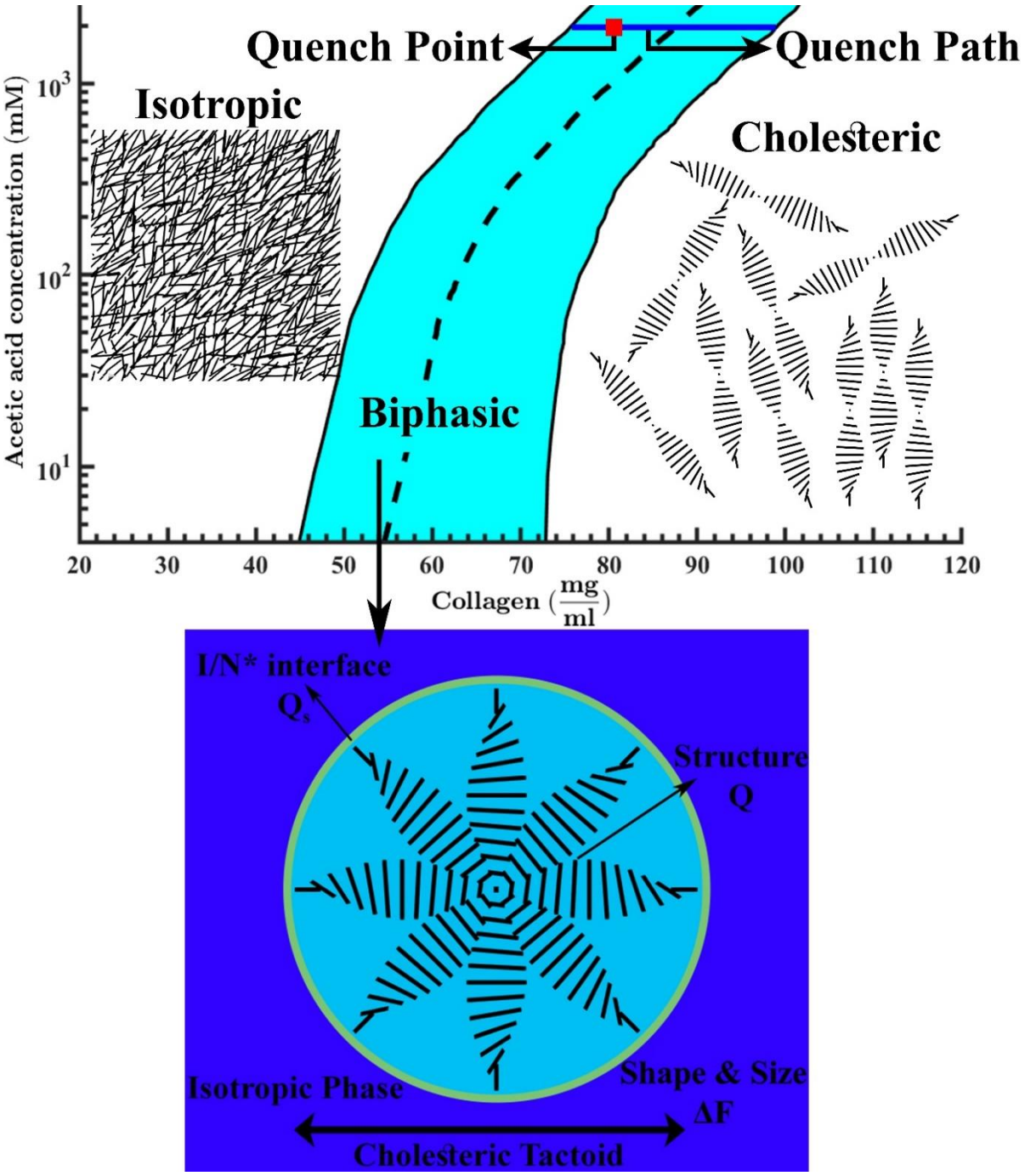

Figure 4-1. Phase diagram of tropocollagen in acidic aqueous solutions. The black solid lines are binodal curves and the black dashed line is phase transition boundary. The quench point and the evolution path are shown by a red square and a blue solid line, respectively. This figure is adapted from reference[20]. The schematics denote the isotropic phase at low collagen concentrations, a typical micron-sized cholesteric drop in an isotropic bulk at intermediate concentrations, and the chiral nematic (N*) or cholesteric phase at higher concentrations.

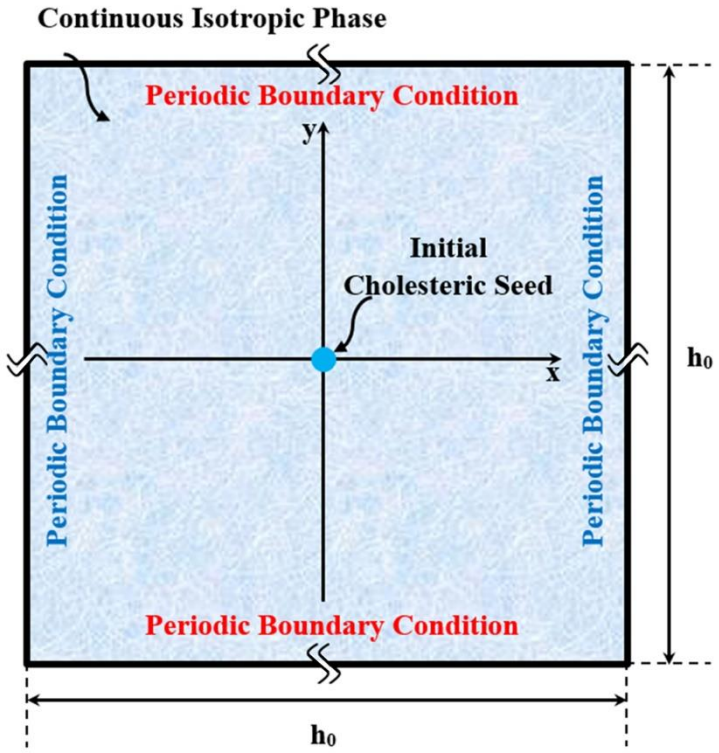

Figure 4-2. Schematic of the computational domain, in which a small chiral nematic drop is initially seeded, and allowed to naturally grow in coexistence with an isotropic phase.

In this work we restrict simulations to a single collagen tactoid with the aim of contributing to the evolving understanding of chiral phase ordering[24, 42, 43]. The simulations are also restricted to 2D. In principle, 3D spatio-temporal simulations can give a full picture of tactoid formation stages. Yet, from practical viewpoint, the present phase ordering/mass transfer coupled nonlinear model with nano-to-micron scales becomes essentially intractable[44]. Furthermore, we have previously shown[45-47] that 2D simulations can provide invaluable predictions, and as discussed later on, in this study the important metrics of size, shape, and structure are not lost when using our 2D simulation box. In particular, we capture bulk disclinations, interfacial anchoring, interfacial biaxiality, growth modes, and self-selected shapes. Hence, this 2D study gives a necessary foundation for future 3D simulations.

The paper is organized as follows. Section 4.5 presents the methodology used in the formulation of self-assembly, including: (1) Formulation of the free energy for a system consisting of charged cholesterogen dispersed in a mixture of water solvent and mobile ions—see subsections 4.5.1-4.5.4. Subsection 4.5.1 defines the **Q**-tensor. In 4.5.2, the free energy of pure charged cholesterogen is developed taking into account the biaxial order parameter. In 4.5.3, the obtained free energy is generalized for a mixture of charged cholesterogen and small-

sized solvent. In 4.5.4, we discuss and incorporate other free energy contributions involved in the evolution of mesophasic state, such as the elasticity of Frank-Oseen-Mermin[28] and gradient contributions, and formation of the I/N* interface. Thus, in 4.5.4, the total free energy of system is formulated. (2) Formulation of governing equations along with the appropriate auxiliary conditions for simulation of liquid-crystalline self-assembly in which a cholesteric nucleus of tropocollagen is initially seeded and allowed to spontaneously growth in coexistence with isotropic phase—see subsections 4.5.5-4.5.6. In 4.5.5, the governing transport equations (Model C) are formulated. Finally, subsection 4.5.6 presents the implementation of self-assembly simulation for nucleation and growth of a single cholesteric tactoid coexisting with an isotropic phase. Section 4.6 presents results of emergence and growth of a cholesteric tactoid. Lastly, the conclusions and nomenclature are summarized in sections 4.7 and 4.8, respectively.

4.5 Continuum methodology for simulation of liquid-crystalline Self-assembly of tropocollagen dispersed in acidic aqueous solutions

4.5.1 Long-Range Description of Molecular Alignment

The long-range orientational order in a liquid-crystalline phase is parameterized by a second-order symmetric traceless tensor called **Q**-tensor[14, 15, 48].

$$\mathbf{Q}=\mathrm{S}\left(\mathbf{nn}-\frac{\boldsymbol{\delta}}{3}\right)+\frac{1}{3}\mathrm{P}(\mathbf{mm}-\mathbf{ll}) \qquad (4-1)$$

where $\boldsymbol{\delta}$ is the Kronecker delta. The orientation of a mesogen is characterized by the orthogonal director triad of $(\mathbf{n},\mathbf{m},\mathbf{l})$. The degree of alignment along the uniaxial director, **n**, and biaxial director, **m**, are S and P, respectively. Due to the quadrupolar symmetry of **Q**-tensor, it possesses the salient feature of head-tail invariance of molecular alignment (i.e. $\mathbf{n}\equiv-\mathbf{n}$, $\mathbf{m}\equiv-\mathbf{m}$ and $\mathbf{l}\equiv-\mathbf{l}$). The largest absolute eigenvalue of **Q**-tensor equals to 2S/3 and the corresponding eigenvector is equivalent of uniaxial director, **n**. The difference between the absolute medium and smallest eigenvalues is 2P/3 and the eigenvector corresponds to the second largest absolute eigenvalue is biaxial director, **m**. Thus, in the isotropic and ordered phases, the **Q**-tensor becomes the 3×3 zero matrix, $\mathbf{Q}=\mathbf{0}$, and nonzero matrix, $\mathbf{Q}\neq0$, respectively.

The uniaxial and biaxial order parameters are also defined in terms of directors/**Q**-tensor or the normalized orientational distribution function on the unit sphere, $\psi(\mathbf{u})$, for any given molecular orientation, **u**:

$$S=\int P_2\big(\cos(\theta)\big)\psi(\mathbf{u})d\Omega=\frac{3\mathbf{n}\cdot\mathbf{Q}\cdot\mathbf{n}}{2} \qquad (4-2)$$

$$P=\int \Delta(\theta,\varphi)\psi(\mathbf{u})d\Omega=\frac{3(\mathbf{m}\cdot\mathbf{Q}\cdot\mathbf{m}-\mathbf{l}\cdot\mathbf{Q}\cdot\mathbf{l})}{2} \qquad (4-3)$$

$d\Omega=\sin(\theta)d\theta d\varphi$ represents a solid angle, and $\theta$and φ are the polar and azimuthal angles. $\Delta(\theta,\varphi)$ is defined as $\frac{3\sin^2(\theta)\cos(2\varphi)}{2}$. As explained below, $P_2\big(\cos(\theta)\big)$ and $\Delta(\theta,\varphi)$ are representative of uniaxiality and biaxiality, respectively. In addition, the normalized distribution function, employed in eqns. (4-2 and 4-3), implies following constraint[49]:

$$\int \psi(\mathbf{u})d\Omega=1 \qquad (4-4)$$

4.5.2 Free Energy Contributions for Pure Charged Cholesterogens; Incorporation of Biaxial Order Parameter

The total dimensionless Helmholtz free energy per particle, $\tilde{F}$, for a dispersion comprising $N_A$charged cholesterogens is[20, 50, 51]:

$$\tilde{F}=\frac{\beta F}{N_A}=\beta\mu^o\,(T)\text{-}1+\ln c_A+\sigma\big(\psi(\mathbf{u})\big)+B_2\big(\psi(\mathbf{u})\big)+M\big(\psi(\mathbf{u})\big) \qquad (4-5)$$

where β, μ^o (T) and c_A stand for thermal energy, standard chemical potential and number density, respectively. The last three terms in eqn. (4-5) account for the contribution of molecular orientation (i.e. uniaxiality and biaxiality) in the mesophasic state. $\sigma\big(\psi(\mathbf{u})\big)$ describes the decrease of orientational entropy upon alignment of the mesogenic molecules.

$$\sigma\big(\psi(\mathbf{u})\big)=\int \psi(\mathbf{u})\ln\big(4\pi\psi(\mathbf{u})\big)\,d\Omega \qquad (4-6)$$

Since we focus on rod-like rigid mesogen, the second virial approximation is capable of accurately describing the excluded volume effect, given by[51, 52]:

$$B_2\big(\psi(\mathbf{u})\big)=c_A\bar{\upsilon}_{AA}\rho\big(\psi(\mathbf{u})\big) \qquad (4-7a)$$

$$\rho\big(\psi(\mathbf{u})\big)=\frac{4}{\pi}\iint \Gamma(\gamma)\psi(\mathbf{u})\psi(\mathbf{u}')\,d\Omega d\Omega' \qquad (4-7b)$$

$$\Gamma(\gamma) = |\sin(\gamma)| \times \left\{1+h\left[-\ln|\sin(\gamma)|-\ln(2)+\frac{1}{2}\right]\right\} \qquad (4-7c)$$

$\overline{\upsilon}_{AA}$ is the average excluded volume defined as $\pi D_{eff}L^2/4$ in which L and D_{eff} denote contour length and effective diameter of tropocollagen. D_{eff} has a dependence on the bare diameter, D=1.5 nm, and concentration[20]. To take biaxiality into consideration, in accordance with[53-55], we make use of the addition theorem for spherical harmonics to express the angle between two rods, γ, in terms of the polar, θ, and azimuthal, φ, angles in spherical coordinate:

$$P_2\big(\cos(\gamma)\big) = P_2\big(\cos(\theta)\big)P_2\left(\cos\big(\theta'\big)\right) + \frac{\Delta(\theta,\varphi)\Delta\big(\theta',\varphi'\big)}{3} \qquad (4-8)$$

First term in eqn. (4-8) is independent from azimuthal angle and represents uniaxiality. Second term is related to biaxial contribution and has the dependence on both polar and azimuthal angles.

The intermolecular interaction and angle between rods interchangeably affect each other because the electrostatic repulsion and twisting favors perpendicular orientation while the van der Waals attraction prefers the parallel alignment (i.e. nematic phase)[51, 52, 56]. Hence, based on our previous work[20] and reference[53], we suggest the net interchain potential expressed by

$$\beta U_i = \beta\big(U'^{elc} - U'^{MS}\big)\upsilon_A P_2\big(\cos(\gamma)\big) \qquad (4-9)$$

where υ_A is the volume of an individual rigid rod, $\upsilon_A = \pi D_{eff}^2 L/4$. U'^{elc} and U'^{MS} are parameters of electrostatic repulsion and a positive constant, respectively. The contribution of intermolecular interaction, $M\big(\psi(\mathbf{u})\big)$, is then obtained by taking average over all possible rod configurations[20]:

$$M\big(\psi(\mathbf{u})\big) = \frac{3}{2}\beta U c_A \upsilon_A^2 \mathbf{Q}:\mathbf{Q} \qquad (4-10)$$

$U = U^{elc} - U^{MS}$ is called the potential of the orientation-dependent intermolecular interactions where U^{elc} and U^{MS} are the strength of electrostatic repulsion and Maier-Saupe constant that is a positive constant independent of temperature. Note that $\mathbf{Q}:\mathbf{Q}$ is related to uniaxial and biaxial order parameters by $2\left(S^2+\frac{P^2}{3}\right)/3$.

We note that the effective diameter reflects the intermolecular repulsion, or to put it another way, the effective thickness of the attached ions on the backbone of tropocollagen. This effective thickness is called double-layer thickness, $\alpha\kappa^{-1}$[51, 52]:

$$D_{eff} = D+\alpha\kappa^{-1} \qquad (4-11)$$

α and κ^{-1}, which are defined as follows, are parameter of double-layer thickness and Debye screening length, respectively:

$$\alpha = \ln A' + \gamma_E + \ln(2) - \frac{1}{2} - \frac{4}{\pi}\left[|\sin(\gamma)|\mathrm{Ei}\left(-\frac{A'}{|\sin(\gamma)|}\right)\right]_i \qquad (4-12a)$$

$$A' = A\frac{e^{\kappa D}}{\kappa D}, A = 2\pi\Lambda^2\lambda_B D \qquad (4-12b)$$

$$[f(\mathbf{u},\mathbf{u}')]_i = \frac{1}{16\pi^2}\iint f(\mathbf{u},\mathbf{u}')d\Omega d\Omega' \qquad (4-12c)$$

$$\kappa^{-1} = (8\pi\lambda_B N_{avo}\varepsilon)^{-\frac{1}{2}} \qquad (4-12d)$$

$$\varepsilon = \frac{1}{2}\sum_i m_i Z_i^2 \qquad (4-12e)$$

where λ_B, N_{avo}, ε, m, Z, Ei(•), γ_E and Λ are the Bjerrum length, Avogadro's number, ionic strength, molar concentration, charge number, the exponential integral defined as $\mathrm{Ei}(x) = -\int_{-x}^{\infty}\frac{\exp(-t)}{t}dt$, Euler constant equals to 0.5772, and linear charge density. A detailed account of parameters' values, their selection and physical significance and physical properties for aqueous acidic collagen I solutions is given in reference[20].

4.5.3 Mixing Free Energy of Binary Dispersions Consisting a Charged Cholesterogen and Small-Sized Solvent

The mixing free energy of the binary solution is given by[50]

$$F = \Delta F_{mixing}(N_A,N_I) = F^s(N_A,N_I) - F^s(N_A,0) - F^s(0,N_I) \qquad (4-13)$$

where $F^s(N_A,N_I)$, $F^s(N_A,0)$ and $F^s(0,N_I)$ are free energies of solution, pure anisotropic component dispersed in isotropic state and isotropic component, respectively. Thus, in this subsection, we shall first derive the free energy of solution, and then formulate the mixing free energy of a binary dispersion by use of eqn. (4-13).

Substituting eqns. (4-7 and 4-10) into eqn. (4-5) leads to the free energy of pure charged chiral nematic rods. The free energy for binary mixture of charged chiral mesogen and small-

sized solvent (water in our case)—denoted by subscript A and I, respectively—is then formulated as

$$\begin{aligned}\beta F^{s}=&N_A\beta\mu_A^{o}+N_I\beta\mu_I^{o}-N_A-N_I+N_A\ln c_A+N_I\ln c_I+N_A\sigma\left(\psi(\mathbf{u})\right)\\&+\overline{\upsilon}_{AA}N_Ac_A\rho\left(\psi(\mathbf{u})\right)+2\overline{\upsilon}_{AI}N_Ic_A+\overline{\upsilon}_{II}N_Ic_I\\&+N_A\beta Uc_A\upsilon_A^2\left(S\left(\psi(\mathbf{u})\right)^2+\frac{1}{3}P\left(\psi(\mathbf{u})\right)^2\right)\end{aligned}\qquad(4-14)$$

Eqn. (4-14) is not usable unless the unknown normalized distribution function, $\psi(\mathbf{u})$, is known. To formulate the normalized distribution function, the total free energy of system subjected to the normalizing constraint, given by eqn. (4-4), is minimized using Euler-Lagrange method. This minimization yields an irreducible algebraic integral equation expressed by

$$\begin{aligned}\ln\left(4\pi\psi(\theta,\varphi)\right)=&\eta'-2\beta Uc_A\upsilon_A^2\left\{SP_2\left(\cos(\theta)\right)+\frac{1}{3}P\Delta(\theta,\varphi)\right\}\\&-\frac{8}{\pi}\overline{\upsilon}_{AA}c_A\int\Gamma(\gamma)\psi\left(\theta',\varphi\right)d\Omega'\end{aligned}\qquad(4-15)$$

Simplicity of free energy expression is essential since our ultimate objective is the self-assembly simulation which in itself is computationally complex. A heavy computational load is expected because the self-assembly process covers a wide range of length scale (i.e. ranging from nano- to macro-scale) and it may go through a variety of complex microscopic mechanisms[43, 57-61]. Thus, to improve tractability, we expand the functional part of eqn. (4-15), $\Gamma(\gamma)$, in terms of the second Legendre polynomial by use of eqn. (4-8):

$$\begin{aligned}\Gamma(\gamma)\approx&\frac{\pi}{4}-\frac{5\pi}{32}\left(1-\frac{11}{8}h\right)\left\{P_2\left(\cos(\theta)\right)P_2\left(\cos\left(\theta'\right)\right)\right.\\&\left.+\frac{1}{3}\Delta(\theta,\varphi)\Delta\left(\theta',\varphi'\right)\right\}\end{aligned}\qquad(4-16)$$

Having substituted eqn. (4-16) into eqn. (4-15), the normalized distribution function is obtained:

$$\psi(\theta,\varphi)=\frac{\exp\left(W\left\{SP_2\left(\cos(\theta)\right)+\frac{P\Delta(\theta,\varphi)}{3}\right\}\right)}{I_{00}}\qquad(4-17)$$

where the I_{00} is a definite integral defined as

$$I_{00}(S,P,W)=\int_0^1\int_0^1\exp\left(W\left\{SP_2(x)+\frac{P\Delta(x,y)}{3}\right\}\right)dxdy\qquad(4-18)$$

W is known as the net cholesteric potential, which is similar to reference[20] and can be parameterized as

$$W=\alpha_w\phi_A \qquad (4-19a)$$

$$\alpha_w=\frac{5}{4}\left(1-\frac{11}{8}h\right)\frac{L}{D_{eff}}-\frac{\pi}{2}D_{eff}^2\beta UL \qquad (4-19b)$$

$\phi_A$is the effective volume fraction and $h=(\kappa D_{eff})^{-1}$. α_W is assumed to only be dependent on concentration of acid throughout the evolution—a reasonable assumption because α_W is mainly affected by concentration of acid[20].

Next the mixing free energy, eqns. (4-20a-c), is obtained by use of eqns. (4-13, 4-14 and 4-17). Detailed account of such algebraic derivation is given in references[20, 50]. Note that hereafter, for convenience, we use ϕ to represent the effective volume fraction of tropocollagen—it can be related to the concentration of tropocollagen in units of mg of tropocollagen pre ml of solution by $C=\frac{\phi}{\alpha_c}$ where α_c is a unit conversion factor. The dimensionless mixing free energy density is:

$$\tilde{f}_{mxing}=\tilde{f}_{iso}+\tilde{f}_h \qquad (4-20a)$$

$$\tilde{f}_{iso}=\frac{\phi\ln(\phi)}{n}+(1-\phi)\ln(1-\phi)+\chi\phi(1-\phi) \qquad (4-20b)$$

$$\tilde{f}_h=\frac{\phi}{n}\left[\frac{3}{4}W\mathbf{Q}:\mathbf{Q}-\ln\left(I_{00}(W,S,P)\right)\right] \qquad (4-20c)$$

where n stands for number of segments on tropocollagen backbone. $\tilde{f}_{iso}$ and $\tilde{f}_h$ describe different physics; the former explains the phase separation which is the well-known Flory-Huggins equation and the latter controls the phase transition (i.e. homogenous contribution). In the absence of biaxiality, P=0, the obtained mixing free energy, eqns. (4-20a-c), is reduced to the validated free energy functional given in ref. [20] which was validated with experimental data of tropocollagen and with previous theoretical studies. It is worth mentioning that with further assumptions the obtained free energy density leads to the formulation given in reference[50] as well as the well-established theory of Onsager—see ESI of reference[20] for further discussion. For numerical tractability, similar to references[53, 62], we make use of a Taylor

expansion in vicinity of I/N* to expand eqn. (4-20c) in a power series of order parameters, S^iP^j—the resulting polynomial is the phenomenological Landau-de Gennes (LdG) theory[63]:

$$\tilde{f}_h = \frac{a}{2}\mathrm{Tr}(\mathbf{Q}^2) - \frac{b}{3}\mathrm{Tr}(\mathbf{Q}^3) + \frac{c}{4}\left(\mathrm{Tr}(\mathbf{Q}^2)\right)^2 \qquad (4-21a)$$

$$a(\phi) = \frac{3}{2}\frac{\alpha_w}{n}\left(1-\frac{\alpha_w\phi}{5}\right)\phi^2 \qquad (4-21b)$$

$$b(\phi) = \frac{9}{70}\frac{\alpha_w^3}{n}\phi^4 \qquad (4-21c)$$

$$c(\phi) = \frac{\alpha_w}{10}b\phi \qquad (4-21d)$$

Although self-assembly simulations by use of the eqns. (4-21a-d) is appreciably more tractable than with eqn.(4-20c), it should be noted that the used expansion may affect the accuracy of simulations in the cases of deep quenches. However, this study only focuses on the self-assembly of shallow quenches into biphasic region which is a narrow region around I/N* boundary, see Figure 4-1.

An order-disorder phase transition takes place if and only if $W=\alpha_w\phi = \alpha_w\alpha_c C>5$ to make the coefficient of second invariant of **Q**-tensor, a, negative. The derived LdG coefficients satisfy two general theoretical expectations; 1) the first-order phase transition (i.e.$B \neq 0$), and 2) two minima correspond to isotropic and ordered phases (i.e.$A<0$and $C>0$) [48]. Furthermore, in the cholesteric phase, W can be about 10, and under such conditions the proposed LdG coefficients becomes similar to the well-established lyotropic LCP Doi's model , were $b \approx c$[14, 15, 64].

4.5.4 Total Free Energy Tailored for Tropocollagen Self-Assembly in Acidic Aqueous Solutions

In addition to $\tilde{f}_{mxing}$ which is capable of describing phase separation and an order–disorder phase transition, for constructing the total free energy of mesogenic solutions, the contributions of gradients should be taken to account[65-67]:

$$\tilde{F}_{net} = \int_{\tilde{V}}\left(\tilde{f}_{iso}+\tilde{f}_h + \tilde{f}_e + \tilde{f}_{cg} + \tilde{f}_c\right)d\tilde{V} \qquad (4-22a)$$

$$\tilde{f}_e = \frac{1}{2}\left(\frac{\xi}{h_0}\right)^2 \left[\left[\tilde{\nabla} \times \mathbf{Q} + 4\pi\left(\frac{h_0}{p_\infty}\right)\mathbf{Q}\right]^2 + \left(\frac{L_2}{L_1}\right)\left[\tilde{\nabla} \cdot \mathbf{Q}\right]^2\right] \qquad (4-22b)$$

$$\tilde{f}_{cg} = \frac{1}{2}\tilde{L}_\phi\left(\tilde{\nabla}\phi\right)^2 \qquad (4-22c)$$

$$\tilde{f}_c = \tilde{L}_{\phi-\mathbf{Q}}\left(\tilde{\nabla}\phi\right)\cdot\left(\tilde{\nabla}\cdot\mathbf{Q}\right) \qquad (4-22d)$$

$\xi=\sqrt{a^3 L_1 \beta}$ is the coherence length in which a^3 stands for the volume of each lattice unit and L_i are elastic constants. $\tilde{\nabla}= h_0\nabla$ is dimensionless gradient in which h_0 denotes a macroscopic length scale and the spatial domain is scaled by h_0, $\tilde{L}_\phi = \frac{L_\phi a^3 \beta}{h_0^2}$and $\tilde{L}_{\phi-\mathbf{Q}} = \frac{L_{\phi-\mathbf{Q}} a^3 \beta}{h_0^2}$ where L_ϕ is cost of interfacial formation and $L_{\phi-\mathbf{Q}}$represents coupling constant. The total free energy as well as the evolution of chiral nematic phase for tropocollagen are mesoscopic because it retains both microscopic length scale, ξ, in a nanometer range and macroscopic length scale, h_0, in the range of micrometers.

4.5.5 Governing Equations for Kinetics of Self-Assembly; Orientational Relaxation, and Uphill Diffusion

Simulations of pattern-formation in fibrous composites, including collagen-based tissues, were first carried out by[64, 67, 68]. Their approaches were based on diffusionless evolution of mesophase, and capable of predicting macroscopic architecture of these materials to a great extent. However, recent studies have revealed the imperative role of diffusion in accurately capturing the growth of order-disorder interface[45, 69]. Hence, for the purpose of realistic self-assembly modeling, in this subsection, we formulate the spatio-temporal evolution of tropocollagen in which the **Q**-tensor augmented with a mass transfer equation.

The cholesteric micro-structures in collagenous biomaterials are formed through the liquid-crystalline self-assembly stage. Two simultaneous mesoscopic mechanisms govern this thermodynamically driven assembly. First, mass transfer mechanism allows tropocollagen macromolecules to diffuse into cholesteric phase (i.e. tropocollagen-rich phase) from isotopic phase (i.e. tropocollagen-lean phase). The mentioned demixing is known as uphill or non-Fickian diffusion and reduces the total free energy of system. Second, orientational relaxation mechanism induces cholesteric architecture inside the formed high-concentration domain. To describe these two phenomena; two coupled fields are required. First, the conserved scalar field

of concentration, C, or equivalently volume fraction, ϕ, governing the phase separation. Secondly, the non-conserved tensorial field of **Q**-tensor by which the orientation of tropocollagen biomacromolecules is primarily specified. The spatio-temporal evolution of {**Q**, ϕ } is found using the time-dependent Ginzburg–Landau (TDGL) formalism, also known as model C in Hohenberg and Halperin classification[40, 41]. The dimensionless form of model C adjusted for self-assembly simulation reads[17, 64, 67, 70, 71]:

$$\frac{\partial \mathbf{Q}}{\partial \tilde{t}} = -\frac{1}{\left(1-\frac{3\mathrm{Tr}(\mathbf{Q}^2)}{2}\right)^2}\left(\frac{\delta \tilde{F}_{net}}{\delta \mathbf{Q}}\right)^{[s]} \qquad (4-23a)$$

$$\frac{\partial \phi}{\partial \tilde{t}} = \widetilde{M}_{\phi}\tilde{\nabla}\cdot\left([\mathbf{I}+\mathbf{Q}]\cdot\tilde{\nabla}\frac{\delta \tilde{F}_{net}}{\delta \phi}\right) \qquad (4-23b)$$

$\frac{\delta \tilde{F}_{net}}{\delta \mathbf{Q}}$ represents functional derivative. $\tilde{t}$ is dimensionless time defined as $\tilde{t} = \frac{tM_{\mathbf{Q}}}{(a^3\beta)}$ where t is time, $\widetilde{M}_{\phi} = \frac{M_{\phi}}{(M_{\mathbf{Q}}h_0^2)}$ in which the mobilities of **Q** and ϕ are $M_{\mathbf{Q}}$ and M_{ϕ}, respectively. Additionally, the superscript [s] indicates that the functional derivative must be symmetric traceless in order to be consistent with the nature of **Q**-tensor—for any given second rank tensor $\mathbf{T}^{[s]} = \frac{(\mathbf{T}+\mathbf{T}^t)}{2} - \frac{\mathrm{Tr}(\mathbf{T})\boldsymbol{\delta}}{3}$ where superscript t denotes transpose.

The system given in eqns. (4-23a-b) is a set of six coupled nonlinear PDEs. Eqn. (4-23a) accounts for the spatio-temporal evolutions of the orientational tensor order parameter. This equation is the compact tensorial form of five independent second-order PDEs. Furthermore, eqn. (4-23b) is a fourth-order PDE, known as the Cahn-Hilliard equation, to describe the concentration field by which the chiral nematic and isotropic phases gradually evolve through the uphill diffusion mechanism.

4.5.6 Computational details

Here we elaborate on the simulation of nucleation and growth of an isolated cholesteric tactoid in a continuous isotropic phase. This simulation consists of a diffusional phenomenon coupled with structural relaxation. The general schematic representation of this implementation is illustrated in Figure 4-2.

As above mentioned, the biomimetic formation of collagen-based tissues starts with dissolving tropocollagen in acidic aqueous solutions to obtain the isotropic phase. In such

condition, a nucleus is thermodynamically allowed to grow, providing its radius is greater than a critical value. In that case, as a single tactoid grows, the tropocollagen rods diffuse from collagen-lean phase to collagen-rich phase, in turn, the isotopic and cholesteric phases become depleted from and enriched in tropocollagen, respectively. The diffusion of tropocollagen from lean phase (isotropic phase) to rich phase (cholesteric phase) continues till a point where the chemical potentials of two phases become identical.

As illustrated in the Figure 4-2, we consider the bulk of system as a square with [-0.5 0.5]×[-0.5 0.5] normalized by h_0. Each pair of sides are subjected to the periodic boundary condition. Initially $\mathbf{Q}$=0 and the phase is isotropic. Afterwards, an initial cholesteric tactoid is seeded by a circular Gaussian distribution with FWHM (full width at half maximum of Gaussian function) greater than the critical drop diameter. The seeding is expressed:

$$\mathbf{Q}|_{t=0} = \left[S_e(\mathbf{n}_e\mathbf{n}_e - \boldsymbol{\delta}/3) + \frac{1}{3}P_e(\mathbf{m}_e\mathbf{m}_e - \mathbf{l}_e\mathbf{l}_e)\right] \times e^{-\frac{1}{2}\left(\left(\frac{x-x_0}{\sigma_x}\right)^2+\left(\frac{y-y_0}{\sigma_y}\right)^2\right)} + \boldsymbol{\Xi} \qquad (4-24a)$$

$$\phi|_{t=0} = (\phi_{ch} - \phi_{iso}) \times e^{-\frac{1}{2}\left(\left(\frac{x-x_0}{\sigma_x}\right)^2+\left(\frac{y-y_0}{\sigma_y}\right)^2\right)} + \phi_{iso} + \Xi \qquad (4-24b)$$

$\boldsymbol{\Xi}$ and Ξ, that are respectively a second rank symmetric traceless random tensor and scalar random number, are included in the modeling to represent the fluctuations existing in a real system. The subscript e indicates the equilibrium condition given by:

$$\mathbf{n}_e = \left[0 \quad \cos\left(\frac{2\pi}{p_\infty}x\right) \quad \sin\left(\frac{2\pi}{p_\infty}x\right)\right] \qquad (4-25a)$$

$$\mathbf{m}_e = \left[0 \quad -\sin\left(\frac{2\pi}{p_\infty}x\right) \quad \cos\left(\frac{2\pi}{p_\infty}x\right)\right] \qquad (4-25b)$$

In accordance with $\mathbf{l} = \mathbf{n} \times \mathbf{m}$, $\mathbf{l}_e$is computed as $[0 \quad 0 \quad 1]$.

Eqns. (4-24a-b and 4-25a-b) describe a nucleus whose center placed at position (x_0,y_0) at a concentration equivalent to the effective volume fraction of ϕ_{ch}. For convenience, we choose the center at (x=0, y=0). The concentration of tropocollagen from the center, which is a cholesteric phase, gradually decreases along the radius to the concentration of continuous isotropic phase, ϕ_{iso}. This approach for simulating the initial nucleus was adapted from[30, 33, 34]. In order to make sure that the initial drop is sufficiently large, we choose the $\sigma_x = \sigma_y = \sigma$ and obtain σ in way that FWHM equals two times the critical diameter: FWHM$=2\sqrt{2\ln 2}\,\sigma = 2D_c = 4R_c$. Classical Nucleation theory[72] provides a rough estimation of the critical radius of a drop as expressed by $R_c = \left|\frac{2\gamma_i}{(c_A\Delta\mu^{iso\text{-}Cho})}\right|$ in which $\gamma_i$and $\Delta\mu^{iso\text{-}Cho}$are the interfacial tension

and the chemical potential difference between isotropic and cholesteric phase[72, 73]. Additionally, eqn.(4-24b) yields the quenched concentration as $\phi_q = \frac{\iint_{CD}\phi|_{t=0}\,dxdy}{\iint_{CD}\,dxdy}$ in which CD denotes the entire system (computational domain). Consequently, ϕ_{iso} plays an appreciable role in the size of tactoid because its value affects the initial amount of tropocollagen existing in the system.

Furthermore, the total conservation of mass is imposed by:

$$\frac{d}{dt}\int_{CD}\phi\,dxdy = 0 \qquad (4-26)$$

Simulation parameters used in this study are summarized in Table 4-1—also readers are referred to the reference[20] for detailed account of parameters selection in order to accurately capture the available experimental data.

Although the $\tilde{L}_{\phi-Q}$, $\tilde{L}_{\phi}$and $\frac{L_2}{L_1}$ have not been documented for tropocollagen, we choose common values which satisfy the energy transformation constraint[74-76]:

$$\frac{\left(\tilde{L}_{\phi-Q}\right)^2}{\tilde{L}_{\phi}\times\left(\frac{L_2}{L_1}\right)} < 1 \qquad (4-27)$$

Eqns. (4-24a-b) in conjunction with the above-explained conditions are solved with an adaptive finite elements technique with biquadratic basis functions (General PDE solver of COMSOL Multiphysics 5.3a). Furthermore, to acquire the acceptable spatial resolution, we considered at least 50 elements per pitch which resulted in nearly 10^4 triangular elements, and temporal resolution was carried out by the Backward Euler method. Convergence, accuracy, and stability were checked using standard techniques—for further information on the method and solution approach, please see the accompanying Supporting Information.

4.6 Results and discussions

In this section, the dynamics of mesophasic evolution and the resulting equilibrium configuration for a shallow quench from the isotropic phase into the cholesteric phase in the presence of one small cholesteric seed are given and discussed; see Figure 4-1and Figure 4-2.

The panels (a-d) in Figure 4-3 show snapshots of a growing tactoid corresponding to dimensionless times 0, 900, 960 and 1100, respectively. Panel (a) shows the initial condition of a small chiral nematic drop seeded in a large isotropic phase area. Note that only a small section of the computational domain, in which the self-assembly is supposed to take place, is shown in Figure 4-3. The computational domain is actually chosen as a fairly large square with length of h_0=100μm in order to make sure that the existing amount of tropocollagen in the system is sufficient for formation of a single cholesteric tactoid with diameter of the order of 30μm—as experimentally observed[21]. The size of initial seed must be greater than a critical value in order for the drop to grow based on the mechanism of uphill diffusion, otherwise downhill diffusion takes place and the initial drop is dissolved in isotropic phase.

Table 4-1. The material properties and parameter values used in the present paper. The square-brackets next to the values indicate the corresponding unit, and [-] shows dimensionless. Note: for those parameters which have not been documented for solutions of tropocollagen, the common values are used instead. Readers are referred to references[20, 21, 64-67] for details of parameter selection.

Parameters	**Values**	**Parameters**	**Values**	**Parameters**	**Values**
$\mathbf{n}$	10 [-]	χ	1.4 [-]	$\frac{L_2}{L_1}$	1[-]
$\tilde{\mathbf{L}}_{\boldsymbol{\phi-Q}}$	-4.4×10^{-7}[-]	$\tilde{L}_\phi$	2.8×10^{-4} [-]	$\tilde{M}_\phi$	1.1×10^{-5} [-]
S_e	1[-]	P_e	10^{-3}[-]	h_0	100 [μm]
$\mathbf{C}_{ch}$	98 [mg/ml]	C_{iso}	79 [mg/ml]	p_∞	10 [μm]

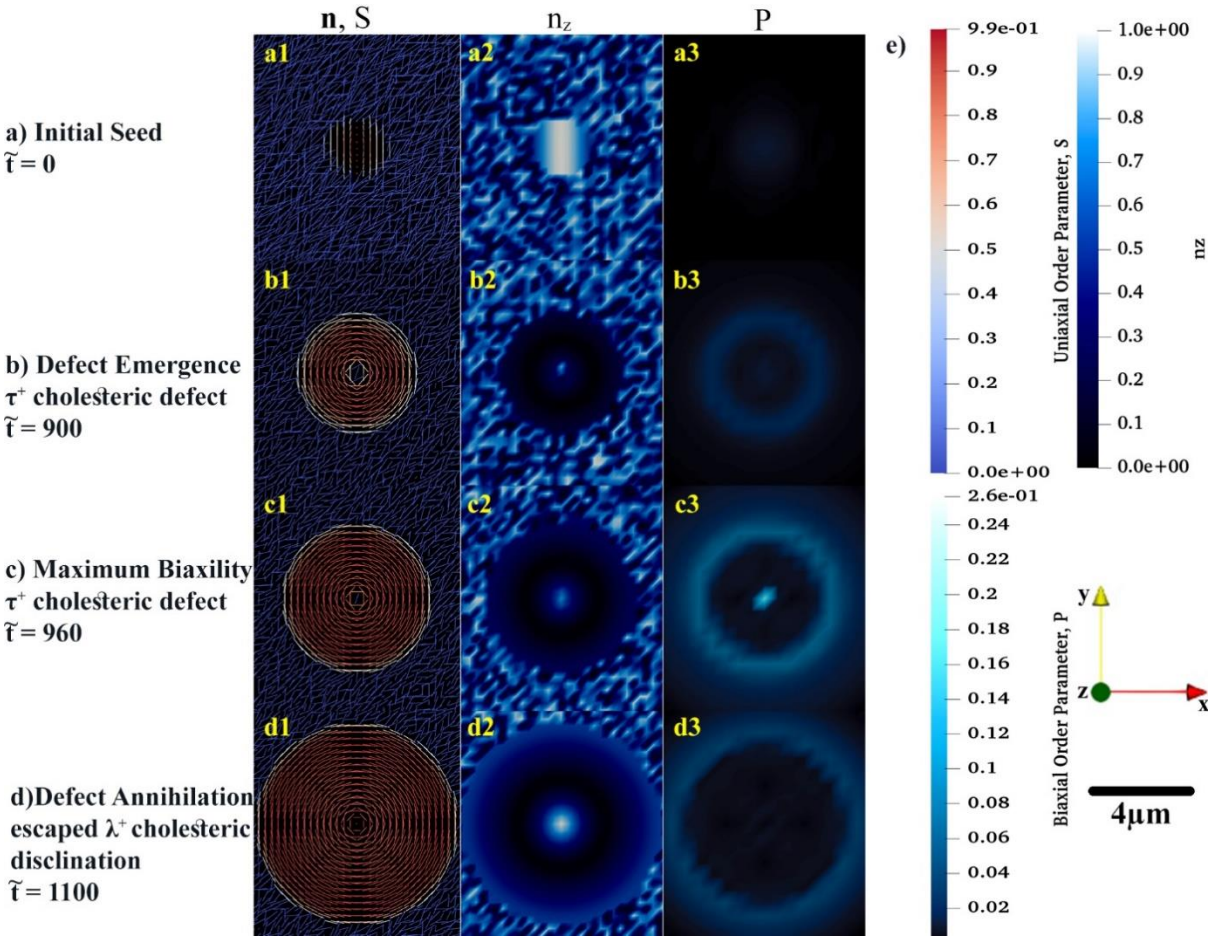

Figure 4-3. The spatial distributions of order parameters, S and P, in conjunction with the director configuration at the early growth of cholesteric tactoid shown in panels a), b), c) and d). In the first column the uniaxial configuration, n, of tropocollagen macromolecules are represented by rods whose color (blue to red) shows the uniaxial order parameter, S. To complete the understanding about the configuration of rods in xy-plane, in the second column, the z component of n is shown by use of a monochromatic blue spectrum. In last column, the monochromatic cyan denotes the variation of biaxial order parameter during the time evolution. Panel e) illustrating the color bars for S, nz and P, the used coordination of system and length-scale bar.

Although the initial configuration of rods is chosen as twisting around x-axis, see panel a1 of Figure 4-3, the rods prefer to be aligned in a concentric configuration, as shown in panel b1. During the early growth of the tactoid, rods attempt to radially twist—the helicoidal axes are along the radii of the circular tactoid. Yet, rods placed at the center of drop exhibit orientational frustration. This frustration emerges in $\tilde{t}=900$, panel b1, and yields a τ^{+1} cholesteric defect. As the tactoid grows, the central rods resolve the orientational frustration with an escaped configuration (see panel d1) known as a nonsingular λ^{+1} cholesteric disclination. These

important predictions may be difficult to be captured experimentally due to intrinsic size length scale resolutions when using optical methods[77-79].

Figure 4-3 (i.e. panels a2, b2, c2 and d2) shows the z component of uniaxial director, **n**. The figures show that the central director regions evolves slower and lags the radial helix formation that results in tangential interfacial orientation experimentally observed for tropocollagen tactoids[38]. The tangential orientation minimizes the interfacial free energy at **n**.**k**=0 where **k** is the interfacial normal vector. This tangential configuration, **n**.**k=0**, emerges when the coupling coefficient, $\tilde{L}_{\phi-\mathbf{Q}}<0$[21, 75, 76, 80]. The structure of the 2D tactoid is a radial helix, with tangential interface orientation at the edge and nonsingular escape orientation at its center.

Of particular interest to this study is incorporation and analysis of biaxial order parameter during the evolution of the cholesteric tactoid. In the third column of Figure 4-3, (i.e. panels a3, b3, c3 and d3), the spatial variation of biaxial order parameter, P, is shown in the early stages of growth. The biaxial order parameter becomes particularly noticeable at the interface and at the defect core. Thus, we found that although the equilibrium biaxiality for rod-like macromolecules is small[27, 53], during the phase ordering it takes a larger value than its equilibrium; the difference between dynamical and equilibrium values for biaxiality may be up to three orders of magnitude.

In the course of time, the **Q**-tensor is relaxed, mass transfer ceases and the structure equilibrates, as shown in Figure 4-4. As depicted in panels a1) and b) of this figure, the equilibrium configuration of tropocollagen rods becomes concentric, also known as onion-like. This defectless configuration, which has a nonsingular λ^{+1} cholesteric disclination at its center, thoroughly matches with the xy-cross-section of Twisted Bipolar Structure (TBS) given in reference[81]. Moreover, the experimental POM image reported in reference[21] confirms TBS for the 3D tropocollagen tactoids. Consequently, the resulting 2D configuration, shown in Figure 4-3 and Figure 4-4, is consistent with experimental observation. Panel a1) of Figure 4-4 shows that the size of tactoid is also consistent with experimental results given in[21]. As can be seen, the diameter of tactoid contains three pitches that each of which has a length of 10µm. Therefore, the tactoid shape becomes a nearly 30µm spherulite. Panel c) in Figure 4-4 represents the equilibrium concentration field. Although a gradient of concentration exists in the interface, the drop remains intact and stable in the isotropic phase. This feature verifies that the growth of cholesteric tactoid is according to the mechanism of uphill diffusion. Panel d) of Figure 4-4 demonstrates that the equilibrium biaxial order parameter P in the interface is nearly

0.04, however its value sharply decreases to 10^{-4} confirmed by previous theoretical studies[27, 53].

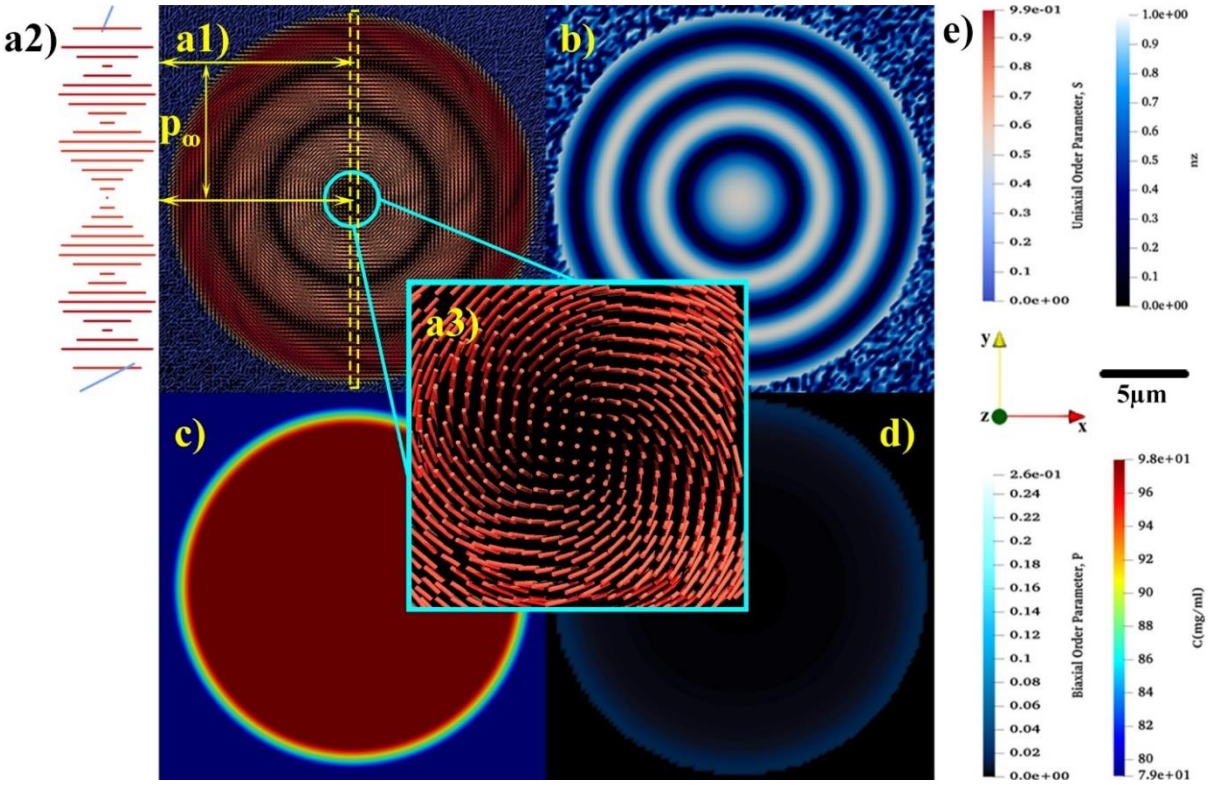

Figure 4-4. The equilibrium spatial distributions of a1) uniaxial order parameter, S, and the relaxed uniaxial director, **n**, b) z component of uniaxial director, c) concentration, and d) biaxial order parameter, P. Panel a2) showing the magnified rotation of tropocollagen placed in the yellow dash-line box. Panel a3) indicating the non-singular escaped λ^{+1} disclination emerges at the center of tactoid. Panel e) representing the color bars for S, n_z, P, and C, the used coordination of system and length-scale bar.

Through the entire evolution we find: (1) the interfacial uniaxial order parameter is approximately S_c=0.39 that is quite close to the critical uniaxial order parameter reported in[20, 21]; (2) The biaxial order parameter at the tactoid's interface is at all times greater than in the interior. The only exception is during initial defect nucleation where biaxiality pronouncedly appears at the core and edge of the 2D drop.

According to the principle of minimum free energy, the kinetic of a spontaneous process follows a path over which the free energy progressively decreases and ends up in a minimum at equilibrium. Figure 4-5 illustrates the averaged free energy contributions through the phase ordering process of tropocollagen dispersed in the constant concentration of 2.9M acetic acid. These spatial averages are defined as

$$\bar{F}_i(\tilde{t}) = \frac{\iint_{CD} \tilde{f}_i \cdot dxdy}{\iint_{CD} dxdy}; \quad i \in \{iso, h, e, cg, c\} \qquad (4-28)$$

The formation of the single cholesteric drop is the interplay of five free energy contributions. The entropic and enthalpic contributing factors in isotropic phase separation are described by Flory-Huggins theory, $\tilde{f}_{iso}$. The LdG theory, $\tilde{f}_h$, also accounts for the homogeneous effect of phase transition. The spatial averages of these contributions are shown by $\bar{F}_{iso}$ and $\bar{F}_h$, respectively. The monotonic decrease in $\bar{F}_{iso}$and $\bar{F}_h$ shows that the phase separation and phase ordering are energetically favorable. In addition, it emphasizes on the lyotropic nature of phase ordering in acidic collagenous dispersions; rods are spontaneously accumulated in cholesteric phase, in turn, removed from the isotropic phase. Hence, $\bar{F}_{net}$which is the summation of all contributions, is considerably affected by contributions of phase separation and phase ordering.

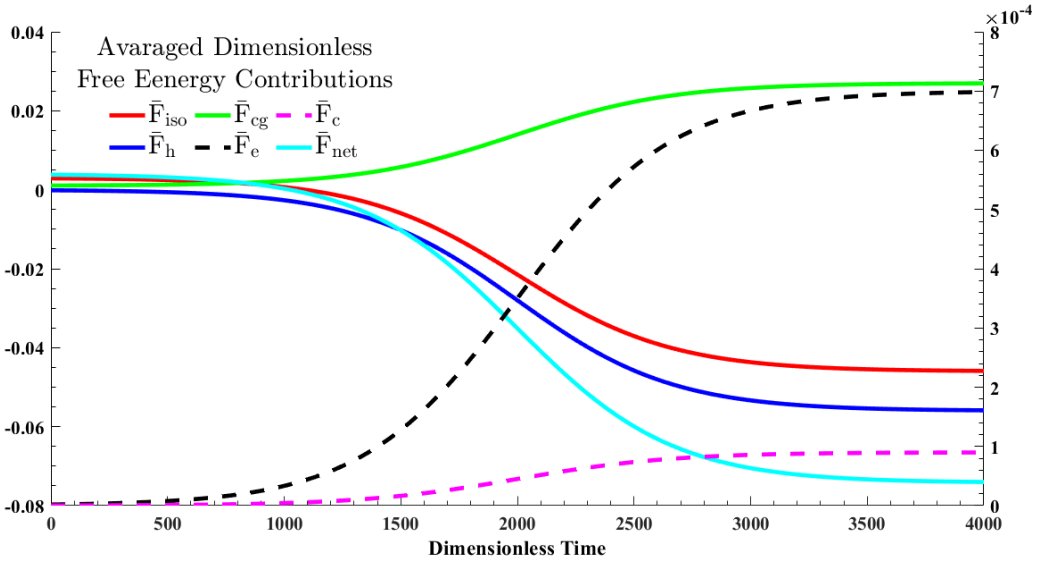

Figure 4-5. The dynamics of the averaged free energy contributions, given in eqn.(4-28), through a shallow quench from an isotropic state into cholesteric phase—the quench point and evolution path are shown in Figure 4-1. The solid lines correspond to the left y-axis and dash lines should be referred to the right y-axis.

In spite of these energetically favorable contributions, formation of I/N* interface and cholesteric configuration inside the tactoid require energy costs which are reflected as penalty terms in the net free energy; see eqns. (4-22a-d). The green solid line in Figure 4-5, $\bar{F}_{cg}$, depicts the cost of interface formation (i.e. mass gradient zone shown in the panel (c) of Figure 4-4). This cost is nearly 40 percent of the energy reduction in either phase separation, $\bar{F}_{iso}$, or phase ordering, $\bar{F}_h$, thus the interfacial formation cost can be compensated. Furthermore, the black

dash line, $\bar{F}_e$, and the purple dash line, $\bar{F}_c$, stand for the average costs for the onion-like configuration of rods inside the chiral nematic tactoid and the tangential configuration in interface, respectively. As seen, the formation cost of the interfacial parallel anchoring, $\bar{F}_c$, is approximately 2 % of the interior cholesteric energy, $\bar{F}_e$.

4.7 Conclusions

Building on our prior work[20], in this study, we have developed and validated a theoretical framework to study the spatio-temporal phase ordering of tropocollagen dispersed in acidic aqueous solutions into 2D drops. By use of the addition theorem for spherical harmonics (eqn. (4-8)), we first incorporated the biaxial order parameter P (eqn. (4-3)) into the orientational entropy (eqn. (4-6)), the second virial approximation (eqn. (4-7a-c)), and the intermolecular interaction (eqn. (4-10)). We then obtained the LdG coefficients (eqns. (4-21a-d)), and formulated the net free energy of system, eqns. (4-22a-d)). To capture the kinetic of the emerging 2D tactoids size, shape, and structure, we relied on the proposed net free energy and phase ordering/mass transfer process (Model C) to establish the governing equations, eqns. (4-23a-b), which were numerically solved under the mentioned auxiliary conditions elaborated in subsection 4.5.6.

Panels (a)-(d) in Figure 4-3 reveal two findings. First, the physical origin for the non-singular escaped λ^{+1} disclination. Basically, in the early evolution a τ^{+1} defect emerges at center of nucleus. As time progresses, the central directors go through a defect shedding stage and the τ^{+1} cholesteric defect evolves into the escaped λ^{+1} disclination. Second, at the interface and defect core region, the biaxial order parameter takes appreciably large value in the early evolution. Furthermore, panels (a1)-(a3) and (b) in Figure 4-4 demonstrate that the resulting equilibrium state of collagen tactoid is an approximately 30μm spherulite in which the rod-shaped macromolecules are aligned in concentric configuration, consistent with experimental observations[21]. Taken together, these results contribute to the development of optimized processing protocols for collagen-based materials and their material property characterization.

4.8 Nomenclature

Symbol	Units	Description
a^3	m^3	volume of each lattice unit
$B_2(\psi(\mathbf{u}))$	[-]	second virial approximation to represent the excluded-volume effect
c_A	m^{-3}	number density
C	mg/ml	concentration of tropocollagen
D_{eff}	m	effective diameter
D	m	bare diameter
$d\Omega$	radian	solid angle
Ei	[-]	exponential integral
$\tilde{f}$	[-]	Dimensionless free energy density
F^s	j	free energy of solution
$\bar{F}_i$	[-]	average of total dimensionless free energy contribution i
h	[-]	magnitude of the twisting effect
ε	molar	ionic strength
k_B	$m^2.kg.s^{-2}.K^{-1}$	Boltzmann constant, $1.38064852 \times 10^{-23}$
$\mathbf{l}$	[-]	$\mathbf{l = n \times m}$
L	m	contour length
L_1 and L_2	j/m	elastic constants
$\tilde{\mathbf{L}}_{\boldsymbol{\phi-Q}}$	[-]	dimensionless coupling parameter
$\tilde{L}_\phi$	[-]	dimensionless cost of interfacial formation
$\mathbf{m}$	[-]	biaxial director
$M(\psi(\mathbf{u}))$	[-]	the orientation-dependent intermolecular interactions
$\widetilde{M}_\phi$	[-]	dimensionless mass-transfer mobility
m_i	molar	molar concentration of i^{th} mobile ion
N_{avo}	mol^{-1}	Avogadro's number, $6.022140857 \times 10^{23}$
N_A and N_I	[-]	number of chiral mesogens and isotropic component
N_T	[-]	total number of lattice site

Symbol	Units	Description
n	[-]	number of segments in the backbone of mesogen
n	[-]	uniaxial director
P	[-]	biaxial director
p_∞	m	pitch
$P_2(\cos(\gamma))$	[-]	second Legendre polynomial of angle between the macromolecules
Q	[-]	quadrupole moment tensor, well-known as **Q**-tensor
S	[-]	macroscopic uniaxial order parameter
U	$j.m^{-3}$	potential of orientation-dependent intermolecular interaction
U_i	j	The net one-body mean field potential of i^{th} rod
U'^{MS}	$j.m^{-3}$	positive constant independent of temperature related to Maier-Saupe parameter
U^{MS}	$j.m^{-3}$	positive constant independent of temperature, Maier-Saupe parameter
U_i^{elc}	j	one-body mean field potential of i^{th} rod for electrostatic interactions (i.e. repulsion and twisting) on the other existing rods in the system
U'^{elc}	$j.m^{-3}$	strength of electrostatic potential (i.e. repulsion and twisting)
U^{elc}	$j.m^{-3}$	strength of electrostatic interaction among the rods (i.e. repulsion and twisting)
u and $\mathbf{u}'$	[-]	The orientations of two rod-like macromolecules
V	m^3	volume of system
W	[-]	net cholesteric potential
x	m	x-component of space
Z_i	[-]	charge number of i^{th} mobile ion
α	[-]	double-layer thickness parameter

Symbol	Units	Description
α_W	[-]	dimensionless constant defined as $\alpha_W = \frac{5}{\phi^*}$where $\phi^*$is the effective volume fraction of tropocollagen
α_c	ml/mg	Unit conversion used for converting the effective volume fraction to concentration in unit of mg/ml
β	j^{-1}	thermal energy
γ	radian	angle between rods
γ_E	[-]	Euler constant, 0.5772
$\boldsymbol{\delta}$	[-]	Kronecker delta
η	[-]	constants determined by normalization of distribution function
θ	radian	polar angle
κ^{-1}	m	Debye screening length
λ_B	m	Bjerrum length
Λ	charge number per meter	linear charge density
μ^o	j	standard particle chemical potential
ξ	m	coherence length or correlation length
$\sigma(\psi(\mathbf{u}))$	[-]	effect of orientational entropy
$\bar{\upsilon}_{AA}$, $\bar{\upsilon}_{IA}$and $\bar{\upsilon}_{II}$	m^3	average excluded-volume between mesogen-mesogen, mesogen-isotropic component and isotropic component- isotropic component.
$\upsilon_A$and υ_I	m^3	molecular volumes of mesogen and isotropic component
φ	radian	azimuthal angle
ϕ	[-]	effective volume fraction of mesogen
χ	[-]	isotropic Flory-Huggins parameter
$\psi(\mathbf{u})$	[-]	single-rod orientational distribution function

4.9 Acknowledgments

SAK acknowledges financial support from the McGill Engineering Doctoral Awards (MEDA) program. This work is supported by a grant from Natural Sciences and Engineering Research Council of Canada (NSERC). ADR is thankful to McGill University for financial support through the James McGill Professorship appointment.

References (Chapter 4)

1. Voet D, Voet JG. Biochemistry. Hoboken, NJ: John Wiley & Sons; 2011.

2. Ashammakhi N, Hasan A, Kaarela O, Byambaa B, Sheikhi A, Gaharwar AK, et al. Advancing Frontiers in Bone Bioprinting. Adv Healthc Mater. 2019.

3. Giraud Guille MM, Mosser G, Helary C, Eglin D. Bone matrix like assemblies of collagen: From liquid crystals to gels and biomimetic materials. Micron. 2005;36(7):602-8.

4. Kurfurst A, Henits P, Morin C, Abdalrahman T, Hellmich C. Bone Ultrastructure as Composite of Aligned Mineralized Collagen Fibrils Embedded Into a Porous Polycrystalline Matrix: Confirmation by Computational Electrodynamics. Front Physics. 2018;6:18.

5. Schwarcz HP, Abueidda D, Jasiuk I. The Ultrastructure of Bone and Its Relevance to Mechanical Properties. Front Physics. 2017;5:13.

6. Levis HJ, Kureshi AK, Massie I, Morgan L, Vernon AJ, Daniels JT. Tissue Engineering the Cornea: The Evolution of RAFT. J Func Biomater. 2015;6(1):50-65.

7. Torbet J, Malbouyres M, Builles N, Justin V, Roulet M, Damour O, et al. Orthogonal scaffold of magnetically aligned collagen lamellae for corneal stroma reconstruction. Biomaterials. 2007;28(29):4268-76.

8. Rastian Z, Putz S, Wang YJ, Kumar S, Fleissner F, Weidner T, et al. Type I Collagen from Jellyfish Catostylus mosaicus for Biomaterial Applications. ACS Biomater Sci Eng. 2018;4(6):2115-25.

9. Boraschi-Diaz I, Wang J, Mort JS, Komarova SV. Collagen Type I as a Ligand for Receptor-Mediated Signaling. Front Physics. 2017;5:11.

10. Perez AG, Nieminen HJ, Finnila M, Salmi A, Pritzker KPH, Lampsijarvi E, et al. Delivery of Agents Into Articular Cartilage With Electric Spark-Induced Sound Waves. Front Physics. 2018;6:7.

11. Poulon F, Chalumeau A, Jamme F, Pallud J, Varlet P, Mehidine H, et al. Multimodal Analysis of Central Nervous System Tumor Tissue Endogenous Fluorescence With Multiscale Excitation. Front Physics. 2018;6:10.

12. Neville AC. Biology of fibrous composites : development beyond the cell membrane. New York, NY, USA: Cambridge University Press; 1993.

13. Mitov M. Cholesteric liquid crystals in living matter. Soft Matter. 2017;13(23):4176-209.

14. Rey AD. Liquid crystal models of biological materials and processes. Soft Matter. 2010;6(15):3402-29.

15. Rey AD, Herrera-Valencia EE. Liquid crystal models of biological materials and silk spinning. 2012;97(6):374-96.

16. Gutierrez OFA, Rey AD. Theory and Simulation of Cholesteric Film Formation Flows of Dilute Collagen Solutions. Langmuir. 2016;32(45):11799-812.

17. Aguilar Gutierrez OF, Rey AD. Biological plywood film formation from para-nematic liquid crystalline organization. Soft Matter. 2017.

18. De Sa Peixoto P, Deniset-Besseau A, Schmutz M, Anglo A, Illoul C, Schanne-Klein M-C, et al. Achievement of cornea-like organizations in dense collagen I solutions: clues to the physico-chemistry of cornea morphogenesis. Soft Matter. 2013;9(47):11241-8.

19. Dehsorkhi A, Castelletto V, Hamley IW, Adamcik J, Mezzenga R. The effect of pH on the self-assembly of a collagen derived peptide amphiphile. Soft Matter. 2013;9(26):6033-6.

20. Khadem SA, Rey AD. Thermodynamic Modelling of Acidic Collagenous Solutions: From Free Energy Contributions to Phase Diagrams. Soft Matter. 2019.

21. Gobeaux F, Belamie E, Mosser G, Davidson P, Panine P, Giraud-Guille MM. Cooperative Ordering of Collagen Triple Helices in the Dense State. Langmuir. 2007;23(11):6411-7.

22. Lovelady HH, Shashidhara S, Matthews WG. Solvent specific persistence length of molecular type I collagen. Biopolymers. 2014;101(4):329-35.

23. Echalier C, Jebors S, Laconde G, Brunel L, Verdie P, Causse L, et al. Sol-gel synthesis of collagen-inspired peptide hydrogel. Mater Today. 2017;20(2):59-66.

24. Bernardino NR, Pereira MCF, Silvestre NM, da Gama MMT. Structure of the cholesteric-isotropic interface. Soft Matter. 2014;10(47):9399-402.

25. Zhou Y, Bukusoglu E, Martinez-Gonzalez JA, Rahimi M, Roberts TF, Zhang R, et al. Structural Transitions in Cholesteric Liquid Crystal Droplets. Acs Nano. 2016;10(7):6484-90.

26. Almeida AP, Canejo JP, Fernandes SN, Echeverria C, Almeida PL, Godinho MHJAM. Cellulose-based biomimetics and their applications. 2018;30(19):1703655.

27. Wulf A. Biaxial order in cholesteric liquid crystals: Phenomenological argument. 1973;59(12):6596-8.

28. Wright DC, Mermin ND. Crystalline liquids: the blue phases. Rev Mod Phys Reviews of Modern Physics. 1989;61(2):385-432.

29. Kamil SM, Bhattacharjee AK, Adhikari R, Menon GI. The isotropic-nematic interface with an oblique anchoring condition. J Chem Phys. 2009;131(17):9.

30. Wincure B, Rey AD. Interfacial nematodynamics of heterogeneous curved isotropic-nematic moving fronts. J Chem Phys. 2006;124(24):13.

31. Wincure B, Rey ADJCM, Thermodynamics. Growth and structure of nematic spherulites under shallow thermal quenches. 2007;19(1):37-58.

32. Wincure B, Rey ADJLC. Computational modelling of nematic phase ordering by film and droplet growth over heterogeneous substrates. 2007;34(12):1397-413.

33. Wincure BM, Rey AD. Nanoscale analysis of defect shedding from liquid crystal interfaces. Nano Lett. 2007;7(6):1474-9.

34. Wincure B, Rey AD. Growth and structure of nematic spherulites under shallow thermal quenches. Continuum Mech Thermodyn. 2007;19(1-2):37-58.

35. PopaNita V, Sluckin TJ, Wheeler AA. Statics and kinetics at the nematic-isotropic interface: Effects of biaxiality. J Phys II. 1997;7(9):1225-43.

36. Mirzaeifard S, Servio P, Rey ADJCES. Molecular Dynamics Characterization of the Water-Methane, Ethane, and Propane Gas Mixture Interfaces. 2019.

37. Mirzaeifard S, Servio P, Rey ADJC, Communications IS. Molecular Dynamics Characterization of Temperature and Pressure Effects on the Water-Methane Interface. 2018;24:75-81.

38. Rey ADJM. Pitch Contributions to the Cholesteric− Isotropic Interfacial Tension. 2000;33(25):9468-70.

39. Wang XJ, Zhou QF. Liquid Crystalline Polymers: World Scientific Publishing Company; 2004.

40. Karttunen M, Vattulainen I, Lukkarinen A. Novel Methods in Soft Matter Simulations: Springer Berlin Heidelberg; 2004.

41. Halperin BI. Theory of dynamic critical phenomena. Phys Today. 2019;72(2):42-3.

42. Zhou Y, Bukusoglu E, Martínez-González JA, Rahimi M, Roberts TF, Zhang R, et al. Structural Transitions in Cholesteric Liquid Crystal Droplets. ACS Nano. 2016;10(7):6484-90.

43. Nyström G, Arcari M, Mezzenga R. Confinement-induced liquid crystalline transitions in amyloid fibril cholesteric tactoids. Nature Nanotechnology. 2018;13(4):330-6.

44. Nos RL, Roma AM, Garcia-Cervera CJ, Ceniceros HD. Three-dimensional coarsening dynamics of a conserved, nematic liquid crystal-isotropic fluid mixture. J Non-Newton Fluid Mech. 2017;248:62-73.

45. Abukhdeir NM, Soulé ER, Rey ADJL. Non-isothermal model for nematic spherulite growth. 2008;24(23):13605-13.

46. Abukhdeir NM, Rey AD. Shape-dynamic growth, structure, and elasticity of homogeneously oriented spherulites in an isotropic/smectic-A mesophase transition. Liquid Crystals. 2009;36(10-11):1125-37.

47. Soule ER, Abukhdeir NM, Rey AD. Thermodynamics, Transition Dynamics, and Texturing in Polymer-Dispersed Liquid Crystals with Mesogens Exhibiting a Direct Isotropic/Smectic-A Transition. Macromolecules. 2009;42(24):9486-97.

48. Gennes PGd, Prost J. The Physics of Liquid Crystals: Clarendon Press; 1995.

49. Doi M. Soft Matter Physics: OUP Oxford; 2013.

50. Matsuyama A, Kato T. Theory of binary mixtures of a flexible polymer and a liquid crystal. J Chem Phys. 1996;105(4):1654-60.

51. Odijk T. Theory of lyotropic polymer liquid crystals. Macromolecules. 1986;19(9):2313-29.

52. Drwenski T, Dussi S, Hermes M, Dijkstra M, Roij Rv. Phase diagrams of charged colloidal rods: Can a uniaxial charge distribution break chiral symmetry? 2016;144(9):094901.

53. Matsuyama A. Biaxiality of cholesteric phases in rod-like polymer solutions. Liquid Crystals. 2015;42(4):423-9.

54. Matsuyama AJLC. Biaxial nematic phases in rod/liquid crystal mixtures. 2011;38(6):729-36.

55. Matsuyama AJMC, Crystals L. Biaxial Nematic Phase in Mixtures of a Liquid Crystal and a Rodlike Polymer. 2011;540(1):42-9.

56. Stroobants A, Lekkerkerker HNW, Odijk T. Effect of electrostatic interaction on the liquid crystal phase transition in solutions of rodlike polyelectrolytes. Macromolecules. 1986;19(8):2232-8.

57. Mirzaeifard S, Abel SM. Confined semiflexible polymers suppress fluctuations of soft membrane tubes. Soft Matter. 2016;12(6):1783-90.

58. Matus Rivas OM, Rey AD. Effects of Sodium and Magnesium Cations on the Aggregation of Chromonic Solutions Using Molecular Dynamics. The Journal of Physical Chemistry B. 2019;123(7):1718-32.

59. Rivas OMM, Rey AD. Molecular dynamics on the self-assembly of mesogenic graphene precursors. Carbon. 2016;110:189-99.

60. Roohnikan M, Toader V, Rey A, Reven L. Hydrogen-Bonded Liquid Crystal Nanocomposites. Langmuir. 2016;32(33):8442-50.

61. Bagnani M, Nystrom G, De Michele C, Mezzenga R. Amyloid Fibrils Length Controls Shape and Structure of Nematic and Cholesteric Tactoids. Acs Nano. 2019;13(1):591-600.

62. Matsuyama A, Kato T. Theory of binary mixtures of a flexible polymer and a liquid crystal. The Journal of chemical physics. 1996;105(4):1654-60.

63. Soule ER, Rey AD. A good and computationally efficient polynomial approximation to the Maier-Saupe nematic free energy. Liquid Crystals. 2011;38(2):201-5.

64. De Luca G, Rey AD. Chiral front propagation in liquid-crystalline materials: Formation of the planar monodomain twisted plywood architecture of biological fibrous composites. Physical review E, Statistical, nonlinear, and soft matter physics. 2004;69(1 Pt 1):011706.

65. Gurevich S, Soule E, Rey A, Reven L, Provatas N. Self-assembly via branching morphologies in nematic liquid-crystal nanocomposites. Physical Review E. 2014;90(2).

66. Das SK, Rey AD. Texture formation under phase ordering and phase separation in polymer-liquid crystal mixtures. J Chem Phys. 2004;121(19):9733-43.

67. De Luca G, Rey AD. Monodomain and polydomain helicoids in chiral liquid-crystalline phases and their biological analogues. Eur Phys J E The European Physical Journal E. 2003;12(2):291-302.

68. De Luca G, Rey AD. Theory and simulation of texture transformations in chiral systems: Applications to biological fibrous composites. In: Mather PT, Broer DJ, Bunning TJ, Walba DM, Zentel R, editors. Advances in Liquid Crystalline Materials and Technologies. Materials Research Society Symposium Proceedings. 7092002. p. 141-6.

69. Soulé ER, Abukhdeir NM, Rey ADJM. Thermodynamics, transition dynamics, and texturing in polymer-dispersed liquid crystals with mesogens exhibiting a direct isotropic/smectic-A transition. 2009;42(24):9486-97.

70. Khabibullaev PK, Gevorkyan EV, Lagunov AS. Rheology of Liquid Crystals: Allerton Press; 1994.

71. Rey AD. Theory and Simulation of Gas Diffusion in Cholesteric Liquid Crystal Films. Molecular Crystals and Liquid Crystals Science and Technology Section A Molecular Crystals and Liquid Crystals. 1997;293(1):87-109.

72. Fletcher NH. SIZE EFFECT IN HETEROGENEOUS NUCLEATION. J Chem Phys. 1958;29(3):572-6.

73. Sear RP. Nucleation: theory and applications to protein solutions and colloidal suspensions. J Phys-Condes Matter. 2007;19(3):28.

74. Rey AD, Servio P, Herrera-Valencia EE. Bioinspired model of mechanical energy harvesting based on flexoelectric membranes. Physical Review E. 2013;87(2):12.

75. Das SK, Rey AD. Computational thermodynamics of multiphase polymer–liquid crystal materials. Computational Materials Science. 2006;38(2):325-39.

76. Das SK, Rey AD. Magnetic Field-Induced Shape Transitions in Multiphase Polymer-Liquid Crystal Blends. Macromolecular Theory and Simulations. 2006;15(6):469-86.

77. Dierking I. Textures of Liquid Crystals: Wiley-VCH; 2003.

78. Yang DK. Fundamentals of Liquid Crystal Devices: Wiley; 2014.

79. Ondriscrawford R, Boyko EP, Wagner BG, Erdmann JH, Zumer S, Doane JW. MICROSCOPE TEXTURES OF NEMATIC DROPLETS IN POLYMER DISPERSED LIQUID-CRYSTALS. J Appl Phys. 1991;69(9):6380-6.

80. Das SK, Rey AD. Colloidal crystal formation via polymer-liquid-crystal demixing. Europhys Lett. 2005;70(5):621-7.

81. Sec D, Porenta T, Ravnik M, Zumer S. Geometrical frustration of chiral ordering in cholesteric droplets. Soft Matter. 2012;8(48):11982-8.

4.10 Supplementary Information

4.10.1 Sequential Steps of Self-assembly Simulations

In this subsection we provide sufficient and necessary details on the computational methodology and software used in this work. The commercial and open source software are standard in scientific computations. Figure 4-6 depicts all steps carried out to simulate the liquid-crystalline self-assembly of tropocollagen for a shallow quench into biphasic zone.

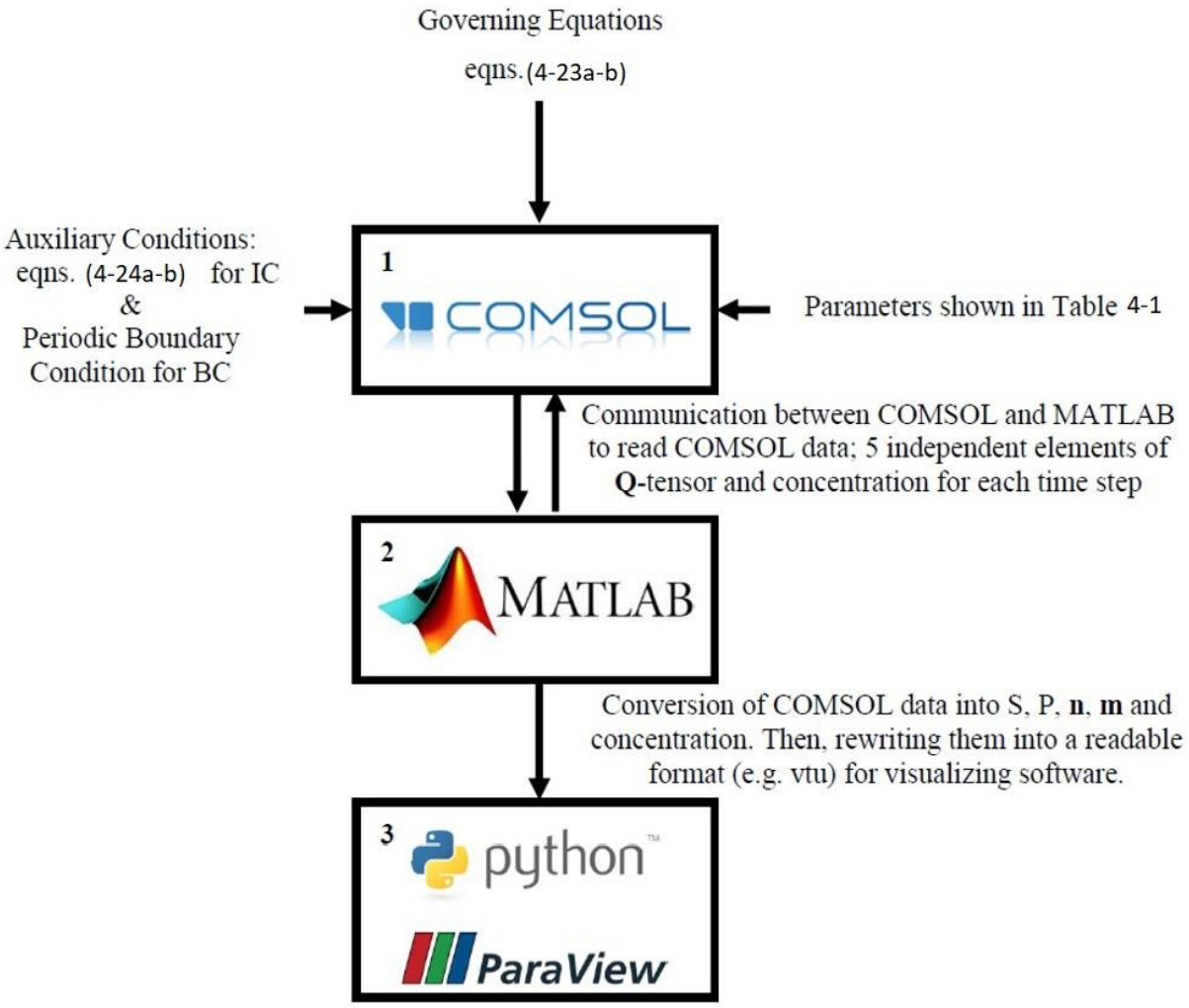

Figure 4-6. Sequential steps of numerical solving of governing equations, data processing and data visualization.

Step 1.

The governing equations (4-23a-b), the auxiliary conditions described in section 4.5.6, and the simulation parameters summarized in Table 4-1 are implemented in the General PDE solver of COMSOL Multiphysics 5.3a. The results of COMSOL simulation—we call it COMSOL data— are 5 independent elements of **Q**-tensor and collagen concentration as function of time and space.

Step 2.

Having finished simulations in COMSOL, MATALB and COMSOL are integrated to transfer the COMSOL data onto MATLAB for next processing. Thereafter, based on information given in section 4.5.1, the COMSOL data are converted to S, P, **n**, **m** and collagen concentration as function time and space. Finally, the results must be rewritten in readable format for the sake of visualization. The Unstructured Grid (*.vtu) format was used in this study, and a sample of this data type is:

Sample of vtu file describing values of S, P, **n**, **m** and concentration:

```
<?xml version="1.0" encoding="UTF-8"?>
<VTKFile type="UnstructuredGrid" version="0.1" byte_order="LittleEndian">
<UnstructuredGrid>
<Piece NumberOfPoints="..." NumberOfCells="...">
<PointData>
<DataArray type="Float64" Name="S" NumberOfComponents="1" Format="ascii">
...
</DataArray>
<DataArray type="Float64" Name="P" NumberOfComponents="1" Format="ascii">
...
</DataArray>
<DataArray type="Float64" Name="UniaxialDiraction" NumberOfComponents="3" Format="ascii">
...     ...     ...
</DataArray>
<DataArray type="Float64" Name="BiaxialDiraction" NumberOfComponents="3" Format="ascii">
...     ...     ...
</DataArray>
<DataArray type="Float64" Name="Concentration" NumberOfComponents="1" Format="ascii">
...
</DataArray>
</PointData>
<CellData/>
<Points>
<DataArray type="Float64" NumberOfComponents="3" Format="ascii">
...     ...     ...
</DataArray>
</Points>
<Cells>
<DataArray type="Int32" Name="connectivity" Format="ascii">
...     ...     ...
</DataArray>
<DataArray type="Int32" Name="offsets" Format="ascii">
...     ...     ...     ...
</DataArray>
<DataArray type="UInt8" Name="types" Format="ascii">
............
</DataArray>
```

```
</Cells>
</Piece>
</UnstructuredGrid>
</VTKFile>
```

Step 3.

ParaView and Python were used together to visualize the obtained vtu files—S, P, **n**, **m** and concentration data.

4.10.2 Technical Details of Numerical Simulations

We used the General PDE solver of COMSOL Multiphysics 5.3a which is based on Generalized Finite Element Method with quadratic Lagrangian basis functions and standard Gaussian quadrature methods. For having an acceptable spatial resolution, we considered at least 50 elements per pitch (i.e. equivalently around 10^4 triangular elements). Time steps were carried out by the Backward Differentiation Formula with variable order (1^{st} to 5^{th}) to attain the specified relative tolerance set at 10^{-5}. Mesh independency, convergence, accuracy, and stability were checked using standard techniques. Furthermore, the computational time is highly affected by the mass transfer equation due to its nonlinearity and high order. Typically, the memory usage ranged from 10 to 14 GB and the CPU time was approximately around 12 hours by use of a PC with Core i7 and 16 GB RAM.

We note that the values of parameters used in this study are summarized in Table 4-1, also readers are referred to references[1-5] for further information about the mesoscopic parameters in self-assembly simulations.

References of Supporting Information (Chapter 4)

1. Khadem SA, Rey AD. Thermodynamic Modelling of Acidic Collagenous Solutions: From Free Energy Contributions to Phase Diagrams. Soft Matter. 2019.

2. Gobeaux F, Belamie E, Mosser G, Davidson P, Panine P, Giraud-Guille MM. Cooperative Ordering of Collagen Triple Helices in the Dense State. Langmuir. 2007;23(11):6411-7.

3. De Luca G, Rey AD. Monodomain and polydomain helicoids in chiral liquid-crystalline phases and their biological analogues. Eur Phys J E The European Physical Journal E. 2003;12(2):291-302.

4. De Luca G, Rey AD. Chiral front propagation in liquid-crystalline materials: Formation of the planar monodomain twisted plywood architecture of biological fibrous composites. Physical review E, Statistical, nonlinear, and soft matter physics. 2004;69(1 Pt 1):011706.

5. Gurevich S, Soule E, Rey A, Reven L, Provatas N. Self-assembly via branching morphologies in nematic liquid-crystal nanocomposites. Physical Review E. 2014;90(2).

Chapter 5. Nucleation and growth of cholesteric collagen tactoids: A time-series statistical analysis based on integration of direct numerical simulation (DNS) and long short-term memory recurrent neural network (LSTM-RNN)

5.1 Preface

Motivated by lack of knowledge about the nucleation-and-growth zone in the biphasic zone of the collagen phase diagram, we employ the governing equations developed in Chapter 4 to determine and exhaustively characterize the nucleation-and-growth zone in the collagen phase diagram developed in Chapter 3. Although the Direct Numerical Simulation (DNS) of self-assembly is considerably accurate, DNS is computationally demanding. The challenges associated with computational cost are addressed by proposing a hybrid approach based on a combination of DNS in conjunction with a machine learning technique. Because the characterizations are computationally expensive, wide-range correlations corresponding to the characterizations are developed by the use of classical and symbolic regressions. Additionally, the physical origin behind the nucleation and growth mechanism is revealed in detail through free energy analyses.

5.2 Graphical Abstract

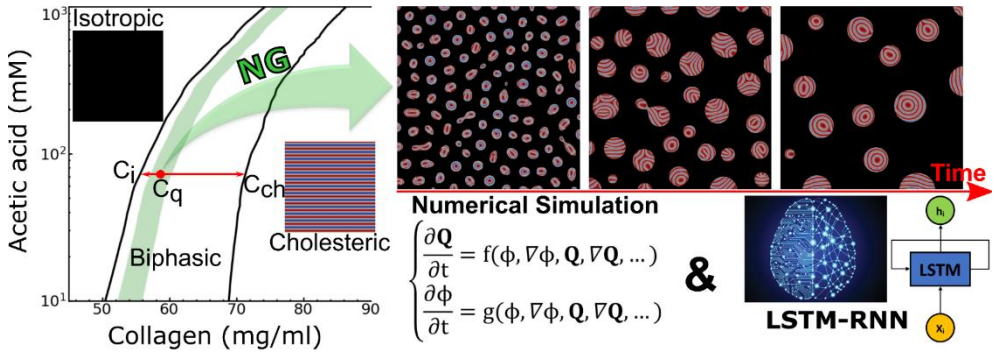

5.3 Abstract

Hypothesis. Liquid-crystalline phase separation by nucleation and growth (NG) is a crucial step in the formation of collagen-based biomaterials. However, the fundamental mechanisms are not completely understood for chiral lyotropic colloidal mesogens such as collagen.

Methodology. To capture the dynamics of NG under a quenching process into the biphasic equilibrium zone, we use direct numerical simulation based on the time-dependent Ginzburg-Landau model allowing minimization of the total free energy comprised of five key contributions: phase separation (Flory-Huggins), ordering (Landau-de Gennes), chiral orientational elasticity (Frank-Oseen-Mermin), interfacial and coupling effects. LSTM-RNN

is applied as a surrogate model to greatly enrich the results. Significant correlations are established using Symbolic Regression.

Findings. We quantify the NG boundaries existing in the collagen phase diagram that has recently been developed and validated by our thermodynamic model[1]. We characterize the three NG stages (induction, nucleation, and coarsening) in terms of tactoids' shape, morphology, growth laws, and population across the NG zone. Wide-range generic correlations are developed, revealing the quench depth dependence of NG characteristics and connecting the sequential NG stages. We confirm experimental observations on time-dependent growth law exponent changes from an initial $n\approx0.5$ for the mass transfer limited regime to $n\approx1$ for the volume-driven phase ordering regime upon increasing quench depth during the nucleation period and having exclusively a value of $n\approx0.5$ for the coarsening period regardless of quench depth. We lastly uncover the underlying physics behind the NG phenomena.

5.4 Keywords

Biological chiral lyotropic liquid crystals, Biomimetic collagen-based biomaterials, Liquid-crystalline self-assembly, Chiral nematic tactoids, Cholesteric nucleation, growth and coarsening, Universal growth laws, Uphill diffusion, Time-dependent Ginzburg-Landau model, Long Short-Term Memory Recurrent Neural Network, Symbolic Regression

5.5 Introduction

Collagen-based tissues, ubiquitously found in both soft and hard humans' organs[2], possess enhanced structure-related properties such as the mechanical properties of bone, tendon, and teeth[3-5]. Owing to the necessity of having these materials artificially available and the fact that collagen as a primary precursor is readily accessible through both mammalian and non-mammalian resources[6], a significant amount of research has been conducted to tailor, optimize and control the fabrication of the versatile collagen-based biomaterials, in particular artificial bone[7-10] and cornea[11,12].

Phase separation is an indispensable and non-trivial part in material processing and interfacial science, particularly for structural material synthesis and design because the dynamics of phase separation (liquid/liquid demixing) is inextricably coupled with the dynamics of phase transition (disorder/ordered transformation), involving a variety of

mesoscopic phenomena such as interface formation, bulk and surface elasticities, bending and torsion curvatures, surface anchoring, and more[13-20].

The concentration-driven processing of collagen-based biomaterials starts from a dilute acidic collagen dispersion in which collagen fibers do not have spatial or orientational ordering, a state called isotropic phase (I). Through the water removal process, the isotropic phase is gradually concentrated and transformed into an ordered phase which is known as chiral nematic or cholesteric phase (N^*). In this liquid-crystalline phase where the collagen dispersion retains both the fluidity of a viscous liquid and the anisotropy of crystals, the primary structural motif of collagen-based biomaterials is formed[7,21-23]. Hence, the fundamental understanding of I/N^* phase separation and chiral ordering in colloidal collagen dispersions is of paramount importance, paving the way for the science-based fabrication of high-performance biomaterials. It should further be noted that many of biological lyotropic LCs (e.g. collagen, β-lactoglobulin amyloid, and cellulose nanocrystals) fall into "colloidal" LCs because their fibers size are considerably larger than that of widely-used thermotropic mesogens like 5CB (e.g. the average length of collagen fibers and 5CB are >300nm and ~1.8nm, respectively)[1,5,24-28]. Notwithstanding the above-mentioned importance, except for a few studies[29,30], the coupling of phase separation and ordering in biological chiral lyotropic LCs have not been adequately addressed as in thermotropic LCs[31-37].

Quenching into the biphasic thermodynamic equilibrium zone may result in phase separation via two well-established mechanisms: nucleation and growth (NG) or spinodal decomposition. Through NG mechanism, drops (referred here as tactoids even if spherically shaped) nucleate where the energy fluctuation overcomes the energy barrier and then go through the coarsening stage, known as Ostwald ripening. Over time, phase separation leads to the formation of chiral tactoids coexisting with the continuous isotropic phase. In contrast, when the isotropic phase undergoes bicontinuous spinodal decomposition (BSD), the unstable isotropic phase unmixes into two phases characterized by interconnected domains[38,39]. There is also the droplet spinodal decomposition (DSD) typically in between the NG and bicontinuous. The focus and scope of the present study is the NG mechanism that generates two-dimensional tactoidal cholesteric drops in chiral lyotropic mesophases based on acidic aqueous solutions of collagen. The main objectives of this work are:

1. Establish the NG zone in the equilibrium thermodynamic phase diagram of acidic collagen solutions, whose binodal lines were validated experimentally in our previous work[1]. Identifying this zone is a primordial task for any collagen processing platform.
2. Characterization of the three NG stages (induction, nucleation, and coarsening) in terms of tactoids' distribution, shape, morphology, growth laws, population, and more across the NG zone. Establishing the quench depth dependence of these global and local quantities associated with the NG using accurate computing generates the broad data to integrate phase separation and chiral phase ordering.
3. Development of wide-range generic correlations for induction time, nucleation duration, growth laws, and tactoids population distribution function.
4. Characterizing and elucidating the fundamental NG mechanisms of collagen chiral tactoids growth in the isotropic matrix phase.

To achieve the objectives, we apply two dimensional Direct Numerical Simulation (DNS) to simulate quenches into the biphasic zone of the collagen phase diagram that we have recently obtained by developing, implementing, and validating a collagen thermodynamic model[1]. The DNS used in this study is based on the time-dependent Ginzburg-Landau relaxation model, allowing for the minimization of the total free energy during the spontaneous quenching process[40]. Despite the significant computational complexities, to find the realistic insights into the NG of collagen tactoids, we retain five key contributions in the total Helmholtz free energy associated with phase separation, chiral phase ordering, bulk orientational elasticity, interfacial energies, and coupling effects. The first three contributions are described by well-established continuum theories as follows; Flory-Huggins, Landau-de Gennes, and Frank-Oseen-Mermin, respectively[41].

Artificial Neural Network (ANN) modeling has recently been used in a wide range of science and engineering applications. ANNs are an effective technique to quickly provide an accurate estimation of target quantities in both experimental and theoretical fields[42-46]. On the other hand, the dynamic simulation of NG by DNS is computationally expensive owing to the need for High-Performance Computing hardware for long run times and more importantly for being intrinsically a multiscale problem, with spatial scales ranging from nanoscale for defect cores and interfaces, to micron ranges for tactoids, to hundreds of microns for the confinement geometry. Likewise, to resolve the fast and slow time scales inherent in chiral ordering, even adaptive time-stepping is insufficient to achieve tractable schemes. To tackle these computational challenges, we employ a combination of DNS with Long Short-Term Memory

(LSTM) Recurrent Neural Networks (RNNs) for some simulations to significantly shorten the run time. After collecting the quench results by either DNS or combination of DNS and LSTM-RNN, we employ symbolic and classical regressions to develop correlations describing the essential quantities of NG including induction time, nucleation period, tactoid population peak, growth laws, and tactoids' population statistics.

The paper is organized as follows. In section 5.6, the modeling and simulation methodology is explained in detail. Section 5.7 discusses the results. Section 5.7.1 characterizes the NG zone in the collagen biphasic zone. Sections 5.7.2-5.7.4 analyzes the three stages of NG; induction, nucleation, and coarsening, respectively. Section 5.7.5 discusses the mechanisms behind the quench depth dependence of NG characteristics. Finally, section 5.7.6 reveals the fundamental physics driving the growth law exponents.

5.6 Methodology

5.6.1 Direct numerical simulation (DNS); energy landscape and governing equations

The total dimensionless free energy $\tilde{F}_{net}$ for chiral LCs dispersed in a small-sized solvent consists of five contributions: (1) isotropic demixing $\tilde{f}_{iso}$, (2) I/N* phase transition $\tilde{f}_h$, (3) elasticity $\tilde{f}_e$, (4) the thermodynamic penalty associated with interface formation $\tilde{f}_{cg}$, and (5) the coupling effect, $\tilde{f}_c$ [1,41,47,48]:

$$\tilde{F}_{net} = \int_{\tilde{V}} \left(\tilde{f}_{iso} + \tilde{f}_h + \tilde{f}_e + \tilde{f}_{cg} + \tilde{f}_c\right) d\tilde{V} \qquad (5-1)$$

$$\tilde{f}_{iso} = \frac{\phi \ln(\phi)}{n} + (1-\phi)\ln(1-\phi) + \chi\phi(1-\phi) \qquad (5-1a)$$

$$\tilde{f}_h = \frac{a(\phi)}{2}\mathrm{Tr}(\mathbf{Q}^2) - \frac{b(\phi)}{3}\mathrm{Tr}(\mathbf{Q}^3) + \frac{c(\phi)}{4}\left(\mathrm{Tr}(\mathbf{Q}^2)\right)^2 \qquad (5-1b)$$

$$\tilde{f}_e = \frac{1}{2}\left(\frac{\xi}{h_0}\right)^2 \left[\left[\tilde{\nabla} \times \mathbf{Q} + 4\pi\left(\frac{h_0}{p_\infty}\right)\mathbf{Q}\right]^2 + \left(\frac{L_2}{L_1}\right)\left[\tilde{\nabla}\cdot\mathbf{Q}\right]^2\right] \qquad (5-1c)$$

$$\tilde{f}_{cg} = \frac{1}{2}\tilde{L}_\phi\left(\tilde{\nabla}\phi\right)^2 \qquad (5-1d)$$

$$\tilde{f}_c = \tilde{L}_{\phi-\mathbf{Q}}\left(\tilde{\nabla}\phi\right)\cdot\left(\tilde{\nabla}\cdot\mathbf{Q}\right) \qquad (5-1e)$$

Eq. (5-1a) describes the Flory-Huggins theory that accounts for mixing free energy of constituents. ϕ, n and χ are the effective volume fraction of collagen fibers, number of segments on the collagen backbone, and the Flory–Huggins interaction parameter, respectively. The first

two terms and last term in eq. (5-1a) take into account the translational entropy and enthalpic contribution, respectively.

Eq. (5-1b) is known as the phenomenological Landau-de Gennes (LdG) theory which describes the phase transition. Tr( )is trace operation. $a(\phi)$,$b(\phi)$and $c(\phi)$ stand for the LdG coefficients and their concentration dependence has recently been quantified for I/N* transformation of collagen in [1][1]. **Q** is a second rank symmetric traceless tensor whose eigenvalues describe orientational order and whose eigenvectors describe the average fiber orientation. For defect-free mono-domain equilibrium cholesteric phases, the **Q**-tensor is biaxial, spatially periodic, and possesses handedness. Owing to the extremely small value of biaxiality for needle-like fibers forming the cholesteric phase, the biaxiality effect is neglected in this study. The spatial periodicity is the pitch p_∞ and the handedness is left or right according to the twist sense of the director **n** (main eigenvector of **Q**). For processes associated with length scales much larger than p_∞, the N* behaves as a layered material.

To consider the energy content of fibers' configuration the Frank-Oseen-Mermin (FOM) theory, eq. (5-1c), is employed. ξ, h_0, and L_i denote coherence length, an arbitrary macro-meter value representing the sample size, and Frank elastic constants, respectively. $\tilde{L}_\phi$ and $\tilde{L}_{\phi-\mathbf{Q}}$ stand for interfacial and coupling constants, respectively. Note that the tilde symbol indicates that the quantity is dimensionless. For detailed information on the formulation of these contributions, see refs [1,39,41,47-54].

NG is a spontaneous process through which the total free energy of the system $\tilde{F}_{net}$ is minimized. To describe this thermodynamically-driven phenomenon, we use the time-dependent Ginzburg-Landau relaxation model which captures the coupled spatio-temporal evolution of the conserved order parameter (OP) ϕ and the non-conserved order parameter **Q**. Thus, the corresponding mixed OP model read[21,40,41,47,55-59]

$$\frac{\partial \mathbf{Q}}{\partial \tilde{t}} = -\frac{1}{\left(1-\frac{3}{2}\mathrm{Tr}(\mathbf{Q}^2)\right)^2}\left(\frac{\delta \tilde{F}_{net}}{\delta \mathbf{Q}}\right)^{[s]} \qquad (5-2a)$$

$$\frac{\partial \phi}{\partial \tilde{t}} = \tilde{M}_\phi \tilde{\nabla}\cdot\left([\mathbf{I}+\mathbf{Q}]\cdot\tilde{\nabla}\frac{\delta \tilde{F}_{net}}{\delta \phi}\right) \qquad (5-2b)$$

where $\widetilde{M}_{\phi}$ is the constant dimensionless relative mobility constants of mass diffusion to orientational relaxation. $\Delta\tilde{F}_{net}/\delta\mathbf{Q}$ and $\delta\tilde{F}_{net}/\delta\phi$ are the functional derivatives with respect to $\mathbf{Q}$ and ϕ, respectively. [s] is the symmetric traceless operator defined as $\mathbf{T}^{[s]} = \frac{(\mathbf{T}+\mathbf{T}^{t})}{2} - \frac{Tr(\mathbf{T})\boldsymbol{\delta}}{3}$ in which $\boldsymbol{\delta}$ is the second rank identity tensor. The actual time, t, is scaled by $t=\tilde{t}\frac{\eta}{ck_BT}$where η, k_B, and T stand for rotational viscosity coefficient, Boltzmann constant, and absolute temperature, respectively. In this model, we neglect bulk flows that may be generated by couplings between the **Q**-tensor velocity $\frac{\partial\mathbf{Q}}{\partial t}$ and translational flow velocity **v** and its gradients $\nabla\mathbf{v}$ during NG[59-63]. The extremely large viscosity of cholesteric permeation flow[64,65], the large rotational viscosity of collagen, the essentially vanishing Ericksen number (flow-to-elasticity ratio)[66], the solid-like behavior along the cholesteric helix axis[67], and an a posteriori validation of the predictions with experimental data justify neglecting self-generated transient bulk convection.

The governing equations, eqs.(5-1 and 5-2), are subjected to the following auxiliary conditions.

$$\text{Initial Conditions:}\begin{cases}\mathbf{Q}(\tilde{t}=0) = \Xi \\ \phi(\tilde{t}=0) = \phi_q + \Phi\end{cases} \qquad (5-3)$$

where ϕ_q is the volume fraction of fibers at the quenching point, Ξ is an arbitrary traceless tensor that represents infinitesimal white noise, and similarly, Φ stands for a scaler white noise[2]. The initial conditions, given in eq.(5-3), indicate that fibers are initially configured without any correlation, and concentration is then quenched into the NG zone. In other words, the system is initially isotropic, t<0. Thereafter, quench into the NG zone takes place at t=0, meaning that while fibers are still in the isotropic phase, $\mathbf{Q}(\tilde{t}=0) = \Xi$ (i.e. no orientational order), the dispersion is concentrated to $\phi(\tilde{t}=0) = \phi_q + \Phi$ where isotropic/cholesteric phases can coexist and gradually be separated via the NG mechanism as time elapses. Regarding the boundary conditions, we use periodic boundary conditions for the **Q**-tensor and the closed-system thermodynamic restriction for mass transfer, ϕ, on the boundaries.

The model given in eqs.(5-1, 5-2) consists of six-coupled nonlinear partial differential equations that describe the spatio-temporal behavior of the six component solution vector: five independent components of the symmetric traceless tensor order parameter **Q**(**x**,t) and the scalar collagen concentration ϕ (**x**,t) . The independent variables are time (t) and the spatial coordinates (**position vector x**). In this work we restrict the physical space to two dimensions

and the position vector in rectangular coordinates is **x**=(x,y). In short, the solution vector for the model used in this paper has six components that depend on time "t" and two spatial coordinates: "x" and "y". In this study, we carry out two dimensional simulations owing to two reasons; (1) the two-dimensional simulations are capable of revealing the underlying physics and accordingly have been widely used in literature[31,33,68-70], (2) the three-dimensional simulations of the NG processes on a statistically large space require unavailable high-performance supercomputers running for enormously long times. As can be seen in the Supplementary Note S1, the two-dimensional simulations studied in the present work are computationally demanding; obviously, three-dimensional simulations require much more computational power than the two-dimensional ones. To obtain reliable statistical results we solve the governing equations on a realistic 500μmx500μm square domain representing experimental samples used for the long pitch length biological LCs[29,71-73]. The two-dimensional DNS is executed using the finite element technique implemented in the General PDE solver of COMSOL Multiphysics 5.3a on our in-house supercomputer (see the Supplementary Note S1 for details of DNS; including the standard material properties used in this study).

5.6.2 Characteristic length

The tactoids population and tactoids area are obtained as two time-series using Image Processing explained in the Supplementary Note S1. Having these time-series, the characteristic length, $\langle L(\tilde{t})\rangle$, is thus computed by[37,74]

$$\langle L(\tilde{t})\rangle = 2\sqrt{\frac{\langle A(\tilde{t})\rangle}{\pi}} \qquad (5-4)$$

where $\langle A(\tilde{t})\rangle$indicates the arithmetic average of the tactoids area at a given time, $\tilde{t}$. Since this study focusses on the NG of cholesteric tactoids embedded in the isotropic phase, the characteristic length $\langle L(\tilde{t})\rangle$ represents the time-dependent average tactoids diameter.

5.6.3 Surrogate model

An alternative to address computationally expensive and hardly tractable simulations is to engineer a fast surrogate model predicting the simulation results[75-78]. As explained below, the

most computationally demanding stage of the NG process is the coarsening period, which is the last stage in this process (see sections 5.7.2-5.7.4). For this reason, the effective surrogate model is one that enables the forecasting of the target time-series (i.e. tactoids population and characteristic length) for a major interval of the coarsening period.

In this regard, as can be seen in Figure 5-1(a), the entire time-series of each target quantity is split into two segments, an early time-series, and a remaining time-series. The entire time-series contains all NG stages of the material transformation process: induction, nucleation, and coarsening until the steady or long time quasi-steady state is reached. The early time-series captures induction, nucleation, and the early coarsening; hence, the remaining time-series is the remainder obtained by subtracting the early time-series from the entire time-series; see Figure 5-1(a). In addition, provided that DNS is used, acquisition of the early time-series requires less computational time than that of the remaining time-series. The effective strategy for fast acquisition of the entire time-series of a target quantity is thus based on a hybrid approach as follows: (1) DNS computes the early time-series which is relatively computationally inexpensive, and (2) the surrogate model deploys the early time-series as the dynamical history of the target quantity in order to rapidly forecast the future of the target quantity (i.e. the remaining time-series); see Figure 5-1(b). The proposed hybrid approach significantly accelerates the NG time-series acquisition owing to the fact that the remaining time-series of the target quantity is rapidly forecasted by the surrogate model in lieu of being computed by the time-consuming DNS.

In general, ANNs are suitable to be considered as the surrogate model in data-driven problems[79-83]. To complete the strategy of fast data acquisition, we thus rely on ANNs that meet the surrogate model's requirements discussed above. The surrogate model required in this study should be capable of time-series forecasting, meaning that the surrogate model learns the dynamical behavior of target quantity from its history (i.e. the early time-series) and then forecasts the future of time-series (i.e. the remaining time-series); see Figure 5-1. In view of time-series forecasting, it has been shown that RNNs often outperform feed-forward neural networks because RNNs benefit from both feed-back and feed-forward connections, leading to memory-based networks[84-89]. Furthermore, LSTM is a special RNN architecture that can effectively deal with the vanishing gradient problem[88,90-93]. We, therefore, selected LSTM-RNNs as the surrogate models and implemented the network models in Python using the Keras library[94]. The LSTM-RNN is trained using the early time-series and then the trained network

is exceptionally capable of predicting the remaining time-series; see Figure 5-1. Readers are referred to the Supplementary Note S2 for further implementation details.

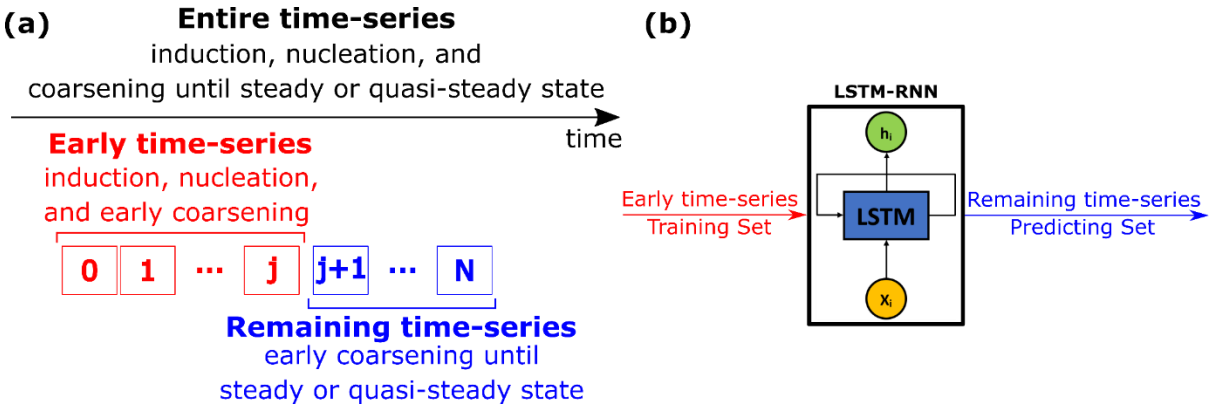

Figure 5-1. (a) Schematic illustration of the terminologies used in this study; squares indicate a time-series of each target quantity (i.e. tactoids population or characteristic length). (b) The input/output of the LSTM-RNN used as a fast surrogate model. The LSTM-RNNs are trained by the early time-series of target quantities and then the trained networks forecast the future of time-series (i.e. remaining time-series).

5.6.4 Symbolic regression

The Symbolic Regression, which is also termed as Symbolic Data Mining using Genetic Programming, is the standard technique to explore the mathematical model that best fits data. In this technique, the essence of the search engine is based on the Genetic Algorithm[95]. In this work, we rely on our in-house package[96] which is significantly faster than conventional Genetic Programming. The operations used to find the tactoids' population are [+, -, *, /, exp]. The "exp" was included in the operations set because "exp" in conjunction with the four basic mathematical operations can accurately produce a variety of increasing/decreasing and convex/concave functions. Moreover, the standard hyperparameters were chosen for the evolutionary optimizer; mutation (0.1), crossover (0.8), and migration (0.1)—readers are referred to reference [96][96] for further information regarding the implementation.

5.7 Results and discussions

5.7.1 Cholesteric tactoids zone in Collagen's equilibrium thermodynamic phase diagram

The miscibility boundaries or binodal lines in the phase diagram of aqueous acidic collagen dispersions are required to predict and characterize the NG of cholesteric tactoids without the

use of trial and error. We have recently developed and validated this phase diagram[1]. Based on the phase diagram and the phase separation regimes (NG, DSD, and BSD) obtained at various quench depths in the biphasic zone, the NG regime existing therein is then identified, as shown by the green zone in Figure 5-2. In the NG regime, multiple chiral nuclei unconditionally nucleate, grow and coarsen in the continuous isotropic phase. This spontaneous phenomenon takes place as the chiral microstructure emergence lowers system energy, meaning that the cholesteric phase is low-energy phase while the isotropic phase is higher. Moreover, the chiral microstructures mainly form rounded shapes which eventually end up as circle-like shapes from a 2D perspective. As explained in the following sections, this study focuses on the NG processes.

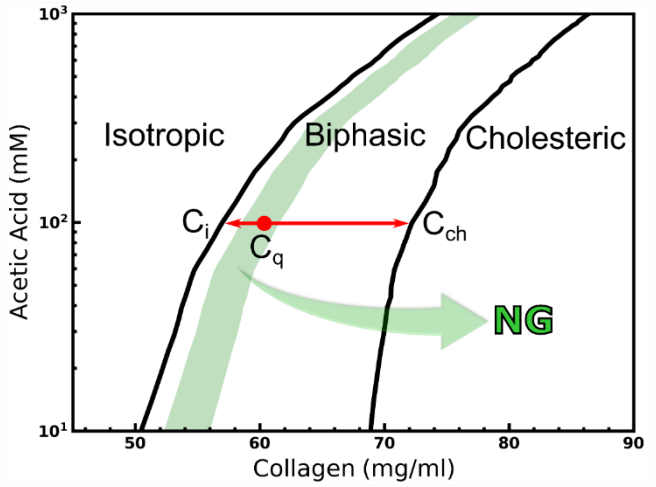

Figure 5-2. The acidic aqueous collagen solution phase diagram in terms of acetic acid (mM) versus collagen concentration (mg/ml). The left and right solid black curves represent the lower and upper binodal curves denoted by Ci and Cch, respectively. The green zone is a computed estimate where the NG regime exists. The red circle is an arbitrary quench point inside the NG zone (green zone), for which the phase separation follows the red arrows. Regardless of where the quenching point is, phase separation leads to two phases; collagen-lean and collagen-rich phases which yield a continuous isotropic matrix phase and dispersed cholesteric tactoids, respectively.

The emergence of cholesteric tactoids in the continuous isotropic phase takes place near the lower binodal (isotropic) curve. Furthermore, this behavior has lately been reported for chromonic LC[97-99]. To quantify the quench depth, we define the quench percentage as

$$\eta_q = \frac{(C_q - C_i)}{(C_{ch} - C_i)} \times 100 \qquad (5-5)$$

where C_q, C_i, and C_h are concentrations of the quenching point, lower and upper binodal boundaries, respectively. Hence, η_q=0% and η_q=100% exhibit the isotropic phase (lower binodal curve) and the fully cholesteric phase (upper binodal curve), respectively. We performed an exhaustive DNS to accurately characterize the biphasic zone, as opposed to solving thermodynamic instability thresholds, as the former proved tractable and accurate. Approximately, 0%<η_q<10% represents the metastable isotropic phase. Quenching into this zone does not result in any phase separation and ordering as the maximum concentration fluctuation therein can't overcome the energy barriers; the existence of the metastable isotropic phase is consistent with the classical phase separation theory[100]. The NG regime, illustrated by the green zone in Figure 5-2, corresponds to approximately 10%<η_q<30%, thus, the width of the NG zone is about 20% of the biphasic width. As discussed below, despite its narrowness, the NG regime retains rich liquid-crystalline behaviors in terms of tactoids shape, morphology, interactions, growth, and population.

5.7.2 Induction period

The simulation results show that phase separation via NG mechanism starts with an induction (lag) period during which tactoids reach the critical size and the thermodynamical driving force directs the growth, in excellent agreement with previous theoretical and experimental studies[17,101-103]. The induction time $\tilde{t}_l$ is defined as the elapsed time after quenching for the emergence of detectable tactoids with a population number $N(\tilde{t}_l) \geq 1$. Simulation results indicate that, for given material properties, the induction time inversely depends on the quench depth (or quench percentage, η_q; see Figure 5-3) and the corresponding correlation obtained by Classical Regression reads:

$$\tilde{t}_l = 2202 + 4.242 \times 10^{+9} \eta_q^{-5.14} \qquad (5-6)$$

indicating a strong sensitivity to quenching depth.

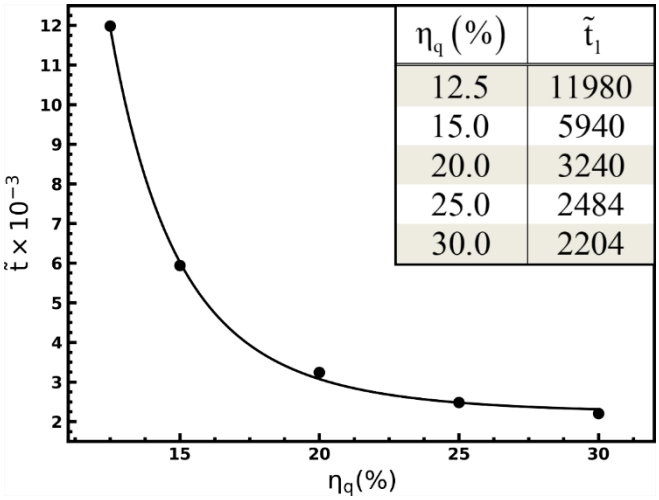

η_q (%)	$\tilde{t}_l$
12.5	11980
15.0	5940
20.0	3240
25.0	2484
30.0	2204

Figure 5-3. The graphical and tabular (inset) representations of induction times at various quench percentages. The induction period takes place during the early stage of the NG processes. The power law is approximately $\tilde{t}_l \approx \eta_q^{-5}$, showing a strong sensitivity to quenching depth.

5.7.3 Nucleation

Following the induction period, phase separation goes through the nucleation process during which multiple chiral nuclei spontaneously emerge and grow throughout the continuous isotropic phase. Hence, both the tactoids population N(t) and the characteristic length <L(t)> (time-dependent averaged diameter) of tactoids increase during the nucleation period (see Figure 5-4). The latter is a manifestation of the expected sequential nucleation.

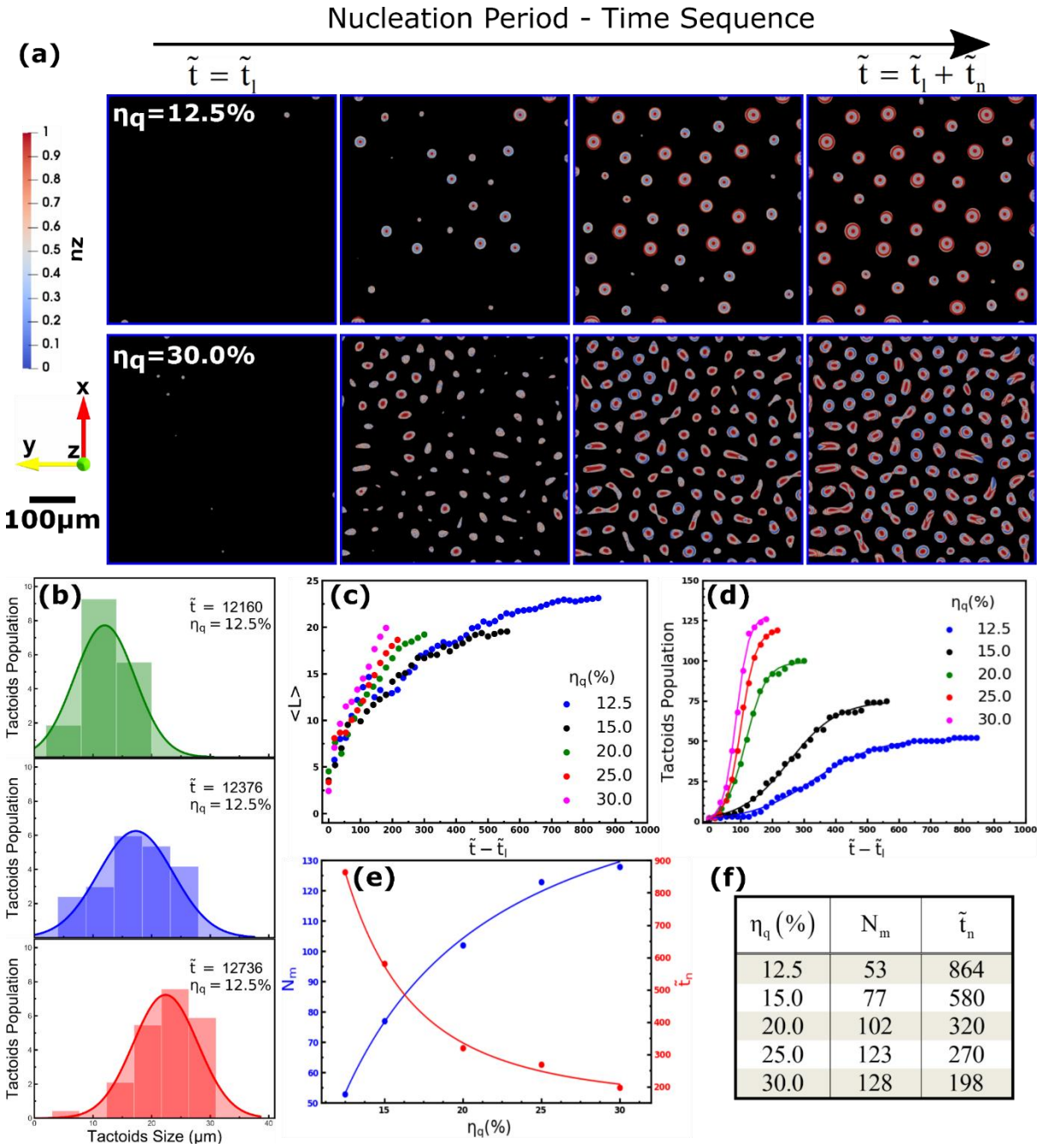

η_q (%)	N_m	$\tilde{t}_n$
12.5	53	864
15.0	77	580
20.0	102	320
25.0	123	270
30.0	128	198

Figure 5-4. **(a)** Evolution of the uniaxial director field at a shallow quench ($\eta_q = 12.5\%$) and a deeper quench ($\eta_q = 30.0\%$). The first and last columns indicate the beginning, $\tilde{t} = \tilde{t}_l$, and the end, $\tilde{t} = \tilde{t}_l + \tilde{t}_n$, of the nucleation period, respectively. The blue-to-red spectrum and black color show the order parameter, S, and isotropic phase, respectively. See the Supplementary Movies S1 through S4 for all the time sequences corresponding to the nucleation period of $\eta_q = 12.5\%$, 15%, 25% and 30%, respectively. **(b)** Size distribution at $\eta_q = 12.5\%$. The size distributions of other quenches has a similar trend. **(c)** The quench depth dependence of characteristic length, $\langle L \rangle$. See the Supplementary Note S3 for the corresponding log-log plots. **(d)** The quench depth dependence of tactoids population, N. **(e)** The quench depth dependence of tactoids population peak, N_m, and nucleation duration, $\tilde{t}_n$. **(f)** The tabular representation of panel (e). NB: the information shown in all panels corresponds to the nucleation period.

Table 5-1. Proposed correlations describing tactoids population, N, and growth laws ⟨L⟩, during nucleation periods. N and ⟨L⟩ are obtained by Symbolic Regression and Classical Regression, respectively.

Nucleation Period $\tilde{t}_l \le \tilde{t} \le \tilde{t}_l + \tilde{t}_n$	Tactoids Population (N) $N=\frac{c_1}{1+\exp(c_2(\tilde{t}-\tilde{t}_l)+c_3)}$				Growth laws (⟨L⟩) $\langle L\rangle = \langle L\rangle_0 + a(\tilde{t}-\tilde{t}_l)^n$			
$\eta_q(\%)$	c_1	$c_2 \times 10^3$	c_3	R^2	$\langle L\rangle_0$	$a \times 10$	n	R^2
12.5	51.53	-10.03	3.325	0.996	3.393	8.225	0.4799	0.970
15	75.04	-13.08	3.334	0.996	3.558	6.983	0.5046	0.980
20	99.01	-31.49	3.668	0.998	4.552	3.391	0.6670	0.976
25	118.9	-43.56	4.428	0.999	3.393	2.762	0.7512	0.971
30	128.10	-49.52	4.450	0.996	2.422	2.749	0.8065	0.970

Increasing the quench depth affects key descriptors of the nucleation period (see Figure 5-4 and Table 5-1):

- **Tactoids Distribution, Shape, and Morphology**. As shown in Figure 5-4**(a)** and the Supplementary Movies S1-S4, for shallow quenches (e.g. η_q=12.5%) tactoids sparsely nucleate and grow; even when the dilute tactoids population reaches its maximum (N_m), the relatively mature tactoids are distant from each other. Moreover, tactoids adopt the circular shape and the fibers therein self-select concentric configuration, which is perfectly consistent with experimental observations[29,71]. On the other hand, for deeper quenches (e.g. η_q=30%), the isotropic phase is more densely populated by chiral tactoids whose shapes are more elongated and even in some cases irregular. The fibers configuration remains almost concentric, see Figure 5-4(**a**).
- **Size Distributions, Universal Growth Laws, and Tactoids Population**. The size distribution follows nearly a Gaussian distribution moving from a small number of small-sized tactoids toward a multitude of bigger tactoids as time elapses. Hence, the characteristic length, which in this study is the average tactoids diameter, and tactoids population grow over time, as seen in Figure 5-4**(b)**. These results are quantified as follows.

  The DNS results, shown in Figure 5-4**(c)** and Table 5-1, accurately confirm the experimental observations[35,36,74,104,105] that: (1) The characteristic length evolves as per the universal growth laws given by

$$\langle L\rangle = \langle L\rangle_0 + a(\tilde{t}-\tilde{t}_l)^n \qquad (5-7)$$
$$\tilde{t}_l \le \tilde{t} \le \tilde{t}_l + \tilde{t}_n$$

(2) Within the NG zone, as quench depth increases the universal growth laws exponent, n, increases from n ≈ 0.5, and ultimately approaches n ≈ 1. Interestingly, simulation results reveal that the smallest tactoids which can grow retains the average diameter around $\langle L \rangle_0 = 2.4 \sim 4.5 \mu m$. This result is of great significance for material processing through the seeding method. Furthermore, the tactoids can reach the size of $19 \sim 23 \mu m$ by the end of the nucleation period which coincides with the beginning of the coarsening period.

Supported by Symbolic Regression, it is found that the tactoids population obeys a sigmoidal growth during the nucleation period; see Figure 5-4**(d)** and Table 5-1. The upper limit of the sigmoidal growth is determined by c_1 which is a dimensionless coefficient; thus c_1 provides insights into the maximum tactoids population which takes place by the end of the nucleation period. The trend of c_1 unequivocally signifies that the deeper quench depth is, the denser the isotropic phase is populated by chiral tactoids. c_2 is also a dimensionless coefficient due to the fact that both $\tilde{t}$ and $\tilde{t}_l$ are dimensionless. The absolute value of c_2 defines the growth rate or steepness of the tactoids population; hence, as can be seen in Figure 5-4**(d)** and Table 5-1, the absolute value of c_2 and the steepness of the tactoids' population increase upon increasing the quench percentage (i.e. quench depth). Lastly, c_3 is a dimensionless coefficient varying slightly with respect to quench percentage and therefore c_3 weakly affects the curve.

It should further be noticed that the correlations proposed for the tactoids population and the growth laws (see Table 5-1) are generic and cover the entire NG regime because the fitting coefficients monotonically vary according to the quench percentage. Hence, the fitting parameters for other quench percentages can be accurately obtained by interpolation.

- **Tactoids Population Peak and Nucleation Duration**. Figure 5-4**(e)** shows that increasing the quench depth drives the emergence of more tactoids over a shorter period. Knowing the tactoids population peak is important as discussed in the subsequent section. Accordingly, by using the Classical Regression, the quench depth dependence of the tactoids population peak which takes place at the end of the nucleation period, $N(\tilde{t} = \tilde{t}_l + \tilde{t}_n) = N_m$, and nucleation duration, $\tilde{t}_n$, read

$$N_m = 167.4 - 2770\eta_q^{-1.262} \qquad (5-8)$$

$$\tilde{t}_n = 149.6 + 9.839 \times 10^5 \eta_q^{-2.861} \qquad (5-9)$$

It is difficult to determine the exact boundaries of the NG zone shown in Figure 5-2since these boundaries are acquired by DNS through a fine scanning procedure. Eq. (5-8) can also serve to determine the lower boundary of the NG zone. In principle, at the lower

boundary of the NG zone, the tactoids population tends to one ($N_m \longrightarrow 1$); correspondingly, the extrapolated value of quench percentage using eq. (5-8) is $\eta_q \approx 10\%$. DNS also confirms this quench percentage leads to the NG regime with a very few tactoids.

These results can be also gleaned from other panels in Figure 5-4; Figure 5-4**(a)** also shows quench depth directly affects the tactoids population, and Figure 5-4**(c)** also implies that quench depth inversely affects the nucleation period.

5.7.4 Coarsening

The outline of this section is as follows. In section 5.7.4.1, we first analyze and characterize coarsening behaviors of a shallow quench (η_q=15%) and a deeper quench (η_q=25%). Section 5.7.4.2 elaborates on the incorporation of LSTM-RNN with DNS to build a large dataset of NG results, followed by the development of correlations based on the constructed dataset by making use of Symbolic Regression and Classical Regression.

5.7.4.1 Coarsening analysis

Shortly after the nucleation period, phase separation is carried out through coarsening in which the Ostwald ripening phenomenon takes place[35,37]. In this long-term process, small tactoids progressively become smaller over time and accordingly redeposit onto larger tactoids on account of reaching a more thermodynamically stable state by minimizing the contact surface of the two phases[106]. Hence, during the coarsening period, the tactoids population decreases while the averaged diameter of tactoids increases. Figure 5-5 and the Supplementary Movies S2 and S3, show that the tactoids coarsening process obeys with high fidelity the Ostwald ripening phenomenon.

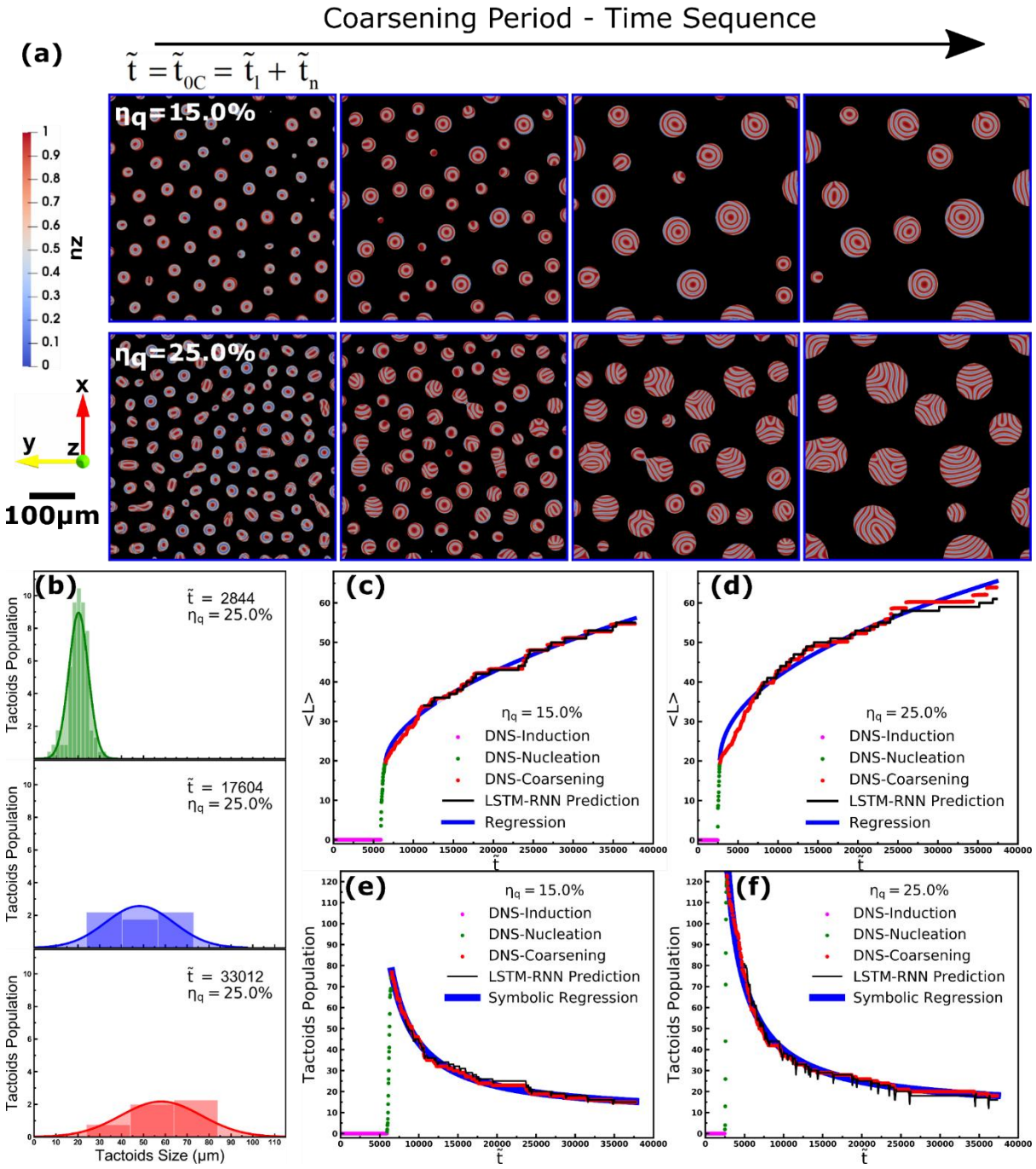

Figure 5-5. **(a)** Evolution of the uniaxial director field during the coarsening period at a shallow quench (η_q=15%) and a deeper quench (η_q=25%). The first column indicates the beginning of coarsening which is coincident with the end of the nucleation period, $\tilde{t} = \tilde{t}_{0C} = \tilde{t}_l + \tilde{t}_n$. The blue-to-red spectrum and black color exhibit order parameter, S, and isotropic phase, respectively. See the Supplementary Movies S2 and S3 for all the time sequence corresponding to the three NG stages for η_q=15% and 25%, respectively. **(b)** Size distribution at η_q=25% during the coarsening period. The size distributions of other quenches have a similar trend during coarsening. **(c,d)** The characteristic length, ⟨L⟩, during the entire quench process at a shallow quench (η_q=15%) and a deeper quench (η_q=25%), respectively. See the Supplementary Note S3 for the corresponding log-log plots during the coarsening period. **(e,f)** The tactoids population during the entire quench process at a shallow quench (η_q=15%) and a deeper quench (η_q=25%), respectively. General Note regarding panels (c-f): the excellent performances of the

LSTM-RNN and the proposed correlations are shown by solid black and blue curves moreover all NG stages obtained by DNS are distinguished by different colors with the circle marker, refer to the legends shown in the graphs.

Increasing the quench depth also affects the coarsening period according to various criteria (see Figure 5-5 and Table 5-2):

- **Tactoids Depopulation Mechanisms, Shape, and Morphology**. As explained above, the tactoids population peak increases with increasing the quench magnitude. This maximum point, $N(\tilde{t} = \tilde{t}_l + \tilde{t}_n) = N_m$, is also coincident with the beginning of the coarsening period. For convenience, the peak time is denoted by $\tilde{t}_{0C} = \tilde{t}_l + \tilde{t}_n$.

  For shallow quenches, e.g. η_q=15%, small tactoids progressively shrink, and consequently, large tactoids grow. More precisely, the small tactoids dissolve into the isotropic phase and then fibers existing in isotropic phase diffuses onto larger tactoids through uphill diffusion mechanism. Hence, the tactoids population decreases solely via the dissolution of small tactoids into the isotropic phase. This type of tactoids population decline reflects the Ostwald ripening phenomenon. Moreover, because there is no coalescence among tactoids, tactoids self-select nearly a circular shape with a concentric or a 2D configuration which is consistent with 3D Radial Spherical Structure (RSS)[107] (see Figure 5-5**(a)** and the Supplementary Movie S2)

  For deeper quenches, e.g. η_q=25%, the Ostwald ripening is performed via two mechanisms; (1) Dissolution of small tactoids into the isotropic phase, which also takes place for shallow quenches and (2) Coalescence of small tactoids with larger tactoids. More importantly, the coalescence results in elliptical tactoids with more defects such as $\tau^{+\frac{1}{2}}$. Note that the elliptical tactoids evolve into nearly circular ones provided that they become isolated from further coalescence and are given sufficient time. Regarding the orientational ordering, in addition to the configurations captured for the shallow quenches, other 2D cholesteric configurations are also observed such as a 2D configuration presented in 3D Planar Bipolar Structure (PBS)[107] (see Figure 5-5**(a)** and the Supplementary Movies S3).
- **Size Distributions, Universal Growth Laws, and Tactoids Depopulation**. The time-series size distributions indicate a time-marching Gaussian distribution moving from a large number of small-sized tactoids to fewer larger tactoids; see Figure 5-5**(b)**. These results are quantified as follows.

Our DNS results confirm the experimental observations[35,37,74,105,108-110] that, regardless of quench depth, the power laws with exponent n ≈ 0.5 describes the growth law for liquid-crystalline materials during the coarsening period in the NG processes; see Figure 5-5**(c,d)** and Table 5-2. It should, however, be noted that Table 5-2 may indicate a subtle systematic dependence of the exponent, n, on the quenching depth, η_q, because as quench depth increases from 12.5% to 30%, the exponent varies from 0.56 to 0.45. The slight deviation of the exponent from 0.5 during the coarsening period has also been reported in the literature[105,108,110]; however, to the best of authors' knowledge, the reason behind such behavior has not yet explained. In partial summary, based on available results in our simulations and past experimental studies, an indisputable conclusion cannot be drawn on the subtle dependence of the exponent on the quench depth, since the unavoidable indeterminacy through the estimation of the exponent values may induce a slight deviation from 0.5. The important examples of indeterminacy are; (1) Regression errors; the exponents, n, are obtained by the regression analysis in both theoretical and experimental studies. (2) Errors corresponding to the determination of each tactoid size at a given time; the characteristic length of each tactoid is determined by counting pixels for which the color intensity exceeds a certain threshold. (3) The intrinsic errors due to the numerical simulations and experimental measurements.

Figure 5-5**(e,f)** demonstrate the tactoids population for the entire time-series, including induction, nucleation, and coarsening. Regardless of the quench depth, the tactoid population declines according to the Ostwald ripening phenomenon during the coarsening period. The decreasing trend of the tactoids depopulation captured for the coarsening period in our simulations, e.g. Figure 5-5**(e,f)**, is in excellent agreement with experimental observations[37].

Using Symbolic Regression, the tactoids population during the coarsening period reads (the Supplementary Note S4 provides details of the development)

$$N = N_m - \frac{\alpha(\tilde{t}-\tilde{t}_{0C})}{(\tilde{t}-\tilde{t}_{0C})+\beta}, \tilde{t} \geq \tilde{t}_{0C} \qquad (5-10)$$

where α and β are positive fitting parameters tabulated in Table 5-2. Eq.(5-10) is developed based on a large data set. For this reason, the developed correlation is remarkably applicable for a long-term coarsening period as $\lim_{\tilde{t}\to\infty} N = N_m - \alpha > 0$; see Figure 5-4**(f)** and Table 5-2. Furthermore, both fitting parameters (α and β) are dimensionless. Upon increasing α while $\alpha < N_m$, the tactoids depopulation is accelerated; therefore, α directly affects tactoids depopulation. On the contrary, β inversely affects tactoids depopulation;

the tactoids' depopulation slows down as β becomes larger, and the tactoids' depopulation accelerates as β decreases. As can be seen in Table 5-2, as the quench depth increases, α and β increase and decrease, respectively, leading to faster tactoids' depopulation.

5.7.4.2 Correlations development of the universal growth laws and tactoids population during coarsening period

The acquisition of the entire time-series of a quenching process using DNS is computationally very demanding even for a high-performance computing facility. In particular, obtaining the simulation results of the coarsening period is significantly more time-consuming compared to induction followed by nucleation; in the present study, simulation of each quenching process approximately takes three weeks and the acquisition of coarsening results takes more than 75% runtime, see the Supplementary Note S1 for more information. On the other hand, a large dataset is required to develop wide-range robust correlations, making correlations development difficult if results are exclusively obtained via DNS.

Furthermore, Figure 5-5**(c-f)** demonstrate the excellent performance of LSTM-RNN in the estimation of major time-series of the coarsening period, which is the most time-consuming part of the simulation as already mentioned. Remarkably, the LSTM-RNN has exceptional effectiveness in the identification of times at which stair-like decrease and increase take place in the tactoids depopulation and characteristic length, respectively.

The successful performance of LSTM-RNN can be leveraged for building a sufficiently large dataset by a combination of the two methods: DNS and LSTM-RNN. Rather than obtaining the entire time-series using DNS, the early time-series is acquired by DNS which takes relatively short runtime (roughly one week per simulation) thereafter the remaining time-series is quickly estimated using the LSTM-RNN trained by the early time-series; see subsection 5.6.3 and Figure 5-1. The LSTM-RNN is a fast surrogate model (which requires nearly an hour for being trained and a minute for estimating the remaining time-series with an ordinary PC) while the computation of the remaining time-series by DNS takes considerably long runtime (approximately two weeks per simulation with a powerful high-performance supercomputer). Having built the dataset, we then employ first the Symbolic Regression to find the best mathematical model representing the tactoids population, and second, Classical Regression to find the optimal fitting parameters for universal growth laws. The details and results of this approach are shown in Figure 5-6and Table 5-2, respectively.

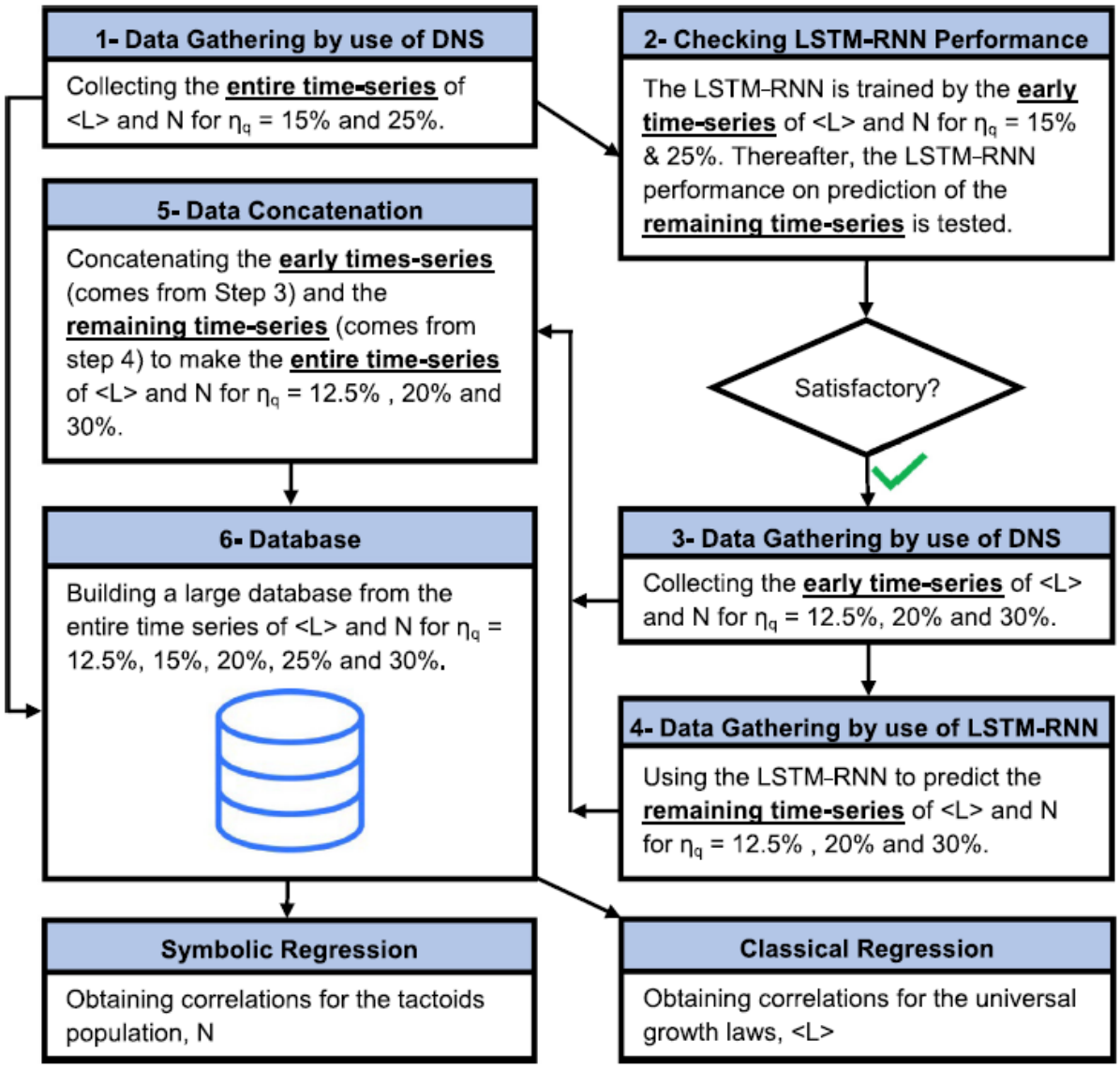

Figure 5-6. Overview of the workflow applied to develop the correlations.

Table 5-2. The proposed correlations describing the tactoids population, N, and the growth laws, ⟨L⟩, during coarsening periods. N and ⟨L⟩ are obtained by Symbolic Regression and Classical Regression, respectively.

Coarsening Period $\tilde{t} \geq \tilde{t}_{0C}$	Tactoids Population (N) $N=N_m-\frac{\alpha(\tilde{t}-\tilde{t}_{0C})}{(\tilde{t}-\tilde{t}_{0C})+\beta}, \tilde{t} \geq \tilde{t}_{0C}$			Growth laws (⟨L⟩) $\langle L\rangle = \langle L\rangle_0 + a(\tilde{t}-\tilde{t}_{0C})^n$			
η_q(%)	α	β	R^2	$\langle L\rangle_0$	a	n	R^2
12.5	52.06	6595	0.989	22.80	0.0951	0.56	0.989
15	69.92	3923	0.998	19.48	0.1219	0.55	0.998
20	91.46	2929	0.989	19.35	0.1981	0.51	0.979
25	111.30	2284	0.997	19.39	0.3274	0.47	0.979
30	115.20	2195	0.998	19.36	0.4725	0.45	0.979

where, as pointed out earlier, $\tilde{t}_{0C} = \tilde{t}_l + \tilde{t}_n$ stands for the time at which the coarsening begins, see Figure 5-3and Figure 5-4**(f)** to obtain the induction time, $\tilde{t}_l$, and the nucleation duration, $\tilde{t}_n$, respectively. The tactoids population peak, N_m, is also given in Figure 5-4**(f)**.

Like correlations developed for the nucleation period (Table 5-1), the salient feature of the proposed correlations for the coarsening period is that the fitting parameters are monotonic with respect to the quench percentage; thus, other quenches can be accurately estimated by interpolation; see Figure 5-7 and Table 5-2. Additionally, Figure 5-7**(a)** vividly reconfirms the growth law exponent $n \approx 0.5$ for the coarsening period.

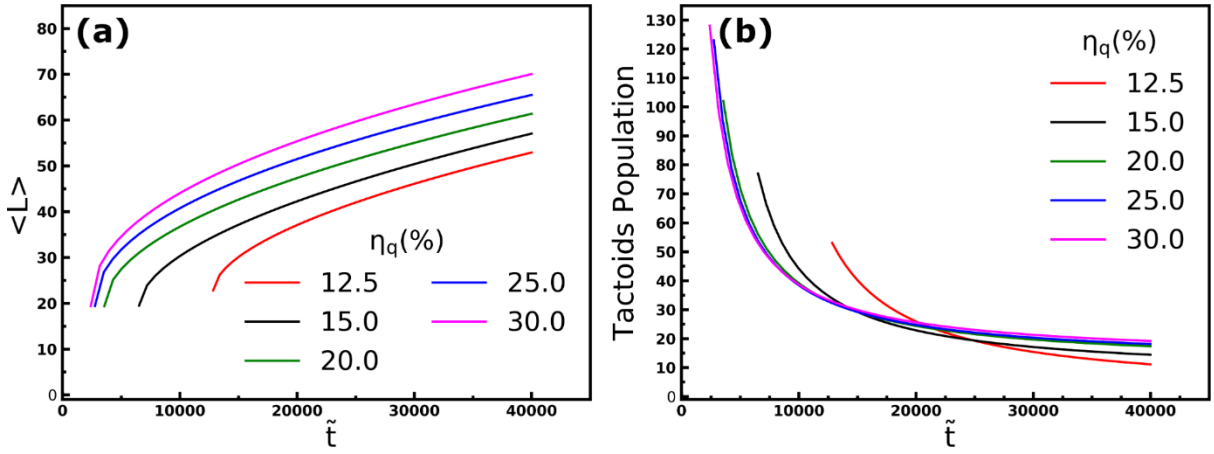

Figure 5-7. The graphical representation of correlations developed for **(a)** the growth laws and **(b)** the tactoids population during coarsening periods. Note that see the Supplementary Note S3 for the log-log plot of the panel (a).

5.7.5 Mechanisms and principles governing the quench depth dependence of the NG characteristics

On the basis of the above discussion, the quench depth dependence of the NG characteristics is summarized in Table 5-3.

Table 5-3. Summary of quench depth dependence of the NG characteristics. Upward and downward arrows qualitatively signify increase and decrease, respectively.

Quench percentage, η_q	↑
Induction time, $\tilde{t}_l$	↓
Nucleation duration, $\tilde{t}_n$	↓
Tactoids population peak, N_m	↑
Growth law exponent, n (During the nucleation period)	↑
Number of coalescences	↑
Tactoids circularity	↓
Number of defects	↑

The physical origin of these behaviors can be explored using free energy analysis. Thus, we formulate the system energy F as the spatial average of the total free energy:

$$F=\frac{\iint_A\left(\tilde{f}_{iso}+\tilde{f}_h+\tilde{f}_e+\tilde{f}_{cg}+\tilde{f}_c\right)dA}{\iint_A dA} \tag{5-11}$$

where A represents the domain in which the NG processes take place; all terms in eq.(5-11) are dimensionless. Figure 5-8 illustrates the variation of the system energy over two complete quenching processes.

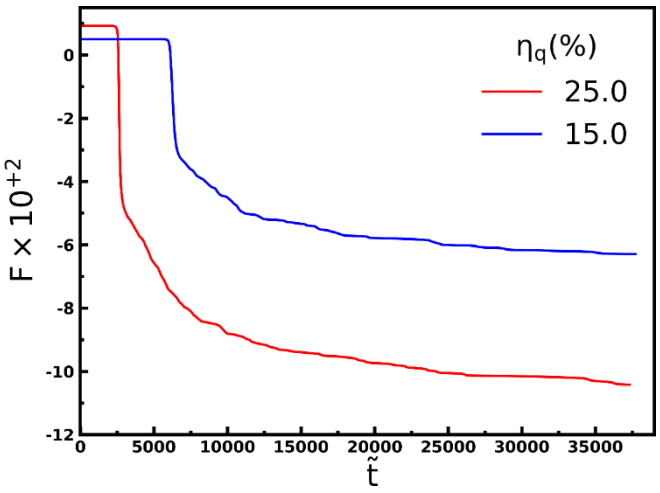

Figure 5-8. Time evolution of system energy at a shallow quench (η_q=15%) and a deeper quench (η_q=25%), see the graph legend.

As shown in eqs. (5-2a, 5-2b), phase separation and ordering are directly governed by free energy driving force, $\delta\tilde{F}_{net}$. The free energy difference between initial and steady states can be an excellent representative of free energy driving force; hence, the free energy driving force is defined as $\Delta F = F(\tilde{t}=0) - F(\tilde{t}=\infty)$. Increasing the quench percentage directly makes the free energy driving force larger, meaning that the spontaneous tendency for the quenching

process increases. For example, $\Delta F|_{\eta_q=25\%}/\Delta F|_{\eta_q=15\%} \approx 1.7$, see Figure 5-8. The deeper quenches thus result in faster self-assembly dynamics, leading to shortening induction and nucleation periods. It should further be noted that the intermediate metastable states are absent during the NG processes studied in the present work; for this reason, the reasoning utilized above (i.e. the higher free energy driving force is imposed on the system, the faster fibers are self-assembled) is valid for our study.

As the quenching process is spontaneous, the system energy initially has a high level due to unstable thermodynamic state imposed by quenching (i.e. isotropic phase while concentration exceeds the order-disorder threshold, see eq.(5-3)), and as self-assembly progresses the system energy goes to a lower level until a plateau is reached. In other words, the free energy driving force ΔF can also be interpreted as the excess energy that should be relieved through the NG process. Hence, the deeper the quench depth is, the more excess energy is imposed on the system; see Figure 5-8. Furthermore, the chiral phase is thermodynamically favorable owing to the lower energy level compared to the isotropic phase. For this reason, it is energetically more favorable that the system increases the amount of the chiral phase (low energy) to relieve more excess energy imposed by increasing quench depth. The system spontaneously does that via two mechanisms; increasing the population of chiral nuclei and making the growth of chiral nuclei faster. That is why upon increasing quench depth, the tactoids population peak and the growth law exponent increases.

So far, from the system energy point of view, it is rationalized why increasing quench depth leads to the emergence of more chiral tactoids. Owing to the fact that the system is thermodynamically closed, increasing in tactoids population gives rise to increasing the tactoids population density. Based on this, the probability of tactoids collision thus goes higher, in turn, the resulting tactoids more deviate from the circular shape and more defects are also formed. Since the energy penalty of the tactoids interface is higher than that of defects existing inside the tactoids, the tactoids have more tendency to become circular and minimize the contact surface between isotropic and cholesteric phases over time, however, defects may be trapped.

5.7.6 Mechanisms and principles governing the growth law exponent, n, during the nucleation period

According to the significant agreements and broad consistency between the results obtained so far and the experimental studies[29,35-37,71,74,104,105], the conclusion can be drawn that the physics of the NG processes can accurately be described by the coupled order parameter model used in this study; see subsection 5.6.1. This coupled order parameter model, known as model C in statistical mechanics[40], comprises of two governing equations: (1) orientational ordering, eq(5-2a), describing the non-conserved order parameter **Q**, and (2) conservation of mass, eq. (5-2b), describing the conserved order parameter, ϕ. We found that the non-diffusive model, meaning the sole consideration of orientational ordering, exclusively results in n = 1, which is known as volume-driven regime[31]; see Figure 5-9. Therefore, the lower exponents that are captured using the diffusive model stem from the coupling of mass diffusion and orientational ordering.

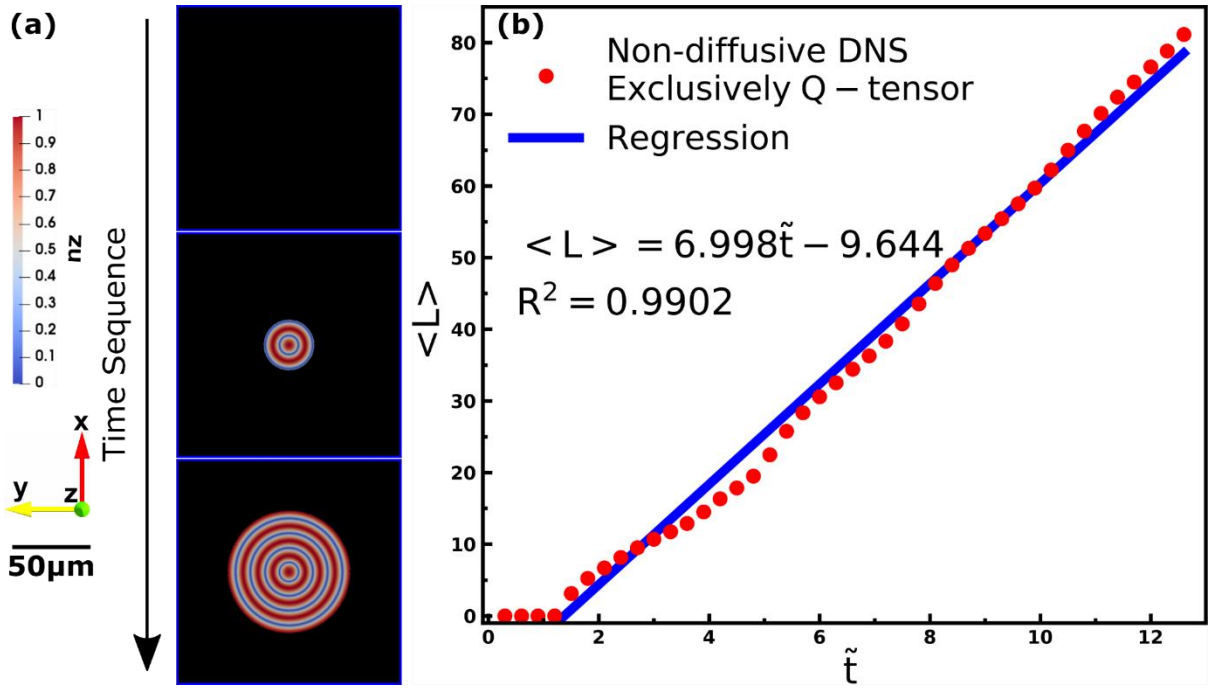

Figure 5-9. **(a)** The time-series images showing the evolution of fibers configuration in a growing cholesteric tactoid. The blue-to-red spectrum and black color exhibit order parameter, S, and isotropic phase, respectively. See the Supplementary Movie S5 for all the time sequence. **(b)** The characteristic length of the growing tactoid depicted in panel (a). NB: the results illustrated in both panels are obtained by the non-diffusive model (i.e. only **Q**-tensor equation is numerically solved).

Taken altogether, for chiral lyotropic LCs, the growth law exponent corresponding to the nucleation period evolves from the mass limited regime (n ≈ 0.5) to the volume-driven regime

(n ≈ 1) as quench depth increases. Furthermore, the coarsening period is mainly governed by the mass diffusion mechanism as the growth law exponent is independently n ≈ 0.5.

5.8 Conclusions

Owing to a broad number of promising applications of collagen-based biomaterials and the significance of I/N^* phase separation in the processing of these versatile biomaterials, this study focuses on the underlying understanding of phase separation and ordering via the NG mechanism in acidic colloidal collagen dispersions. We employed the DNS technique to dynamically capture the phase separation and ordering of chiral nuclei growing from the unstable isotropic phase. Our study was performed on a two-dimensional square (500μmx500μm) which is statistically large enough to acquire realistic results. In the light of the realistic domain and the proposed hybrid approach (DNS/LSTM-RNN), the findings not only are consistent with available experimental studies but also reveal original physics behind the NG quenching processes.

Through systematic simulation and analysis of various quench depths guided a previously experimentally validated thermodynamic model[1], we found and targeted the NG regime existing in the biphasic zone of the acidic aqueous collagen solution phase diagram.

The NG regime occupies ≈ 20% of the biphasic zone and emerges near the isotropic binodal curve, see Figure 5-2. Quenching into the NG regime results in two coexisting phases; cholesteric tactoids (collagen-rich dispersed phase) and isotropic phase (collagen-lean continuous phase). Thereafter, we characterized all the three NG stages (induction, nucleation, and coarsening) across the NG zone and developed generic, wide-range, and robust correlations for crucial quantities. The characterization results are summarized as follows; (also see the Supplementary Movies S1-S4 showing the simulation of the NG quenching process at different quench percentages, facilitating the understanding of the quench depth dependence of NG characteristics).

Induction. The quenching process starts with the induction period that is inversely proportional to quench depth; see Figure 5-3. The quench depth dependence of the induction period is also formulated by regression as shown in eq.(5-6).

Nucleation. Increasing quench depth leads to increasing the tactoids population density, moreover, more elongated tactoids are formed while the fibers' configuration independently

remains largely concentric; see Figure 5-4**(a)**. During the nucleation period, both the tactoids population and the average diameter increase; see Figure 5-4**(b)**. By using Symbolic Regression, we found that the tactoids population sigmoidally grows to eventually reach a maximum, moreover, classical regression analysis confirms that the average diameters of tactoids increase according to universal growth laws (eq. (5-7)). The growth law exponent varies from n ≈ 0.5 to n ≈ 1 for shallow to deep quenches, agreeing with experimental observations[35,36,74,104,105]. The growth law results reveal that tactoids with average diameter 2.4~4.5μm are practically able to grow and the average diameter roughly reaches 19~23μm by the end of nucleation, see Figure 5-4**(c,d)** and Table 5-1. Furthermore, the tactoids population peak and nucleation duration are directly and inversely correlated with quench depth, see Figure 5-4**(e,f)** and eqs.(5-8, 5-9).

Coarsening. During the coarsening period, tactoids depopulation takes place while the average diameter of tactoids grows. It was found that the tactoids depopulation, i.e. the Ostwald ripening phenomenon, takes place via two mechanisms; (1) Dissolution of small tactoids into the isotropic phase, then redeposition onto larger tactoids through uphill diffusion. (2) Coalescence of small tactoids with larger ones. The former is predominant for shallow quenches while both mechanisms are involved for deeper quenches. The shallow quenches result in more circular tactoids with concentric or RSS configurations and deeper quenches induce more elongated tactoids retaining richer chiral nematic morphologies such as PBS in addition to concentric and RSS. Regarding defect, the deeper quench depth is, the more defects are formed, see Figure 5-5**(a,b)**. To capture the coarsening results, we employed a combination of LSTM-RNN and DNS for the certain quenches to reduce the computational costs and build a large dataset of results. Afterward, similar to the nucleation period, Symbolic Regression and Classical Regression were employed to explore the mathematical model representing the tactoids population and the growth laws, respectively. It was revealed that the tactoids population decline follows a fractional model, eq.(5-10), and the growth law exponent is n ≈ 0.5 regardless of quench depth, agreeing with experimental studies[35,37,105], see Figure 5-5**(c-f)**,6,7 and Table 5-2. In our study, the generality of the exponent of growth laws during both nucleation and coarsening periods for LCs becomes clearer because our simulations were tailored for collagen whereas the experimental studies cited for the validation employed different classes of LCs. It should further be noted that all the chiral nematic configurations captured throughout both nucleation and coarsening periods are in excellent agreement with experimental studies[29,71,111].

Having obtained the NG results, a free energy analysis was utilized to shed light on the physics governing the captured behaviors. It was demonstrated that increasing quench depth leads to increasing the free energy driving force, making the dynamics of self-assembly faster, see Figure 5-8. For this reason, induction and nucleation periods are inversely affected by quench depth. Furthermore, it was rationalized that the system favors having more chiral phase (low energy) in response to increasing quench depth because this behavior facilitates the relief of more excess energy imposed by quenching, leading to increasing the tactoids population and making the growth faster during the nucleation period. As the tactoids population goes higher in the given closed system, the number of coalescences goes higher, in turn, more elongated tactoids with more defects are formed.

We then showed that the non-diffusive model (only considering the orientational ordering model given by eq.(5-2a)) exclusively produces the growth law exponent $n \approx 1$; see Figure 5-9 and Supplementary Movie 5. Thus, the non-Fickian mass transfer incorporated into the simulation, eq.(5-2b), has a profound effect to deliver realistic results, moreover, it was concluded that the lower growth law exponents are due to the coupling of orientational ordering, eq.(5-2a), and mass transfer, eq.(5-2b).

Taken together these simulation results, scaling laws, mechanisms, and principles governing nucleation and growth of chiral collagen drops are a significant and novel contribution to the ongoing biomimetic efforts in bioengineering and medical applications.

In our future studies, aiming at the development of collagen-based biomaterials processing, we will target two objectives. (1) In the present study, we have delineated and characterized the NG zone in the biphasic region of the collagen phase diagram (see the green region in Figure 5-2). The exhaustive DNS investigation should also be carried out to explore other phase separation mechanisms and patterns formation processes existing across the biphasic zone. (2) Integration of DNS and artificial intelligence methods to reduce the numerical complexity required to solve the governing equations, eqs.(5-1 and 5-2), has been shown to be accurate and efficient. In the future, we plan to build on the current approach to map out the extensive parametric space and condense our results into practical scaling laws and engineering correlations. These crucial results effectively guide the existing trial-and-error fabrications of the sought-after collagen-based biomaterials.

5.9 Acknowledgments

SAK acknowledges financial support from the McGill Engineering Doctoral Awards (MEDA) program. ADR is thankful to McGill University for financial support through the James McGill Professorship appointment. This research is supported by a Sinergia grant from the Swiss National Science foundation (CRSII5_189917/1).

References (Chapter 5)

1 Khadem, S. A. & Rey, A. D. Thermodynamic Modelling of Acidic Collagenous Solutions: From Free Energy Contributions to Phase Diagrams. Soft Matter, doi:10.1039/C8SM02140F (2019).

2 Voet, D. & Voet, J. G. Biochemistry. (John Wiley & Sons, 2011).

3 Weiner, S., Traub, W. & Wagner, H. D. Lamellar bone: structure–function relations. Journal of structural biology **126**, 241-255 (1999).

4 Fratzl, P. & Weinkamer, R. Nature's hierarchical materials. Progress in materials Science **52**, 1263-1334 (2007).

5 Mitov, M. Cholesteric liquid crystals in living matter. Soft Matter **13**, 4176-4209, doi:10.1039/C7SM00384F (2017).

6 Rastian, Z., Putz, S., Wang, Y. J., Kumar, S., Fleissner, F., Weidner, T. & Parekh, S. H. Type I Collagen from Jellyfish Catostylus mosaicus for Biomaterial Applications. ACS Biomater. Sci. Eng. **4**, 2115-2125, doi:10.1021/acsbiomaterials.7b00979 (2018).

7 Giraud Guille, M. M., Mosser, G., Helary, C. & Eglin, D. Bone matrix like assemblies of collagen: From liquid crystals to gels and biomimetic materials. Micron **36**, 602-608, doi:https://doi.org/10.1016/j.micron.2005.07.005 (2005).

8 Pontremoli, C., Izquierdo-Barba, I., Montalbano, G., Vallet-Regi, M., Vitale-Brovarone, C. & Fiorilli, S. Strontium-releasing mesoporous bioactive glasses with anti-adhesive zwitterionic surface as advanced biomaterials for bone tissue regeneration. Journal of Colloid and Interface Science **563**, 92-103, doi:10.1016/j.jcis.2019.12.047 (2020).

9 Lee, S. J., Won, J. E., Han, C., Yin, X. Y., Kim, H. K., Nah, H., Kwon, I. K., Min, B. H., Kim, C. H., Shin, Y. S. & Park, S. A. Development of a three-dimensionally printed scaffold grafted with bone forming peptide-1 for enhanced bone regeneration with in vitro and in vivo

evaluations. Journal of Colloid and Interface Science **539**, 468-480, doi:10.1016/j.jcis.2018.12.097 (2019).

10 Ye, K. Q., Liu, D. H., Kuang, H. Z., Cai, J. Y., Chen, W. M., Sun, B. B., Xia, L. G., Fang, B., Morsi, Y. & Mo, X. M. Three-dimensional electrospun nanofibrous scaffolds displaying bone morphogenetic protein-2-derived peptides for the promotion of osteogenic differentiation of stem cells and bone regeneration. Journal of Colloid and Interface Science **534**, 625-636, doi:10.1016/j.jcis.2018.09.071 (2019).

11 Torbet, J., Malbouyres, M., Builles, N., Justin, V., Roulet, M., Damour, O., Oldberg, Å., Ruggiero, F. & Hulmes, D. J. S. Orthogonal scaffold of magnetically aligned collagen lamellae for corneal stroma reconstruction. Biomaterials **28**, 4268-4276, doi:https://doi.org/10.1016/j.biomaterials.2007.05.024 (2007).

12 De Sa Peixoto, P., Deniset-Besseau, A., Schmutz, M., Anglo, A., Illoul, C., Schanne-Klein, M.-C. & Mosser, G. Achievement of cornea-like organizations in dense collagen I solutions: clues to the physico-chemistry of cornea morphogenesis. Soft Matter **9**, 11241-11248, doi:10.1039/C3SM52097H (2013).

13 Choi, F., Chen, R. & Acosta, E. J. Predicting the effect of additives on wormlike micelle and liquid crystal formation and rheology with phase inversion phenomena. Journal of Colloid and Interface Science **564**, 216-229 (2020).

14 Xu, Y., Atrens, A. & Stokes, J. R. Structure and rheology of liquid crystal hydroglass formed in aqueous nanocrystalline cellulose suspensions. Journal of colloid and interface science **555**, 702-713 (2019).

15 Moore, J. E., McCoy, T. M., Marlow, J. B., Pottage, M. J., Mudie, S. T., Pearson, G. R., Wilkinson, B. L. & Tabor, R. F. Rich liquid crystal phase behavior of novel alkyl-tri (ethylene glycol)-glucoside carbohydrate surfactants. Journal of colloid and interface science **540**, 410-419 (2019).

16 Mirzaeifard, S. & Abel, S. M. Confined semiflexible polymers suppress fluctuations of soft membrane tubes. Soft Matter **12**, 1783-1790, doi:10.1039/C5SM02556G (2016).

17 Mirzaeifard, S., Servio, P. & Rey, A. D. Characterization of nucleation of methane hydrate crystals: Interfacial theory and molecular simulation. Journal of colloid and interface science **557**, 556-567 (2019).

18 Mirzaeifard, S., Servio, P. & Rey, A. D. J. C. E. S. Molecular Dynamics Characterization of the Water-Methane, Ethane, and Propane Gas Mixture Interfaces. (2019).

19 Mirzaeifard, S., Servio, P., Rey, A. D. J. C. & Communications, I. S. Molecular Dynamics Characterization of Temperature and Pressure Effects on the Water-Methane Interface. **24**, 75-81 (2018).

20 Mirzaeifard, S., Servio, P. & Rey, A. D. Multiscale Modeling and Simulation of Water and Methane Hydrate Crystal Interface. Crystal Growth & Design **19**, 5142-5151, doi:10.1021/acs.cgd.9b00578 (2019).

21 Aguilar Gutierrez, O. F. & Rey, A. D. Biological plywood film formation from para-nematic liquid crystalline organization. Soft Matter, doi:10.1039/C7SM01865G (2017).

22 Gutierrez, O. F. A. & Rey, A. D. Theory and Simulation of Cholesteric Film Formation Flows of Dilute Collagen Solutions. Langmuir **32**, 11799-11812, doi:10.1021/acs.langmuir.6b03443 (2016).

23 Neville, A. C. Biology of Fibrous Composites: Development Beyond the Cell Membrane. (Cambridge University Press, 1993).

24 Rahimi, M., Roberts, T. F., Armas-Pérez, J. C., Wang, X., Bukusoglu, E., Abbott, N. L. & de Pablo, J. J. Nanoparticle self-assembly at the interface of liquid crystal droplets. Proceedings of the National Academy of Sciences **112**, 5297-5302 (2015).

25 Meseck, G. R., Terpstra, A. S. & MacLachlan, M. J. Liquid crystal templating of nanomaterials with nature's toolbox. Current Opinion in Colloid & Interface Science **29**, 9-20 (2017).

26 Li, Y., Jun-Yan Suen, J., Prince, E., Larin, E. M., Klinkova, A., Thérien-Aubin, H., Zhu, S., Yang, B., Helmy, A. S., Lavrentovich, O. D. & Kumacheva, E. Colloidal cholesteric liquid crystal in spherical confinement. Nature Communications **7**, 12520, doi:10.1038/ncomms12520 (2016).

27 Almeida, A. P., Oliveira, J., Fernandes, S. N., Godinho, M. H. & Canejo, J. P. All-cellulose composite membranes for oil microdroplet collection. Cellulose, 1-13 (2020).

28 Saraiva, D. V., Chagas, R., Abreu, B. M. d., Gouveia, C. N., Silva, P. E., Godinho, M. H. & Fernandes, S. N. Flexible and Structural Coloured Composite Films from Cellulose Nanocrystals/Hydroxypropyl Cellulose Lyotropic Suspensions. Crystals **10**, 122 (2020).

29 Nyström, G., Arcari, M. & Mezzenga, R. Confinement-induced liquid crystalline transitions in amyloid fibril cholesteric tactoids. Nature Nanotechnology **13**, 330-336, doi:10.1038/s41565-018-0071-9 (2018).

30 Gobeaux, F., Belamie, E., Mosser, G., Davidson, P., Panine, P. & Giraud-Guille, M. M. Cooperative Ordering of Collagen Triple Helices in the Dense State. Langmuir **23**, 6411-6417, doi:10.1021/la070093z (2007).

31 Abukhdeir, N. M., Soulé, E. R. & Rey, A. D. J. L. Non-isothermal model for nematic spherulite growth. **24**, 13605-13613 (2008).

32 Soule, E. R., Abukhdeir, N. M. & Rey, A. D. Thermodynamics, Transition Dynamics, and Texturing in Polymer-Dispersed Liquid Crystals with Mesogens Exhibiting a Direct Isotropic/Smectic-A Transition. Macromolecules **42**, 9486-9497, doi:10.1021/ma901569y (2009).

33 Wincure, B. M. & Rey, A. D. Nanoscale analysis of defect shedding from liquid crystal interfaces. Nano Lett. **7**, 1474-1479, doi:10.1021/nl0701408 (2007).

34 Wincure, B. & Rey, A. D. Growth and structure of nematic spherulites under shallow thermal quenches. Continuum Mech. Thermodyn. **19**, 37-58, doi:10.1007/s00161-007-0043-z (2007).

35 Dierking, I. Domain growth scaling at the isotropic-to-cholesteric liquid crystal transition. The Journal of Physical Chemistry B **104**, 10642-10646 (2000).

36 Chan, H. & Dierking, I. Growth laws for the phase ordering dynamics of the B 1 phase of a bent-core liquid crystal. Physical Review E **70**, 021703 (2004).

37 Bronnikov, S. & Dierking, I. Time resolved statistical analysis of liquid crystal nucleus growth from the isotropic melt. Physical Chemistry Chemical Physics **6**, 1745-1749 (2004).

38 Reyes, C. G., Baller, J., Araki, T. & Lagerwall, J. P. F. Isotropic–isotropic phase separation and spinodal decomposition in liquid crystal–solvent mixtures. Soft Matter **15**, 6044-6054, doi:10.1039/C9SM00921C (2019).

39 Das, S. K. & Rey, A. D. Texture formation under phase ordering and phase separation in polymer-liquid crystal mixtures. J. Chem. Phys. **121**, 9733-9743, doi:10.1063/1.1804494 (2004).

40 Hohenberg, P. C. & Halperin, B. I. Theory of dynamic critical phenomena. Reviews of Modern Physics **49**, 435-479, doi:10.1103/RevModPhys.49.435 (1977).

41 Rey, A. D. Liquid crystal models of biological materials and processes. Soft Matter **6**, 3402-3429, doi:10.1039/B921576J (2010).

42 Chen, Y., Shen, L., Li, R., Xu, X., Hong, H., Lin, H. & Chen, J. Quantification of interfacial energies associated with membrane fouling in a membrane bioreactor by using BP and GRNN artificial neural networks. Journal of Colloid and Interface Science (2020).

43 Pauletto, P., Gonçalves, J., Pinto, L., Dotto, G. & Salau, N. Single and competitive dye adsorption onto chitosan–based hybrid hydrogels using artificial neural network modeling. Journal of colloid and interface science **560**, 722-729 (2020).

44 Arshadi, M., Abdolmaleki, M., Eskandarloo, H. & Abbaspourrad, A. A supported dendrimer with terminal symmetric primary amine sites for adsorption of salicylic acid. Journal of colloid and interface science **540**, 501-514 (2019).

45 Tanzifi, M., Yaraki, M. T., Kiadehi, A. D., Hosseini, S. H., Olazar, M., Bharti, A. K., Agarwal, S., Gupta, V. K. & Kazemi, A. Adsorption of Amido Black 10B from aqueous solution using polyaniline/SiO2 nanocomposite: Experimental investigation and artificial neural network modeling. Journal of colloid and interface science **510**, 246-261 (2018).

46 Szilagyi, B. & Nagy, Z. K. Aspect ratio distribution and chord length distribution driven modeling of crystallization of two-dimensional crystals for real-time model-based applications. Crystal Growth & Design **18**, 5311-5321 (2018).

47 Khadem, S. A. & Rey, A. D. Theoretical Platform for Liquid-Crystalline Self-Assembly of Collagen-Based Biomaterials. **7**, doi:10.3389/fphy.2019.00088 (2019).

48 Gurevich, S., Soule, E., Rey, A., Reven, L. & Provatas, N. Self-assembly via branching morphologies in nematic liquid-crystal nanocomposites. Physical Review E **90**, doi:10.1103/PhysRevE.90.020501 (2014).

49 Gupta, G. & Rey, A. D. Texture Rules for Concentrated Filled Nematics. Physical Review Letters **95**, 127802, doi:10.1103/PhysRevLett.95.127802 (2005).

50 Wulf, A. Biaxial order in cholesteric liquid crystals: Phenomenological argument. **59**, 6596-6598, doi:10.1063/1.1680039 (1973).

51 Wright, D. C. & Mermin, N. D. Crystalline liquids: the blue phases. Rev. Mod. Phys. Reviews of Modern Physics **61**, 385-432 (1989).

52 Doi, M. & Edwards, S. F. The theory of polymer dynamics. Vol. 73 (oxford university press, 1988).

53 Gennes, P. G. d. & Prost, J. The Physics of Liquid Crystals. (Clarendon Press, 1995).

54 Nayani, K., Chang, R., Fu, J., Ellis, P. W., Fernandez-Nieves, A., Park, J. O. & Srinivasarao, M. Spontaneous emergence of chirality in achiral lyotropic chromonic liquid crystals confined to cylinders. Nature Communications **6**, 8067, doi:10.1038/ncomms9067 (2015).

55 Das, S. K. & Rey, A. D. Computational thermodynamics of multiphase polymer–liquid crystal materials. Computational Materials Science **38**, 325-339, doi:https://doi.org/10.1016/j.commatsci.2005.10.009 (2006).

56 Das, S. K. & Rey, A. D. Colloidal crystal formation via polymer–liquid-crystal demixing. EPL (Europhysics Letters) **70**, 621 (2005).

57 Yang, X., Forest, M. G., Li, H., Liu, C., Shen, J., Wang, Q. & Chen, F. Modeling and simulations of drop pinch-off from liquid crystal filaments and the leaky liquid crystal faucet immersed in viscous fluids. Journal of Computational Physics **236**, 1-14 (2013).

58 Zhou, C., Yue, P. & Feng, J. J. Dynamic simulation of droplet interaction and self-assembly in a nematic liquid crystal. Langmuir **24**, 3099-3110 (2008).

59 Grecov, D. & Rey, A. D. Shear-induced textural transitions in flow-aligning liquid crystal polymers. Physical Review E **68**, 061704 (2003).

60 Sgalari, G., Leal, G. & Feng, J. The shear flow behavior of LCPs based on a generalized Doi model with distortional elasticity. J. Non-Newton. Fluid Mech. **102**, 361-382 (2002).

61 Tsuji, T. & Rey, A. D. Effect of long range order on sheared liquid crystalline materials Part 1: compatibility between tumbling behavior and fixed anchoring. J. Non-Newton. Fluid Mech. **73**, 127-152 (1997).

62 Zhou, R., Forest, M. G. & Wang, Q. Kinetic structure simulations of nematic polymers in plane Couette cells. I: The algorithm and benchmarks. Multiscale Modeling & Simulation **3**, 853-870 (2005).

63 Rey, A. D. Flow and texture modeling of liquid crystaline materials. Rheol. Rev **6**, 71-135 (2009).

64 Rey, A. D. Generalized cholesteric permeation flows. Physical Review E **65**, 022701 (2002).

65 Rey, A. D. Simple shear and small amplitude oscillatory rectilinear shear permeation flows of cholesteric liquid crystals. Journal of Rheology **46**, 225-240 (2002).

66 Rey, A. D. Structural transformations and viscoelastic response of sheared fingerprint cholesteric textures. J. Non-Newton. Fluid Mech. **64**, 207-227 (1996).

67 Rey, A. D. Theory of linear viscoelasticity of chiral liquid crystals. Rheologica acta **35**, 400-409 (1996).

68 Zhang, C., Acharya, A., Walkington, N. J. & Lavrentovich, O. D. Computational modelling of tactoid dynamics in chromonic liquid crystals. Liquid Crystals **45**, 1084-1100 (2018).

69 Khare, S., Kodambaka, S., Johnson, D., Petrov, I. & Greene, J. Determining absolute orientation-dependent step energies: a general theory for the Wulff-construction and for anisotropic two-dimensional island shape fluctuations. Surface science **522**, 75-83 (2003).

70 Bhattacharjee, A. K. Stochastic kinetics reveal imperative role of anisotropic interfacial tension to determine morphology and evolution of nucleated droplets in nematogenic films. Scientific reports **7**, 1-13 (2017).

71 Bagnani, M., Azzari, P., Assenza, S. & Mezzenga, R. Six-fold director field configuration in amyloid nematic and cholesteric phases. Scientific Reports **9**, 12654, doi:10.1038/s41598-019-48996-3 (2019).

72 Bagnani, M., Azzari, P., de Michele, C., Arcari, M. & Mezzenga, R. Submitted: Elastic Constants of Biological Filamentous Colloids: Estimation and Implications on Nematic and Cholesteric Tactoid Morphologies. acs nano (2020).

73 Almohammadi, H., Bagnani, M. & Mezzenga, R. Flow-induced order-order transitions in amyloid fibril liquid crystalline tactoids. arXiv preprint arXiv:2002.06983 (2020).

74 Bronnikov, S., Nasonov, A., Racleş, C. & Cozan, V. Kinetics of the Isotropic-Ordered Phase Transition in Binary Mixtures of Mesogenic Monomers and Polymers. Soft Materials **6**, 119-128 (2008).

75 McBride, K. & Sundmacher, K. Overview of Surrogate Modeling in Chemical Process Engineering. Chem. Ing. Tech. **91**, 228-239, doi:10.1002/cite.201800091 (2019).

76 Khadem, S. A. & Boozarjomehry, R. B. Development of Systematic Framework for an Intelligent Decision Support System in Gas Transmission Network. Industrial & Engineering Chemistry Research **54**, 10768-10786, doi:10.1021/acs.iecr.5b01681 (2015).

77 Hassanpour, H., Corbett, B. & Mhaskar, P. Integrating Dynamic Neural Network Models with Principal Component Analysis for Adaptive Model Predictive Control. Chemical Engineering Research and Design, doi:https://doi.org/10.1016/j.cherd.2020.03.031 (2020).

78 Kheradmandi, M. & Mhaskar, P. Model predictive control with closed-loop re-identification. Computers & Chemical Engineering **109**, 249-260 (2018).

79 Li, H., Zhang, Z. & Liu, Z. Application of artificial neural networks for catalysis: a review. Catalysts **7**, 306 (2017).

80 Chojaczyk, A., Teixeira, A., Neves, L. C., Cardoso, J. & Soares, C. G. Review and application of artificial neural networks models in reliability analysis of steel structures. Structural Safety **52**, 78-89 (2015).

81 Dougherty, M. A review of neural networks applied to transport. Transportation Research Part C: Emerging Technologies **3**, 247-260 (1995).

82 De Luna, P., Wei, J., Bengio, Y., Aspuru-Guzik, A. & Sargent, E. (Nature Publishing Group, 2017).

83 LeCun, Y., Bengio, Y. & Hinton, G. Deep learning. Nature **521**, 436-444, doi:10.1038/nature14539 (2015).

84 Brezak, D., Bacek, T., Majetic, D., Kasac, J. & Novakovic, B. in 2012 IEEE Conference on Computational Intelligence for Financial Engineering & Economics (CIFEr). 1-6 (IEEE).

85 Smith, C. & Jin, Y. Evolutionary multi-objective generation of recurrent neural network ensembles for time series prediction. Neurocomputing **143**, 302-311 (2014).

86 Shahnazari, H. Fault diagnosis of nonlinear systems using recurrent neural networks. Chemical Engineering Research and Design **153**, 233-245 (2020).

87 Shahnazari, H., Mhaskar, P., House, J. M. & Salsbury, T. I. Modeling and fault diagnosis design for HVAC systems using recurrent neural networks. Computers & Chemical Engineering **126**, 189-203 (2019).

88 Bengio, Y., Simard, P. & Frasconi, P. Learning long-term dependencies with gradient descent is difficult. IEEE transactions on neural networks **5**, 157-166 (1994).

89 Bengio, Y. Artificial neural networks and their application to sequence recognition. (1993).

90 Hochreiter, S. & Schmidhuber, J. Long short-term memory. Neural computation **9**, 1735-1780 (1997).

91 Greff, K., Srivastava, R. K., Koutník, J., Steunebrink, B. R. & Schmidhuber, J. LSTM: A search space odyssey. IEEE transactions on neural networks and learning systems **28**, 2222-2232 (2016).

92 Fischer, T. & Krauss, C. Deep learning with long short-term memory networks for financial market predictions. European Journal of Operational Research **270**, 654-669 (2018).

93 Ma, X., Tao, Z., Wang, Y., Yu, H. & Wang, Y. Long short-term memory neural network for traffic speed prediction using remote microwave sensor data. Transportation Research Part C: Emerging Technologies **54**, 187-197 (2015).

94 Chollet, F. Keras, https://github.com/keras-team/keras, https://keras.io. (2015).

95 Koza, J. R. & Koza, J. R. Genetic programming: on the programming of computers by means of natural selection. Vol. 1 (MIT press, 1992).

96 Khadem, S. A., Jahromi, I. R., Zolghadr, A. & Ayatollahi, S. Pressure and temperature functionality of paraffin-carbon dioxide interfacial tension using genetic programming and dimension analysis (GPDA) method. Journal of Natural Gas Science and Engineering **20**, 407-413 (2014).

97 Kim, Y.-K., Shiyanovskii, S. V. & Lavrentovich, O. D. Morphogenesis of defects and tactoids during isotropic–nematic phase transition in self-assembled lyotropic chromonic liquid crystals. Journal of Physics: Condensed Matter **25**, 404202 (2013).

98 Nayani, K., Fu, J., Chang, R., Park, J. O. & Srinivasarao, M. Using chiral tactoids as optical probes to study the aggregation behavior of chromonics. Proceedings of the National Academy of Sciences **114**, 3826-3831 (2017).

99 Lydon, J. Chromonic review. Journal of Materials Chemistry **20**, 10071-10099 (2010).

100 Doi, M. Soft Matter Physics. (OUP Oxford, 2013).

101 Petri, M., Menzel, A., Bunk, O., Busse, G. & Techert, S. Concentration effects on the dynamics of liquid crystalline self-assembly: time-resolved X-ray scattering studies. The Journal of Physical Chemistry A **115**, 2176-2183 (2011).

102 Chan, P. K. & Rey, A. D. Polymerization-induced phase separation. 2. Morphological analysis. Macromolecules **30**, 2135-2143 (1997).

103 Zuev, V. V. & Bronnikov, S. Self-assembling in a living supramolecular linear nematic polymer-like system. Liquid Crystals **35**, 1293-1298 (2008).

104 Diekmann, K., Schumacher, M. & Stegemeyer, H. Nucleus growth in liquid crystals. Liquid crystals **25**, 349-355 (1998).

105 Bronnikov, S., Racleş, C., Nasonov, A. & Cazacu, M. Kinetics of the nematic ordered phase growth during a temperature quench of an isotropic siloxane-azomethine polymer. Liquid crystals **33**, 1015-1019 (2006).

106 Ratke, L. & Voorhees, P. W. Growth and Coarsening: Ostwald Ripening in Material Processing. (Springer Berlin Heidelberg, 2013).

107 Sec, D., Porenta, T., Ravnik, M. & Zumer, S. Geometrical frustration of chiral ordering in cholesteric droplets. Soft Matter **8**, 11982-11988, doi:10.1039/c2sm27048j (2012).

108 Bronnikov, S., Kostromin, S. & Zuev, V. V. Kinetics of the isotropic–nematic phase transition in melted multi-component liquid crystal mixtures upon cooling. Phase Transitions **83**, 302-310 (2010).

109 Dierking, I. & Russell, C. Universal scaling laws for the anisotropic growth of SmA liquid crystal bâtonnets. Physica B: Condensed Matter **325**, 281-286 (2003).

110 Bronnikov, S. & Dierking, I. Quench depth dependence of liquid crystal nucleus growth: A time resolved statistical analysis. Physica B: Condensed Matter **358**, 339-347 (2005).

111 Bagnani, M., Nystrom, G., De Michele, C. & Mezzenga, R. Amyloid Fibrils Length Controls Shape and Structure of Nematic and Cholesteric Tactoids. Acs Nano **13**, 591-600, doi:10.1021/acsnano.8b07557 (2019).

5.10 Supporting Information

5.10.1 Supplementary Note S1: Details of obtaining results from DNS

1	The governing equations either diffusive or non-diffusive is implemented in the General PDE solver of COMSOL Multiphysics 5.3a. The important numerical settings are listed below: (1) Basis functions are biquadratic. (2) Time stepping is carried out by the Backward Euler method. (3) The stability of numerical solutions and mesh-independence are satisfied by having at least 60 elements per pitch length, $p_{\infty}=20\mu m$. NB: each of the simulations approximately uses 200 GB RAM with 32 Processors and takes three weeks (roughly five days for nucleation and sixteen days for coarsening).	COMSOL Multiphysics
2	MATLAB is used to communicate with COMSOL in order to extract dependent variables (five independent elements of **Q**-tensor and one concentration field) and independent variables (mesh, time and space). Note that, in this stage, the **Q**-tensor elements are converted to uniaxial order parameter and director field[1-3]. Finally, the extracted data are written in unstructured file format(.vtu) as described in our previous work[1].	MATLAB
3	By using interactive communication of ParaView and Python, all the scaler fields (uniaxial order parameter and concentration field) along with the director filed (uniaxial director field representing fibers orientation) can be dynamically visualized. All the time-series images are produced in this stage.	ParaView & Python
4	In this stage, OpenCV and Python are used for the sake of Image Processing to extract the time-series quantities such as tactoids population and their sizes from the time-series images.	OpenCV & Python

Figure 5-10. The overview of workflow applied to obtain results; from computing the results using DNS to Image Processing in regards to data extraction.

Furthermore, the material properties used in DNS are

Table 5-4. The material properties and parameter values used in the DNS. The square-brackets show the corresponding unit.

Parameters	Values	Parameters	Values	Parameters	Values
$\mathbf{n}$	5 [-]	χ	1.6 [-]	$\frac{L_2}{L_1}$	21[-]**
$\tilde{L}_{\phi-Q}$	-8×10^{-8}[-]	$\tilde{L}_{\phi}$	7×10^{-4} [-]	$\tilde{M}_{\phi}$	2.5×10^{-5} [-]
C_{ch}	98 [mg/ml]	C_{iso}	79 [mg/ml]	p_{∞}	20 [μm]

**$\frac{L_2}{L_1} = 2\frac{k}{k_2}$-1, $\frac{k}{k_2} = 11$ where $k_1=k_3=k$ and k_1, k_2, and k_3 are Frank elastic constants[3].

5.10.2 Supplementary Note S2: Details of LSTM-RNNs implemented in the present study

Table 5-5. Hyperparameters used for the LSTM-RNNs

	<L>	N
LSTM layers	2	2
units	30	15
dropout-rate	0.2	0.2
activation function	hyperbolic tangent	hyperbolic tangent
loss	'mean_squared_error'	'mean_squared_error'
optimizer	'adam'	'adam'
learning rate	0.01	0.01
epochs	200	100

The dropout-rate of 0.2 was applied to avoid model-overfitting.

5.10.3 Supplementary Note S3: Log-log plots of the universal growth laws

Since the power laws are transformed into linear laws in a log-log coordinate system, it is advantageous to plot the universal growth laws in the log-log scale. As can be seen in Table 5-1 and Table 5-2, the universal growth laws follow a generic power law as follows.

$$\langle L\rangle = \langle L\rangle_0 + a(\tilde{t}-\tilde{t}_0)^n \quad \text{(S1)}$$

$\tilde{t}_0 = \tilde{t}_l, \tilde{t}_l \leq \tilde{t} \leq \tilde{t}_l + \tilde{t}_n$,Nucleation period

$\tilde{t}_0 = \tilde{t}_{0C} = \tilde{t}_l + \tilde{t}_n, \tilde{t} \geq \tilde{t}_{0C}$,Coarsening period

where $\langle L \rangle_0$is the initial tactoid size at the beginning of each period, a and n stand for fitting parameters. Taking the log operator from both sides of eq.(S1) reveals the linearity behind the growth laws in logarithmic coordinates.

$$\begin{aligned} Y &= A + nX \\ A &= \ln(a) \\ X &= \ln(\tilde{t}\text{-}\tilde{t}_0) \\ Y &= \ln(\langle L \rangle - \langle L \rangle_0) \end{aligned} \quad \text{(S2)}$$

Given the mapping above, universal growth laws are transformed as follows.

- **Nucleation Period,** Figure 5-4**(c)**

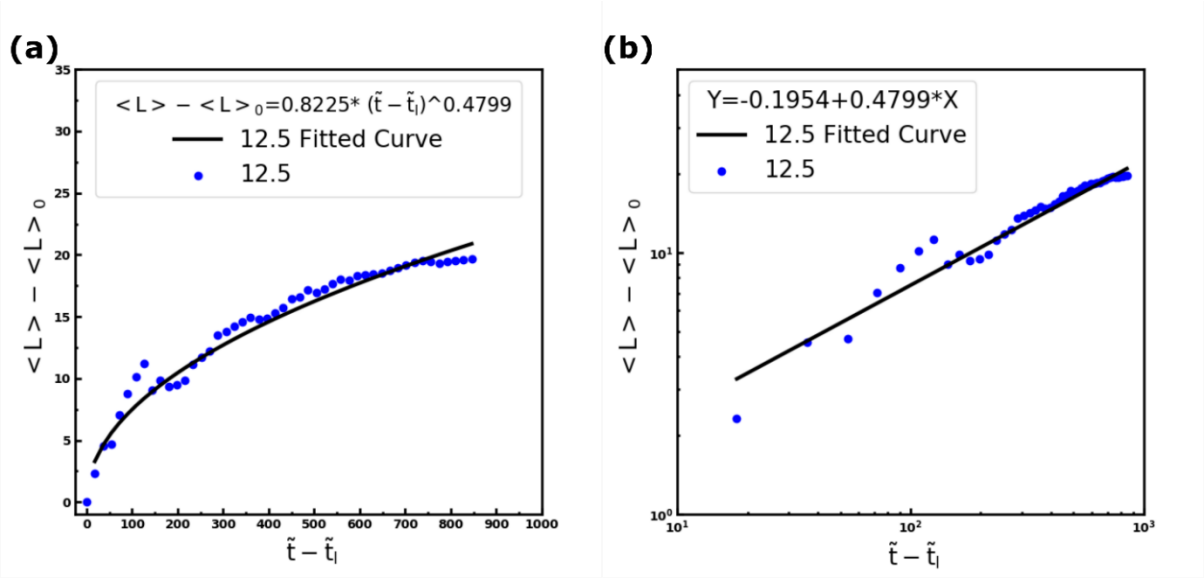

Figure 5-11. **(a)** Linear and **(b)** logarithmic scale plots of the characteristic length (i.e. tactoids average diameter) during the nucleation period for $\eta_q = 12.5\%, R^2$=0.970.

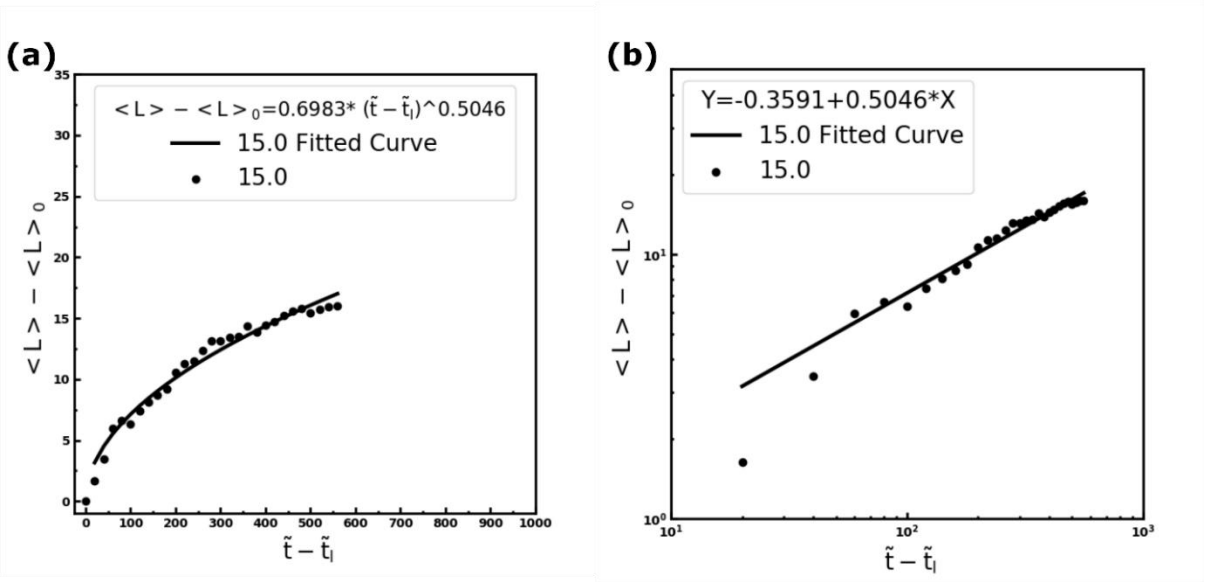

Figure 5-12. **(a)** Linear and **(b)** logarithmic scale plots of the characteristic length (i.e. tactoids average diameter) during the nucleation period for $\eta_q = 15.0\%, R^2 = 0.980$.

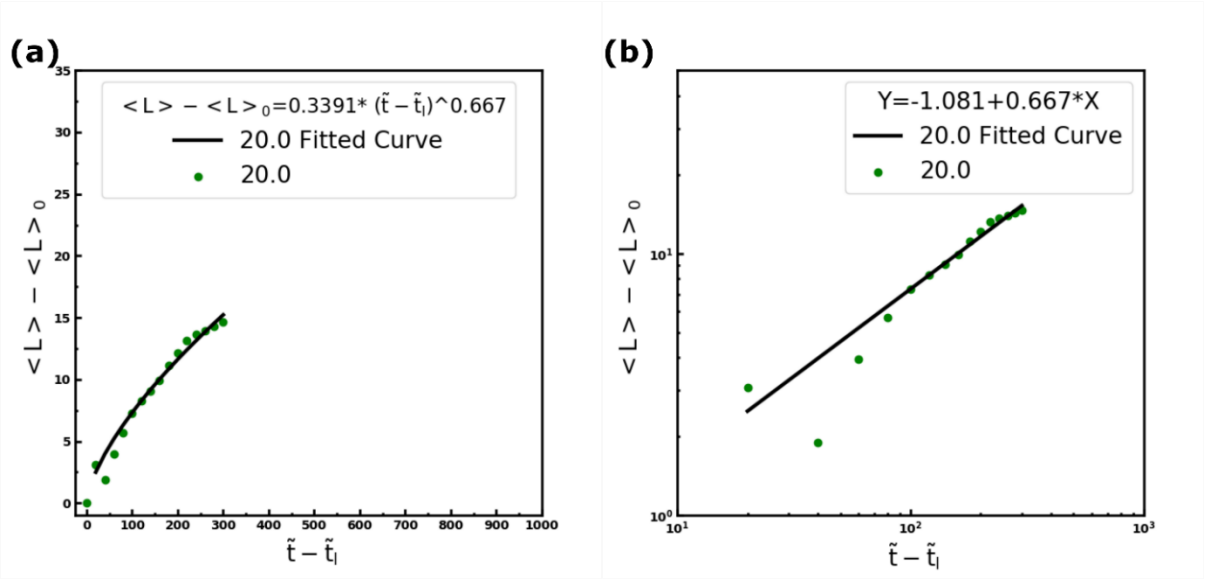

Figure 5-13. **(a)** Linear and **(b)** logarithmic scale plots of the characteristic length (i.e. tactoids average diameter) during the nucleation period for $\eta_q = 20.0\%, R^2 = 0.976$.

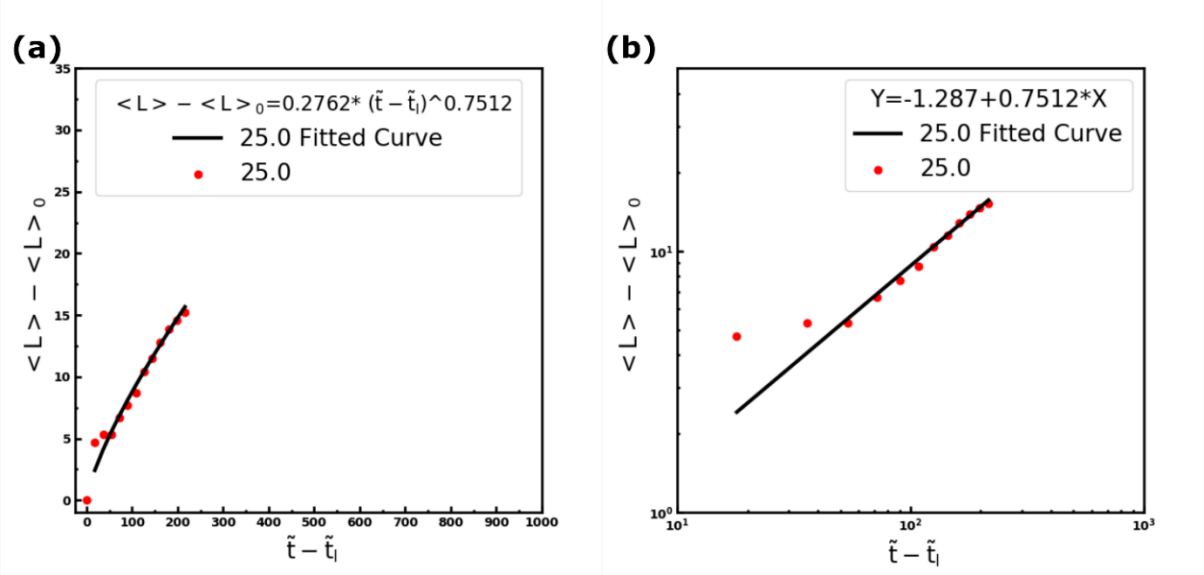

Figure 5-14. **(a)** Linear and **(b)** logarithmic scale plots of the characteristic length (i.e. tactoids average diameter) during the nucleation period for $\eta_q = 25.0\%, R^2$=0.971.

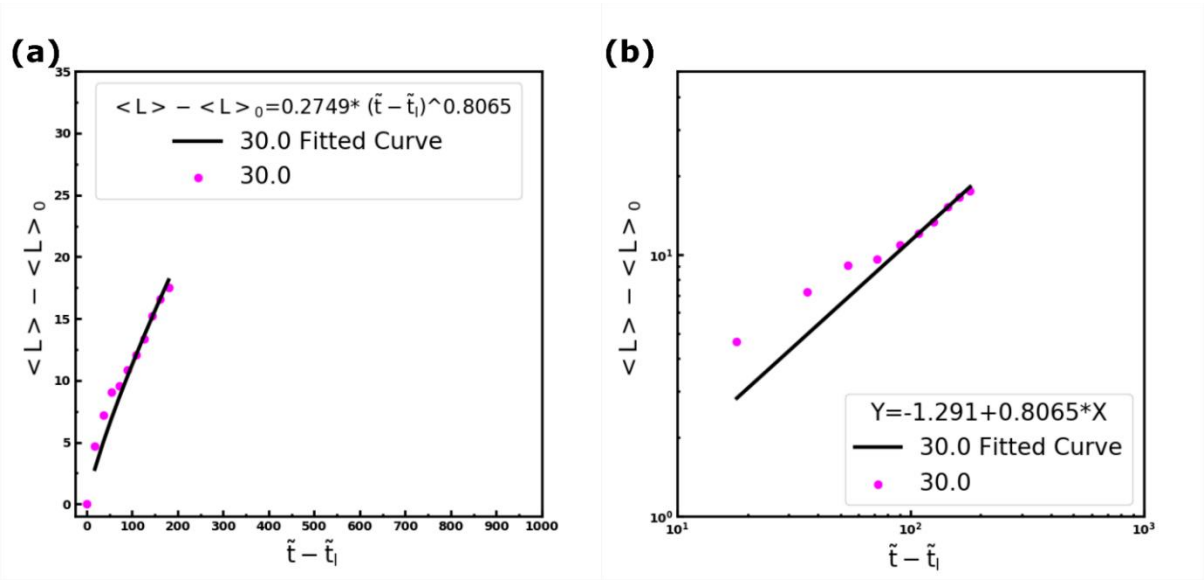

Figure 5-15. **(a)** Linear and **(b)** logarithmic scale plots of the characteristic length (i.e. tactoids average diameter) during the nucleation period for $\eta_q = 30.0\%, R^2$=0.970.

- **Coarsening Period,** Figure 5-5**(c)**

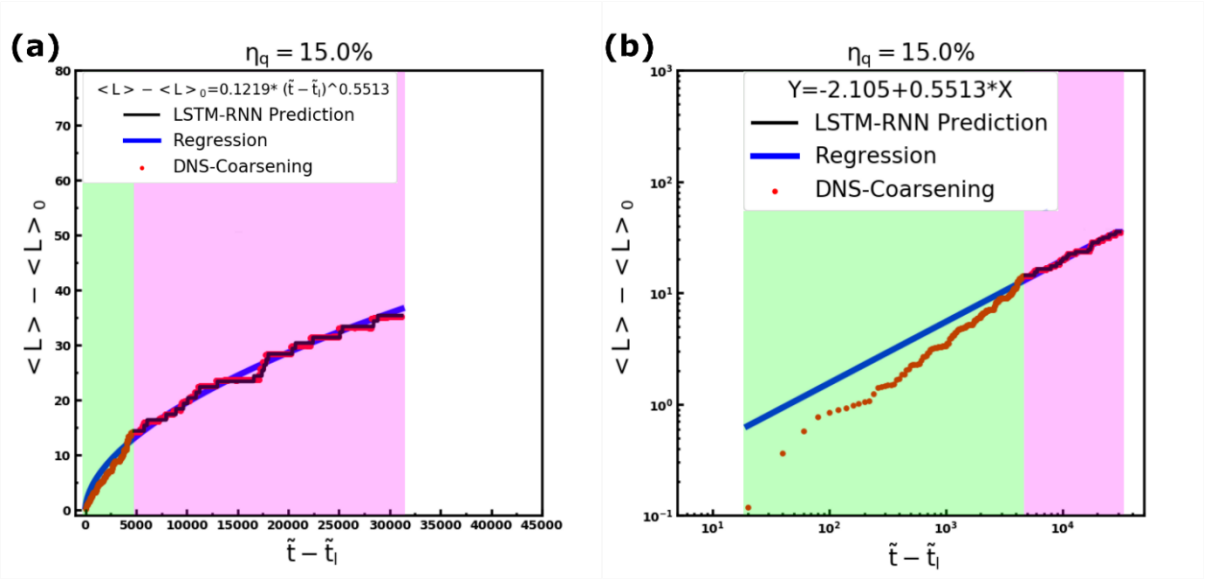

Figure 5-16. **(a)** Linear and **(b)** logarithmic scale plots of the characteristic length (i.e. tactoids average diameter) during the coarsening period for $\eta_q = 15.0\%, R^2 = 0.998$. The green zones in the panels (a) and (b) correspond to the same time interval, moreover, the pink zones show the remaining time interval. At the beginning of the coarsening period, the slight deviation of the curve fitted with the DNS results is magnified in the logarithmic scale (see the green zones).

- **Coarsening Period,** Figure 5-5**(d)**

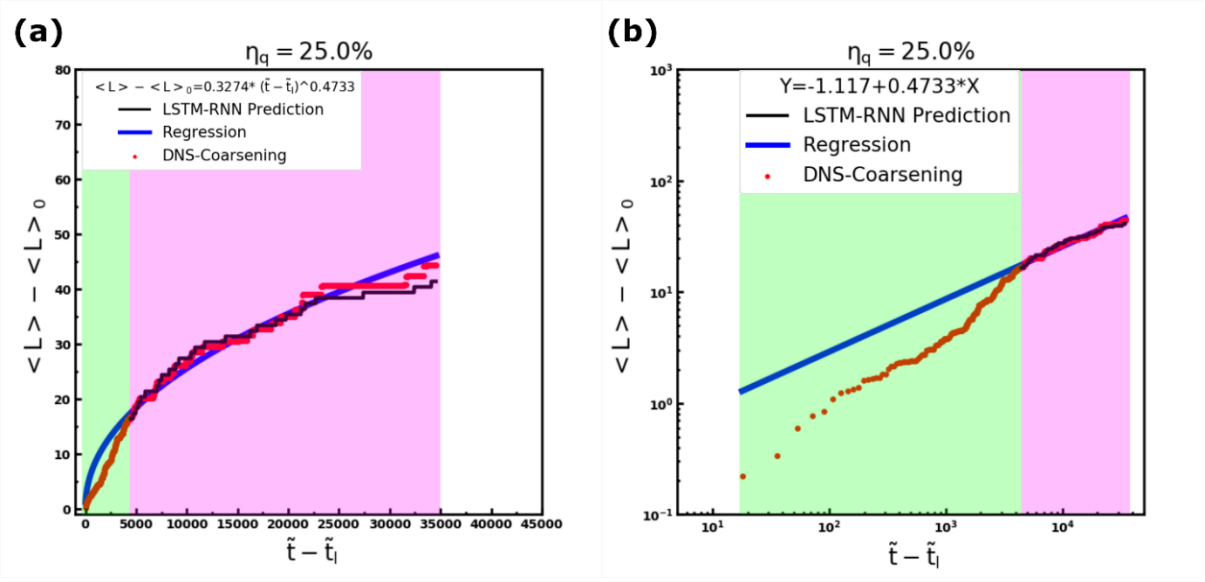

Figure 5-17. **(a)** Linear and **(b)** logarithmic scale plots of the characteristic length (i.e. tactoids average diameter) during the coarsening period for $\eta_q = 25.0\%, R^2 = 0.979$. The green zones in the panels (a) and (b) correspond to the same time interval, moreover, the pink zones show the remaining time interval. At the beginning of the coarsening period, the slight deviation of the curve fitted with the DNS results is magnified in the logarithmic scale (see the green zones).

- **Coarsening Period,** Figure 5-7**(a)**

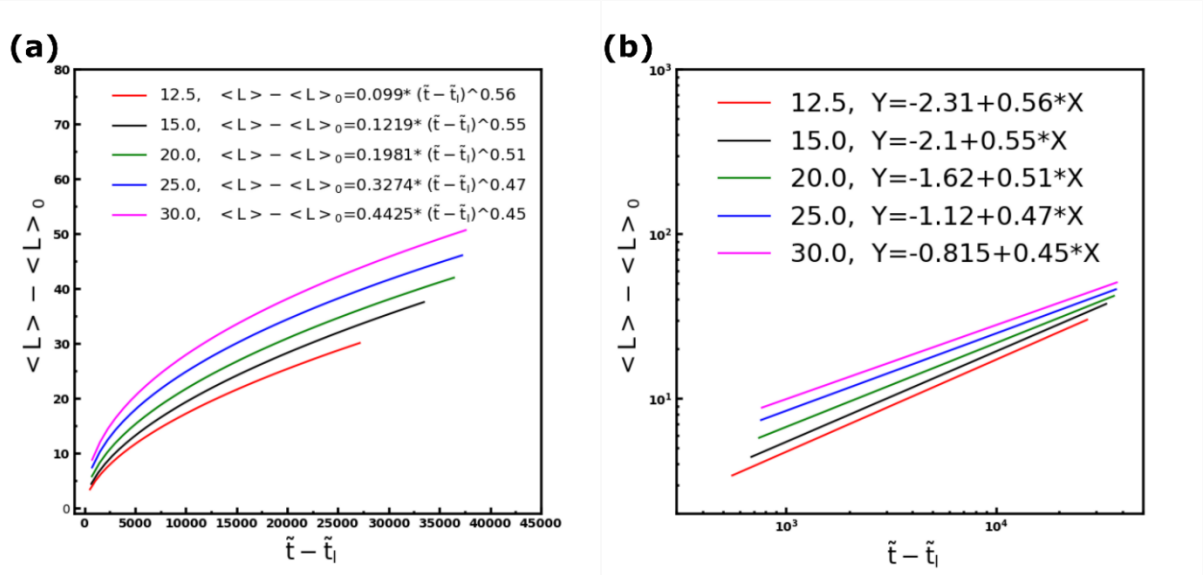

Figure 5-18. **(a)** Linear and **(b)** logarithmic scale plots of the characteristic length (i.e. tactoids average diameter) during coarsening period for $\eta_q(\%)$ =12.5, 15.0, 20.0, 25.0, and 30.0, and the corresponding $R^2$are 0.989, 0.998, 0.979, 0.979, and 0.979, respectively.

5.10.4 Supplementary Note S4: Formulation of the tactoids depopulation during the coarsening period

As tactoids population starts with N_m and declines over time, we introduce $N - N_m$as the independent variable to the Symbolic Regression algorithm. Then, the algorithm found a fractional model as $-(p_1\tilde{t} + p_2)/(\tilde{t} + p_3)$. The obtained model excellently meet the boundary condition between nucleation and coarsening periods; $N - N_m = 0$ at $\tilde{t} = \tilde{t}_{0C}$, leading to $p_2 = -p_1\tilde{t}_{0C}$. Doing further mathematical operations, the tactoids depopulation is rewritten as eq.(5-10).

5.10.5 Supplementary Movies

Movie S1	12.5% Quench Nucleation Period & Early Coarsening	https://youtu.be/A-rFdNGaIGo
Movie S2	15.0% Quench Induction & Nucleation & Coarsening Periods	https://youtu.be/11vp384sx20
Movie S3	25.0% Quench Induction & Nucleation & Coarsening Periods	https://youtu.be/SGbJeT-os8I
Movie S4	30.0% Quench Nucleation Period & Early Coarsening	https://youtu.be/51DkRlhcJ3E
Movie S5	Non-diffusive Model	https://youtu.be/3IGt8fzhQcg

References of Supporting Information (Chapter 5)

1 Khadem, S. A. & Rey, A. D. Theoretical Platform for Liquid-Crystalline Self-Assembly of Collagen-Based Biomaterials. **7**, doi:10.3389/fphy.2019.00088 (2019).

2 Wincure, B. & Rey, A. D. Growth and structure of nematic spherulites under shallow thermal quenches. Continuum Mech. Thermodyn. **19**, 37-58, doi:10.1007/s00161-007-0043-z (2007).

3 Murugesan, Y. K. & Rey, A. D. Modeling Textural Processes during Self-Assembly of Plant-Based Chiral-Nematic Liquid Crystals. **2**, 766-785 (2010).

Chapter 6. Relaxation dynamics in bio-colloidal cholesteric liquid crystals confined to cylindrical geometry

6.1 Preface

Through an experimental study carried out by our ETH-Zurich collaborator, two distinct relaxation dynamics are identified for β-lactoglobulin amyloid fibrils (BLG) and cellulose nanocrystals (CNC), which are called slow-fast and smooth relaxation, respectively. Building on the governing equations formulated in Chapter 4, the relaxations are simulated. The excellent agreement between simulation results and experimental observations confirms the success of the proposed modeling and numerical techniques used to solve the governing equations. We then rely on the simulation to explore the physics behind the distinct relaxation dynamics; thereby generalizing the relaxation dynamic behaviors in terms of material properties such as pitch length and coherence length. Additionally, a systematic approach based on the combination of simulation and experiment is proposed to estimate viscoelastic properties such as Landau elastic constant (L_1) and rotational viscosity.

6.2 Abstract

Para-nematic phases, induced by unwinding chiral helices, spontaneously relax to a chiral ground state through phase ordering dynamics that are of great interest and crucial for applications such as stimuli-responsive and biomimetic engineering. In this work, we characterize the cholesteric phase relaxation behaviors of β-lactoglobulin amyloid fibrils and cellulose nanocrystals confined into cylindrical capillaries, uncovering two different equilibration pathways. The integration of experimental measurements and theoretical predictions reveals the starkly distinct underlying mechanism behind the relaxation dynamics of β-lactoglobulin amyloid fibrils, characterized by slow equilibration achieved through consecutive sigmoidal-like steps, and of cellulose nanocrystals, characterized by fast equilibration obtained through smooth relaxation dynamics. Particularly, the specific relaxation behaviors are shown to emerge from the order parameter of the unwound cholesteric medium, which depends on chirality and elasticity. The experimental findings are supported by direct numerical simulations, allowing to establish hard-to-measure viscoelastic properties without applying magnetic or electric fields.

6.3 Introduction

Unwinding the helices of a chiral nematic liquid crystal drives the cholesteric phase (N*) to a para-nematic phase (PN)[1], characterized by a higher energy state compared to the equilibrium chiral nematic phase. Thus, the para-nematic phase thermodynamically tends to relax by relieving the excess free energy[2]. Through this thermodynamically driven relaxation, unwound helices forming a para-nematic state are spontaneously self-reconstructed leading to a chiral ground state; the PN-N* transition is thus self-driven. The dynamics of self-reconstruction (relaxation) in biological chiral lyotropic liquid crystals (BCLLCs) is of particular interest for forming retarder films and cholesterol color filters[3], plasmonic mesostructured materials[4], stimuli-responsive materials design[2,5-8], and processing of advanced materials[9] such as biomimetic film formation[10,11] replicating, for example, structural motifs of cortical bone and cornea[12,13]. Despite its importance, the prediction and quantification of the relaxation dynamics of BCLLCs have remained up to date non-trivial and challenging both experimentally and theoretically.

The confinement geometry can potentially affect relaxation dynamics as it has a considerable impact on the relaxed configuration[14-22]. The confinement geometry considered herein is a micron-sized cylindrical capillary for which the ground states of chiral mesogens have been extensively studied[17,18,23]. Given that the capillary diameter in our study is greater than the pitch length (i.e. $\frac{D}{p_\infty} = 6$ and $\frac{D}{p_\infty} = 13$ for BLG and CNC, respectively), the ground state of fibers macroscopic orientation eventually ends up into a concentric configuration in which the chiral helices are aligned along the cylinder diameters [17,19,24]. This microstructure is of importance in biomimicry as it, for example, mimics the osteon architecture which is the essential part of compact bone[13].

Furthermore, viscoelastic properties, such as elastic constants and rotational viscosity, play significant roles in the relaxation dynamics of liquid crystals (LCs). Another importance of viscoelastic properties is their usages in LC rheology nematodynamics, and flow-processing of fibers and films[1,25-31] such as biomimetic material design through coating[10]. Yet, the estimation of these properties has been a long-lasting challenge in the area of mesogenic solutions[32,33]. In particular, these properties strongly depend on concentration regimes; dilute ($c < \ell^{-3}$), semidilute ($\ell^{-3} < c < d^{-1}\ell^{-2}$), and concentrated ($c > d^{-1}\ell^{-2}$) where c, ℓ and d denote number density, length, and diameter of fibers, respectively[32]. The first two regimes have been partially understood whereas the last one, in which a liquid-crystalline phase emerges, has not been

adequately addressed, particularly for BCLLCs[32-34]. The difficulty in the estimation of viscoelastic properties of BCLLCs stems from the fact that standard techniques for viscoelastic properties measurements are based on applying a magnetic or electrical field to reorient mesogenic constituents[35-39] and, in general, these techniques are not readily applicable for BCLLCs due to their low diamagnetic and dielectric susceptibilities[39,40]. In this case, the convenient alternative is flow-alignment[1,41-43]. To destabilize and unwind the chiral helices, rather than employing external fields such as magnetic or electric field, we thus rely on the surface tension-driven flow-induced orientation (FIO)[25] created during capillary filling.

In the present study, we execute a methodology that allows quantifying spatio-temporal relaxation of chiral biological LCs confined to cylindrical capillaries, which corresponds to the spontaneous PN-N* transition. In particular, we characterize the relaxation behavior of BLG and CNC. Surprisingly, we uncovered that these two similar bio-colloidal LCs relax through considerably different pathways. BLG slowly relaxes through consecutive steps; each of these steps corresponds to a temporary slow formation of cholesteric layers, followed by a rapid equilibration which forms a sequence of plateaus, yielding slow-fast mode. The second system investigated, CNC, relaxes faster and with a smoother and continuous behavior characterized by the absence of plateaus, yielding smooth mode. The section 'Distinct relaxation dynamics' elaborates these findings along with other different relaxation behaviors in detail. Thereafter, in the section 'Mechanisms of BLG and CNC relaxations', we characterize and explain the essential mechanisms behind the novel relaxation dynamics. In this regard, we use direct numerical simulations showing that we can quantitively predict these relaxation dynamics in excellent agreement with experimental observations. After establishing the relaxation mechanisms, we reveal the physics behind the explored mechanisms and generalize the physical rules governing the relaxation dynamics in the section 'Understanding the physical origins of relaxation mechanisms'. In this section, our results reveal that the relaxation dynamics of BCLLCs confined to cylindrical capillaries generically obey the slow-fast or the smooth behaviors governed by a delicate interplay of chirality, viscoelasticity, and confinement geometry. Lastly, in section 'Properties estimation and relaxation time controllers', we propose a systematic framework to estimate fundamental viscoelastic properties without applying magnetic or electric fields, which is of particular interest for the BCLLCs. In addition to validating the estimated properties acquired by the proposed framework, the physical factors controlling the relaxation time are discussed.

6.4 Results

6.4.1 Distinct relaxation dynamics

Figure 6-1(a-l) show the sequences of microscopy images analyzed by PolScope[46]. The analysis allows extrapolating the average of fibers' orientation over the thickness of capillary tube and the 2D fibers' orientation is represented according to the colormap shown in Figure 6-1(f); for example, the pink color which is ubiquitous in the POM images indicates that fibers are aligned parallel to the central axis (y-axis), Figure 6-1(a-l,o). Initially (right after filling capillaries), the fibrils located close to the center of the cylindrical capillary form a para-nematic phase with a director field parallel to the central axis of the cylinder due to flow-induced alignment during capillary filling (described by pink color). Shortly thereafter (within the first 20 minutes), dark zones emerge in the center of the capillaries and some cholesteric fingerprints are already visible near the walls.

During equilibration, chiral fronts form and propagate from the wall inwards and gradually replace the dark areas, showing how the system is progressively equilibrated by the self-reconstruction of unwound chiral helices, Figure 6-1(a-l),Supplementary Movies 1,2. The physical origin of the initial dark areas emerging from the para-nematic phase cannot be interpreted unequivocally since the absence of birefringence can correspond to different scenarios. In fact, the fibers' orientation in the dark areas (i.e. capillary middle) can represent three different situations: (1) Fibers do not possess mesogenic correlation and the phase could be isotropic although the fibers' concentration is a constant equal to the cholesteric bulk (i.e. the upper binodal miscibility boundary). (2) Fibers are aligned normal to the plane and thus the phase is nematic; (3) The cholesteric helices are aligned normal to the plane and the light path, thus the phase could be already cholesteric. Determining the fibers' configuration in the dark areas is addressed below.

To rationalize the observations, we define the dimensionless normalized relaxation progress:$R(t) = \frac{\bar{q}(t)}{q_\infty}$, where $\bar{q}(t) = \frac{2\pi}{\bar{p}(t)}$, $\bar{q}(t)$ and $\bar{p}(t)$are the spatially-averaged chiral wavevector and pitch length, respectively. This quantity, R, provides insight into the amount of space occupied by the cholesteric phase at any given time in the system. The relaxation progress, R, ranges from 0 to 1; for R=0, there is no chiral nematic phase in the system, and when R=1, the chiral nematic phase fills the sample and the system reaches the ground state. To obtain $\bar{q}(t)$, each time-series POM snapshot is partitioned into approximate monodomains, and $\bar{q}(t)$ is then computed as the weighted average of local chiral wavevectors:$\bar{q}(t) = \sum \frac{A_i q_i}{A}$

where A, $A_i$and q_i indicate the total area of the snapshot, area of the cholesteric zone and chiral wavevector for the i-th partition, respectively. Figure 6-1(m,n) show the time evolution of R for BLG and CNC, respectively. R starts with an initial value representing the chiral nematic layers that are near the bounding surface at the very beginning of the experiment. Eventually, R reaches unity, indicating the equilibration is complete all over the field of view and the concentric and monodomain configurations are formed in circular cross-sections and lateral planes, respectively; schematically shown in Figure 6-1(o). Note that the monodomain fingerprint gradually appearing from top and bottom toward the center in the POM images is due to the spatial average of concentric configuration progressively forming from the capillary wall towards the capillary center. In other words, the 2D fingerprint on the lateral plane provides insight into the 3D configuration exiting inside the capillary; see Figure 6-1(a-l,o).

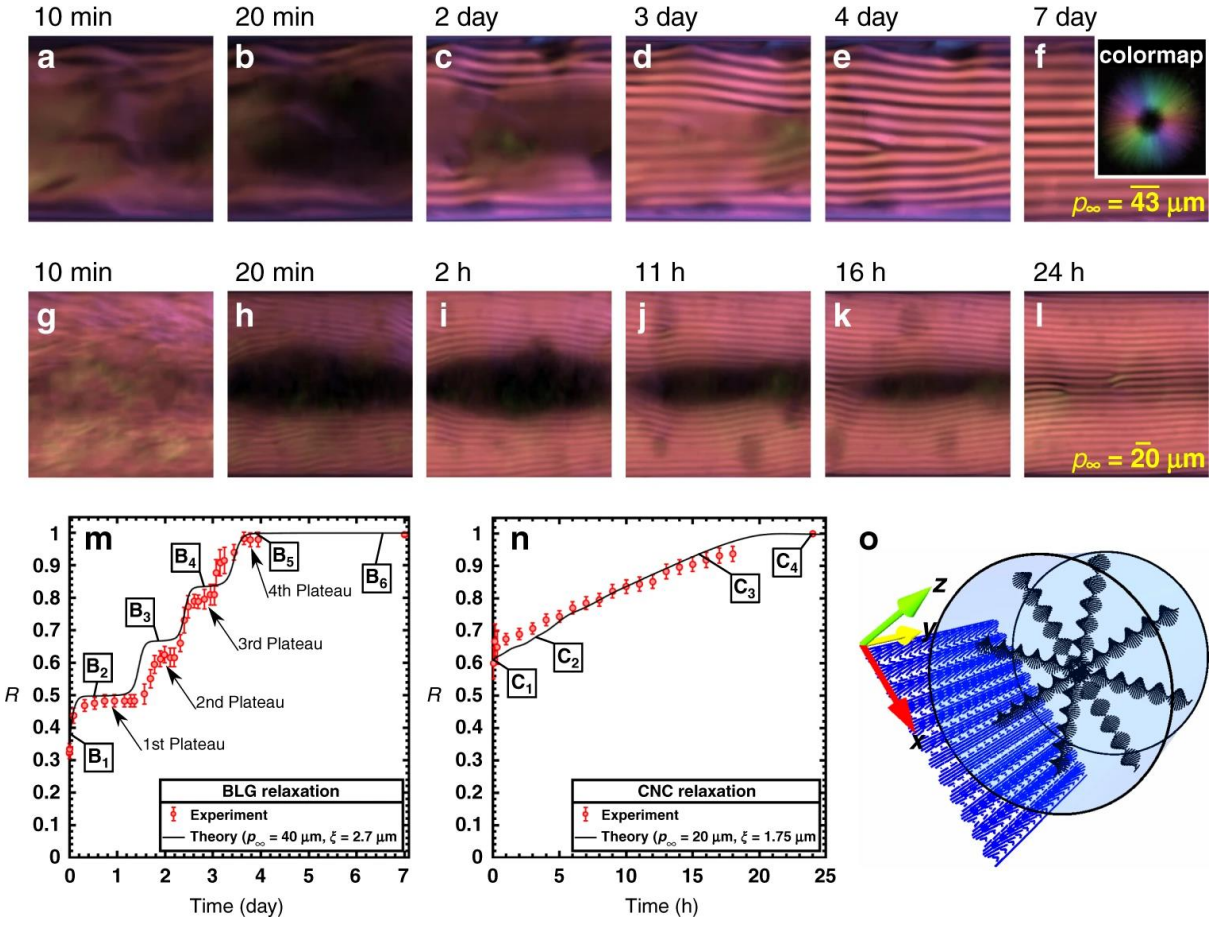

Figure 6-1. **Slow-fast and smooth relaxation dynamics corresponding to BLG and CNC, respectively. (a-f)** Time-series snapshots of BLG microscopy (POM) images. **(g-l)** Time-series snapshots of CNC microscopy (POM) images. The images shown in panels(a-l) were experimentally acquired using the LC PolScope device and different colors represent different director field orientations which are appreciated according to the colormap depicted as the inset in the panel (f). See Supplementary Note 1 for the detailed discussion on the mapping between fibers orientation and colormap. Note that the colormap shown as the inset in the panel (f) is

applicable for all the microscopy images studied in this work. Over the relaxation time, cholesteric fingerprints progressively propagate into the unwound state (dark zone). Times elapsed from the beginning of relaxation are shown on top-left corners; min and hr stand for minutes and hours, respectively. **(m)** Experimental observation and numerical simulation on the normalized relaxation progress curve, R, for BLG. The labels B_1 to B_6 correspond to Figure 6-2. **(n)** Experimental observation and numerical simulation on the normalized relaxation progress curve, R, for CNC. The labels C_1 to C_4 correspond to Figure 6-3. **(o)** The coordinate system used throughout this study along with a schematic illustration of a capillary tube indicating the ground state of fibers configuration in a circular cross-section in the xz-plane, known as concentric, and the averaged fibers configuration in a lateral plane in the xy-plane, known as chiral monodomain. The averaged fibers configuration on the lateral plane is representative of the colormap PolScop analysis shown in the panels (a-l).

BLG and CNC are similar from various viewpoints; these BCLLCs are aqueous solutions of semi-rigid rod-like bio-colloidal LCs characterized by a long pitch length ($p_{\infty,BLG}$=43μm and $p_{\infty,CNC}$=20μm), high aspect ratio (ℓ_{BLG}=652nm and ℓ_{CNC}=325nm, D_{BLG}=4nm, D_{CNC}=4.6nm, $(\ell/D)_{BLG}$=163, and $(\ell/D)_{CNC}$=71), similar polydispersity, critical concentrations, and densities (Supplementary Note 2, Table 6-1)[14,21,22,44,45]. Lastly, as estimated in this study, BLG and CNC possess similar rotational viscosity coefficients, L_1 Landau elastic constants, and coherence lengths (Table 6-1 and Table 6-2). Surprisingly, although BLG and CNC have multiple physical properties that are similar and are confined into an identical capillary tube, $D=260\mu m$, they manifest remarkably different relaxation according to these three criteria:

The first difference is the characteristic time required for the spontaneous PN-N* transition during which the fibers equilibrate from the unwound state (i.e. non-equilibrium para-nematic) to the chiral ground state, see Figure 6-1. BLG closely reaches the equilibrium state 4 days after capillary filling. In the time span of 4 to 7 days, relaxation has minor progress and defects may be released over this period; see Figure 6-1(a-f,m). The relaxation of CNC suspension only takes 1 day to reach equilibrium; see Figure 6-1(g-l,n). Hence, the relaxation time of BLG is nearly four times longer compared to CNC. It is important to notice that at the beginning of the relaxation process, when compared with BLG, CNC has more intact chiral helices near the walls; see Figure 6-1(b,h). This fact is also highlighted in Figure 6-1(m,n), where R, evolves from 0.6 to 1 as relaxation progresses for CNC, while it goes from 0.3 to 1 for BLG. Indeed, the higher initial relaxation progress is, the shorter time would be expected for achieving the relaxed state; thus, the higher initial relaxation progress of CNC, R=0.6, certainly plays role in shortening the relaxation time. To achieve a quantitative comparison between the two

relaxation behaviors, we compute the relaxation rates for the two systems. The relaxation progress of CNC evolves by 40% over 1 day for reaching the equilibrium point (R=1), while it evolves by 70% over 4 days for BLG and therefore the relaxation rates are 40% and 17.5% per day respectively confirming that CNC relaxation is more than two times faster compared to BLG.

The second difference between these two systems involves the number of trapped defects at equilibrium. As shown in Figure 6-1(a-l), the ground state of BLG shows fewer defects compared to CNC. It has already been shown that, for a given pitch length, more defects emerge provided the geometric size increases[47], here the geometric size is the diameter of the cylindrical capillary. Similarly, at a fixed capillary diameter D=260µm, the number of defects increases when the pitch length is shorter. For BLG, $p_{\infty,BLG} = 43\mu m$, and for CNC, $p_{\infty,CNC} = 20\mu m$, corresponding to zero and four defects respectively; see Figure 6-1(f,l). The ratio of geometric size to pitch length is thus an indicator for the number of generated defects; BLG relaxation gives rise to fewer defects compared to CNC suspension owing to $\frac{D}{p_{\infty,BLG}} = 6$ and $\frac{D}{p_{\infty,CNC}} = 13$. Another factor controlling the number of trapped defects is the relaxation time. Faster relaxation dynamics lead to more trapped defects as defects do not have time to be expelled. Thus, the CNC faster relaxation dynamic should also be taken to account as a promoter of trapped defects. Taken together, the number of defects is directly and inversely proportional to $\frac{D}{p_{\infty}}$ and the relaxation time, respectively. Therefore, it is ideally expected that the defect-less ground state can be achieved as long as $\frac{D}{p_{\infty}}$ and the relaxation time are sufficiently small and long, respectively. It should also be taken into consideration that the defect-less structure is achieved on a defined region of interest (260µm×260µm) for BLG as shown in Figure 6-1(a-f), Figure 6-2; however, it is impractical to reach the defect-less structure on a large domain (e.g. 600µm×260µm) even after equilibration, see Supplementary Note 3.

Although the defect analysis discussed above was performed on the region of interest (260µm×260µm), Supplementary Note 3 demonstrates that the chosen system size is statistically large enough to extend the concluded results regarding the number of trapped defects to larger regions. As shown in Supplementary Figure 3, the number of defects trapped in the BLG system is less compared to CNC on a larger region (600µm×260µm) after equilibration (10 days for BLG and 3 days for CNC). Additionally, the defects existing in the capillary are mobile and thus can translate in and/or out the system investigated

(260µm×260µm); however, the results already discussed are always statistically valid; see Supplementary Movies 1,2, Supplementary Note 3.

Finally, these two materials differ on how the speed of relaxation changes over time. As shown in Figure 6-1(m), BLG relaxes over consecutive steps consisting of four plateaus, which we described as slow-fast relaxation behavior. During each plateau, there is no discernible change in the total area of the striped zone, reflecting that cholesteric phase formation slows down considerably, as discussed below. However, in the CNC suspension, the relaxation is characterized by a smooth behavior, where no clear plateau can be detected, see Figure 6-1(n).

The liquid crystal rotational viscosity is the resistance to rotations of the average macroscopic director orientation[32,33]. For this reason, it is expected that the longer relaxation time observed for BLG can be attributed to higher rotational viscosity of BLG. However, there has not yet been any report on rotational viscosities and relaxation trends of these two bio-colloids, and the physical origins behind the different behaviors remain up to date unexplored. The solid lines shown in Figure 6-1(m,n) are the predictions obtained by direct numerical simulations of the time-dependent **Q**-tensor continuum model of cholesteric liquid crystals that describes the total free energy minimization. In our work, the net free energy of the system is comprised of free energy functionals given by the well-established continuum theories of Landau-de Gennes (LdG) and Frank-Oseen-Mermin (FOM)[25,32,48,49]; see section 'Direct numerical simulation'. As shown in Figure 6-1(m,n), the adopted theoretical approach predicts both the slow-fast and smooth relaxation dynamics for BLG and CNC, respectively. Hence, we rely on continuum liquid crystal theory to first explore the physics behind the observations and secondly to estimate viscoelastic properties, including rotational viscosity coefficient which allows us rationalizing the fast and slow relaxation behaviors of CNC and BLG, respectively.

6.4.2 Mechanisms of BLG and CNC relaxations

As shown in Figure 6-2, the theoretical and experimental results consistently show that cholesteric layers (i.e. the striped bands in POM images) are gradually formed from the top and bottom walls on the lateral plane. As can be seen in our results, the relaxation (the PN-N* transition) spontaneously takes place through the chiral front propagation; the cholesteric fingerprints radially propagate from the circular wall inward through the unwound para-nematic medium until the concentric configuration is achieved. This configuration is expected

since the capillary diameter is larger than pitch length[17,19], $\frac{D}{p_\infty} = 6$ (Supplementary Note 4 and Movie 3).

The mechanism of BLG relaxation generally consists of two phases (Supplementary Movies 3, 4) that can be described as

Phase (I): This phase takes place over a considerably short time span in the early relaxation. During Phase (I), all fibers, which are in the para-nematic state, lose their initial order parameter, $S_i = 0.6$[42], and then turn into a low-order-parameter para-nematic state (nearly isotropic), $S_{d,\,BLG} \approx 0.33$ (Figure 6-2,Supplementary Movies 3,4).

Phase (II): Right after rapid formation of the para-nematic medium with a low order parameter (i.e. Phase (I)), relaxation goes through Phase (II) in which a circular chiral front propagates and rewinds the fibers. As can be seen in Supplementary Movies 3,4, Phase (II) in BLG relaxation follows a time-periodic mechanism in which one half-pitch cholesteric layer is formed. The formation of each half-pitch consists of four stages; these stages are discussed in Supplementary Note 5 .

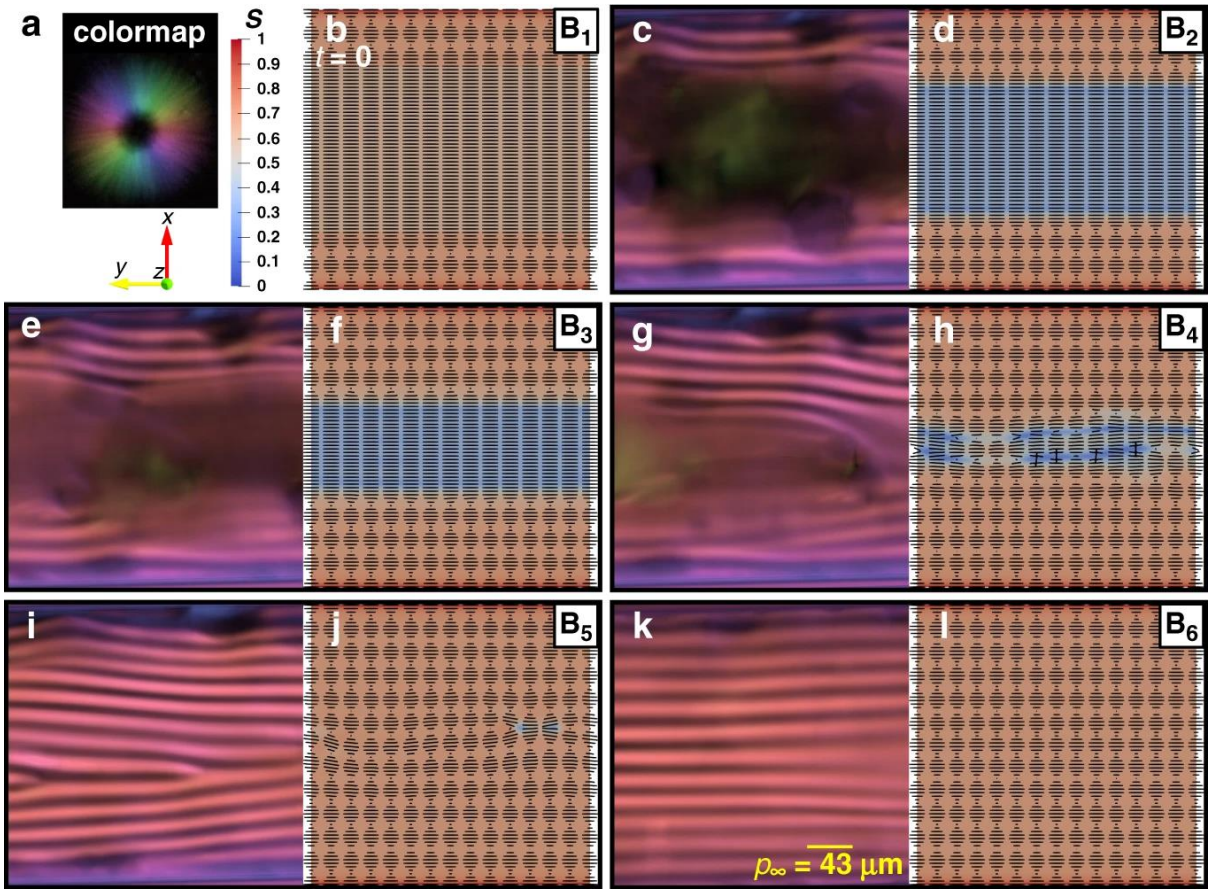

Figure 6-2. **Mechanism of slow-fast dynamic in BLG relaxation. (a)** The colormap indicating the fibers orientation in the experimental POM panels captured by the LC PolScope device (see Supplementary Note 1 for further information), the blue-to-red spectrum showing the order parameter, S, computed by direct numerical simulation (see Supplementary Note 6 for further information), and the coordinate system. **(b)** Initialization of director field in direct numerical simulation, representing the initial configuration of fibers. **(c, e, g, i, k)** The experimental POM panels corresponding to the B_2 to B_6 stages shown in Figure 6-1(m). **(d, f, h, j, l)** The schematic fibers orientation and their order parameter computed by direct numerical simulation in the lateral plane for the B_2 to B_6 stages shown in Figure 6-1(m). . General Note: the label numbers from B_1 through B_6 are marked in Figure 6-1(m).

The slow-fast relaxation observed for BLG consists of 4 sigmoid-like steps, and each of which ideally corresponds to the formation of a circular half-pitch, $\frac{p_\infty}{2}$. In particular, the label numbers B_2, B_3, B_4, and B_5 in Figure 6-1(m) and Figure 6-2correspond to the circular formation of $\frac{3p_\infty}{2}$, $\frac{4p_\infty}{2}$, $\frac{5p_\infty}{2}$ and $\frac{6p_\infty}{2}$, respectively (see more details in Supplementary Note 4). This behavior is confirmed by simulations and is consistent with the experimental analysis concerning both fibers configuration and trapped defects; however, the simulation prediction of cholesteric layers formation is slightly overestimated. For this reason, the theoretical prediction of relaxation progress, R, is slightly higher than the experimental data.

Figure 6-3 illustrates representative images of the equilibration sequence for CNC fibers, showing that this system relaxes through similar mechanisms, achieving concentric configuration as expected from previous works[17,19], see Supplementary Note 4. During Phase (I), the order parameter of CNC fibers that are in the para-nematic medium is dramatically dropped to $S_{d,\,CNC} \approx 0$ at the beginning of relaxation despite their initial order parameter $S_i=0.6$[42] and as a consequence, isotropic phase emerges from the para-nematic medium, followed by Phase (II), where the chiral front propagates into an isotropic medium (Supplementary Movie 5).

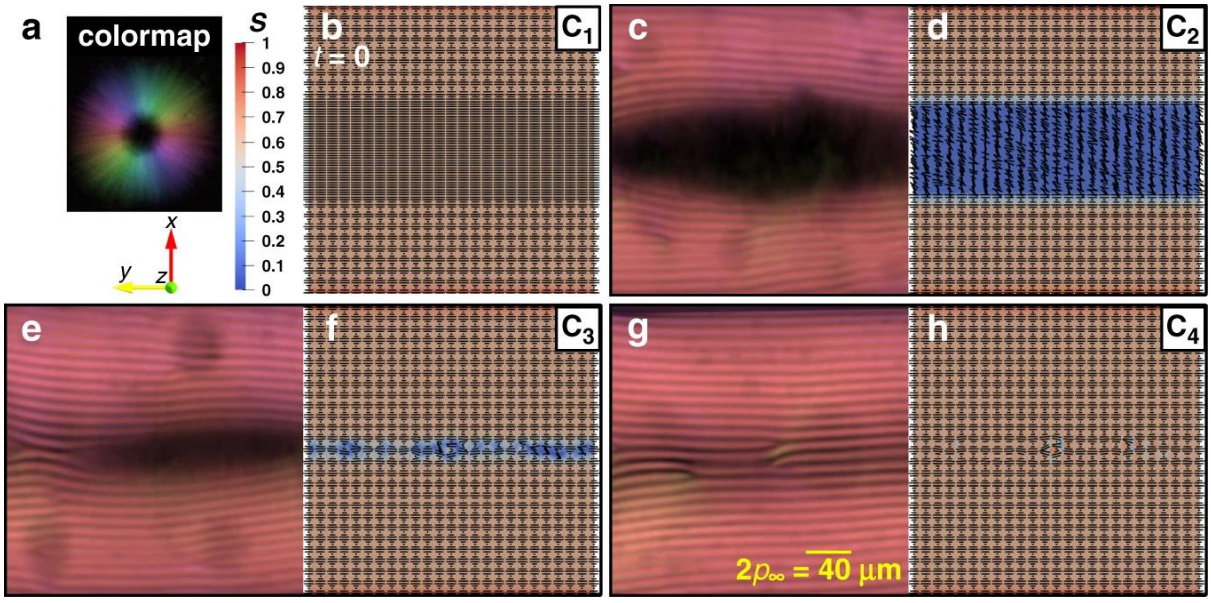

Figure 6-3. **Mechanism of smooth dynamic in CNC relaxation. (a)** The colormap indicating the fiber orientation in the experimental POM panels captured by the LC PolScope device (see Supplementary Note 1 for further information), the blue-to-red spectrum showing the order parameter, S, computed by direct numerical simulation (see Supplementary Note 6 for further information), and the coordinate system. **(b)** Initialization of director field in direct numerical simulation, representing the initial configuration of fibers. **(c, e, g)** The experimental POM panels corresponding to the C_2 to C_4 stages shown in Figure 6-1(n). **(d, f, h)** The schematic fibers orientation and their order parameter computed by direct numerical simulation in the lateral plane for the C_2 to C_4 stages shown in Figure 6-1(n). General Note: the label numbers from C_1 through C_4 are marked in Figure 6-1(n).

According to the LdG theory, the critical order parameter at the order-disorder phase transition can be considered as $S_c=0.25$[32], which means that, if $S > S_c$ fibers possess orientational ordering, otherwise fibers lose their correlations and the phase becomes isotropic, see Supplementary Note 7. The simulation results reveal that, during the early relaxation, order parameters of BLG and CNC fibers in the para-nematic mediums have dropped to $S_{d,\,BLG} \approx 0.33$ and $S_{d,\,CNC} \approx 0$, respectively. Hence, at the beginning of the relaxation, the fibers in the

para-nematic state in the middle of the capillary decrease their order parameter during Phase (I) and the solutions become weakly anisotropic and nearly isotropic for BLG and CNC, respectively. These theoretical predictions are in excellent agreement with POM images because the dark zone in POM images of BLG is slightly blended with a faint reddish color indicating that the fibers therein possess an extremely week orientational ordering and are aligned parallel to the central axis of the capillary, see Figure 6-1(a-f) and Figure 6-2(c,e,g,i,k). On the other hand, the middle of POM images of CNC is almost dark without any other color denoting that the fibers therein are in the completely isotropic phase, see Figure 6-1(g-l) and Figure 6-3(c,e,g). Consequently, this supports the assumption we made in the experimental analysis on the dark zones observed in the microscopy images; the dark zones should be considered isotropic areas or para-nematic with extremely low order parameter, and not nematic nor cholesteric with axes parallel to the light path.

6.4.3 Understanding the physical origins of relaxation mechanisms

As above-mentioned, it is found that the relaxation mechanisms can generally be described by two consecutive phases. This section reveals the physics behind the explored mechanisms in terms of the free-energy landscape.

According to Equations(6-7 through 6-9), two factors mainly govern relaxation dynamics; pitch length and coherence length. For a given cylindrical capillary, the impacts of these factors are shown in Figure 6-4(a,b). The simulations suggest that smooth relaxation can change to slow-fast relaxation and vice versa. For instance, for a given pitch length, smooth relaxation gradually switches to (emerges from) slow-fast relaxation, upon decreasing (increasing) the coherence length.

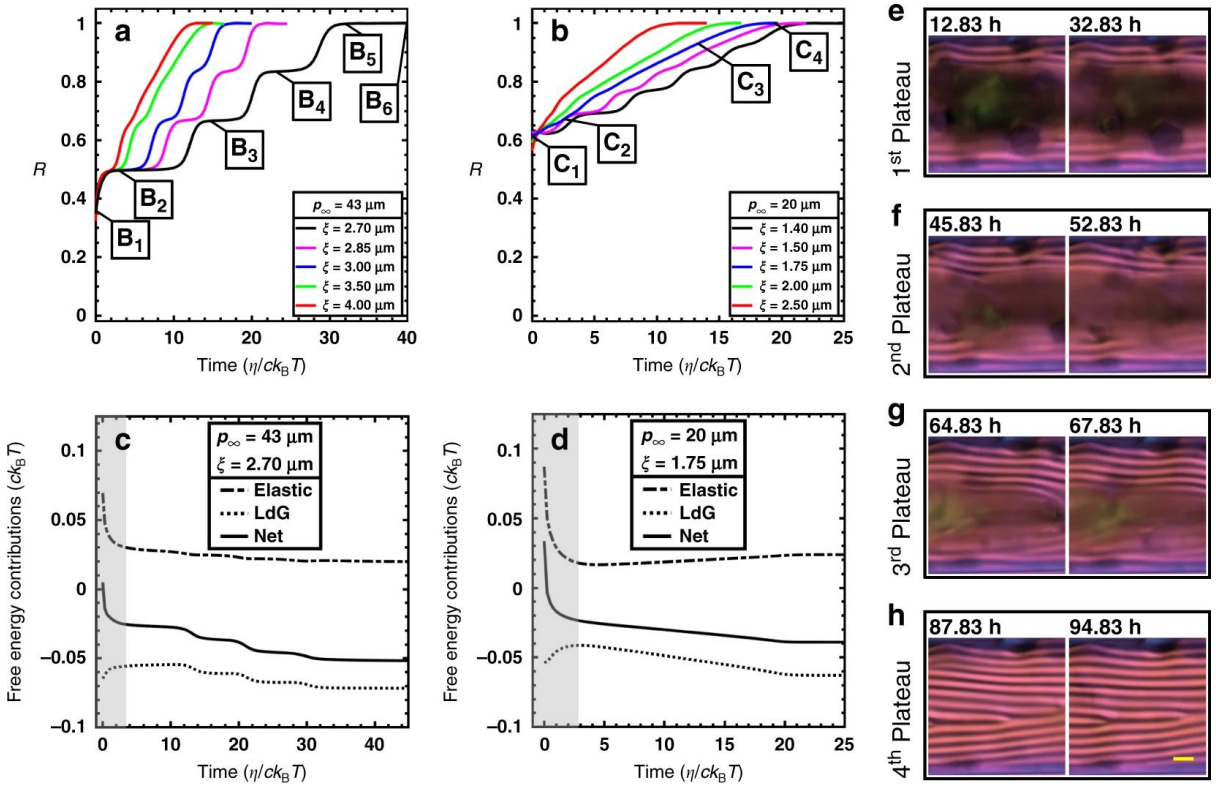

Figure 6-4. **The generic mechanism of relaxation dynamics. (a, b)** Parametric analyses of the normalized relaxation progress, R, showing that smooth relaxation dynamics arise, provided coherence length is greater than a threshold. η stands for the rotational viscosity coefficient. **(c, d)** The interplay between homogeneous and elastic free energies, and the resulting net free energy. The grey-hatched zones indicate the period over which the order parameter of the para-nematic phase is dropped, Phase (I), and the remaining white-hatched zones correspond to front propagation, Phase (II). During the former and the latter, as can be appreciated by net free energy behavior, elastic and homogeneous contributions mainly control net free energy, respectively. Note that all graphs exhibit the spatial-averaged quantities and the panels (c) and (d) correspond to the BLG and CNC relaxations, respectively. **(e-h)** POM images showing no significant change in the cholesteric zone during each of the four BLG plateaus marked in Figure 6-1(m). These POM images were experimentally acquired using the LC PolScope device. Scale bar is p_∞=43µm.

In liquid-crystalline phases, the coherence length ξ describes the distance over which long-range orientational order varies[49] and is expected to be in the nano-meter range for small-sized rod-shaped mesogens such as 5CB (ℓ_{5CB}=1.8nmand $\xi_{5CB} \approx$ 7nm)[50]. In particular, ξ is directly correlated with length of rod-shaped mesogen[51], and ξ is thus expected to be in the micro-meter range for long fibrous mesogens since their contour lengths are two orders of magnitude longer compared to small-sized mesogens (e.g. ℓ_{BLG}=652nmand ℓ_{CNC}=325nm). As illustrated in Figure 6-4(a,b), the parametric analyses shed light on the fact that the observed relaxation dynamics are induced for a micro-meter range of coherence length defined in Equation(6-2).

The coherence lengths that best fit the experimental data of BLG and CNC shown in Figure 6-1 (m,n) are: $\xi_{BLG} = 2.7\mu m$ and $\xi_{CNC} = 1.75\mu m$, respectively.

Before proceeding in elucidating the mechanism of cholesteric layers formation, it is important to quantify the impact of order parameter reduction on the free energy contributions. The homogeneous and gradient elastic free energy contributions to the net free energy are given by the LdG and FOM theories are[16,25,52-55]:

$$f_{net} = f_h + f_g \qquad (6-1)$$

The homogeneous free energyf_h decreases when the order parameter increases from a low to the equilibrium value, therefore, this contribution promotes orientational ordering. The gradient elastic free energy f_g is the energy cost of orientational configuration and is minimum when the ground state is achieved. The decreasing order parameter results in decreasing f_g since Equation(6-9) shows that there is a factor of S in all the terms of f_g (see Supplementary Note 8 for more discussion about the impact of order parameter reduction on the free energy contributions). In partial summary, the order parameter reduction increases the homogeneous contribution and decreases the gradient elastic contribution.

As mentioned earlier, the mechanisms behind the relaxation dynamics are described by two consecutive phases as follows:

Phase (I): early relaxation depicted by the grey-hatched zones in Figure 6-4(c,d). During this short period, fibers in the para-nematic medium decrease their order parameter. This unexpected behavior can be explained by analyzing the free energy contributions. The ground state is inherently chiral nematic, thus the para-nematic alignment, which represents unwound chiral helices, gives rise to an excess elastic free energy and, in consequence, rises the net free energy immediately before relaxation starts; see t=0 in Figure 6-4(c,d). Because the elastic free energy is weighted by the coherence length squared and the para-nematic alignment is unfavorable owing to the concentric ground state, the excess elastic energy is intensified by increasing of coherence length and/or decreasing of pitch length; see Supplementary Notes 8 for the detailed discussion.

To reduce the total excess energy imposed by the initial para-nematic alignment, fibers existing in the para-nematic phase decrease their order parameter to decrease the dominant gradient elastic free energy, although an order parameter reduction is energetically unfavorable for the less costly homogeneous contribution; see Figure 6-4(c,d). The order parameter of the

para-nematic medium thus drops to a low value, S_d, shortly after the relaxation starts. Therefore, the more excess elastic energy, the more the order parameter of the para-nematic medium should drop. Taken altogether, the pitch length and coherence length are directly and inversely proportional to the order parameter of the para-nematic medium, S_d, respectively (Supplementary Notes 8,9).

Since S_d is either close to or lower than the order parameter at the phase transition, $S_c=0.25$, a dark zone emerges and persists in the POM images while the relaxation continues; for example, Figure 6-1(a-b,g-h) shows that Phase (I) is completed during the first 15-20 minutes for both BLG and CNC. When the emergence of dark zones in the time-series POM images is completed, Phase (I) terminates. Also, during the early relaxation, i.e. Phase (I), the order parameter reduction largely affects the gradient elastic contributions compared to homogeneous contribution; hence order parameter reduction results in reducing the net free energy, see Figure 6-4(c,d).

Phase (II): front propagation illustrated in Figure 6-4(c,d). As the front propagates inward through the para-nematic medium with the order parameter of S_d, the dark zone progressively shrinks, see Figure 6-1(a-l),Figure 6-2,Figure 6-3,Figure 6-4(e-h).S_d, which depends on both the pitch length and the coherence length, is a key factor to determine whether relaxation dynamics become slow-fast or smooth. Numerical simulation supported by experimental observations shows that if $S_d \approx 0$, the para-nematic phase becomes essentially isotropic and the smooth relaxation takes place as discussed for CNC relaxation. As S_d gradually increases, the plateaus are more pronounced. Eventually, relaxation ends up with slow-fast mode in cases that $S_d \approx 0.3-0.4$like such as BLG relaxation having $S_{d,\,BLG} = 0.33$ (Supplementary Note 9). As can be seen in Figure 6-4(e-h), during the plateaus, there is an insignificant change in the formed cholesteric layers, which slows down the relaxation.

Because, as already explained, S_d directly and inversely depends on the pitch length and coherence length, we conclude that a decrease (an increase) in the pitch length and/or increase (decrease) of the coherence length drives the relaxation toward smooth (slow-fast) dynamics, see Supplementary Figure 12. Finally, regardless of the S_d value, Phase (II) ends by reaching the self-selected ground state of a concentric due to $\frac{D}{p_\infty} > 1$, which is in agreement with previous studies[17,19].

In addition to the coherence length and pitch length, geometric confinement is expected to have a significant impact on relaxation(Supplementary Note 10). This effect is beyond the scope of this work, which is based on a single diameter capillary.

6.4.4 Properties estimation and relaxation time controllers

The quantitative agreement between experimental observations and theoretical predictions (Figure 6-1(m,n)) provides a way to obtain quantitative estimates of the rotational viscosity coefficient η and coherence length ξ. Knowing the coherence length, Equation(6-2)[25,49,53,56-60]

$$\xi = \sqrt{\frac{L_1}{ck_BT}} \qquad (6-2)$$

where k_B and T stand for Boltzmann's constant, and temperature, it is then possible to calculate the elastic constant L_1(Supplementary Note 11).

Table 6-1. BLG and CNC properties obtained by the experiment and/or simulation. See Supplementary Note 2 for further information on the properties.

	w_f(%)†	ρ_f(g.ml^{-1})†	ℓ(nm)†	d(nm)†	S_e	ξ(μm)	η(P)	L_1(N)
BLG	2.8	1.3	652±400	3.75±0.8	0.66	2.70	1.1×10^6	7.8×10^{-11}
CNC	2.7	1.5	325±168	4.5±1.0	0.61	1.75	5.6×10^5	4.2×10^{-11}

Table 6-1 shows that the equilibrium order parameter computed by numerical simulation is consistent with the results of the analytical equation formulated in previous theoretical studies[25,49]. The elastic constantL_1, which is related to Frank's elastic constants[52], is in the range used in other studies[24,61-63]. To the best of authors' knowledge, there has not been any report in the literature concerning rotational viscosity coefficients of BCLLCs. There, however, exists a few studies where rotational viscosity coefficients have experimentally been measured for large molecular-weight LCs, reporting 2.8×10^5P and 9.9×10^5P for PBLG and mesogenic polyesters, respectively[35,36]. As justified in reference[36], in comparison to thermotropic LCs, BCLLCs possess a large rotational viscosity coefficient because the relaxation time of thermotropic LCs is in range of milliseconds while BCLLCs ranges from hours to days.

Having rotational viscosity coefficients of BLG and CNC estimates, we can answer whether lower rotational viscosity of CNC is the reason behind its fast relaxation dynamic. The rotational viscosity γ is [25,32]

$$\gamma = \eta(1 - S^2)^2 \qquad (6-3)$$

and increases with decreasing S. The results shown in Table 6-2 confirm that the rotational viscosity of BLG is larger than that of CNC throughout the relaxation in the order of $\frac{\gamma_{CNC}}{\gamma_{BLG}} \approx 0.57 - 0.64$. Therefore, lower rotational viscosity of CNC speeds the relaxation.

Table 6-2. Order parameter and rotational viscosity of para-nematic mediums. ‡ signifies the local minima, see Supplementary Note 5 and Movies 4, 6.

		Phase (I)	Phase (II)		Equilibrium
BLG	S_d	0.33	0.23‡	0.33	0.66
	$\gamma(P) \times 10^{-5}$	8.73	9.87‡	8.73	3.5
CNC	S_d	0	0		0.61
	$\gamma(P) \times 10^{-5}$	5.6	5.6		2.2

The free-energy driving force also contributes to the relaxation kinetics as the phase ordering rate is (see section 'Direct numerical simulation' and Equation(6-5))

$$\text{ordering rate} = \frac{\text{free energy driving force}}{\text{rotational viscosity}} \qquad (6-4)$$

The difference between initial and equilibrium net free energy is representative of the free-energy driving force, ΔF. Based on Figure 6-4(c,d), we conclude that the free-energy driving force for relaxation of CNC is also larger than that of BLG, $\frac{\Delta F_{CNC}}{\Delta F_{BLG}} = 1.28$. Consequently, CNC relaxation is faster because of two synergetic effects; (1) lower rotational viscosity and (2) higher free-energy driving force.

6.5 Discussion

We integrated theoretical and experimental approaches to elucidate the relaxation dynamics (i.e. the spontaneous PN-N* transition) of cylindrically confined BCLLCs with planar anchoring. The analyses of the relaxation dynamics of BLG and CNC reveal that, despite the noticeable similarities between these two biological mesogens, their relaxation behaviors differ considerably. Specifically, BLG slowly relaxes through a slow-fast dynamic while CNC relaxation is fast with a smooth dynamic, Figure 6-1. Given the success of liquid-crystal continuum theory in the prediction of relaxation dynamics, we employed standard models to rationalize the mechanisms of relaxation in cylindrical confinement governed by a spontaneous interplay of chirality and viscoelasticity. The following two points should be taken into account

regarding the modeling and simulation implemented in this study. First, the results presented here are based on the strong planar anchoring supported by experimental observations. Previous studies[64-66] have shown that the effect of anchoring can be significant. Regarding our study, we also anticipate that different anchoring may affect relaxation dynamics; however, it requires future studies. Second, the hydrodynamics is reasonably neglected from the modeling (see section 'Direct numerical simulation'). This reasonable simplifying assumption leads two deviations in the simulation results from experimental observations; (1) simulation predicts that the chiral fronts almost evenly propagate inward while the POM images show that the front propagation is slightly uneven, see Figure 6-2 and Figure 6-3. For this reason, the simulations can overestimate or underestimate R over the time evolution, see Figure 6-1(m,n). (2) The defect motion cannot be fully tracked since the weak orientation-induced backflow is not considered. However, this insignificantly affects R.

The relaxation generally takes place through two phases; see Figure 6-2 and Figure 6-3. Phase (I); this phase describes the early relaxation. The para-nematic alignment existing at the beginning of relaxation leads to increase of the elastic free energy f_g as the system is away from the equilibrium; see Figure 6-4(c,d). The excess energy of f_g is then relieved (decreased) to some extent as the order parameter of the unwound medium decreases to a low value, S_d, Supplementary Note8. Even though the order parameter reduction also increases the homogenous contribution, f_h, the net free energy, f_{net}, decreases because f_{net} is significantly affected by f_g compared to f_h during Phase (I), see Figure 6-4(c,d). The dark zones emerging in the middle of the POM images are thus attributed to the low value of S_d. $S_d$is directly and inversely affected by the pitch length and the coherence length, respectively (Supplementary Notes 8,9). Phase (II); during this phase, the chiral front propagates through the low-order-parameter medium. As the front propagates, the cholesteric layers are formed and their order parameter evolves from a low value, S_d, into the equilibrium valueS_e(Supplementary Movies 4,5). As can be seen in Figure 6-4(c,d), during Phase (II), f_h dominates the net free energy; for this reason and the fact that f_h decreases upon ordering, cholesteric layers formation leads to further decrease of net free energy. Besides, we found that the type of relaxation dynamics can be determined by the value of S_d; the propagation through the significantly low-order-parameter para-nematic medium (i.e. the isotropic medium), $S_d \approx 0$, results in a smooth relaxation dynamic, and higher values of S_d lead to slow-fast dynamics (Supplementary Notes 8,9).

Lastly, we proposed a systematic framework to estimate elastic constants and rotational viscosity. Besides the reasonable estimations shown in Table 6-1 and Table 6-2, we showed that two factors control the relaxation time: rotational viscosity and free-energy driving force. Therefore, our study introduces a new general methodology where the experimental mapping of cholesteric pitch evolution over time, benchmarked by numerical simulations, allows recovering fundamental properties of the filamentous chiral bio-colloid under investigation, some of which are notably difficult to obtain via alternative methods.

6.6 Methods

6.6.1 Preparation of BLG cholesteric bulk

Amyloid fibrils were prepared by heating a pH 2, 2 wt% β-lactoglobulin solution at 90° for 5 hours. Mature amyloids were shortened and homogenized using an immersion mixer for one minute. The amyloid solution was purified with dialysis against pH 2 milliQ for 5 days using semipermeable membranes (MWCO 100kDa) and then up-concentrated to reach the isotropic nematic coexistence regime with reverse osmosis against 5 wt % 35KDa PEG solution using semipermeable membranes (MWCO 6-8kDa). The solution was equilibrated for several weeks until complete phase separation was reached (see Supplementary Note 12).

6.6.2 Preparation of CNC cholesteric bulk

Cellulose nanocrystal solution was prepared by mixing 2.5 wt% freeze-dried CNC (FPInnovations) in milliQ water. To disperse CNC, the solution was ultra-sonicated for 2 minutes and centrifuged for 20 minutes at 12 000 rcf. The supernatant was collected, and the solution equilibrated for several days until a macroscopic phase separation was achieved (see Supplementary Note 12).

6.6.3 Preparation of BLG and CNC samples for optical microscopy

The cylindrical capillaries (VitroTubes, Vitrocom) of inner diameter 260 µm were filled with bulk cholesteric phase (BLG:2.8 wt% and CNC:2.7 wt%) through capillary suction, by immersion of the capillaries into the anisotropic solutions (see Supplementary Note 12). The capillary tubes were immediately sealed with UV glues to avoid evaporation.

6.6.4 PolScope

The relaxation dynamic was recorded using an optical microscope combined with an LC-PolScope universal compensator, allowing the quantitative analysis of birefringence[46]. In particular, after focusing on a region of interest in the middle of the cuvettes, time-series images with a specific time step were collected and analyzed with PolScope. The device is used for birefringence imaging to analyze with high sensitivity and high resolution the spatial and temporal variations of the phase delay in anisotropic materials and to provide pixel-by-pixel information of local optical anisotropy together with a mapping of the slow axis orientation of birefringence regions.

6.6.5 Direct numerical simulation

The capillaries are exclusively filled with the fully cholesteric phase existing at the constant equilibrium concentration and then immediately sealed (see the section 'Preparation of BLG and CNC samples for optical microscopy'); hence, the concentration of the system remains a constant equal to the upper binodal concentration throughout the relaxation time. Moreover, during the relaxation, it is impossible that the system spontaneously splits into two distinct concentrations, meaning that the low-order-parameter phase (dark zone) and high-order-parameter phase (fingerprint zones) are depleted and concentrated, respectively. This can be proven by proof by contradiction; based on the mass conservation law, if the dark zone becomes fiber-lean then the fingerprint zones become more fiber-rich. Under this condition, the fingerprint zones sharply approach the gel phase. However, time-series POM images do not point to such condition (see Supplementary Movies 1,2). Altogether, the relaxation dynamics presented in this study takes place in a thermodynamically closed system at constant concentration field without appreciable variation. Owing to the insignificant mass exchange, the mass continuity equation is reasonably neglected.

The essential physics which is necessary to be taken to account is the spatio-temporal dynamics of fibers orientation. The liquid-crystalline ordering is described by the second-order symmetric traceless tensor, $\mathbf{Q}(\mathbf{x}, t)$, whose eigenvalues and eigenvectors correspond to the order parameters and the macroscopic orientation of mesogens, respectively. The spatio-temporal orientational relaxation follows the time-dependent Ginzburg-Landau (TDGL) model whereby $\mathbf{Q}(\mathbf{x}, t)$is thermodynamically allowed to evolve toward equilibrium[25].

$$\underbrace{\frac{\partial \mathbf{Q}}{\partial t}}_{\text{ordering rate}} = -\frac{1}{\gamma}\underbrace{\left(\frac{\delta F_{net}}{\delta \mathbf{Q}}\right)^{[s]}}_{\text{driving force}} \qquad (6-5)$$

$$\frac{\partial \mathbf{Q}}{\partial \tilde{t}} = -\frac{1}{\left(1-\frac{3Tr(\mathbf{Q}^2)}{2}\right)^2}\left(\frac{\delta \tilde{F}_{net}}{\delta \mathbf{Q}}\right)^{[s]} \qquad (6-6)$$

Equation(6-6) is the dimensionless form of Equation(6-5). The actual time, t, and the dimensionless time, $\tilde{t}$, are related by $t = \frac{\tilde{t}\eta\xi^2}{L_1}$. $[s]$ and Tr indicate symmetric traceless and trace tensorial operations, respectively. $\delta\tilde{F}_{net}/\delta\mathbf{Q}$ shows the functional derivative of total dimensionless free energy, $\tilde{F}_{net}$, with respect to $\mathbf{Q}$-tensor. $\tilde{F}_{net}$is comprised of two contributions; homogeneous effect of phase ordering, $\tilde{f}_h$, described by the LdG theory and the gradient effect of elasticity, $\tilde{f}_g$, given by the FOM theory[25,32,49]:

$$\tilde{F}_{net} = \int_{\tilde{V}} \left(\tilde{f}_h + \tilde{f}_g\right) d\tilde{V} \qquad (6-7)$$

$$\tilde{f}_h = \frac{1}{2}\left(1-\frac{U}{3}\right)Tr(\mathbf{Q}^2) - \frac{1}{3}UTr(\mathbf{Q}^3) + \frac{1}{4}U\left(Tr(\mathbf{Q}^2)\right)^2 \qquad (6-8)$$

$$\tilde{f}_g = \frac{1}{2}\left(\frac{\xi}{h_0}\right)^2\left[\left[\tilde{\nabla}\times\mathbf{Q} + 4\pi\left(\frac{h_0}{p_\infty}\right)\mathbf{Q}\right]^2 + \alpha\left[\tilde{\nabla}\cdot\mathbf{Q}\right]^2\right] \qquad (6-9)$$

U denotes the nematic potential parameterized as $U = \frac{3c}{c^*}$ in which the asterisk shows the order-disorder phase transition. h_0 is an arbitrary macroscopic length scale which is representative of sample size. $\alpha$is the anisotropic ratio defined as $\alpha = \frac{L_2}{L_1}$ in which L_i are elastic constants[52]. In our present simulations, we found that the contribution of $\left[\tilde{\nabla}\cdot\mathbf{Q}\right]^2$ was not significant.

As can readily be appreciated through the POM images, both BLG and CNC have strong planar anchoring with the inner capillary surface. To capture this state, the governing equations are subjected to

$$\mathbf{Q}(\mathbf{x},t)|_{surface} = \begin{bmatrix} \frac{-1}{3} & 0 & 0 \\ 0 & \frac{2}{3} & 0 \\ 0 & 0 & \frac{-1}{3} \end{bmatrix} \qquad (6-10)$$

Equation(6-10) indicates that fibers located on the bounding surface are aligned parallel to the central axis of the capillary with strong anchoring, S=1. Furthermore, as shown in Figure 6-2(b) and Figure 6-3(b), fibers existing in the bulk are initially aligned along the central axis of the capillary; thus, the initial condition is set as

$$\mathbf{Q}(\mathbf{x}, t{=}0)|_{\text{bulk}} = S_i \begin{bmatrix} \frac{-1}{3} & 0 & 0 \\ 0 & \frac{2}{3} & 0 \\ 0 & 0 & \frac{-1}{3} \end{bmatrix} \qquad (6-11)$$

where S_i, as mentioned earlier, stands for initial order parameter and equals to 0.6[42]. Readers are referred to Supplementary Note 13 for a detailed discussion on the numerical simulation methods.

Lastly, the relaxation progress, $R(t)$, can also be parameterized in terms of **Q**-tensor.

$$R(t) = \frac{\int_A \frac{\mathbf{Q}:\nabla\times\mathbf{Q}}{\mathbf{Q}:\mathbf{Q}}\,dA}{\left(\int_A \frac{\mathbf{Q}:\nabla\times\mathbf{Q}}{\mathbf{Q}:\mathbf{Q}}\,dA\right)_e} \qquad (6-12)$$

where subscript e indicates equilibrium, and integration is over the lateral plane in which the striped pattern (twisting monodomain) is formed, see Figure 6-1(o) and Supplementary Note 14.

In the modeling used in this study based on Equations(6-5 through 6-11), there is no external stress, see Supplementary Note 15. Furthermore, hydrodynamics is reasonably negligible because of three reasons. First, as already explained, the orientational relaxation takes place in the closed system in which; there does not exist any external velocity driving force such as pressure difference, gravity (the filled capillaries were kept horizontally throughout the experiments), moving surface, and so on. Second, as above-mentioned, there is no appreciable concentration gradient in the system; hence, the hydrodynamics induced by mass transport becomes negligible. Third, the self-generated transient bulk convection is insignificant owing to following reasons; the viscosity of cholesteric permeation flow is extremely large[31], the rotational viscosity of BLG and CNC is also considerably large (see Table 6-2), the essentially vanishing Ericksen number (flow-to-elasticity ratio)[67], the solid-like behavior along the cholesteric helix axis[68], and the a posteriori validation and high fidelity of the predictions with experimental data.

6.7 Acknowledgments

SAK acknowledges financial support from the McGill Engineering Doctoral Awards (MEDA) program. ADR is thankful to McGill University for financial support through the James McGill Professorship appointment. This research is supported by a Sinergia grant from the Swiss National Science foundation (CRSII5_189917/1).

References (Chapter 6)

1 Gutierrez, O. F. A. & Rey, A. D. Theory and Simulation of Cholesteric Film Formation Flows of Dilute Collagen Solutions. Langmuir **32**, 11799-11812, (2016).

2 Kose, O., Tran, A., Lewis, L., Hamad, W. Y. & MacLachlan, M. J. Unwinding a spiral of cellulose nanocrystals for stimuli-responsive stretchable optics. Nat. Commun.**10**, 510, (2019).

3 De La Cruz et al, Cellulose-based reflective liquid crystal films as optical filters and solar gain regulators. ACS Photonics **5**, 2468-2477 (2018).

4 Liu, Q., Campbell, M. G., Evans, J. S. & Smalyukh, I. I. Orientationally ordered colloidal co-dispersions of gold nanorods and cellulose nanocrystals. Adv. Mater. **26**, 7178-7184 (2014).

5 Li et al, Colloidal cholesteric liquid crystal in spherical confinement. Nat. Commun. **7**, 12520, (2016).

6 Mitov, M. & Dessaud, N. Going beyond the reflectance limit of cholesteric liquid crystals. Nat. Mater. **5**, 361-364, (2006).

7 Kim, Y.-K., Wang, X., Mondkar, P., Bukusoglu, E. & Abbott, N. L. Self-reporting and self-regulating liquid crystals. Nature **557**, 539-544, (2018).

8 Cho, S., Li, Y., Seo, M. & Kumacheva, E. Nanofibrillar stimulus-responsive cholesteric microgels with catalytic properties. Angewandte Chemie **128**, 14220-14224 (2016).

9 Jeong et al, Chiral Nematic Fluids as Masks for Lithography. Adv. Mater. **24**, 381-384, (2012).

10 Chung et al, Biomimetic self-templating supramolecular structures. Nature **478**, 364 (2011).

11 Almeida et al, Cellulose-based biomimetics and their applications. Adv. Mater. **30**, 1703655 (2018).

12 Jin et al, Biomimetic Self-Templated Hierarchical Structures of Collagen-Like Peptide Amphiphiles. Nano Lett. **15**, 7138-7145, (2015).

13 Mitov, M. Cholesteric liquid crystals in living matter. Soft Matter **13**, 4176-4209, (2017).

14 Nyström, G., Arcari, M. & Mezzenga, R. Confinement-induced liquid crystalline transitions in amyloid fibril cholesteric tactoids. Nat. Nanotech. **13**, 330-336, (2018).

15 Wang, P.-X., Hamad, W. Y. & MacLachlan, M. J. Structure and transformation of tactoids in cellulose nanocrystal suspensions. Nat. Commun. **7**, 11515, (2016).

16 Zhou et al, Structural Transitions in Cholesteric Liquid Crystal Droplets. ACS Nano **10**, 6484-6490, (2016).

17 Kitzerow, H. S., Liu, B., Xu, F. & Crooker, P. P. Effect of chirality on liquid crystals in capillary tubes with parallel and perpendicular anchoring. Phys. Rev. E **54**, 568-575, (1996).

18 Ambrožič, M. & Žumer, S. Chiral nematic liquid crystals in cylindrical cavities. Phys. Rev. E **54**, 5187-5197, (1996).

19 Enz, E. & Lagerwall, J. Electrospun microfibres with temperature sensitive iridescence from encapsulated cholesteric liquid crystal. Jour. Mater, Chem. **20**, 6866-6872, (2010).

20 Nayani et al, Spontaneous emergence of chirality in achiral lyotropic chromonic liquid crystals confined to cylinders. Nat. Commun. **6**, 8067, (2015).

21 Bagnani, M., Nystrom, G., De Michele, C. & Mezzenga, R. Amyloid Fibrils Length Controls Shape and Structure of Nematic and Cholesteric Tactoids. Acs Nano **13**, 591-600, (2019).

22 Bagnani, M., Azzari, P., Assenza, S. & Mezzenga, R. Six-fold director field configuration in amyloid nematic and cholesteric phases. Sci. Rep. **9**, 12654, (2019).

23 Ondris-Crawford, R. J., Ambrožič, M., Doane, J. W. & Žumer, S. Pitch-induced transition of chiral nematic liquid crystals in submicrometer cylindrical cavities. Phys. Rev. E **50**, 4773-4779, (1994).

24 Fukuda, J.-i. & Žumer, S. Quasi-two-dimensional Skyrmion lattices in a chiral nematic liquid crystal. Nat. Commun. **2**, 246 (2011).

25 Rey, A. D. Liquid crystal models of biological materials and processes. Soft Matter **6**, 3402-3429, (2010).

26 Forest, M. G., Wang, Q., Zhou, R. & Choate, E. P. Monodomain response of arbitrary aspect ratio nematic polymers in general linear planar flows. J. Non-Newton. Fluid Mech. **118**, 17-31 (2004).

27 Grecov, D. & Rey, A. D. Theoretical and computational rheology for discotic nematic liquid crystals. Mol. Cryst. Liq. Cryst. **391**, 57-94 (2003).

28 Rey, A. D. & Denn, M. M. Dynamical phenomena in liquid-crystalline materials. Ann. Rev. Fluid Mech. **34**, 233-266 (2002).

29 Tsuji, T. & Rey, A. D. Effect of long range order on sheared liquid crystalline materials Part 1: compatibility between tumbling behavior and fixed anchoring. J. Non-Newton. Fluid Mech. **73**, 127-152 (1997).

30 Larson, R. G. & Larson, R. G. The Structure and Rheology of Complex Fluids. (1999).

31 Rey, A. D. Generalized cholesteric permeation flows. Phys. Rev. E **65**, 022701 (2002).

32 Doi, M. & Edwards, S. F. The theory of polymer dynamics. Vol. 73 (1988).

33 Doi, M. Soft Matter Physics. (2013).

34 Maguire, J., McTague, J.-P. & Rondelez, F. Rotational diffusion of sterically interacting rodlike macromolecules. Phys. Rev. Lett. **45**, 1891 (1980).

35 Moore, J. S. & Stupp, S. I. Orientation dynamics of main-chain liquid crystal polymers. 2. Structure and kinetics in a magnetic field. Macromolecules **20**, 282-293, (1987).

36 Sridhar, C. G., Hines, W. & Samulski, E. T.. Polypeptide liquid crystals: Magnetic susceptibility, twist elastic constant, rotational viscosity coefficient, and poly-γ-benzyl-L-glutamate sidechain conformation. Jour. Chem. Phys. **61**, 947-953 (1974).

37 Gennes, P. G. d. & Prost, J. The physics of liquid crystals. 2nd ed. edn, xvi, 597 pages : illustrations ; 24 cm. (1995).

38 Dogic, Z. & Fraden, S. Cholesteric phase in virus suspensions. Langmuir **16**, 7820-7824 (2000).

39 Frka-Petesic, B., Radavidson, H., Jean, B. & Heux, L. Dynamically controlled iridescence of cholesteric cellulose nanocrystal suspensions using electric fields. Adv. Mater. **29**, 1606208 (2017).

40 Zhao et al, Advances in biological liquid crystals. Small **15**, 1900019 (2019).

41 Rey, A. D. Flow alignment in the helix uncoiling of sheared cholesteric liquid crystals. Phys. Rev. E **53**, 4198-4201, (1996).

42 Aguilar Gutierrez, O. F. & Rey, A. D. Biological plywood film formation from para-nematic liquid crystalline organization. Soft Matter, (2017).

43 Rey, A. D. A model of capillary rise of nematic liquid crystals. Langmuir **19**, 3677-3685 (2003).

44 Bertsch et al, Ion-induced formation of nanocrystalline cellulose colloidal glasses containing nematic domains. Langmuir **35**, 4117-4124 (2019).

45 Usov et al, Understanding nanocellulose chirality and structure–properties relationship at the single fibril level. Nat. Commun. **6**, 7564, (2015).

46 Shribak, M. & Oldenbourg, R. Techniques for fast and sensitive measurements of two-dimensional birefringence distributions. Appl. Opt. **42**, 3009-3017, (2003).

47 Pospisil et al, Orientation relaxation dynamics in cellulose nanocrystal dispersions in the chiral liquid crystalline phase. Langmuir **34**, 13274-13282 (2018).

48 Murugesan, Y. K., Pasini, D. & Rey, A. D. Defect textures in polygonal arrangements of cylindrical inclusions in cholesteric liquid crystal matrices. Soft Matter **9**, 1054-1065 (2013).

49 De Luca, G. & Rey, A. D. Chiral front propagation in liquid-crystalline materials: Formation of the planar monodomain twisted plywood architecture of biological fibrous composites. Phys. Rev. E **69**, 011706, (2004).

50 Rahimi et al, Nanoparticle self-assembly at the interface of liquid crystal droplets. Proc. Nat. Acad. Sci. **112**, 5297-5302 (2015).

51 De Gennes, P. G. Short Range Order Effects in the Isotropic Phase of Nematics and Cholesterics. Mol. Cryst. Liq. Cryst. **12**, 193-214, (1971).

52 Muševič, I. Liquid Crystal Colloids. (2017).

53 Wright, D. C. & Mermin, N. D. Crystalline liquids: the blue phases. Rev. Mod. Phys. **61**, 385-432 (1989).

54 Khadem, S. A. & Rey, A. D. Thermodynamic Modelling of Acidic Collagenous Solutions: From Free Energy Contributions to Phase Diagrams. Soft Matter, (2019).

55 Khadem, S. A. & Rey, A. D. Theoretical Platform for Liquid-Crystalline Self-Assembly of Collagen-Based Biomaterials. **7**, Front. Phys. (2019).

56 Gupta, G. & Rey, A. D. Texture Rules for Concentrated Filled Nematics. Phys. Rev. Lett. **95**, 127802, (2005).

57 De Luca, G. & Rey, A. D. Point and ring defects in nematics under capillary confinement. Jour. Chem. Phys. **127**, 104902 (2007).

58 Zhang, R., Zhou, Y., Rahimi, M. & De Pablo, J. J. Dynamic structure of active nematic shells. Nat. Commun. **7**, 13483 (2016).

59 Martínez-González et al, Directed self-assembly of liquid crystalline blue-phases into ideal single-crystals. Nat. Commun. **8**, 15854 (2017).

60 De Luca, G. & Rey, A. D. Ringlike cores of cylindrically confined nematic point defects. Jour. Chem. Phys. **126**, 094907 (2007).

61 Seč, D., Čopar, S. & Žumer, S. Topological zoo of free-standing knots in confined chiral nematic fluids. Nat. Commun. **5**, 3057 (2014).

62 Nych, A., Fukuda, J.-i., Ognysta, U., Žumer, S. & Muševič, I. Spontaneous formation and dynamics of half-skyrmions in a chiral liquid-crystal film. Nat. Phys. **13**, 1215 (2017).

63 Sec, D., Porenta, T., Ravnik, M. & Zumer, S. Geometrical frustration of chiral ordering in cholesteric droplets. Soft Matter **8**, 11982-11988, (2012).

64 Otten, R. H. J. & van der Schoot, P. Capillary Rise of an Isotropic−Nematic Fluid Interface: Surface Tension and Anchoring versus Elasticity. Langmuir **25**, 2427-2436, (2009).

65 Wang et al, Controlled Multistep Self-Assembling of Colloidal Droplets at a Nematic Liquid Crystal–Air Interface. Phys. Rev. Lett. **123**, 087801 (2019).

66 Zhou, Y., Senyuk, B., Zhang, R., Smalyukh, I. I. & de Pablo, J. J. Degenerate conic anchoring and colloidal elastic dipole-hexadecapole transformations. Nat. Commun. **10**, 1-8 (2019).

67 Rey, A. D. Structural transformations and viscoelastic response of sheared fingerprint cholesteric textures. J. Non-Newton. Fluid Mech. **64**, 207-227 (1996).

68 Rey, A. D. Theory of linear viscoelasticity of chiral liquid crystals. Rheo. acta **35**, 400-409 (1996).

6.8 Supporting Information (Chapter 6)

Supplementary Figure 1.

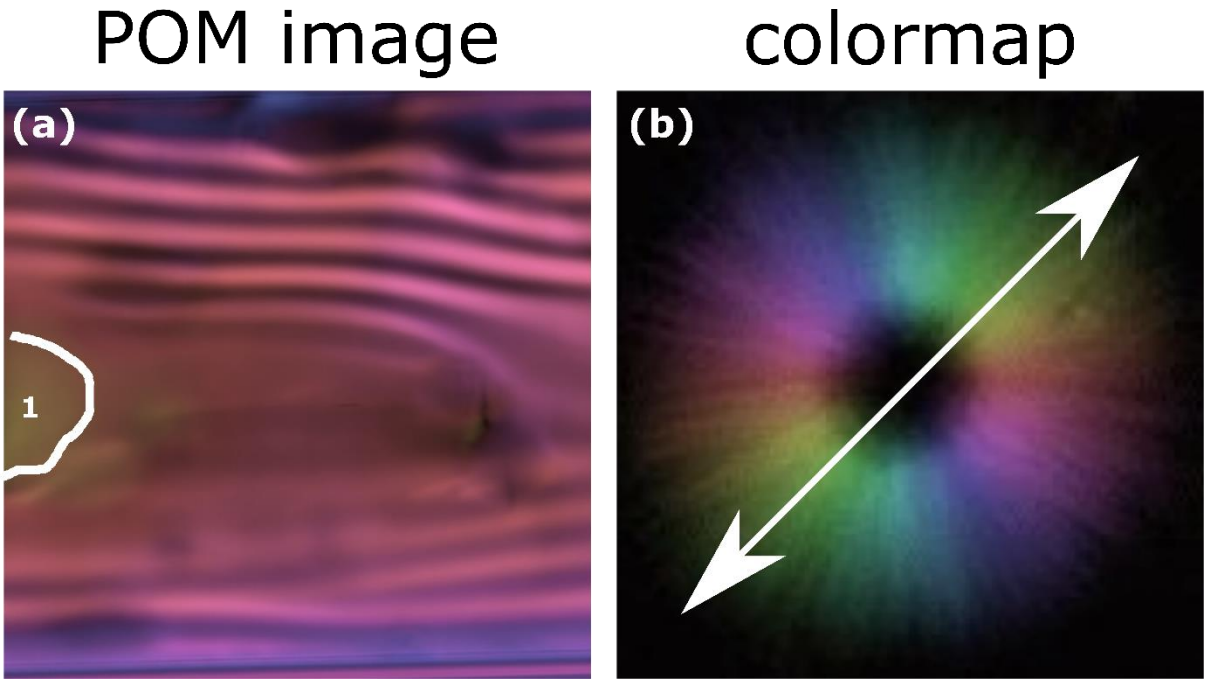

Supplementary Figure 1 | Mapping between microscopy (POM) image and the colormap. **(a)** Representative microscopy (POM) image, and **(b)** the colormap.

Supplementary Figure 2.

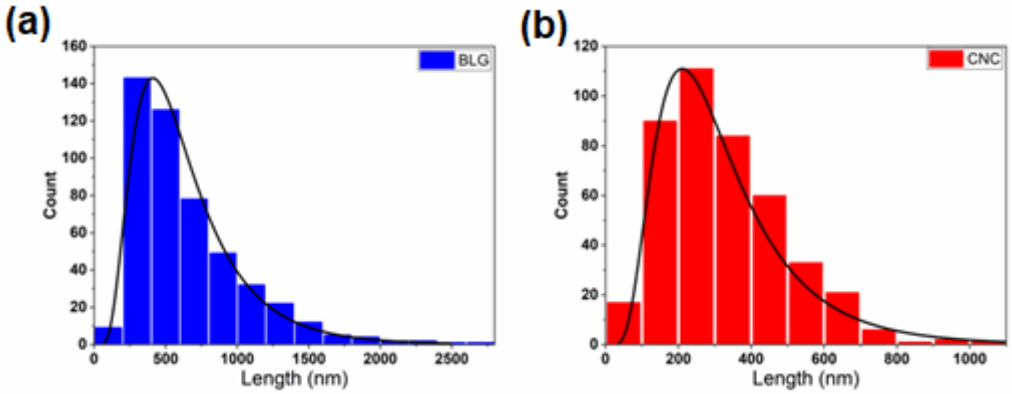

Supplementary Figure 2 | Amyloid and cellulose length distributions. The length distributions of particles extracted from AFM measurements are plotted as histograms and fitted as log-normal distributions (black lines) for BLG amyloid fibrils and CNC in **(a)** and **(b)**, respectively. The average contour length results 652±400 nm and 325±168 nm for BLG and CNC, respectively. The average heights of the fibrils (corresponding to the diameter of the rods) resulted 3.75±0.8 and 4.5±1.0 nm for BLG and CNC, respectively.

Supplementary Figure 3.

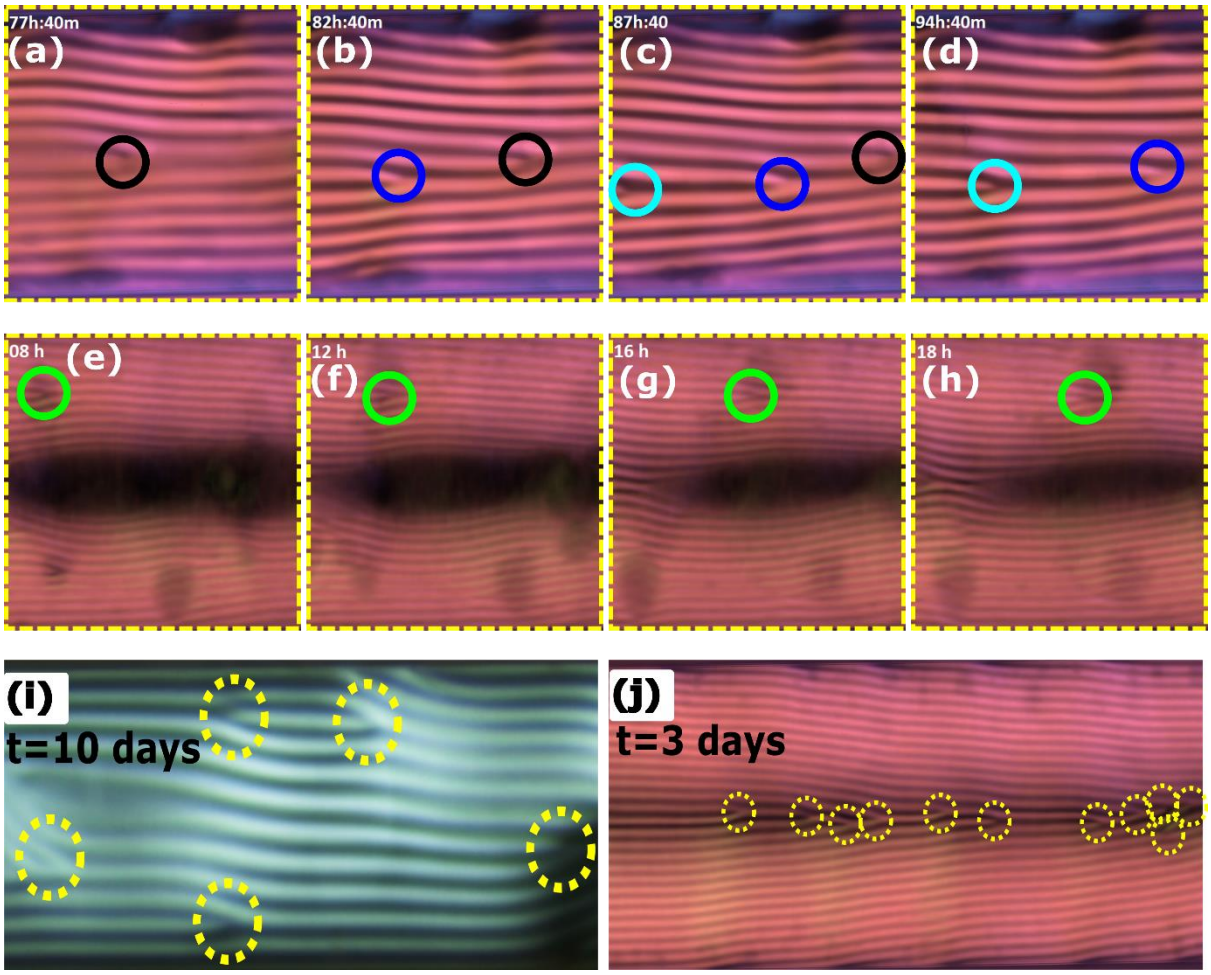

Supplementary Figure 3 | Defects Analysis. The PolScope images depicting the movement of defects for **(a-d)** β-lactoglobulin amyloid fibrils (BLG) and **(e-h)** cellulose nanocrystals (CNC). In the panels (a-h), the circles show defects, and each defect is shown with a unique color. **(i)** The representative POM images of BLG and **(j)** PolScope colormap representation for CNC. In the panels (i, j), the dashed circles show defects; hence, there are 5 defects for BLG and 11 defects for CNC on the larger region (600µm×260µm) after equilibration (10 days for BLG and 3 days for CNC).

Supplementary Figure 4.

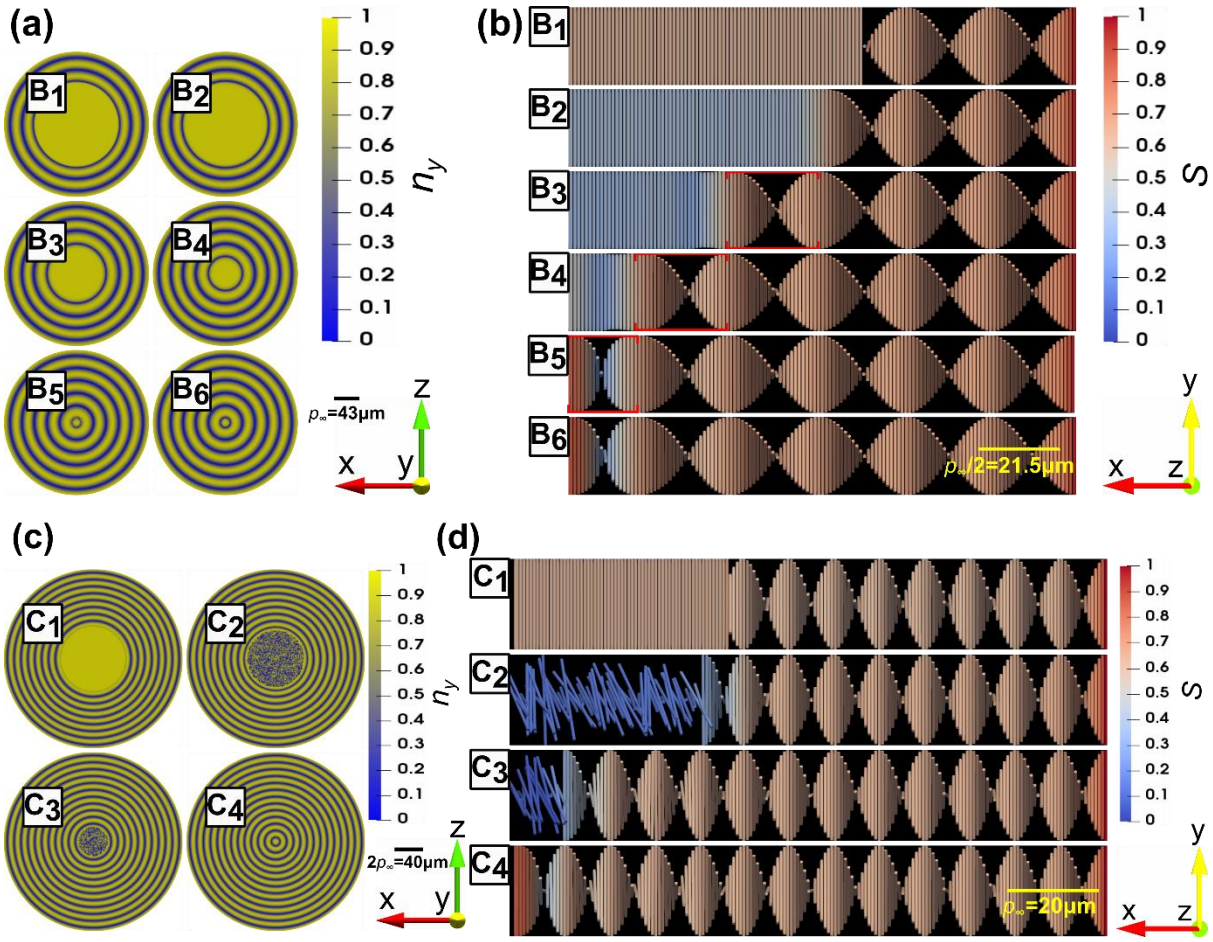

Supplementary Figure 4 | Circular chiral front propagation and fibers configuration along the capillary radius. (a, c) Sequential snapshots of a circular cross-section through the capillary tube demonstrating y-component of the director filed, n_y. Yellow and blue thus exhibit where fibers are parallel and perpendicular to the central axis of the cylinder, respectively. **(b, d)** Fibers orientation along the radius of circular cross-sections depicted in the panels (a, c), respectively. General Note: (a, b) and (c, d) correspond to BLG and CNC, respectively.

Supplementary Figure 5.

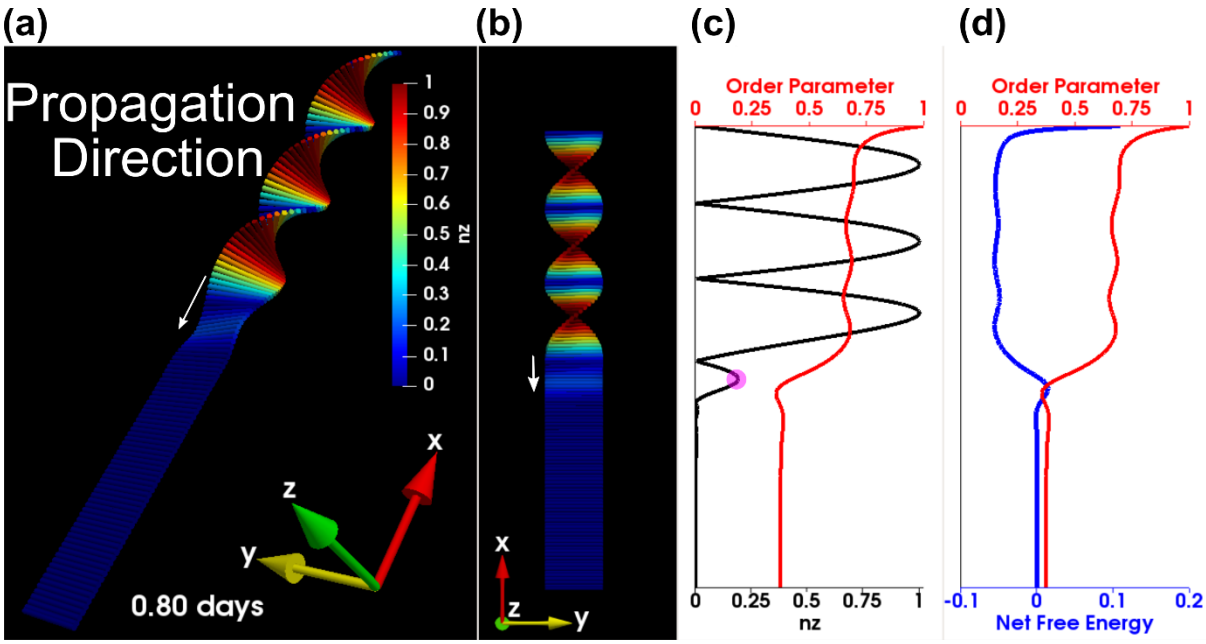

Supplementary Figure 5 | First essential stage in BLG front propagation, i.e. Phase(II). **(a, b)** Fibers configuration along the radius of the capillary cylinder at two different angles of view and color shows z-component of the director field, i.e. fiber configuration. **(c)** Quantitative representation of z-component, bottom axis, and order parameter, top axis, along the helix depicted in panel (b). **(d)** Order parameter, top axis, and net free energy, bottom axis, along the helix depicted in (b). Note: y-axes in the panels (c, d) are the length of the helix shown in the panel (b).

Supplementary Figure 6.

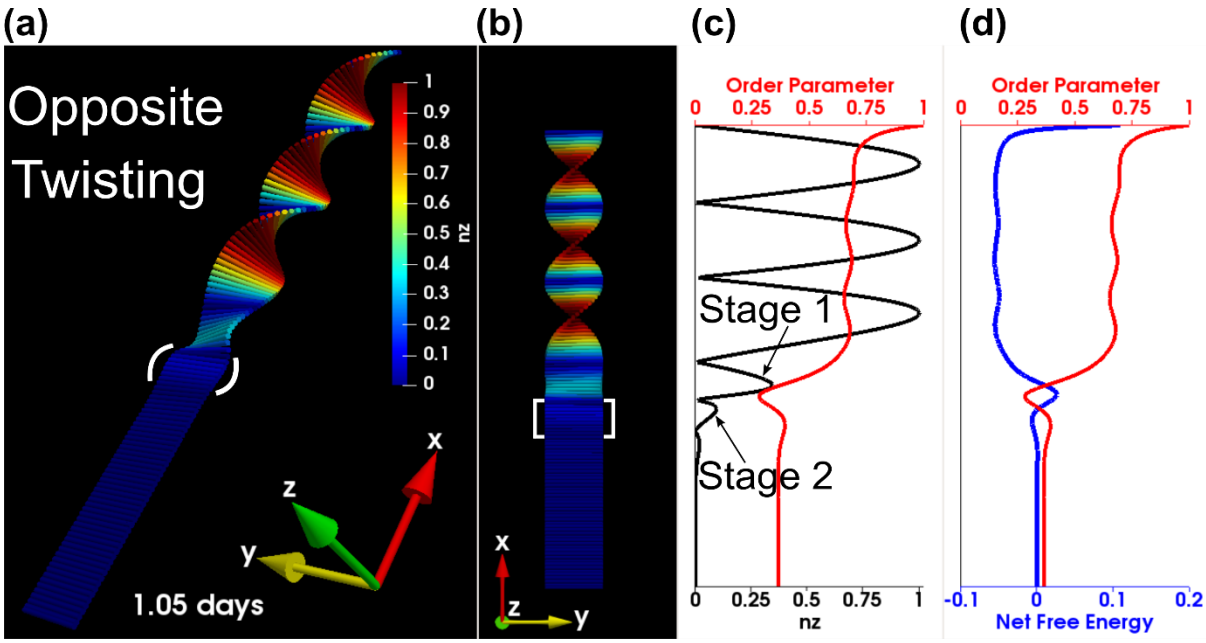

Supplementary Figure 6 | Second essential stage in BLG front propagation, i.e. Phase(II). **(a, b)** Fibers configuration along the radius of the capillary cylinder at two different angles of view and color shows z-component of the director field, i.e. fiber configuration. **(c)** Quantitative representation of z-component, bottom axis, and order parameter, top axis, along the helix depicted in panel (b). **(d)** Order parameter, top axis, and net free energy, bottom axis, along the helix depicted in (b). Note: y-axes in the panels (c, d) are the length of the helix shown in the panel (b).

Supplementary Figure 7.

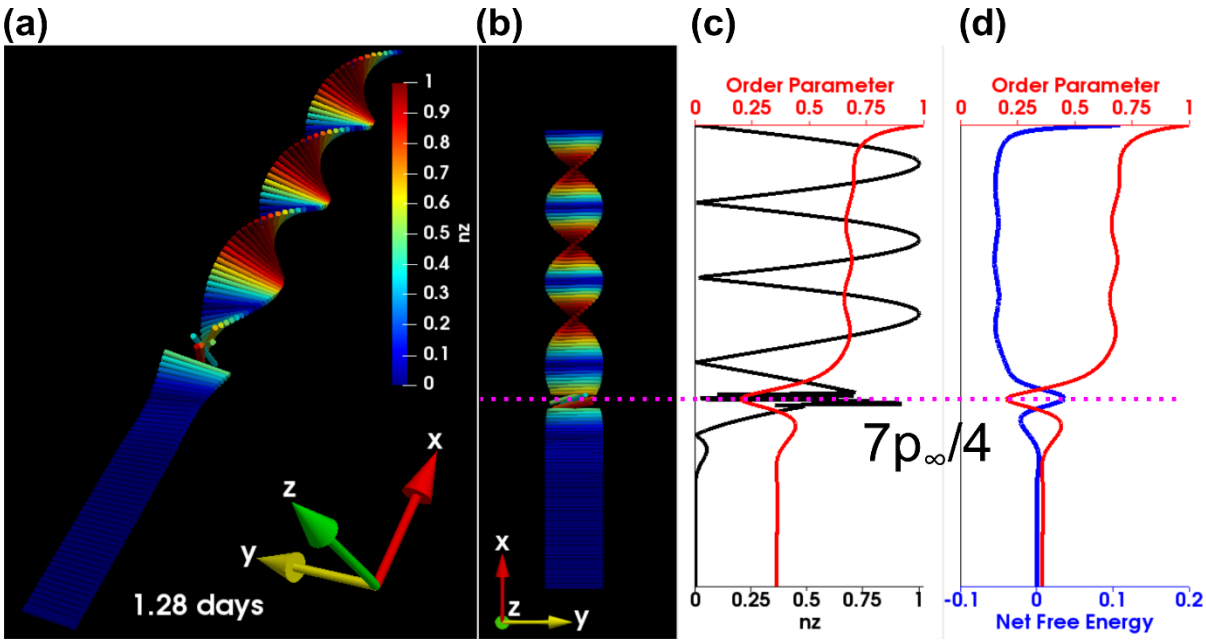

Supplementary Figure 7 | Third essential stage in BLG front propagation, i.e. Phase(II). **(a, b)** Fibers configuration along the radius of the capillary cylinder at two different angles of view and color shows z-component of the director field, i.e. fiber configuration. **(c)** Quantitative representation of z-component, bottom axis, and order parameter, top axis, along the helix depicted in panel (b). **(d)** Order parameter, top axis, and net free energy, bottom axis, along the helix depicted in (b). Note: y-axes in the panels (c, d) are the length of the helix shown in the panel (b).

Supplementary Figure 8.

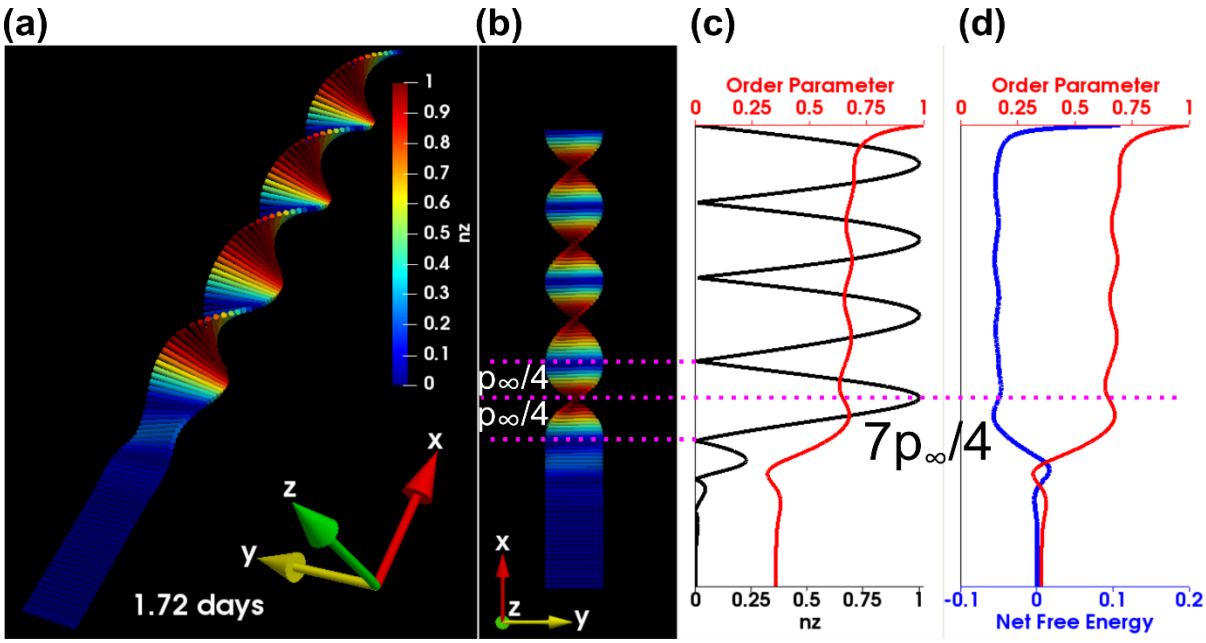

Supplementary Figure 8 | Fourth essential stage in BLG front propagation, i.e. Phase(II). **(a, b)** Fibers configuration along the radius of the capillary cylinder at two different angles of view and color shows z-component of the director field, i.e. fiber configuration. **(c)** Quantitative representation of z-component, bottom axis, and order parameter, top axis, along the helix depicted in panel (b). **(d)** Order parameter, top axis, and net free energy, bottom axis, along the helix depicted in (b). Note: y-axes in the panels (c, d) are the length of the helix shown in the panel (b).

Supplementary Figure 9.

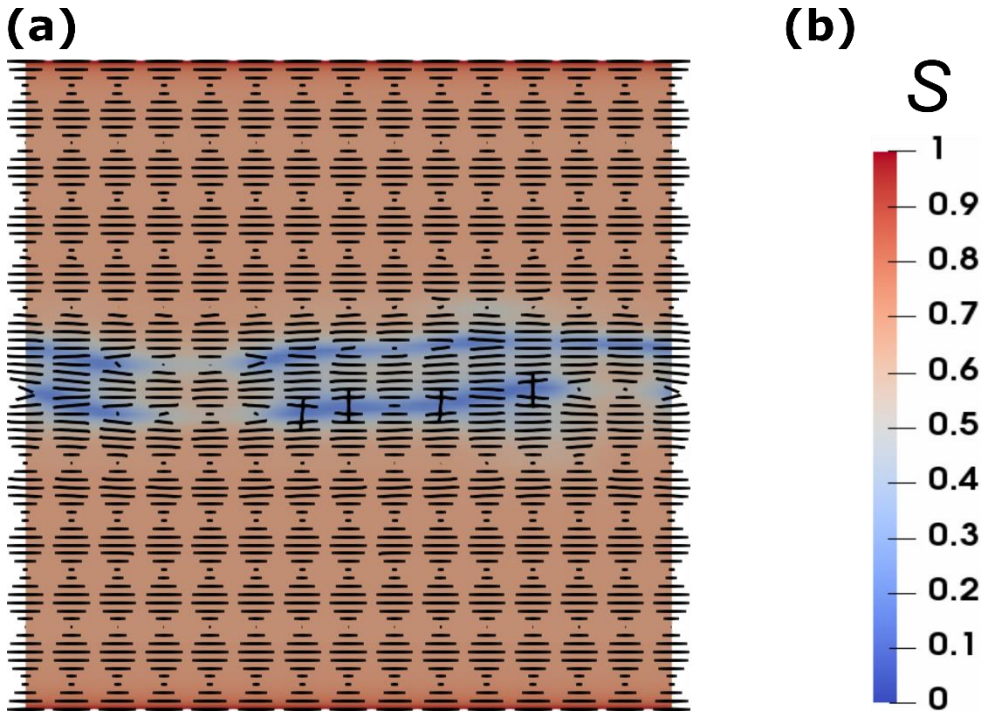

Supplementary Figure 9 | Representative numerical simulation results. (a) Fibers orientation is schematically shown by the director filed and their corresponding order parameter is represented by the blue-to-red spectrum. **(b)** The blue-to-red spectrum.

Supplementary Figure 10.

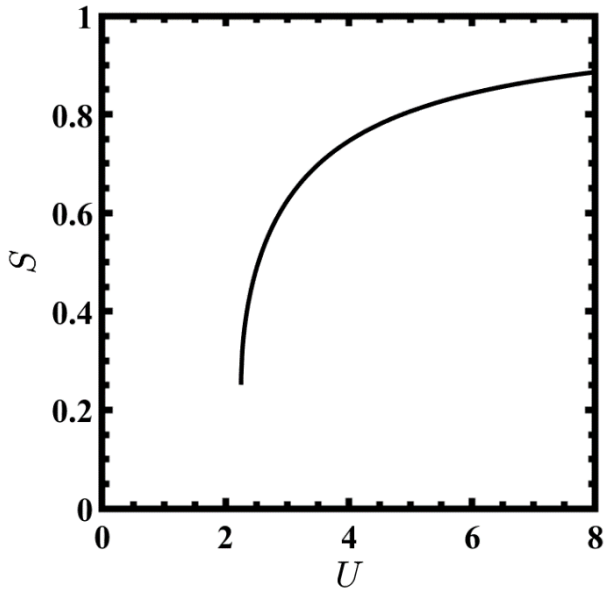

Supplementary Figure 10 | A typical order parameter behavior. The order parameter abruptly drops to zero if the concentration is less than a critical value.

Supplementary Figure 11.

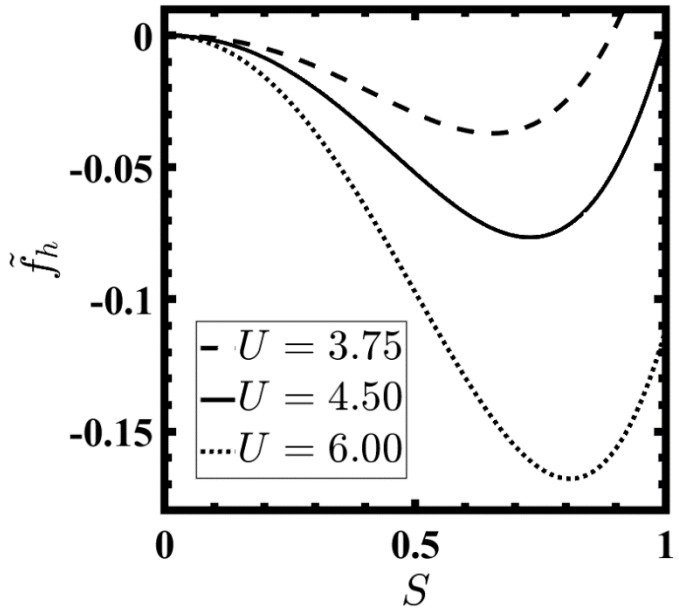

Supplementary Figure 11 | A typical homogenous free energy behavior. Homogenous free energy variation with respect to order parameter at various nematic potentials, $U = \frac{3c}{c^*}$.

Supplementary Figure 12.

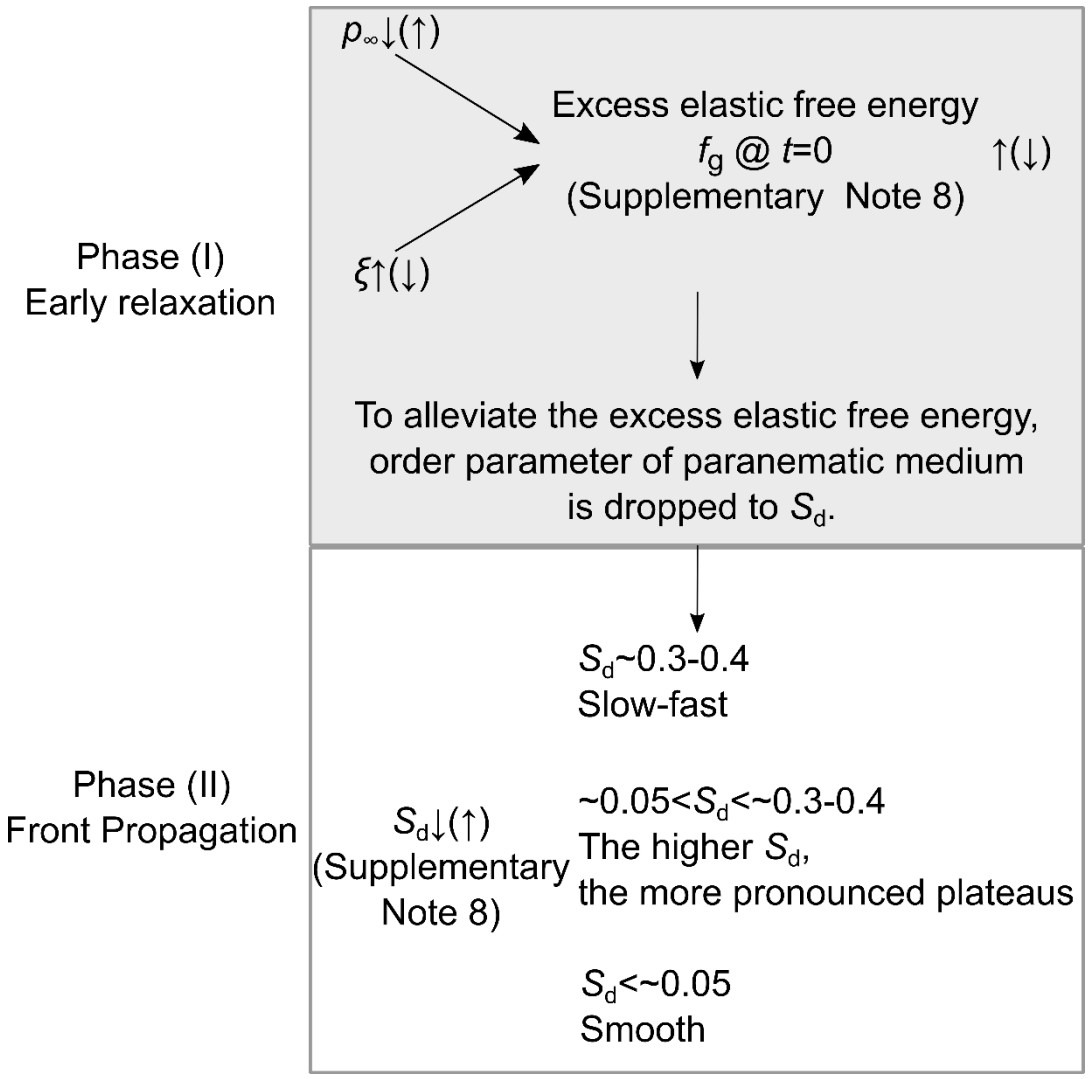

Supplementary Figure 12 | General mechanism governing relaxation dynamics. Summarizing scheme of the impact of coherence length and pitch length on the order parameter of the para-nematic, S_d, and the resulting relaxation dynamics. Upward and downward arrows qualitatively indicate increase and decrease, respectively.

Supplementary Figure 13.

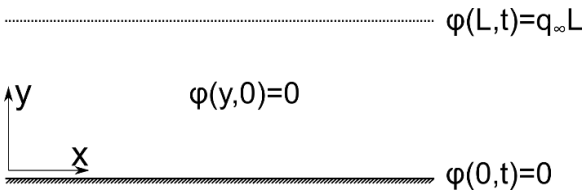

Supplementary Figure 13 | Schematic of an unconfined planar geometry. The bottom line indicates the substrate and the top dash line is the upper boundary condition.

Supplementary Figure 14.

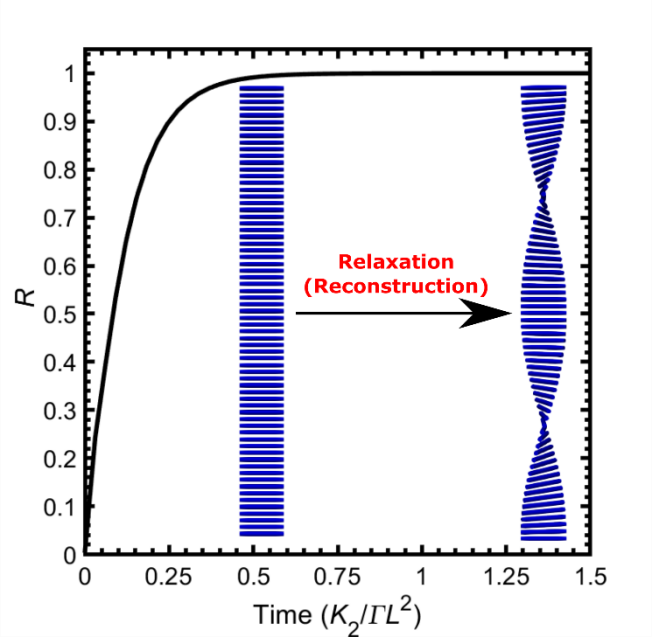

Supplementary Figure 14 | Relaxation dynamics in an unconfined planar geometry. The normalized relaxation progress, R, has the first-order dynamic in an unconfined planar geometry.

Supplementary Figure 15.

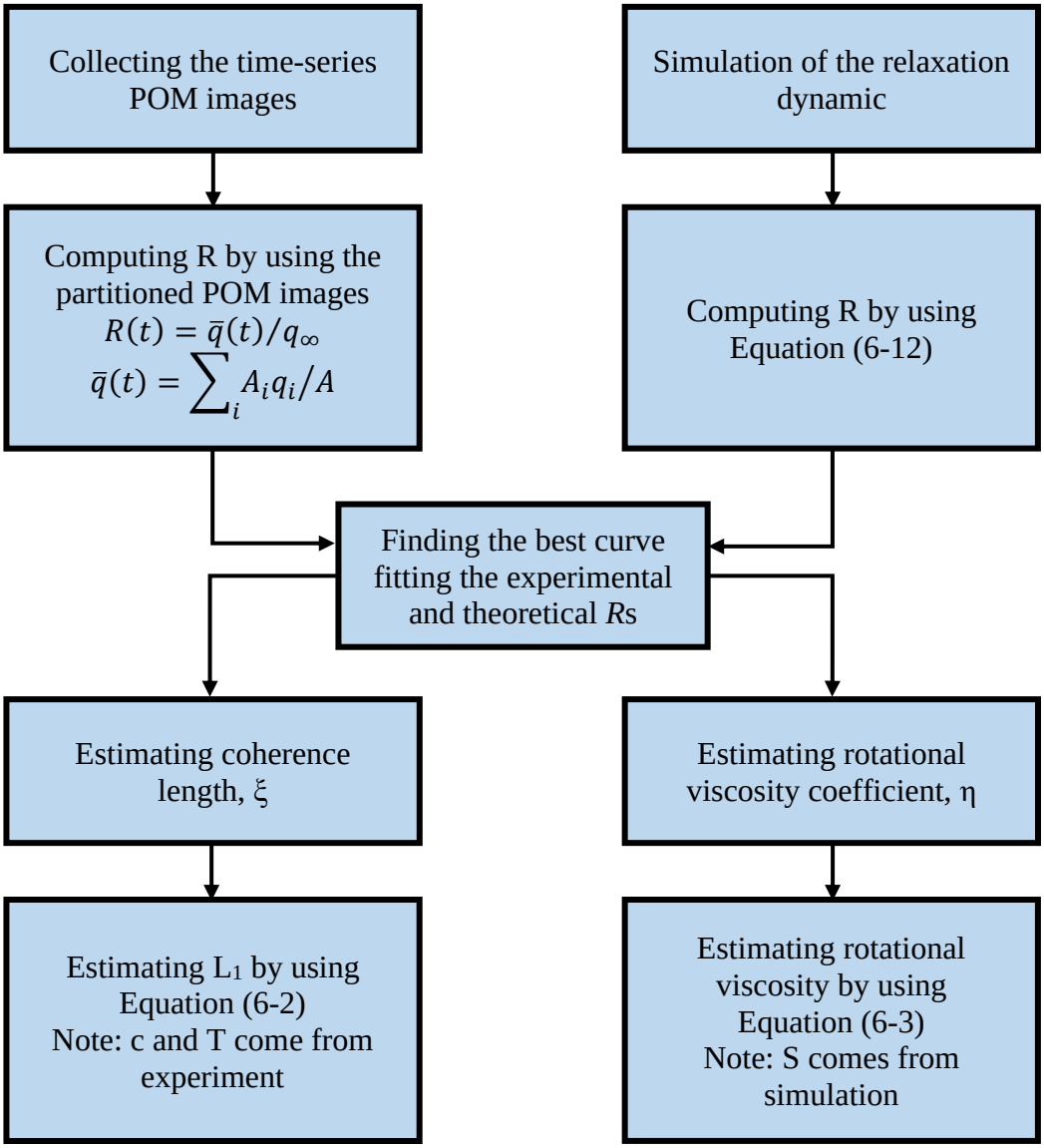

Supplementary Figure 15 | The systematic framework of estimating viscoelastic properties.

Supplementary Figure 16.

Supplementary Figure 16 | Photograph of phase-separated BLG or CNC dispersion sandwiched between crossed polarizers. From the top to the bottom, phases are Air, Isotropic and Cholesteric, respectively. Note BLG and CNC exactly look like each other in the shown container.

Supplementary Figure 17.

(a)

Simulation Results	Geometry used
Figure 1(m,n)	2D
Figure 2(b, d, f, h, j, l)	2D
Figure 3(b, d, f, h)	2D
Figure 4(a-d)	2D
Supplementary Figure 4	3D
Supplementary Figures 5-8	3D
Supplementary Figure 9	2D
Supplementary Figures 18-20	2D
Supplementary Movie 3	3D
Supplementary Movie 4	3D
Supplementary Movie 5	3D
Supplementary Movie 6	3D

(b)

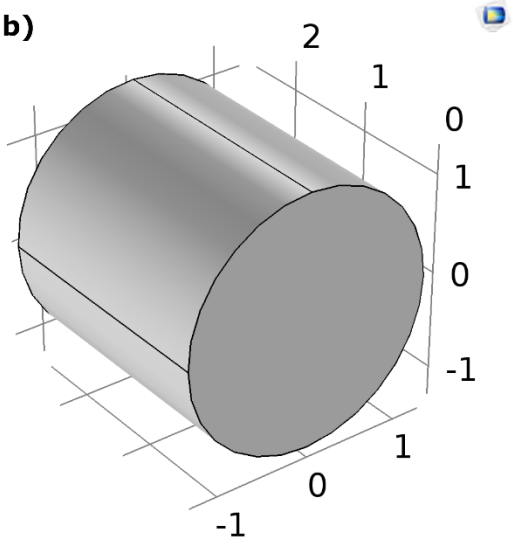

(c)

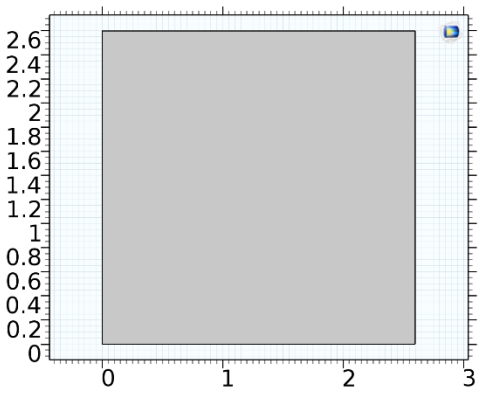

Supplementary Figure 17 | Summary of the geometries used in the present study. (a) The list of Figures and Movies, and the corresponding dimensionalities. **(b)** Representative 3D simulation box. **(c)** Representative 2D simulation box.

Supplementary Figure 18.

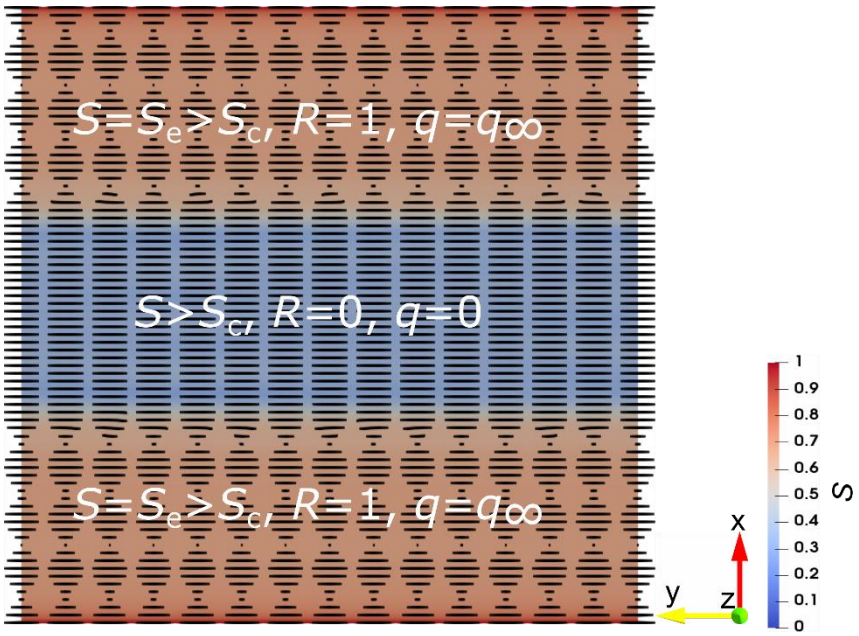

Supplementary Figure 18 | Representative simulation results for BLG. A representative snapshot depicting the BLG relaxation and the corresponding R, q, S, and director field (**n**).

Supplementary Figure 19.

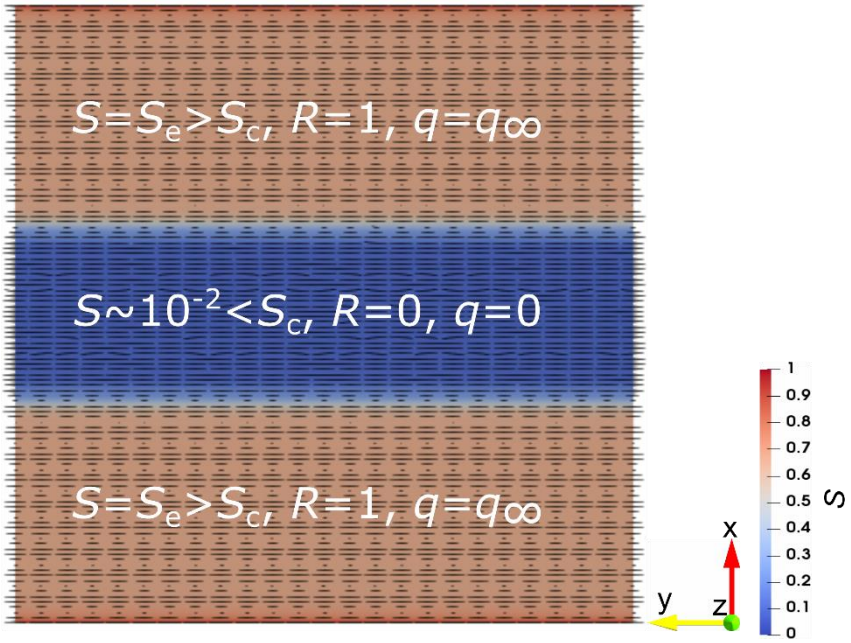

Supplementary Figure 19 | Representative simulation results for CNC. A representative snapshot computed for the CNC relaxation and the corresponding R, q, S, and director field (**n**).

Supplementary Figure 20.

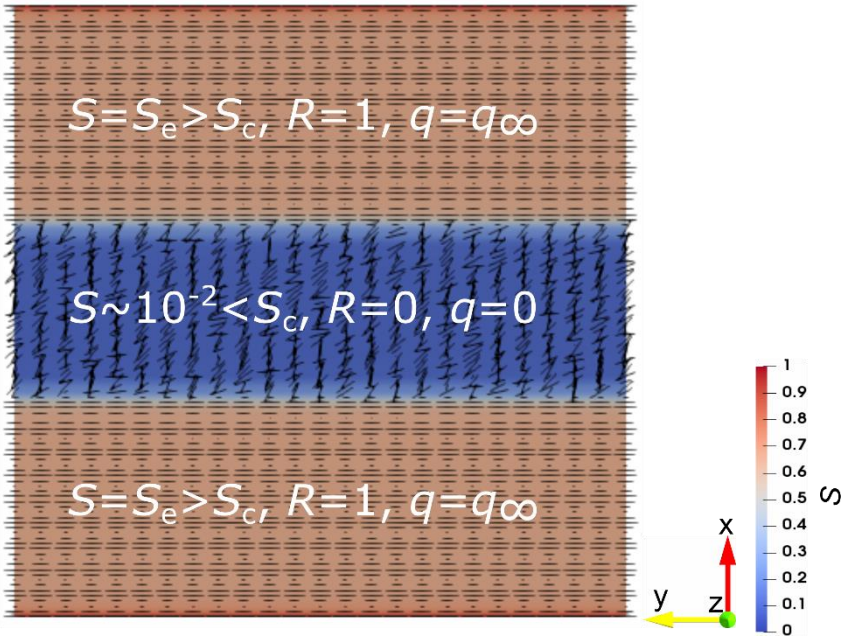

Supplementary Figure 20 | The snapshot visualized for the Supplementary Figure 19.

Supplementary Table 1.

Supplementary Table 1. Impact of parameters on the elastic free energy. Upward and downward arrows qualitatively indicate increase and decrease, respectively.

$p_\infty \downarrow$ and if the phase is para-nematic (e.g. in our simulation, the initial phase is para-nematic specified by $\mathbf{n} = [0 \quad 1 \quad 0]$)	$\tilde{f}_g \uparrow$
$S \downarrow$	$\tilde{f}_g \downarrow$
$\xi \downarrow$	$\tilde{f}_g \downarrow$

Supplementary Table 2.

Supplementary Table 2. Parameters used in the present study to capture the dynamics of orientational relaxation.

Parameter	Value
U	4.5
α	19

Supplementary Note 1.

Figure 6-1 (a-l), Figure 6-2(c, e, g, i, k), Figure 6-3(c, e, g), and Figure 6-4(e-h) depict microscopy (POM) images captured experimentally. The fibers orientation at each point of the POM image can be appreciated by the correspondence between the color of that point and the colormap. For example, region 1 in Supplementary Figure 1**(a)** is approximately between yellow and green. By color mapping with the colormap, we conclude that fibers therein nearly make 45° with the horizontal axis, see the representative arrow shown in the Supplementary Figure 1**(b)**. Similarly, the pink color which is dominant shows the horizontal alignment.

Supplementary Note 2.

The mass fractions, $w_f(\%)$, were gravimetrically measured as triplicate, giving the same results so there is no error bar available.

The volume densities, $\rho_f(g.ml^{-1})$, were extracted from the literature[1,2].

The length distributions of the rods studied in this paper have been extracted from the atomic force microscopy (AFM) analysis. In particular, 20 µL of 0.01 wt% rods solutions were deposited on freshly cleaved mica for two minutes, rinsed with milliQ water, and scanned with a Multimode VIII scanning probe microscope (Bruker, USA). The images were acquired in tapping mode at ambient condition and the distributions of amyloid fibrils and cellulose nanocrystals (Supplementary Figure 2) were extracted using the open-source code FiberApp[3].

Supplementary Note 3.

We observed that: (1) defects can move throughout the samples, Supplementary Figures 3(a-h), (2) defects may be trapped even after the equilibrium, and (3) number of the trapped defects for CNC is greater than BLG, Supplementary Figures 3(i, j).

Supplementary Note 4.

Supplementary Figures 4(a, c) show that for both BLG and CNC, the chiral front propagates radially, and the ground state domain becomes concentric.

Supplementary Figure 4(b) and Figure 6-1(m) show that each plateau corresponds to the formation of a half-pitch cholesteric layer; new layers are highlighted by red brackets.

Supplementary Figure 4(d) shows the front propagation of CNC through the para-nematic medium with an extremely low order parameter (i.e. isotropic medium).

Supplementary Note 5.

In order to reveal the mechanism of front propagation during Phase (II) for the BLG relaxation, we examined the formation of the cholesteric layers and found that the formation of each half-pitch, $\frac{p_\infty}{2}$, which is equivalent to one sigmoid-like step, obeys four stages (Supplementary Movie 6 reveals the mechanism in full detail).

During Phase (II), the orientational order parameter reduction increases the net free energy since this is largely controlled by the homogeneous free energy, see Figure 6-4(c, d) and Supplementary Note 8.

Stage (1) in Phase (II): Formation of a weakly chiral layer. During this stage, the chiral front propagates radially inwards replacing the para-nematic phase, see panels (a-c) of Supplementary Figure 5. Across the formed chiral layer, the order parameter decreases and, in turn, the net free energy increases, see panels (c, d) of Supplementary Figure 5. As discussed below, the equilibrium order parameter is $S_e = 0.66$, therefore the configuration of the fibers in Stage 1 is not as robust as that of the ground state and, in consequence, the formed layer is weakly chiral.

Stage (2) in Phase (II): Formation of a weakly chiral layer twisting oppositely. While the weakly chiral front (Stage 1) propagates further, a subtle chiral front emerges with the opposite twisting direction which can be seen by comparison of the panel (a) in Supplementary Figure 5 and Supplementary Figure 6. As a result, there exist two maxima in the z-component of the director field; top and bottom peaks correspond to the formed chiral layers in Stage 1 and Stage 2, respectively. Where these two chiral fronts meet, the order parameter further drops locally which leads to a further increase of net free energy; see panels (c, d) of Supplementary Figure

6. The chirality of Stage 2 is weaker than that of Stage 1 because the thickness and the order parameter of the chiral layer in Stage 2 are less compared to Stage 1. Therefore, the chirality formed in stage 2 is extremely weak, for this reason, the layer formed in this stage is weakly chiral. We note that this opposite twisting front is a short-lived transient state formed across a few micrometers of the helix and, as can be seen through the Stage 3 and Stage 4, does not affect the overall handedness of cholesteric phase.

Stage (3) in Phase (II): Local order parameter destruction. Fibers located at the intersection of two chiral fronts further lose their order parameter and become essentially isotropic ($S \leq S_c = 0.25$); thereby locally gaining further excess energy. As shown in panels (c, d) of Supplementary Figure 7, loss of order parameter (i.e. being isotropic) and energy accumulation at the intersection are reflected as a minimum and a maximum in order parameter and net free energy profiles, respectively. Interestingly, these extrema take place at $\frac{7p_\infty}{4}$ where the orientation of the fibers is supposed to be in azimuthal direction (i.e. perpendicular to the central axis of the capillary).

Stage (4) in Phase (II): Simultaneous formation of two $\frac{p_\infty}{4}$ cholesteric layers. The locally stored energy at $\frac{7p_\infty}{4}$, where the order parameter is also minimum and the fibers' configuration is essentially isotropic, is relieved. This excess energy relief then creates two local propagating chiral fronts at $\frac{7p_\infty}{4}$ by which two one-fourth of the pitch, $\frac{p_\infty}{4}$, are formed both inward and outward, see panels (a-c) of Supplementary Figure 8.

Supplementary Figure 8 also corresponds to the beginning of the formation of the next chiral layer. Supplementary Movies 4, 6 confirm that these four stages are periodically repeated until reaching to the ground state.

Supplementary Note 6.

Figure 6-2(b, d, f, h, j, l) and Figure 6-3(b, d, f, h) show the order parameter of fibers by use of the blue-to-red spectrum. The blue and red color display low and high order parameter, respectively. Supplementary Figure 9 shows a representative fibers orientation and their order parameter captured by simulation. Note that, throughout our work, the order parameter was obtained by direct numerical simulation.

Supplementary Note 7.

The order-disorder phase transformation is considered as a first-order transition because physical quantities undergo a sharp change through the interface[4]. In this study, we employed the LdG and FOM theories; for this approach, the order parameter has been analytically derived as [5]

$$S = \frac{1}{4} + \frac{1}{4}\sqrt{9 - \frac{24}{U} - \frac{96}{U}\pi^2\left(\frac{\xi}{p_\infty}\right)^2} \quad (1)$$

The unique role of the pitch on S was previously discussed [5]. The typical behavior of the order parameter thus looks like Supplementary Figure 10. If concentration does not reach the phase transition threshold, the phase is isotropic and S=0. Upon exceeding the concentration threshold, the liquid-crystalline phase emerges, and S achieves a finite value less than unity. The order parameter at this jump is called the critical order parameter which has been substantially discussed [6-10]. The relatively low critical order parameter in our study is thus $S_c = \frac{1}{4}$.

In this study, $S<S_c$ takes place while the concentration remains at the cholesteric bulk (see section 'Direct numerical simulation').

Supplementary Note 8.

The homogeneous free energy is a polynomial of uniaxial, S, and biaxial, P, order parameters because of[6,11]

$$\mathrm{Tr}(\mathbf{Q}^2) = \frac{2}{3}\left(S^2 + \frac{1}{3}P^2\right) \quad (2)$$

$$\mathrm{Tr}(\mathbf{Q}^3) = \frac{2}{9}(S^3 - SP^2) \quad (3)$$

In order to understand the behavior of the homogeneous free energy, $\tilde{f}_h$, with respect to the order parameter, it is reasonable to use the widely-accepted assumption of neglecting the biaxial contribution because the biaxial order parameter is considerably smaller compared to uniaxial order parameter, $P \approx 0$[7]. Thus, the homogeneous free energy is expressed as

$$\tilde{f}_h = \frac{1}{3}\left(1\text{-}\frac{U}{3}\right)S^2 - \frac{2U}{27}S^3 + \frac{U}{9}S^4 \quad (4)$$

Supplementary Figure 11 shows that homogenous free energy decreases when the order parameter evolves from a low value to the equilibrium point. Hereafter, for the sake of simplicity, we use the order parameter rather than the uniaxial order parameter throughout the article.

Given the formulation of gradient elastic free energy along with the **Q**-tensor definition, one can see that there is a factor S in all terms.

$$\mathbf{Q} = \mathrm{S}\left(\mathbf{nn} - \frac{\boldsymbol{\zeta}}{3}\right) \tag{5}$$

$$\tilde{f}_g = \frac{1}{2}\left(\frac{\xi}{h_0}\right)^2 \left[\left[\tilde{\nabla} \times \mathbf{Q} + 4\pi\left(\frac{h_0}{p_\infty}\right)\mathbf{Q}\right]^2 + a\left[\tilde{\nabla} \cdot \mathbf{Q}\right]^2\right] \tag{6}$$

where $\boldsymbol{\zeta}$ is the 3D unit dyadic. Reduction in the order parameter leads to decrease of the **Q**-tensor, Supplementary Equation (5), in turn, all penalty terms in gradient elasticity, Supplementary Equation (6), become smaller. For simplicity to show the impact of order parameter reduction on the gradient elastic free energy contribution, it is reasonable to assume that the order parameter is independent of space. In this case, the long-range elastic free energy is rewritten as

$$\tilde{f}_g = \frac{1}{2}\left(\frac{\xi}{h_0}\right)^2 S^2 \left[\left[\tilde{\nabla} \times \left(\mathbf{nn} - \frac{\boldsymbol{\zeta}}{3}\right) + 4\pi\left(\frac{h_0}{p_\infty}\right)\left(\mathbf{nn} - \frac{\boldsymbol{\zeta}}{3}\right)\right]^2 + a\left[\tilde{\nabla} \cdot \left(\mathbf{nn} - \frac{\boldsymbol{\zeta}}{3}\right)\right]^2\right] \tag{7}$$

More specifically, the elastic-free energy is weighted by the squared order parameter and the squared coherence length. Therefore, a reduction in the magnitude of the order parameter leads to a lower gradient elastic free energy.

Aside from the impact of order parameter and coherence length on the elastic free energy, the pitch length can also have an impact on elastic free energy, especially affecting the early relaxation. The excess elastic free energy is higher for smaller pitch lengths as the deviation from the ground state increases. Supplementary Table 1 summarizes how elastic free energy is affected by the order parameter, coherence length, and pitch length. It should, however, be mentioned that we did not apply the simplifying assumption of the constant order parameter in direct numeric simulations.

Supplementary Note 9.

In the given confinement, the relaxation dynamics depend on pitch length and coherence length. In this section, we focus on how a relaxation dynamic gradually switches from a slow-fast relaxation dynamic to a smooth relaxation dynamic and vice versa.

The impact of pitch length, coherence length, and order parameter on the elastic free energy are summarized in Supplementary Table 1. Interaction between these parameters determines the type of relaxation dynamics, see Supplementary Figure 12. Depending on material-related properties of pitch length and coherence length, an excess elastic free energy is induced at the beginning of relaxation as a result of the non-equilibrium configuration of fibers (i.e. para-nematic phase). As explained in the Supplementary Note 8 and shown in Supplementary Table 1, Supplementary Figure 12, the excess elastic free energy is positively and inversely affected by the coherence length and pitch length, respectively. The next step in the relaxation is to relieve excess energy by reducing the order parameter. This step takes place to cancel out, or at least to alleviate the initial excess energy. So far Phase (I) is completed. Phase (II) is chiral front propagation. Using direct numerical simulations, we found that there can be three cases for type of relaxation dynamics as illustrated in Supplementary Figure 12.

Supplementary Note 10.

The purpose of this section is to show that confinement, i.e. curvature of the capillary, has a considerable impact on relaxation dynamics. The well-established Frank-Oseen (FO) free energy can also describe the relaxation dynamics of a single helix[12].

$$f_{FO} = \frac{1}{2}K_1(\nabla \cdot \mathbf{n})^2 + \frac{1}{2}K_2(\mathbf{n} \cdot (\nabla \times \mathbf{n}) + q_\infty)^2 + \frac{1}{2}K_3\big(\mathbf{n} \times (\nabla \times \mathbf{n})\big) \cdot \big(\mathbf{n} \times (\nabla \times \mathbf{n})\big) \quad (8)$$

K_1, K_2, K_3 stand for splay, twist and bend modes of deformation, respectively. **n** is unit vector representing the fibers' orientation. Before proceeding to reveal the curvature role in relaxation dynamics by making use of Frank-Oseen, it should be mentioned that Frank-Oseen is a subset of the **Q**-tensor Frank-Oseen-Mermin gradient energy, Equation (6-9). These two methods, FO and FOM, can be converted to each other by use of **Q**-tensor definition, Supplementary Equation (5), and mapping between L_i and K_i discussed in references[12,13].

To meet the constraint of unit length, the unit vector is considered as $\mathbf{n} = \begin{bmatrix}\sin(\varphi(y,t)) & 0 & \cos(\varphi(y,t))\end{bmatrix}$ where $\varphi(y,t)$ is the angle between the director and x-axis. This consideration simplifies the elasticity free energy as

$$f_{F0} = \frac{1}{2}K_2\left(q_\infty - \frac{\partial\varphi(y,t)}{\partial y}\right)^2 \tag{9}$$

By use of Supplementary Equation (9), the Leslie–Ericksen model reduces to

$$\frac{\partial\varphi}{\partial t} = \frac{K_2}{\Gamma}\frac{\partial^2\varphi}{\partial y^2} \tag{10}$$

where Γis rotational viscosity of a single helix. Given Supplementary Figure 13, the initial and boundary conditions are expressed by

$$\text{IC: } \varphi(y,0) = 0 \tag{11}$$

$$\text{BC: } \begin{cases} \varphi(0,t) = 0 \\ \varphi(L,t) = q_\infty L \end{cases} \tag{12}$$

Therefore, the analytical solution of relaxation dynamics reads

$$\varphi(y,t) = q_\infty y + \sum_{k=1}^{\infty} A_k \sin\left(\frac{k\pi}{L}y\right)\exp\left(-\frac{K_2}{\Gamma}\left(\frac{k\pi}{L}\right)^2 t\right) \tag{13}$$

$$A_k = 2\frac{(-1)^k L q_\infty}{k\pi} \tag{14}$$

Note that the upper boundary condition comes from the steady solution, $\varphi(L) = q_\infty L$. Knowing the steady-state solution yields the instantaneous chiral wavevector definition as $q(y,t) = \frac{\varphi(y,t)}{y}$ which meets both boundaries of relaxation (i.e. $q(y,0) = 0$ and $q(y,\infty) = q_\infty$). Therefore, the relaxation progress, R, is expressed as

$$R = \frac{\bar{q}(t)}{q_\infty} = 1 + \sum_{k=1}^{\infty}\left(\frac{2(-1)^k}{k\pi}\right)\left(\int_0^L \frac{\sin\left(\frac{k\pi}{L}\zeta\right)}{\zeta}d\zeta\right)\exp\left(-\frac{K_2}{\Gamma}\left(\frac{k\pi}{L}\right)^2 t\right) \tag{15}$$

The Supplementary Figure 14 illustrates that relaxation generally obeys the first-order dynamic in an unconfined planar geometry. Thus, slow-fast relaxation does not emerge for the unconfined planar system.

In conclusion, relaxation dynamics also depend on the curvature. Characterizing the curvature impact on relaxation is beyond the scope of this work.

Supplementary Note 11.

As can be seen in Supplementary Figure 15, the best curves fitting the experiment and simulation result in estimation of rotational viscosity coefficient, η, and coherence length, ξ. Then, L_1 and rotational viscosity are estimated by use of Equation (6-2) and Equation (6-3), respectively.

Supplementary Note 12.

The capillaries were filled with the birefringent solution which is the bulk cholesteric. According to the thermodynamics of phase equilibria, the bulk cholesteric is at a constant concentration equal to the upper binodal curve, see Supplementary Figure 16.

Supplementary Note 13.

The finite element (FE) technique with biquadratic basis functions was employed to carry out the simulations. In this regard, the governing equations, Equations (6-5 through 6-9), along with axillary conditions, Equations (6-10 and 6-11), and parameters tabulated in Supplementary Table 2 were implemented in the General PDE solver of COMSOL Multiphysics 5.3a on our in-house supercomputer. Note that the model used in this study is a tensorial equation, leading to five second-order time-dependent nonlinear coupled PDEs. Time stepping was executed using Backward Differentiation Formula (BDF) with varying orders from one (known as the backward Euler method) to five.

All simulations are performed in a 3D computational domain except those which are intended for comparison with the POM images. Supplementary Figure 17 shows the geometries and the simulation type used in this study.

Supplementary Note 14.

The dimensionless normalized relaxation progress curve, R, is computed in the lateral plane (xy-plane), see Figure 6-1(o). The ideal director field representing a monodomain along with x-axis reads

$$\mathbf{n} = [\sin(q_\infty z) \quad -\cos(q_\infty z) \quad 0] \tag{16}$$

Moreover, we have $\mathbf{Q}:\nabla\times\mathbf{Q} = S^2\mathbf{nn}:\nabla\times\mathbf{nn}$—this identity is proven in accordance with **Q**-tensor definition and tensorial operations, explained as follows.

The **Q**-tensor is defined as $\mathbf{Q} = S\left(\mathbf{nn} - \frac{\boldsymbol{\delta}}{3}\right)$ in which $\boldsymbol{\delta}$ denotes the second rank unit dyadic. Substitution of **Q**-tensor definition in $\mathbf{Q}:\nabla\times\mathbf{Q}$ yields

$$\mathbf{Q}:\nabla\times\mathbf{Q} = S\left(\mathbf{nn} - \frac{\boldsymbol{\delta}}{3}\right):\nabla\times\mathbf{Q} = S\mathbf{nn}:\nabla\times\mathbf{Q} - S\frac{\boldsymbol{\delta}:\nabla\times\mathbf{Q}}{3} \tag{17}$$

As $\boldsymbol{\delta}:\nabla\times\mathbf{Q} = \mathrm{Tr}(\nabla\times\mathbf{Q})$ and $\mathrm{Tr}(\nabla\times\mathbf{Q}) = 0$due to the symmetric traceless property of the **Q**-tensor, Supplementary Equation (17) reduces to

$$\mathbf{Q}:\nabla\times\mathbf{Q} = S\mathbf{nn}:\nabla\times\mathbf{Q} \tag{18}$$

Once again using the **Q**-tensor definition to find the equivalent form of the curl of **Q**-tensor, $\nabla\times\mathbf{Q} = S\nabla\times\mathbf{nn}$, and Supplementary Equation (18) finally gives

$$\mathbf{Q}:\nabla\times\mathbf{Q} = S^2\mathbf{nn}:\nabla\times\mathbf{nn} \tag{19}$$

Having substituted Supplementary Equation (16) into Supplementary Equation (19), the relation between **Q**-tensor and the relaxed chiral wavevector becomes $q_\infty = \frac{-\mathbf{Q}:\nabla\times\mathbf{Q}}{S^2}$. In addition, knowing the fact that $\mathbf{Q}:\mathbf{Q} = \frac{2S^2}{3}$ leads to

$$q_\infty = -\frac{2}{3}\frac{\mathbf{Q}:\nabla\times\mathbf{Q}}{\mathbf{Q}:\mathbf{Q}} \tag{20}$$

Because the quantity on the right-hand side approaches to the definite value of the relaxed chiral wavevector in the course of time, in order to quantify the relaxation, we define the dimensionless spatio-temporal chiral wavevector as

$$\tilde{q}(\tilde{\mathbf{x}},\tilde{t}) = -\frac{2}{3}\frac{\mathbf{Q}:\tilde{\nabla}\times\mathbf{Q}}{\mathbf{Q}:\mathbf{Q}} \tag{21}$$

Supplementary Equation (21) satisfactorily meets the limits of relaxation because it is simplified to $\tilde{q}(\tilde{\mathbf{x}},\tilde{t}) = 0$ (equivalently $\tilde{p}_\infty(\tilde{\mathbf{x}},\tilde{t}) = \infty$) and $\tilde{q}(\tilde{\mathbf{x}},\tilde{t}) = \tilde{q}_\infty = \frac{2\pi}{\tilde{p}_\infty}$for achiral and

chiral nematic phases, respectively. The tilde symbol denotes dimensionless quantities (e.g. $\widetilde{\nabla} = h_0\nabla$). Hereafter, we omit the tilde for brevity.

Owing to fact that Supplementary Equation (21) is derived for the ideal director field represented in Supplementary Equation (16), and knowing that $\bar{q}(t)$is computed by direct numerical simulation, there could be a slight difference in the prediction of q_∞ at equilibrium. In this regard, we re-define the chiral wavevector as $q(\mathbf{x},t) = -\frac{\chi \mathbf{Q}:\nabla\times\mathbf{Q}}{\mathbf{Q}:\mathbf{Q}}$ and therefore

$$\bar{q}(t) = -\frac{\chi}{A_t}\int_A \frac{\mathbf{Q}:\nabla\times\mathbf{Q}}{\mathbf{Q}:\mathbf{Q}}\,dA \tag{22}$$

where A_t stand for the total area of the lateral plane (xy-plane). χ plays a scaling role in order to reach q_∞. χ is quite close to the ideal value that is 0.67, see Supplementary Equation (21). For example, $\chi_{BLG} = 0.63$ and $\chi_{CNC} = 0.59$. The exact value of χ can also be formulated by the use of the relaxation boundary condition that $q_\infty = -\frac{\chi}{A_t}\left(\int_A \frac{\mathbf{Q}:\nabla\times\mathbf{Q}}{\mathbf{Q}:\mathbf{Q}}\,dA\right)_e$ in which subscript e shows the equilibrium point. Therefore, the relaxation progress, $R(t) = \frac{\bar{q}(t)}{q_\infty}$, is expressed by

$$R(t) = \frac{\int_A \frac{\mathbf{Q}:\nabla\times\mathbf{Q}}{\mathbf{Q}:\mathbf{Q}}\,dA}{\left(\int_A \frac{\mathbf{Q}:\nabla\times\mathbf{Q}}{\mathbf{Q}:\mathbf{Q}}\,dA\right)_e} \tag{23}$$

Now that the normalized relaxation progress, Supplementary Equation (23) or Equation (6-12), is formulated and our experimental-theoretical approach reveals that the dark zone in the POM images is a para-nematic phase with the order parameter of nearly 0 to 0.4, the conceptual understanding of this quantity (R) deserves more discussion. As explained in the paper, when R is computed via the discretization of the time-series POM images, R is taken to be 0 and 1 in dark and fingerprint partitions, respectively. R=0 is equivalent to q=0 signifying that the phase is para-nematic and R=1 indicates $q=q_\infty$ representing that the phase is cholesteric. In the case of BLG relaxation (i.e. Figure 6-2), the R distribution theoretically becomes as what is shown in Supplementary Figure 18.

In the case of CNC, the para-nematic phase loses its order parameter to an extremely low value, $S\sim10^{-2}$, see Supplementary Figure 19.

The actual fibers' orientation can be understood in light of two factors. First, the uniaxial director field, **n**, representing the average fibers' orientation. Second, the uniaxial order

parameter, S, describing the strength of fibers alignment around **n**. Fibers lie perfectly parallel to **n** if S=1 and the resulting phase becomes more crystal-like. In the case of $S \approx S_c \sim 0.7$, fibers retain both fluidity and crystallinity (orientational order), corresponding to the liquid-crystalline phase. Finally, $S<S_c$ indicates that the actual fibers' orientation can be less aligned around **n**; hence, the phase possesses more fluid-like characteristics rather than crystalline ones[5,8,10,14-16]. As explained in the Supplementary Note 7, there is no unanimous agreement on the S_c value; however, $S_c=0.25$ suits for the theory used in our study. Accordingly, wherever $S<S_c$, the fibers' orientation is randomly visualized in order to emphasize the concept of critical order parameter and the fact that orientational ordering is weak, see Supplementary Figure 20.

Wherever $S<S_c$, the phase can also be called isotropic due to the fact that the correlation existing among fibers is insignificant. However, the distinguishing point that should be taken into account is that the concentration of the isotropic phase is still at the upper binodal curve, which is unequivocally greater than the critical order-disorder transition, see "Direct numerical simulation" section for discussion on the concentration field in the present study.

Supplementary Note 15.

The purpose of this note is to show that the **Q**-tensor spatio-temporal evolution equation can be projected into the vector force balance equation containing the divergence of the total stress tensor. The spatio-temporal orientational ordering is expressed by

$$\gamma \frac{\partial \mathbf{Q}}{\partial \mathrm{t}} = -\left(\frac{\partial \mathrm{f}}{\partial \mathbf{Q}}\right)^{[\mathrm{s}]} + \left(\nabla \cdot \left(\frac{\partial \mathrm{f}}{\partial \nabla \mathbf{Q}}\right)\right)^{[\mathrm{s}]} = \mathbf{H}^{[\mathrm{s}]} \tag{24}$$

where f is the Helmholtz free energy density per unit volume and **H** is the molecular field. To derive the 3D force balance equation, the double inner product of Supplementary Equation (24) and $\nabla \mathbf{Q}$ yields

$$\gamma(\nabla \mathbf{Q}) : \left(\frac{\partial \mathbf{Q}}{\partial \mathrm{t}}\right) = -(\nabla \mathbf{Q}) : \left\{\left(\frac{\partial \mathrm{f}}{\partial \mathbf{Q}}\right)^{[\mathrm{s}]} + \left(\nabla \cdot \left(\frac{\partial \mathrm{f}}{\partial \nabla \mathbf{Q}}\right)\right)^{[\mathrm{s}]}\right\} \tag{25}$$

Knowing that **Q** is symmetric traceless leads to dropping [s], and using the transpose of third-order tensors, we rewrite Supplementary Equation (25) as:

$$\gamma\left(\frac{\partial \mathbf{Q}}{\partial \mathrm{t}}\right) : (\nabla \mathbf{Q})^{\mathrm{T}} = -\left(\frac{\partial \mathrm{f}}{\partial \mathbf{Q}}\right) : (\nabla \mathbf{Q}\ \ )^{\mathrm{T}} + \left(\nabla \cdot \left(\frac{\partial \mathrm{f}}{\partial \nabla \mathbf{Q}}\right)\right) : (\nabla \mathbf{Q})^{\mathrm{T}} = \mathbf{H} : (\nabla \mathbf{Q})^{\mathrm{T}} \tag{26}$$

Given that f can be considered as homogenous and gradient contributions, we then formulate the gradient of f.

$$f = f(\mathbf{Q}, \nabla\mathbf{Q}) = f_h(\mathbf{Q}) + f_g(\mathbf{Q}, \nabla\mathbf{Q}) \tag{27}$$

$$\nabla f = \frac{\partial f}{\partial \mathbf{Q}} : (\nabla\mathbf{Q})^T + \frac{\partial f}{\partial \nabla\mathbf{Q}} \vdots (\nabla\nabla\mathbf{Q})^T \tag{28}$$

Now we focus on the last term $\frac{\partial f}{\partial \nabla\mathbf{Q}} \vdots (\nabla\nabla\mathbf{Q})^T$which can be written as $\frac{\partial f}{\partial \nabla_p \mathbf{Q}_{mo}} \vdots \nabla_i\nabla_p\mathbf{Q}_{mo}$ by making use of a dual index notation method (Einstein and indicial free) to facilitate the subsequent tensor derivations:

$$\begin{aligned} &\frac{\partial f}{\partial \nabla_p \mathbf{Q}_{mo}} \vdots \nabla_i\nabla_p\mathbf{Q}_{mo} = \frac{\partial f}{\partial \nabla_p \mathbf{Q}_{mo}} \vdots \nabla_p\nabla_i\mathbf{Q}_{mo} = \\ &\nabla_p \cdot \left\{ \frac{\partial f}{\partial \nabla_p \mathbf{Q}_{mo}} : \nabla_i\mathbf{Q}_{mo} \right\} - \left(\nabla_p \cdot \left(\frac{\partial f}{\partial \nabla_p \mathbf{Q}_{mo}} \right) \right) : \nabla_i\mathbf{Q}_{mo} \end{aligned} \tag{29}$$

Or equivalently

$$\frac{\partial f}{\partial \nabla\mathbf{Q}} \vdots (\nabla\nabla\mathbf{Q})^T = \nabla \cdot \left\{ \frac{\partial f}{\partial \nabla\mathbf{Q}} : (\nabla\mathbf{Q})^T \right\} - \left(\nabla \cdot \left(\frac{\partial f}{\partial \nabla\mathbf{Q}} \right) \right) : (\nabla\mathbf{Q})^T \tag{30}$$

Substituting Supplementary Equation (30) into Supplementary Equation (28) yields

$$-\nabla f + \nabla \cdot \left\{ \frac{\partial f}{\partial \nabla\mathbf{Q}} : (\nabla\mathbf{Q})^T \right\} = -\frac{\partial f}{\partial \mathbf{Q}} : (\nabla\mathbf{Q})^T + \left(\nabla \cdot \left(\frac{\partial f}{\partial \nabla\mathbf{Q}} \right) \right) : (\nabla\mathbf{Q})^T \tag{31}$$

Comparing Supplementary Equations (26, 31) results in

$$\gamma \left(\frac{\partial \mathbf{Q}}{\partial t} \right) : (\nabla\mathbf{Q})^T = -\nabla f + \nabla \cdot \left\{ \frac{\partial f}{\partial \nabla\mathbf{Q}} : (\nabla\mathbf{Q})^T \right\} = \mathbf{H} : (\nabla\mathbf{Q})^T \tag{32}$$

Additionally, we know that the mechanical bulk total elastic stress tensor $\mathbf{T}$ is

$$\mathbf{T} = f\,\mathbf{I} + \mathbf{T}^E \tag{33}$$

$$\mathbf{T}^E = -\frac{\partial f_g}{\partial \nabla\mathbf{Q}} : (\nabla\mathbf{Q})^T \tag{34}$$

where $\mathbf{T}^E$ is the Ericksen stress tensor, and the pressure p=-f is minus the free energy density. Then, the bulk vector force balance Supplementary Equation (25) reads:

$$-\gamma(\nabla\mathbf{Q}) : \left(\frac{\partial \mathbf{Q}}{\partial t} \right) = \nabla \cdot \mathbf{T} \tag{35}$$

The total stress tensor, Supplementary Equations (33, 34), carries information on f and $-\frac{\partial f_g}{\partial \nabla \mathbf{Q}} : (\nabla \mathbf{Q})^T$. The vector mechanical force balance, Supplementary Equation (35), carries less information than the original tensorial **Q**-tensor equation, Supplementary Equation (24) since the former is a vector equation and the latter a tensor equation. Consequently, when we simulate the **Q**-tensor process in the absence of mass velocity (**v**=0), the **Q**-tensor model carries more information by just focusing on the tensorial variational derivative of the free energy instead of the vectorial divergence of the stress.

The total elastic stress **T** is always present $\mathbf{T} \neq \mathbf{0}$ and, in consequence, the elastic force **F** which is the divergence of the total bulk elastic stress is also nonzero, $\mathbf{F} = \nabla \cdot \mathbf{T} \neq \mathbf{0}$ as **F** is balanced by $\gamma \left(\frac{\partial \mathbf{Q}}{\partial t}\right) : (\nabla \mathbf{Q})^T + \mathbf{F} = \mathbf{0}$. To sum up, there is no applied external stress in this experiment or in this model, and there is only internal stress (**T**) properly embedded in the modeling used in this study.

References of Supporting Information (Chapter 6)

1 Nyström, G., Arcari, M. & Mezzenga, R. Confinement-induced liquid crystalline transitions in amyloid fibril cholesteric tactoids. Nat. Nanotech. **13**, 330-336, (2018).

2 Nyström, G., Arcari, M., Adamcik, J., Usov, I. & Mezzenga, R. Nanocellulose fragmentation mechanisms and inversion of chirality from the single particle to the cholesteric phase. ACS nano **12**, 5141-5148 (2018).

3 Usov, I. & Mezzenga, R. FiberApp: an open-source software for tracking and analyzing polymers, filaments, biomacromolecules, and fibrous objects. Macromolecules **48**, 1269-1280 (2015).

4 Gobeaux et al. Cooperative Ordering of Collagen Triple Helices in the Dense State. Langmuir **23**, 6411-6417, (2007).

5 De Luca, G. & Rey, A. D. Chiral front propagation in liquid-crystalline materials: Formation of the planar monodomain twisted plywood architecture of biological fibrous composites. Phys. Rev.E, **69**, 011706, (2004).

6 Khadem, S. A. & Rey, A. D. Thermodynamic Modelling of Acidic Collagenous Solutions: From Free Energy Contributions to Phase Diagrams. Soft Matter, (2019).

7 Khadem, S. A. & Rey, A. D. Theoretical Platform for Liquid-Crystalline Self-Assembly of Collagen-Based Biomaterials. Front. Phy., **7**, (2019).

8 Matsuyamaa, A. & Hirashima, R. Phase separations in liquid crystal-colloid mixtures. Jour. Chem. Phys. **128**, 11, (2008).

9 Das, S. K. & Rey, A. D. Computational modelling of multi-phase equilibria of mesogenic mixtures. Comp. Mat. Sci. **29**, 152-164, (2004).

10 Doi, M. & Edwards, S. F. The theory of polymer dynamics. Vol. 73 (1988).

11 Gennes, P. G. d. & Prost, J. The Physics of Liquid Crystals. (1995).

12 Muševič, I. Liquid Crystal Colloids. (2017).

13 Zhang, R., Zhou, Y., Rahimi, M. & De Pablo, J. J. Dynamic structure of active nematic shells. Nat. Commun. **7**, 13483 (2016).

14 De Luca, G. & Rey, A. D. Ringlike cores of cylindrically confined nematic point defects. Jour. Chem. Phy. **126**, 094907 (2007).

15 Gupta, G. & Rey, A. D. Texture rules for concentrated filled nematics. Phys. Rev. Lett. **95**, 127802 (2005).

16 De Luca, G. & Rey, A. D. Point and ring defects in nematics under capillary confinement. Jour. Chem. Phy. **127**, 104902 (2007).

Chapter 7. Conclusions and Outlook

7.1 General Conclusions

In summary, we have successfully developed a Helmholtz free energy that is capable of accurately determining the isotropic-to-cholesteric thermodynamic equilibrium concentration boundaries for chiral rod-like mesogens dispersed in an aqueous solution; notably, the resulting model is applicable to BCLLCs. The developed thermodynamic model was then carefully tested and validated for collagen fibers dispersed in acidic aqueous solutions. The results were in great agreement with available experimental data as well as fully consistent with fundamental LC theory and polymer science.

Building on that thermodynamic model, which was developed from first principles and validated, we thereafter proceeded to formulate and solve governing equations for BCLLCs self-assembly to finally obtain a full mesoscopic (ranging from nano to micro length scale) description of the BCLLCs structure and concentration as a function of time and space—the equations are time-dependent nonlinear Partial Differential Equations (PDEs); five second-order PDEs and one fourth-order PDE for describing the orientation of fibers and mass transfer, respectively. Solving the governing equations yielded the following outcomes : (1) An in-depth understanding of the cholesteric growth in the meta-stable isotropic zone (i.e. the zone bounded between the lower binodal boundary and the lower NG boundary) was obtained. (2) The NG zone existing in the biphasic zone, where multi tactoids grow unconditionally, was explored. After that, the NG zone was thoroughly discussed in fundamental terms such as tactoids' size, morphology, population, growth laws, and more. (3) Dynamical relaxations of BCLLCs, especially BLG and CNC, from para-nematic to cholesteric (PN-N*) were explored and elucidated in detail.

The specific technical conclusions that can be drawn from each research chapter are summarized as follows.

Chapter 3 : Thermodynamic modelling of acidic collagenous solutions: from free energy contributions to phase diagrams

Several simultaneous physics are involved in the BCLLCs self-assembly: excluded volume affecting orientational and translational entropy (i.e. Onsager's theory), the orientation-dependent attractive interactions due to van der Waals interactions (i.e. Maier–Saupe theory),

the Columbic repulsion as a result of like-charges attached on the fibers' backbone, elasticity, chirality, and enthalpic contribution. Except for Columbic repulsion, the other phenomena come from previous well-known theories. To avoid computationally demanding approaches such as Poisson–Boltzmann theory, we developed a simplified model to take into account the contribution of Columbic repulsion. Finally, all these phenomena and interactions were integrated to develop the net Helmholtz free energy tailored for colloidal rod-like cholesterogens dispersed in a small-sized monomeric solvent. Having completed the theory and modeling formulation stage, the model was evaluated according to a variety of criteria: available experimental data and consistency with the previous well-established theories in both liquid crystal and polymer science. In this regard, for collagen fibers dispersed in acidic aqueous solutions, LC concentration as a function of solvent concentration and temperature as a function of LC concentration binodal lines were constructed. The former is in excellent agreement with the partial experimental phase diagram reported. The latter shows a chimney-like shape which is consistent with the principles of polymeric solutions comprising rod-like rigid polymers dispersed in a monomeric solvent. The proposed model is also consistent with the past well-known theories such as Landau–de Gennes (LdG) and Onsager. Furthermore, the validation was successful in fulfilling other criteria such as the isotropic-to-cholesteric (I/N*) order parameter, first-order phase transition, and agreement with other past impactful studies.

We then proceeded to understand the impact of each physics contributing to the isotropic-to-cholesteric phase transition. In this regard, we found that phase ordering is mainly affected by the excluded-volume, the impact of the intermolecular interactions (repulsion, twisting, and attraction) is moderate, and the impact of macroscopic chirality is negligible. We additionally explored that, as acid concentration increases, i.e. pH decreases, in consequence, the linear charge density increases, leading to narrowing the biphasic zone.

Chapter 4 : Theoretical Platform for Liquid-Crystalline Self-Assembly of Collagen-Based Biomaterials

Building on Chapter 3, we included biaxiality into the Helmholtz free energy. Consistent with previous theoretical studies, the biaxiality of chiral nematic liquid crystals was found negligible at the ground state. We then formulated the dynamical governing equations through which both the conserved field (LC concentration) and the non-conserved field (fibers orientation) can be captured as a function of time and space. We thus relied on the Helmholtz

free energy and the governing equations to elucidate the cholesteric growth of small chiral seed growing in an isolated fashion – meaning that no tactoidal collisions take place. The salient feature of the proposed modeling and simulation is that the self-assembly is precisely captured in multi-scale time and space. As a result, we explored that a τ^{+1} defect forms in the center of the growing tactoid at the beginning of growth—The defect size and tactoid size are in the range of nanometer and micrometer, respectively. As time elapses, the frustration effect that generated a singular defect vanishes, and a low energy non-singular escaped λ^{+1} disclination appears in a short time span. This finding is of prime importance for nano-particle dispersed in cholesterics since the high energy spot like a τ^{+1} defect attracts nano-particle to relieve excess energy.

Chapter 5 : Nucleation and growth of cholesteric collagen tactoids: A time-series statistical analysis based on integration of direct numerical simulation (DNS) and long short-term memory recurrent neural network (LSTM-RNN)

In Chapter 5, we employed the governing equations developed in Chapter 4 to investigate the kinetics of phase separation and ordering associated with the NG mechanism for colloidal collagen fibers dispersed in acidic solutions. Through simulations of self-assembly at different quenches (i.e. different concentrations) in the biphasic zone of the equilibrium phase diagram developed in Chapter 3, we first identified the NG zone. Each NG quench contains three stages: induction, nucleation, and coarsening. For each of these stages, we then revealed the quench dependency of fundamentals quantities such as induction time, nucleation duration, and tactoids' size, population, morphology, growth laws, and more across the NG zone. After delivering exhaustive characterization of the NG zone, we used the free energy analyses to rationalize the quench dependence of fundamentals quantities. Owing to the fact that the DNS of each NG quench is computationally expensive, we used a hybrid method based on DNS and LSTM-RNN in the cascade fashion to reduce the computational cost. This hybrid approach not only further expands the results associated with the tactoids' population, but also proposes a systematic framework to use LSTM-RNN as a surrogate fast-response model by which part of time-dependent results is estimated significantly faster compared to DNS. Having obtained a rich database on the characterization, we then used classical and symbolic regression to formulate wide-range engineering correlations for the characterizations, facilitating future studies.

We furthermore addressed a fundamental question that what physics governs the growth laws' exponent during nucleation and coarsening for BCLLCs. We demonstrated that the non-diffusive model (i.e. the model without mass transfer consideration) only results in $n \approx 1$. In other words, we concluded that if $n \rightarrow 1$ indicates that a self-assembly mechanism in which orientational ordering is dominant and mass transfer is weak. Also, the lower exponents are due to interactions between conserved and non-conserved fields, i.e. mass transfer and long-range orientational ordering, respectively.

Chapter 6 : Relaxation dynamics in bio-colloidal cholesteric liquid crystals confined to cylindrical geometry

Through an experimental study performed by our ETH-Zurich collaborators, two distinct dynamics were observed for the relaxation from para-nematic to cholesteric (PN-N*) in BLG and CNC dispersions. We then found that DNS is capable of accurately predicting the observations. Building on DNS and free energy analyses, we revealed that the different dynamics are due to the interplay between chirality, viscoelasticity, and confinement. The interplay consequently affects the order parameter of the mesophasic medium, leading to different dynamics. Moreover, we generalized that there can be considered two prime categories for PN-N* relaxations of BCLLCs, depending on the chirality and elasticity for given cylindrical confinement. We called these categories slow-fast and smooth relaxation, taking place for BLG and CNC, respectively.

In addition, owing to the accuracy of DNS in the prediction of the relaxation dynamics, a systematic approach was proposed by which some of the mesophasic properties including viscoelastic ones can be estimated (e.g. rotational viscosity, rotational viscosity coefficient, coherence length, elastic constant (L_1), and order parameter of the medium). It should be further noted that the proposed method for measuring viscoelastic properties is by far more convenient in comparison with the conventional ones.

7.2 Contributions to Original Knowledge

The current Ph.D. thesis contributed to the findings of both thermodynamics and kinetics of BCLLCs self-assembly. We particularly focused on the phase diagram, cholesteric growth in absence of tactoidal collisions, cholesteric nucleation and growth in which tactoidal collisions

are inevitable, and dynamics of relaxation from para-nematic to cholesteric, which all have not been understood before despite their vital roles in material science and engineering.

The following list is a summary of the original contributions to knowledge emanating from the present Ph.D. thesis.

- Developed, implemented, and validated the Helmholtz free energy which is capable of accurately providing a full mesoscopic description of BCLLCs self-assembly in both thermodynamic and kinetics contexts.
- Determined the lower and upper binodal phase transition boundaries for collagen dispersions through which the isotropic, biphasic, and cholesteric zones are delineated in the phase diagram. These phase transition boundaries are presented in the phase diagrams as follows; LC concentration vs. solvent concentration and temperature vs. LC concentration.
- Explored the physics controlling the phase transitions in collagen dispersions; the phase transition is mainly controlled by excluded volume, and moderately by interchain attractive and repulsive interactions, and almost unaffected by macroscopic chirality.
- Explored the defect formation and escape through the evolution of a cholesteric tactoid. At the center of the growing tactoid, a nanometer-sized τ^{+1} defect is formed in the early growth regime, thereafter over a short time span, the defect is transformed into a non-singular escaped λ^{+1} disclination and the tactoid then evolves to micrometer size.
- Determined the nucleation and growth zone in the biphasic zone of the collagen phase diagram.
- Characterized the nucleation and growth zone in the terms of fundamental quantities such as induction time, nucleation duration, droplets' size, morphology, population, growth laws, and more.
- Proposed a hybrid approach based on DNS and LSTM-RNN to reduce computational cost in self-assembly simulations.
- Formulated wide-range correlations showing the quench dependence of fundamental quantities named above.

- Elucidated the physical origins behind the nucleation and growth mechanism notably the quench dependence of fundamental quantities and growth laws' exponents during nucleation and coarsening.
- Revealed the mechanisms and the governing physics of PN-N* relaxations in BCLLCs dispersions.
- Proposed a systematic novel approach to measure viscoelastic properties such as Landau elastic constant (L_1) and rotational viscosity, which are barely measurable for BCLLCs with conventional methods.

7.3 Recommendations for Future Work

The following list summarizes suggested research avenues for future studies. These suggestions are derived from the current Ph.D. thesis.

- In addition to nematic and cholesteric phases, it has recently been reported that the collagen dispersions may possess other liquid crystalline phases such as orthogonal [1]. It is thus legitimate to explore the location of other liquid crystalline phases in the phase diagram presented in Chapter 3.

- As explained in Chapter 5, DNS is computationally demanding. In this chapter, LSTM-RNN is utilized as a surrogate model by which tactoids' population is estimated considerably faster. Therefore, devising fast-response techniques such as applying machine learning methods to predict other quantities deserve consideration.

- We investigated cholesteric growth in the meta-stable isotropic zone and the NG zone. It is recommended that future studies are defined to characterize the rest of the biphasic zone in which other mechanisms of phase separation and ordering can take place (e.g. negative tactoids)

- Our results for the relaxation of BCLLCs from PN-N* were obtained for cylindrical confinement. However, we showed that confinement geometry can have an impact on the relaxation dynamics. As a result, future works on the confinement impact on the relaxation dynamics can be beneficial, leading to the generalization of the results obtained in Chapter 6.

References

1. Tidu, A.; Ghoubay-Benallaoua, D.; Teulon, C.; Asnacios, S.; Grieve, K.; Portier, F.; Schanne-Klein, M.-C.; Borderie, V.; Mosser, G., Highly concentrated collagen solutions leading to transparent scaffolds of controlled three-dimensional organizations for corneal epithelial cell colonization. Biomaterials science **2018,** 6 (6), 1492-1502.